Fluorescent nanodiamonds as a sensor and life science probe

Von der Fakultät 8 Mathematik und Physik der Universität Stuttgart
zur Erlangung der Würde eines Doktors der Naturwissenschaften
(Dr. rer. nat.) genehmigte Abhandlung

Vorgelegt von

Torsten Rendler

aus Offenburg

Hauptberichter:	Prof. Dr. Jörg Wrachtrup
Mitberichter:	Prof. Dr. Peter Michler

Tag der mündlichen Prüfung: 18. Dezember 2017

3. Physikalisches Institut der Universität Stuttgart

2018

Dedicated to the memory of my Father
Günther Rendler (†2015).

I miss you more than words can say.

Contents

Title i

Contents v

List of Figures ix

List of Tables xiii

List of Abbreviations xiv

List of special units xxi

1. Summary 1

2. Zusammenfassung 9

3. Basics 17

3.1. Single molecule spectroscopy 17

3.1.1. Confocal scanning microscopy 17

3.1.2. (Auto-)correlation function 19

3.2. Nanodiamonds 25

3.2.1. Diamond 25

3.2.2. Production of (nano)diamond 25

3.2.3. The surface of (nano)diamond 28

3.2.4. Color defects in (nano)diamond 31

3.2.5. Creating color centers in (nano)diamond 46

3.2.6. Size effects and stability of color centers 48

3.3. Basic principles of electron paramagnetic resonance and nuclear magnetic resonance . . . 49
3.3.1. Spins interacting with oscillating magnetic fields . . . 49
3.3.2. Rabi nutations . . . 50
3.3.3. The Bloch equations . . . 51
3.4. Quantum mechanical description of spin systems . . . 52
3.4.1. The von Neumann equation . . . 52
3.4.2. Quantum Master equation . . . 53
3.4.3. Controlling Spins . . . 55
3.4.4. Sensing in a coherent superposition . . . 64
3.4.5. Noise spectroscopy . . . 68
3.5. Cells . . . 80

4. Molecular sized fluorescent nanodiamonds 87
4.1. Setup . . . 88
4.2. Photoluminescence spectra . . . 90
4.3. Lifetime measurements . . . 92
4.4. Emission rate of SiV^- in MNDs . . . 94
4.4.1. Auto-correlation and weak signals . . . 95
4.4.2. Detailed analysis of single dim spot . . . 97
4.4.3. Data from collaboration partners . . . 101
4.5. Summary, Conclusion and Outlook . . . 103

5. CW nano thermometry in living cells 105
5.1. Experimental setup . . . 106
5.2. Control experiments . . . 108
5.2.1. Sample characterization . . . 108
5.2.2. Binding of ND-TPP to mitochondria . . . 111
5.2.3. Cell viability: Influence of laser irradiation . . . 114
5.2.4. Cell viability: Influence of CCCP . . . 116
5.3. CW nano thermometry . . . 117
5.3.1. Robustness of CW nano thermometry . . . 117
5.3.2. The monitor function r . . . 128

5.3.3. Protocol to measure temperature in cells with the "two point"-method . . . 137
5.3.4. CW nano thermometry in living HepG2 cells: CCCP stimulation . . . 139
5.4. Summary, Conclusion and Outlook . . . 140

6. Robust-pulsed nano thermometry 143
6.1. Designing a Cooperative Optimal Control D-Ramsey Pulse . . . 144
6.2. Simulations . . . 147
6.2.1. Optimizing an Cooperative Optimal Control D-Ramsey Pulse 148
6.2.2. Comparison to other pulse schemes . . . 156
6.3. Experiments . . . 162
6.3.1. Setup . . . 162
6.3.2. Coop-D-Ramsey: single NV in bulk diamond . . . 165
6.3.3. Coop-D-Ramsey: single NV in a fixed ND . . . 168
6.3.4. Coop-D-Ramsey: single NV in a rotating ND . . . 171
6.4. Summary, Conclusion and Outlook . . . 176

7. Chemical sensing 179
7.1. Experimental characterization of hybrid sensor platform . . . 183
7.1.1. Experimental determination of robustness in spin inversion utilizing linear chirp pulses. . . . 183
7.1.2. Theoretical determination of robustness in spin inversion utilizing linear chirp pulse. . . . 190
7.1.3. Characterization of Control Samples ND-HPMA and ND-HPMA-Gd . . . 194
7.1.4. pH sensor . . . 201
7.1.5. Redox potential sensor . . . 205
7.1.6. Deep analysis of spin lattice relaxation time . . . 207
7.2. Simulations . . . 208
7.2.1. Modeling NV relaxometry influenced by Gd(III)-complexes . 208
7.2.2. Simulation results: Spherical nanodiamonds . . . 214
7.3. Summary, Conclusion and Outlook . . . 221

A. CW nano thermometry **223**
A.1. Testing absorption of microwave structure 223
A.1.1. Setup: Temperature change of NV versus Thermistor 223
A.1.2. Setup: Measuring the absorption of used sample chamber design 224
A.1.3. Ionic strength of surrounding and microwave heating 224
A.2. Individual results for CCCP stimulation of single HepG2 cells. . . . 225
A.3. Endocytosis: Introducing NDs into living cells 227
A.4. TPP-modification of nanodiamonds 227
A.5. Stimulation of HepG2 cells with CCCP 228
A.6. MTT Assay for cell viability test after CCCP stimulation 228

B. Robust-pulsed nano thermometry **229**

C. Chemical sensing **233**
C.1. Buffer Systems: pH Sensor 233
C.2. Buffer Systems: Redox Sensor 233
C.3. Sensitivity calculation for T_1 relaxometry. 234

Acknowledgements **237**

List of Publications **241**

Bibliography **243**

List of Figures

3.1. Basic principle of a epi-illuminated-confocal microscope 18
3.2. Phase diagramm of carbon 26
3.3. Electronic structure of the Nitrogen Vancancy center in diamond . . 32
3.4. Dependence of the NV charge state for different laser excitation wavelengths 34
3.5. Controlling the charge state of NVs 35
3.6. ODMR and spin state readout 42
3.7. The SiV in diamond 45
3.8. Adiabatic Passage: The BIR pulse. 58
3.9. Cooperative pulse design 63
3.10. Sensing in a coherent superposition with NV. 67
3.11. Rate mode for spin $S = 1$ system 69
3.12. Spectral density function S 73
3.13. NV versus substitutional nitrogen in NDs 74
3.14. Gadolinium-Complex as a contrast agent 75
3.15. Γ distribution for ND ensemble 78
3.16. Eukaryotic cell 80
3.17. The structure of a mitochondria 82
3.18. The respiration chain is highlighted. 83

4.1. Confocal setup 88
4.2. Filter setup 89
4.3. Exemplary background and transmission corrected spectra of SiV^- decorated MNDs 90
4.4. Overall shift of spectra in MND sample 91
4.5. Lifetime analysis of MND sample 93

4.6. Intensity analysis of MND sample 94
4.7. Filter setup and consequence for data acquisition, when performing an auto-correlation on weak signals 96
4.8. Saturation behavior and photoluminescence spectra of a dim spot . 97
4.9. Second order auto-correlation function of a dim spot 99
4.10. Deep analysis of single fluorescent spot 100
4.11. Size of MND sample 102

5.1. Setup cw nano thermometry 107
5.2. ND-TPP: contrast and linewidth 109
5.3. ND sample used for CW nano thermometry 110
5.4. Diffusion analysis of bare ND versus ND-TPP 112
5.5. Diffusion analysis of bare ND versus ND-TPP 113
5.6. Cell viability: influence of laser irradiation 115
5.7. Cell viability: HepG2 cell line 116
5.8. Influence of laser irradiation during nano thermometry 120
5.9. Influence of magnetic field on NV transition 122
5.10. Influence of microwave irradiation on temperature measurement . . 125
5.11. Influence of microwave irradiation on temperature measurement . . 126
5.12. Influence of pH on CW nano thermometry 127
5.13. Monitor function r depending on contrast and linewidth 132
5.14. The monitor function r is shot noise limited 136
5.15. Protocol of temperature measurements inside a living cell 138
5.16. Average temperature before and after CCCP stimulation living cells 139

6.1. Schematic representation of D-Ramsey 145
6.2. Simulated evolution of Coop-D-Ramsey for different projector combinations 146
6.3. Addressable fraction of an ensemble versus B_1 field orientation . . . 149
6.4. Optimization of Coop-D-Ramsey pulse parameters 151
6.5. Minimum pulse length for Coop-D-Ramsey 153
6.6. Comparing different sets of projectors 155
6.7. Signal amplitude of D-Ramsey using square pulses 157
6.8. Optimizing pulse parameters for BIR4 159

6.9. Optimizing pulse parameters for BIR4 . . . 160
6.10. Signal amplitude of D-Ramsey using BIR4 pulses . . . 161
6.11. Setup . . . 163
6.12. Bode diagram of the used AWG AWG2041 . . . 164
6.13. FFT magnitude and phase plot of an Optimal Control pulse . . . 165
6.14. Characterization of single NV . . . 166
6.15. Coop-D-Ramsey performed on single NV in bulk . . . 167
6.16. Characterization of single NV . . . 169
6.17. Coop-D-Ramsey performed on single NV in a ND . . . 170
6.18. Compensation of external magnetic fields . . . 171
6.19. Characterization of a single NV in a rotating ND . . . 173
6.20. Analysis of Coop-D-Ramsey for a rotating ND . . . 174
6.21. Temperature measurement using a Coop-D-Ramsey . . . 175

7.1. Chemical sensing with NV in ND . . . 180
7.2. Overview of chemical sensor species . . . 181
7.3. Experimental setup for chemical sensor species . . . 182
7.4. T_1 measurement utilizing a linear chirp pulse . . . 184
7.5. Comparing excitation bandwidth of linear chirp vs. square pulse . . 185
7.6. Performance of linear chirp pulse versus sweep speed: . . . 186
7.7. Microwave power dependence of measurement contrast using a linear chirp pulse . . . 188
7.8. Relative enhancement in sensitivity using chirp pulse vs square pulse 189
7.9. Adiabicity factor Q . . . 189
7.10. Simulation: Robustness of linear chirp pulse vs. square pulse . . . 190
7.11. Simulation: Robustness of a linear chirp pulse vs. square pulse (angular dependence): . . . 192
7.12. Simulation: Average performance of chirp pulse versus driving strength 193
7.13. Characterization of ND-HPMA . . . 195
7.14. Characterization of ND-HPMA-Gd . . . 196
7.15. pH response of control sample ND-HPMA and ND-HPMA-Gd . . . 198
7.16. Response of control sample ND-HPMA and ND-HPMA-Gd on glutathione (GSH) . . . 199

7.17. Response of control sample ND-HPMA-Gd to changes in ionic strength of the buffer system 200
7.18. Response of control sample ND-HPMA-Gd to changes in excitation power 201
7.19. pH response of pH-sensor 202
7.20. T_1 change versus pH in solution, buffer system 2 203
7.21. T_1 contrast image of pH sensor 204
7.22. Response of redox potential sensor to reduction agent GSH 206
7.23. Deep analysis of spin lattice relaxation time 207
7.24. Simulating the T_1 contrast for a certain T_1 time 211
7.25. Description of simulation model 212
7.26. Individual Gd concentration per nanodiamond (ND) 214
7.27. T1 dependence on polymer layer thickness 216
7.28. T_1 dependence on Gd(III)-concentration for a fixed polymer layer thickness 217
7.29. Comparing simulation to experimental results. 218
7.30. Calculated Gd(III) release for the pH sensor. 219
7.31. Calculated Gd(III) release for the redox sensor. 219

A.1. Testing influence of microwave heating 223
A.2. Testing microwave absorption of used sample chamber. 224
A.3. Individual results for CCCP stimulation of single HepG2 cells. . . . 226

List of Tables

3.1. Classification of diamond 25

7.1. Deep analysis of spin lattice relaxation time 207

List of Abbreviations

MSD	mean square displacement
AC-HRTEM	aberration corrected high resolution transmission electron microscopy
ADP	adenosine diphosphate
AFM	atomic force microscope
AOM	acusto optical modulator
APD	avalanche photo diode
APTES	(3-aminopropyl)triethoxysilane
ATP	adenosine triphosphate
AWG	arbitrary waveform generator
BFGS	Broyden-Fletcher-Goldfarb-Shanno algorithm
BIR	B_1 insensitive rotation

BW	bandwidth
CCCP	carbonylcyanid-m-chlorphenylhydrazone
CVD	chemical vapor deposition
cw	continuous wave
DNA	deoxyribonucleic acid
EPR	electron paramagnetic resonance
FCS	fluorescence correlation spectroscopy
FFT	fast fourier transformation
FID	free induction decay
fND	fluorescent nanodiamond
FNE	Frobenius norm error
FPE	Fokker-Planck equation
FWHM	full-width-half-maximum
GRAPE	gradient ascent pulse engineering
GSH	glutathione

GSSG	glutathione disulfide
HBT	Hanbury-Brown and Twiss
HE	Hahn-echo
HEPES	4-(2-hydroxyethyl)-1-piperazineethanesulfonic acid
HMM	hidden markov model
HPHT	high-pressure-high-temperature
HPMA	poly[(2-hydroxypropyl)methacrylamide]
HRTEM	high resolution transmission electron microscopy
ICP-OES	induced coupled plasma optical emission spectrometry
ICP-MS	induced coupled plasma mass spectrometry
IR	irreducible representation
IRF	instrument response function
LCAO	linear combination of atomic orbitals
MMP	mitochondrial membrane potential

MND	meteoric nanodiamond
MRI	magnetic resonance imaging
MW	microwave
ND	nanodiamond
NMR	nuclear magnetic resonance
NMRD	nuclear magnetic resonance dispersion
NV	nitrogen vacancy center
NV^-	negatively charged nitrogen vacancy center
NV^0	neutral nitrogen vacancy center
NV^+	positively charged nitrogen vacancy center
ODMR	optical detected magnetic resonance
PALM	photo-activated localization microscopy
PBS	phosphate-buffered saline
PC	photonic crystal
PCB	printed circuit board

PDMS	polydimethylsiloxane
PL	photoluminescence
PLE	photoluminescence emission
QIP	quantum information processing
RDX	hexogen
ROS	reactive oxygen species
SBR	signal to background ratio
SiV	silicon vacancy
SiV^-	negatively charged silicon vacancy
SiV^0	neutral silicon vacancy
SMS	single molecule spectroscopy
SNR	signal to noise ratio
STED	stimulated emission depletion
STORM	stochastic optical reconstruction microscopy

SVD	singular value decomposition
T_1	longitudinal relaxation time
T_2	transverse relaxation time
T_2^*	free evolution time
TCSPC	time-correlated single photon counting
TD-DFT	time-dependent density functional theory
TNT	trinitrotoluol
TPP	triphenylphosphine
TRIS	tris(hydroxymethyl)aminomethane
UNCD	ultra small nano crystalline diamond
ZFS	zero field splitting
ZPL	zero phonon line

List of special units

$^{\circ}C$	Temperature unit of the centigrade scale
cps	Counts per second
dBm	Power unit scale in decibels related to 1 mW as reference
eV	Electronvolt
G	Gauss: 1×10^{-4} T
IU	International Unit: The unit describes a mass or a volume. But the value of 1 IU can be different for different substances and depends on the biological activity or effect.
M	Molarity: mole per liter
ppm	Parts per million
S	Siemens: unit of electric conductance
Spl	Sample

wt%	Weight percent: mass weighted relative amount of substance related to the overall mass of a mixture

1. Summary

With the capability to detect single fluorescent molecules in combination with confocal microscopy a new field in life science heralded. Optical techniques allow precise analysis of nanometer-sized fluorescent single objects. Modern apparatus are able to resolve even nanometers sized structures just by optical means using so called super resolution techniques like photo-activated localization microscopy (PALM), stochastic optical reconstruction microscopy (STORM) or stimulated emission depletion (STED). With increased resolution capabilities also the requirements on the used probe increase: On the one hand they have to be as small as possible, as localization precision can be limited by its overall size. One the other hand super-resolution techniques like STORM require strong laser illumination. Therefore the used probe must be as photo-stable as possible. Color centers in diamond could serve as an alternative to commonly used organic dyes, as they exhibit almost no photobleaching. The latter also applies to other solid state systems like quantum dots. However, their surface has to be additionally passivated to increase bio-compatibility. The overall size of quantum dot systems therefore increases to $\sim 10\,\mathrm{nm}$. Diamond itself is chemically inert and even as a nano particle toxicity towards living organisms has not been observed so far.
In addition, the fluorescence signal of specific probes can encode information about the local environment, and sensitivity to local viscosity, pH, temperature or individual chemical compounds has been shown. As these sensors are typically in the order of some nanometers, highly localized monitoring of a desired quantity is possible. Following this approach a huge manifold of molecular sized systems have been developed using different kinds of strategies: for example, by monitoring changes in the fluorescence lifetime, photoluminescence (PL) spectra or overall emission strength. Thereby it is a big challenge to design a sensor, which is selectively responding to a desired quantity and, in case of organic dyes, not to

degrade over time.
Besides organic and inorganic probes also for color centers in diamond sensing at the nanoscale has been established. The most promising candidate is the so called nitrogen vacancy center (NV). Due to its optical and spin properties in the negative charges state, electric fields, magnetic fields and temperature can be sensed, even at room temperature. Up to now the majority of experiments have been performed within bulk diamond material. One reason for that kind of approach is, that NVs in bulk material show better spin properties then for example in NDs, as less paramagnetic defects within the host and on the surface are present. However, sensing typically requires proximity to the sample. Monitoring for example the magnetic field of a spin ensemble on the surface of the diamond allows approximately $\sim 50\,\mathrm{nm}$ sensing range. NDs could contribute to overcome this limitation, as for example living cells can take up nano particles quite easily. By the uptake of nanodiamonds, one can address intracelullar structures inside living cells. In addition, the nature of the surface and the connected chemical groups allow to control the destination of nano particles.
In principle, also NVs in NDs can be coherently controlled within a complex environment like cells. However, proper spin state adjustment can be challenging, if the host ND starts to tumble. Therefore it is important to develop methods that allow robust sensing schemes. A simple ansatz uses ND with a high density of NV. Its electron paramagnetic resonance (EPR) signature is probed in a continuous wave fashion and contains all possible defect orientations within the diamond nano crystal. If clustering of several nanoparticles occurs, the measured EPR signature shows a powder spectrum. With this method one can access changes in the ms regime. However, the acquired EPR signatures often shows strong inhomogeneous broadening around several MHz and has lower spin contrast. The overall sensitivity to a certain quantity is one order of magnitude lower compared to single NVs in bulk material even if an ensemble is probed.
Another strategy is the use of high quality NDs that only host few NVs in combination with robust spin control techniques. One example of such a technique is the adiabatic passage, which is also used in classical EPR and nuclear magnetic resonance (NMR). Thereby one slowly changes the effective magnetic field within the rotating frame of the spin system. In a classical view

the magnetic moment (equivalent to spin) will follow the effective magnetic field to a desired adjustment. The huge diversity of adiabatic pulses allow proper spin control, but due to the fact that the effective field in the rotating frame has to be changed slowly, the overall length of the pulse can be quite prolonged. In the worst case the latter may exceed the available coherence time in the system. In the last decade even more advanced versions of robust spin control have been developed, mostly based on optimal control theory. The numerically optimized pulse can be adjusted in robustness against for example detuning from resonance or overall driving strength of the spin transitions. Thereby the compiled pulse is often much shorter than an adiabatic passage.

In the present thesis molecular sized meteoric nanodiamonds (MNDs) decorated with silicon vacancy (SiV) have been spectroscopically analyzed on single emitter level. Therefore a confocal setup has been used, of which the sensitivity was maximized to the negatively charged silicon vacancy (SiV^-) fluorescence allowing to detect even a small number of weak fluorescent emitters. The measured average lifetime of 2.1 ns (spread: 1 ns) and spectra correspond well to literature values in polycrystalline synthetic nanodiamonds. In addition, the average spectral positions of the zero phonon line (ZPL) is shifted towards the blue in comparison to literature values, which is in good agreement with observations made by collaboration partners performed on the very same sample in a powder spectra. Theoretical calculations by collaboration partners suggest that the observed shift is a consequence of a quantum confinement effect opening the band-gap of nanodiamonds, which results in a shift of the SiV fluorescent levels. An individual spot containing a few emitters has been analyzed. Its spectrum shows two clear distinguishable peaks around the SiV^- ZPL. Using signal autocorrelation, it has been estimated that around (3 ± 1) emitters are located within the confocal detection volume. In addition, the analyzed emitters show a blinking behavior. Analyzing the fluorescent time trace *via* an hidden Markov model suggests 3 emitters within the detection volume. The saturation intensity of a single emitter has been estimated to be 12.7 kcps. Experimental results are partially published in [214].

The second part of this thesis examines the sensing capabilities of the negatively charged nitrogen vacancy center (NV^-) in NDs for temperature measurements inside living cells with an ensemble approach. There has been an ongoing debate between experimental work and theoretical prediction, if an endogenous temperature change within a living cell can occur and on which scale. To contribute to this debate, a confocal microscope has been modified with a cell incubator system allowing to detect simultaneously multiple color channels and to perform optical detected magnetic resonance (ODMR). One channel allows the identification of mitochondria inside living cell, another one to detect fluorescent NDs. The nanodiamonds have been conjugated with triphenylphosphine (TPP). TPP is a lipophilic cation, which utilizes the mitochondrial membrane potential (MMP) to drive its accumulation within the mitrochondria. TPP modified nanodiamonds should therefore accumulate in the direct vicinity of mitochondria. By stimulating the cell *via* the ionophore carbonylcyanid-m-chlorphenylhydrazone (CCCP), an uncoupling of the oxidative phosphorylation has been introduced. During this procedure heat is produced. The heat results in a change of temperature, which leads to a shift of the NV^-s electron spin transitions. To measure the shift, a center of mass approach has been developed based on monitoring at 2 points the EPR signature of NV^-. To track the change in the transition frequencies that are also a function of temperature, a feedback loop was designed. The feedback loop hereby locks the frequency of the main microwave source onto the fine structure constant or zero field splitting (ZFS) of the NV spin system. The calculated sensitivity of the given ND sample is $700\,\mathrm{mK}/\sqrt{\mathrm{Hz}}$ and is limited by shot noise. Several control experiments have been performed: By analyzing the diffusion of TPP modified ND, a more sticky behavior within the cell then for unmodified nanodiamonds is suggested. This indicates that the TPP modification supports accumulation of modified NDs on the mitochondrial surface. In addition, cell viability under the influence of laser illumination has been checked: Cells exposed to strong laser light do not show a significant difference to the control without intense exposure. In addition, the experimentally used laser power does not lead to significant heating effects. Stimulation with CCCP dissipates the MMP, but does not reduce cell viability within the used concentration. To excite NVs spin transitions, microwaves have

to be applied to the sample. Increasing the ionic strength within the sample chamber leads to heating during the application of microwave. But the measured temperature shift suggests, that local changes in the ionic strength cannot lead to measurable temperature changes on the micro- or nano-scale.
Comparable experimental work in literature shows an increase of several Kelvin over several minutes after stimulating single cells. In this work no change in temperature has been observed in average over 9 individual measurements. The estimated uncertainty is 0.1 K for the averaged temperature response for a time resolution of 30 s. This findings are consistent with classical calculations considering the overall energy stored within a single living cell.

The third part of this thesis is heading towards the development of robust pulsed nano-thermometry using the so called D-Ramsey schema. To this end optimak control theory was applied. To optimize the compiled microwave pulses to a desired functionality, the package "dynamo" developed by Ville Bergholm and Shai Machnes has been used. "Dynamo" utilizing the so called gradient ascent pulse engineering (GRAPE) method in combination with the Broyden-Fletcher-Goldfarb-Shanno algorithm (BFGS). In addition, "Dynamo" allows a cooperative pulse design by applying quantum state filters at a desired position in time. Therefore the explicit spin Hamiltonian of NV has to be formulated. After designing the needed quantum state filters the compiled pulses have been tested on fixed NVs in bulk diamond and nanodiamonds. The latter are later transversely fixed in a 5 % agarose matrix and the performance of a Coop-D-Ramsey has been tested under slow rotation of the ND. An maximum signal contrast of almost 80 % has been reached in all experiments. For comparison, the original D-Ramsey using square pulses only reaches half the contrast for same experimental conditions. The overall pulse length needed and the robustness against changes in resonance frequency as well as driving amplitude has been verified by simulations. Afterwards the latter are compared to other pulse schema like adiabatic pulses.

The fourth part of this thesis focus on the use of NV within an modular sensing system. The NV is a suitable sensor for physical quantities. Chemical

related parameters like pH or chemical potential are hard to access. Therefore an hybrid sensor system based on spin relaxometry has been developed in cooperation with the Institute of Organic Chemistry and Biochemistry AS CR in Prague. A polymer was grown on the surface of nanodiamonds and host Gd-complexes *via* a selective cleavable linker. The Gd-complex relaxes the spin state of NV^-. If the linker is cleaved by activation, the Gd-complexes are released leading to an increase of the spin lattice relaxation time of NV. Whereas the group in Prague synthesized and pre-characterized the analyzed samples, the target within this thesis is the development of an proper physical model of the system, and to describe NV relaxometry. In addition, the sensor platform in terms of applicability has been tested in the frame work of confocal microscopy. Therefore a model for Gd-Complexes in a thin shell on the surface of NDs was adapted, accounting for multiple randomly distributed NVs inside the ND. To describe the observed relaxation a stretched exponential was introduced. The model has been applied to two exemplary types of sensors. The first one is sensitive to changes in pH, whereas the second one to the existence of a reducing agent in the vicinity of the sensor. Both sensors are built to be irreversible, meaning that the desired quantity is measured *via* the change of the spin lattice relaxation time T_1 over time. To measure T_1 the spin state $|0\rangle$ is probed. Especially in nanodiamonds charge state dynamics of NV can occur as change in fluorescence over time. Because of that, an microwave pulse has to be applied in an additional control measurement to distiguish between charge and spin dynamics. As already mentioned before, quantum state adjustment can be quite challenging, as the orientation of NV can change relative to the driving field vector. To this end an adiabatic passage in form of an linear chirp pulse has been utilized. By simulations and experimental results an overall enhancement of a factor more then 2 in sensitivity is found, by using chirp instead of simple square pulses. Mapping the measured T_1 into a Gd-concentration with the aid of the performed simulation results, show good agreement between the release constant obtained by such fluorescent measurements and induced coupled plasma mass spectrometry (ICP-MS) experiments done by collaboration partners. Plotting the release rate versus pH, reveals an linear behavior in logarithmic scale. For the fluorescent measurements a slide saturation to lower pH values is visible. The same analysis

was done for the chemical redox sensor for different GSH concentrations and two different pH. Thereby the release rate for pH 7.4 is almost one order of magnitude lower than at pH 8.0. This is qualitatively consistent with literature, as the reductive behavior of GSH is pH dependent. Control samples with an non-cleavable linker do show only slight changes in T_1 for changes in the ionic strength or pH of different buffer solution. Simulation results suggest that no significant swelling or collapse of the polymer shell occurs, which could affect the read out of the sensor. Due to the robustness of the developed schema one can discriminate between activated and freshly prepared sensor units in a 2D confocal scan. Experimental results have been published in reference [159].

2. Zusammenfassung

Die Fähigkeit einzelne fluoreszierende Moleküle mittels konfokaler Mikroskopie aufzulösen, eröffnete ein neues Feld in der Molekularbiologie. Mittlerweile ist es sogar möglich einzelne fluoreszierende Objekte im Nanometerbereich mit Techniken wie PALM, STORM oder STED aufzulösen. Das erhöhte Auflösungsvermögen schafft neu Anforderungen an die verwendeten fluoreszierenden Marker: Einerseits müssen diese möglichst klein sein, da die Lokalisierungsgenauigkeit zunehmend durch die räumliche Größe des Markers limitiert werden könnte, und zum anderen werden für besonders hochaufgelöste Bilder mittels STORM relative starke Laserleistungen benötigt, was eine gewisse Photostabilität des Markers voraussetzt. Farbzentren in Diamant stellen hierbei eine mögliche Alternative zu den häufig verwendete organischen Farbstoffen dar, da erstere eine wesentlich höhere Photostabilität aufweisen. Dies trifft auch auf andere Festkörpersysteme wie zum Beispiel Quantenpunkte zu. Allerdings muss deren Oberfläche zusätzlich passiviert werden, um die in Zell Experimenten gewünschte Biokompatibilität zu erreichen. Dies führt zu einer Vergrößerung des gesamten Systems auf ungefähr 10 nm. Hingegen existieren einige Farbzentren im Diamant selbst in Wirtskristallen molekularer Größe. Diamant selbst ist chemisch inert und toxisches Verhalten von Nanodiamanten wurde bis jetzt nur im geringem Maße beobachtet. Deswegen benötigen Nanodiamanten keine zusätzliche Ummantelung was die Gesamtgröße der Markers auf wenige Nanometer reduziert.
Das Fluoreszenzsignal einiger Marker kann zudem Informationen über die lokale Umgebung enthalten und fungieren deshalb im übertragenen Sinne als Sensor. Empfindlichkeit gegenüber Viskosität, pH-Wert, Temperatur oder einzelner chemischer Verbindungen sind möglich. Da entsprechende Systeme typischerweise ein Größenordnung von einigen Nanometern besitzen, ist eine hochgradig lokalisierte Bestimmung einer gewünschten Größe möglich. Diesem Ansatz

folgend wurden eine große Anzahl von Sonden entwickelt, die auf verschiedensten Ansätzen basieren: Um mögliche Änderungen in einer zu untersuchenden Größe zu identifizieren, werden Veränderungen in zum Beispiel der Fluoreszenzlebensdauer, des Photolumineszenzspektrums oder der Gesamtemissionsstärke beobachtet. Eine große Herausforderung hierbei ist es, die Sonde so zu gestalten, dass sie spezifisch auf nur einen gewünschten Parameter reagiert und nicht im Laufe der Zeit degradiert.
Neben organischen und anorganischen Sensoren, können physikalische Größen auch mit Hilfe von Farbzentren im Diamant bestimmt werden. Einer der vielversprechendsten Kandidaten ist der sogenannte Stickstoff-Fehlstellen-Defekt (NV). Aufgrund seiner optischen und Spin Eigenschaften im negativen Ladungszustand, können elektrische Felder, Magnetfelder und Temperatur selbst bei Raumtemperatur bestimmt werden. Bislang werden aber hauptsächlich NVs innerhalb eines Diamantplättchens verwendet. Ein Grund dafür ist, dass einzelne NVs in besonders reinen Kristallen bessere Spin-Eigenschaften zeigen als in Nano-Partikeln, da produktionsbedingt weniger paramagnetische Defekte im Wirtskristall und auf der Oberfläche des Diamanten vorhanden sind. Die Messung einer bestimmten physikalischen Größe erfordert jedoch in der Regel eine gewisse Nähe zur untersuchten Probe. Will man zum Beispiel ein Spin-Bad auf der Oberfläche eines Diamanten bestimmen, kann nur ein Volumen bis ca. $\sim$ 50 nm über der Diamant Oberfläche untersucht werden. Nanodiamanten (ND) könnten dazu beitragen, diese Einschränkung zu überwinden. Lebende Zellen, zum Beispiel, können Nanopartikel recht einfach aufnehmen. Durch das Einbringen von Nanodiamanten könnten somit auch innerzellular Strukturen, die sogenannten Organellen, untersucht werden. Eine chemische Modifikation der Oberflächengruppen erlaubt es außerdem, gezielt Strukturen innerhalb einer lebenden Zelle zu adressieren.
Obwohl der Spinzustand von NVs in NDs prinzipiell in einer komplexen Umgebung wie Zellen kohärent kontrolliert werden kann, ist es schwierig den gewünschten Spin-Zustand deterministisch einzustellen, wenn es dem Wirtskristall möglich ist, seine Orientierung während einer laufenden Messung zu ändern. Es ist daher wichtig Messmethoden zu entwickeln, die diesbezüglich robust sind. Im einfachsten Ansatz werden deswegen stark mit NV dotierte NDs verwendet.

Die Elektronen Spin Resonanz (ESR) Signatur wird dabei meistens über kontinuierliche Mikrowelleneinstrahlung ausgelesen und enthält alle möglichen Defektorientierungen des Kristalls. Bilden sich kleinere Anhäufungen aus mehreren Partikeln, so entspricht die gemessen ESR-Signatur einem Pulverspektrum. Mit dieser Methode können zeitliche Änderungen im Bereich von Millisekunden erfasst werden. Das gemessene ESR-Signal zeigen jedoch häufig eine starke inhomogene Verbreiterung um mehrere MHz, und der gemessene Spin-Kontrast ist vergleichsweise niedrig: Die Empfindlichkeit ist im Allgemeinen um eine Größenordnung geringer im Vergleich zu einzelnen NVs im Diamantplättchen, auch wenn eine große Anzahl von NVs gleichzeitig ausgelesen wird.
Eine alternative Strategie ist die Verwendung von besonders reinen Nanodiamanten, die nur wenige NVs enthalten, in Kombination mit robusten Spin-Kontroltechniken. Ein Beispiel für eine solche Technik ist die adiabatische Passage, die auch in der klassischer ESR und Kernspinresonanz (NMR) verwendet wird. Hierbei ändert sich das effektive Magnetfeld, das innerhalb eines mit dem Spin rotierenden Bezugsystem definiert ist, wesentlich langsamer als die charakteristische Prezissionsgeschwindingkeit um das effektive Magnetfeld. Klassisch betrachtet folgt das magnetische Moment (äquivalent zum Spin) dem effektiven Magnetfeld und kann so gezielt eingestellt werden. Die große Vielfalt an adiabatischen Pulsen ermöglicht eine präzise Justage in einen gewünschten Zustand. Aber aufgrund der Tatsache, dass das effektive Magnetfeld nur sehr langsam geändert werden darf, kann die Zeitspanne in der ein Spin-Zustand eingestellt wird sehr lang werden. Im ungünstigsten Fall überschreitet sie die verfügbare Kohärenzzeit des Spinsystem. Während der letzten Jahrzehnte wurden noch fortschrittlichere Versionen der robusten Spin-Kontrolle entwickelt, die hauptsächlich auf der Theorie der optimalen Steuerung basieren. Ein dabei numerisch optimierter Puls kann in seiner Robustheit beispielsweise gegen Resonanzverschiebungen oder Treiberstärke der Spinübergänge eingestellt werden, und die Zustandänderung erfolgt in wesentlich kürzer Zeit, als dies für adiabatische Pulse der Fall ist.

In der vorliegenden Arbeit wurden meteoritische Nanodiamanten molekulare Größen, die zusätzlich mit SiV verziert sind, spektroskopisch analysiert. Die Sensitivität des verwendeten konfokalen Mikroskops wurde hierfür

auf die Fluoreszenz von SiV^- maximiert und erlaubt die Detektion weniger fluoreszierender Emitter.
Die gemessene mittlere Lebensdauer von 2.1 ns (Streuung: 1 ns) und das Photolumineszenz-Spektrun entsprechen den Literaturwerten in polykristallinen synthetischen Nanodiamanten. Außerdem sind die spektralen Positionen des Nullphononenübergangs (ZPL) in Richtung höherer Energien verschoben. Dies stimmt qualitative mit den Beobachtungen von Kooperationspartnern überein, die ähnliche Analysen an derselben Probe in Pulverform durchgeführt haben. Laut theoretischen Analysen der Kooperationspartner, kann die Verschiebung als Konsequenz eines Quantisierungseffektes interpretiert werden, der mit der Vergrößerung der Bandlücke von Nanodiamanten einhergeht und zu einer Blauverschiebung der SiV^- typischen Fluoreszenz führt.
Eine Detailanalyse eines schwach leuchtenden Objektes nach aufbringen der Probe auf ein Quarz Deckglass wurde durchgeführt. Das Spektrum zeigt zwei deutlich unterscheidbare Peaks, die jeweils SiV^- Fluoreszenz zugeordnet werden können. Mittels Signalautokorrelation wurde ermittelt, dass sich etwa (3 ± 1) Emitter innerhalb des konfokalen Detektionsvolumens befinden. Zusätzlich zeigt die Fluoreszenz der Emitter ein An-Aus-Verhalten. Die Analyse der Fluoreszenz-Zeitsignals wurde mit Hilfe eines Hidden-Markov-Modells analysiert. Drei Emitter innerhalb des Detektionsvolumens sind gemäß der Analyse am wahrscheinlichsten. Die Sättigungsintensität eines einzelnen Emitters wurde auf 12.7 kcps geschätzt. Die experimentellen Ergebnisse sind teilweise in [214] veröffentlicht.

Der zweite Teil dieser Arbeit befasst sich mit Temperatur-Messungen in lebenden Zellen mit Hilfe von Nanodiamanten. Für diesen Teil der Arbeit wurden stark mit NV^- dotierte NDs verwendet. Bis heute wird eine Debatte über mögliche endogene Temperaturänderung innerhalb lebender Zellen und in welcher Größenordnung diese auftritt, geführt. Dabei legt eine Vielzahl experimenteller Arbeiten eine Temperaturänderung von einigen Kelvin nahe, was im Widerspruch zu simplen theoretischen Überlegungen ist. Zur Klärung dessen wurde ein konfokales Mikroskop mit einem Zell-Inkubator modifiziert, das gleichzeitig die Detektion mehrere Farb-Kanäle und optische detektierter

Spin-Resonanz mittels Mikrowellen Anregung erlaubt. Ein Farbkanal wird zur Identifikation der zellinternen Mitochondrien verwendet. Ein weiterer um die Position fluoreszierender NDs zu erfassen. Die verwendeten Nanodiamanten sind hierbei mit TPP konjugiert. TPP ist ein lipophiles Kation, das das mitochondirale Membran Potential (MMP) nutzt, um innerhalb der Mitochondrien zu akkumulieren. TPP modifizierte Nanodiamanten halten sich somit in der direkten Umgebung der Mitochondrien auf. Durch Stimulation der Zelle über das Ionophor CCCP wurde eine Entkopplung der oxidativen Phosphorylierung initialisiert. Während dieser Prozedur wird Wärme erzeugt, die zu einer Verschiebung der ESR-Übergänge der NVs führt. Um die Verschiebung zu messen, wurde eine Schwerpunkts-Analyse des optisch detektierten ESR-Spektrums verwendet, die auf der Beobachtung zweier Punkte im Spektrum basiert. Um die Übergänge während einer möglichen Temperaturänderung zu verfolgen, wurde eine Rückkopplung in das Messverfahren integriert. Die Rückkopplungsschleife koppelt dabei die Frequenz der verwendeten Mikrowellenquelle an die Feinstruktur-Konstante des NV -Spinsystems. Die berechnete Empfindlichkeit der verwendeten ND-Probe ist $700\,\mathrm{mK}/\sqrt{\mathrm{Hz}}$ und wird durch Schrotrauschen begrenzt. Es wurden mehrere Kontrollexperimente durchgeführt: Eine Diffusionanalyse von TPP modifizierten NDs ergab, dass diese sich innerhalb der Zelle weniger frei als nicht modifizierte Nanodiamanten bewegen können. Dies wird als Indiz gewertet, dass die TPP Modifikation auch bei Nanodiamanten eine Akkumulation an der mitochondrialen Oberfläche bewirkt. Zusätzlich wurde die Zellviabilität unter dem Einfluss von Laserbestrahlung überprüft: Zellen, die starkem Laserlicht ausgesetzt sind, sind danach nicht weniger Lebensfähig als eine Kontrolle ohne intensive Belichtung. Die im Experiment verwendete Laserleistung führt zu keiner messbaren Temperatur Erhöhung innerhalb des konfokalen Detektionsvolumens. Stimulation mit CCCP zerstört das mitochondriale Membranpotential, reduziert aber nicht die Lebensfähigkeit der Zellen durch die im Experiment verwendeten Konzentrationen. Zum Auslesen der ESR Signatur werden Mikrowellen verwendet. Da das verwendete Zellmedium zum größten Teil aus Wasser besteht, ist Absorption von Mikrowellenstrahlung zu erwarten. Erhöht man die Ionenstärke innerhalb der Probenkammer führt dies zu einer Erwärmung durch Mikrowelleneinstrahlung. Der gemessene Temperaturunterschied deutet jedoch darauf hin, dass lokale

Änderungen der Ionenstärke nicht zu messbaren Temperaturänderungen auf Mikro- bzw. Nanoskala führen können.
Vergleichbare experimentelle Arbeiten in der Literatur zeigen nach Stimulation einzelner Zellen mehrere Kelvin Temperatur Unterschied, oftmals über mehrere Minuten. In dieser Arbeit wurde keine Temperaturänderung beobachtet. Dabei wurde über 9 Einzelmessungen gemittelt. Diese Ergebnisse stimmen mit klassischen Berechnungen überein, die die Gesamtenergie einer einzelnen lebenden Zelle berücksichtigen. Die geschätzte Unsicherheit der gemittelten Messung ist $\sim 0.1\,\mathrm{K}$ für eine Zeitauflösung von 30 s.

Der dritte Teil dieser Arbeit befasst sich mit der Entwicklung robuster gepulster Nano-Thermometrie auf Basis des sogenannten D-Ramsey-Schemas. Letzteres ermöglicht es mit NV^- Temperatur Unterschiede zu messen. Das D-Ramsey-Schema wurde mittels "Theorie zur optimale Steuerung" in numerisch optimierte robuste Pulse in ein Coop-D-Ramsey-Schema übersetzt, das trotz Variationen der Rabi Amplitude und spektraler Änderungen der ESR-Resonanzlinien das Verhalten einer D-Ramsey beibehält. Um die Puls-Sequenz auf eine gewünschte Funktionalität zu optimieren, wurde das von Ville Bergholm und Shai Machnes entwickelte Paket "Dynamo" verwendet. "Dynamo" basiert auf der sogenannte "Gradienten basierenden Pulse Entwicklungs"-Methode in Kombination mit dem Quasi Newtonschen Verfahren nach Broyden, Fletcher, Goldfarb und Shanno. Darüber hinaus ermöglicht "Dynamo" ein kooperatives Pulsdesign durch Anwendung von Quantenzustandsfiltern. Kooperativität bedeutet hierbei, dass einzelne Pulsesegmente innerhalb einer gepulsten Sequenz, Fehler andere Segmente kompensieren können.
Der explizite Spin-Hamilton-Operator des NV^- Spin- Systems wurde formuliert. Nachdem die benötigten Quantenzustandsfilter entworfen wurden, wurden optimierte Pulse an NVs in Diamantplättchen und Nanodiamanten getestet. Letztere werden später transversal in einer 5 %igen Agarosematrix fixiert, und die Leistungsmerkmale einer Coop-D-Ramsey wurden unter langsamer Rotation eines ND getestet.
In allen Experimenten wurde ein maximaler Signal-Kontrast von fast 80 %

erreicht. Zum Vergleich, die ursprüngliche D-Ramsey mit simplen Rechteck Pulsen erreicht nur die Hälfte des Kontrastes für die gleichen experimentellen Bedingungen. Die erforderliche Gesamtpulslänge und die Robustheit gegenüber Änderungen der Resonanzfrequenz sowie der Treiberamplitude wurden anhand von Simulationen verifiziert. Danach werden letztere mit anderen Pulsschemata wie dem adiabatische Pulse Schema BIR-4 verglichen. Auch eine BIR-4-D-Ramsey erreicht nicht den Signal-Kontrast einer Coop-D-Ramsey. Die getestet adiabatischen Pulse sind zeitlich zudem um fast eine Größenordnung länger.

Der vierte Teil dieser Arbeit befasst sich mit der Verwendung von NV in einer modularen Sensorplattform. Das NV^- ist ein geeigneter Sensor für physikalische Größen. Chemische Parameter wie pH-Wert oder das chemische Potenzial sind schwer zugänglich. Deshalb wurde in Zusammenarbeit mit dem Institut für Organische Chemie und Biochemie AS CR in Prag ein hybrides Sensorsystem auf Basis von Spin-Relaxometrie entwickelt. Ein spezielles Polymer wird auf der Oberfläche der Nanodiamanten synthetisiert, das Gd(III)-Komplexe über einen selektiven spaltbaren Linker an die Oberfläche bindet. Der Gd(III)-Komplex erzeugt ein stochastisch fluktuierendes Magnetfeld, das die Gitterrelaxationszeit T_1 der NV^- reduziert. Wird der Linker durch Aktivierung gespalten, werden die Gd(III)-Komplexe freigesetzt, was zu einer Erhöhung von T_1 führt. Während die Gruppe in Prag die analysierten Proben synthetisierte und vorcharakterisierte, war das Ziel dieser Arbeit die Entwicklung einer physikalischen Modelierung des Systems und dessen Beschreibung über NV Relaxometrie. Zusätzlich wurde die Sensorplattform hinsichtlich der Anwendbarkeit im Rahmen der konfokalen Mikroskopie getestet. Daher wurde ein Modell für Gd(III)-Komplexe in einer dünnen Schale auf der Oberfläche von NDs adaptiert. Um die beobachtete Relaxation zu beschreiben, wurde die gestreckte Exponentialfunktion verwendet. Das Modell wurde auf zwei beispielhafte Typen von Sensoren angewendet. Der erste ist empfindlich gegenüber Änderungen des pH-Werts, während der zweite die Existenz eines Reduktionsmittels in der Nähe des Sensors nachweist. Beide Sensoren sind so konstruiert, dass sie irreversibel arbeiten. Dies bedeutet, dass die gewünschte Größe über die Änderung von T_1 über die Zeit gemessen wird. Um T_1 zu messen, muss der zeitliche Verlauf des Spinzustandes $|0\rangle$ ermittelt werden. Insbesondere die zeitliche Änderung der

Fluoreszenz für NVs in Nanodiamanten kann auch durch Ladungszustandsdynamik beeinflusst werden. Aus diesem Grund muss in einer zusätzlichen Kontrollmessung der Spinzustand des NVs mittels Mikrowelle geändert werden um zwischen Ladungs- und Spin Dynamik unterscheiden zu können. Wie bereits erwähnt, kann eine Einstellung eines erwünschen Spinzustandes recht schwierig werden, wenn die Orientierung von NV relativ zum Treiberfeld variabel ist. Zu diesem Zweck wurde eine adiabatische Passage in Form eines linearen Chirp-Pulses verwendet. Sowohl Simulationen als auch Experiment ergeben eine um Faktor 2 bessere Empfindlichkeit, wenn ein Chirp anstelle eines einfachen Rechteckimpulses verwendet wird. Mit Hilfe der Simulationsergebnisse kann die gemessene T_1 in eine Gd(III)-Konzentration überführt werden. Die so errechneten Gd(III)-Komplex Freisetzungskonstanten der Fluoreszenzmessungen stimmen gut mit den von Kooperationspartnern durchgeführten Experimenten überein. Die logarithmisch dargestellte Freisetzungsrate gegenüber dem pH zeigt ein lineares Verhalten. Für die Fluoreszenzmessungen ist eine Sättigung zu niedrigeren pH-Werten sichtbar. Ähnliche Analysen wurden für den chemischen Redox-Sensor für verschiedene GSH-Konzentrationen und zwei verschiedene pH-Werte durchgeführt. Die Freisetzungsrate für pH 7.4 ist fast eine Größenordnung niedriger als für pH 8.0. Dies stimmt qualitativ mit dem in der Literatur beschriebenen Verhalten überein, da das Reduktionsvermögen von GSH pH-abhängig ist. Kontrollproben mit einem nicht spaltbaren Linker zeigen nur geringfügige Änderungen in T_1 für Änderungen der Ionenstärke oder des pH-Werts verschiedener Pufferlösungen. Erhaltene Simulationsergebnisse deuten darauf hin, dass keine signifikante Quellung oder ein Zusammenbruch der Polymerhülle auftritt, die das Auslesen des Sensors beeinträchtigen könnte. Aufgrund der Robustheit des entwickelten Schemas kann in einem 2D-Konfokalscan zwischen aktivierten und frisch vorbereiteten Sensoreinheiten unterschieden werden. Die Ergebnisse dieses Projekts wurden teilweise in [159] veröffentlicht.

3. Basics

In the following introductory chapter the underlying theoretical framework of this thesis is assembled. As a starting point single molecule spectroscopy (SMS) and its basic techniques to characterize single molecule emitters are discussed. Then, diamond with a focus on nanodiamonds is introduced and their capability to host fluorescent sensors is discussed. Afterwards general sensing scheme and their theoretical background will be outlined. Finally, a general intoduction into living cells is given as they serve as a test system for *in vivo* applications.

3.1. Single molecule spectroscopy

The analysis of even the smallest structural compartments in organisms is a central desire to nowadays scientific efforts. Therefore sensitive apparatus must to be used, enabling the possibility to detect and resolve the species under study. An established method for this purpose, is the so called single molecule spectroscopy, where the emission of single fluorescent probes is monitored *via* confocal microscopy.

3.1.1. Confocal scanning microscopy

Confocal microscopy is based on idea to illuminate and detect emission from only a small region of interest. In that way parasitic background from other parts of the sample are greatly suppressed. In the so called epi-illuminated confocal microscope (see figure 3.1) a light source, typically a laser, is first collimated and deflected by a semi-transparent mirror onto an objective that focuses the laser beam (excitation beam) into the focal plain, located in the sample. If a fluorescent probe is located in the focus that can be excited by the light source, it will emit photons. The photons collected by the objective will leave the objective's backside as a collimated

beam (detection beam) and pass the semi-transparent mirror. Another lens is used to focus the emitted photons onto a pinhole with a typical size of 30 µm to 150 µm. Afterwards the pinhole is mapped onto a detector with an additional lens system. The pinhole further improves suppression of background signal, as only light from the initial illuminated small region inside the sample focus can pass the pinhole without being altered. Typically the fluorescence of single emitters under study is more then 5 to 7 orders of magnitude lower then the actual laser excitation scattering back into the pinhole. For suppression spectral filtering has to be applied to cut of the laser light. Therefore typically interference filters are used and there exist a huge manifold of different vendors, but also absorptive filtering based on vapor cells has been demonstrated [207].

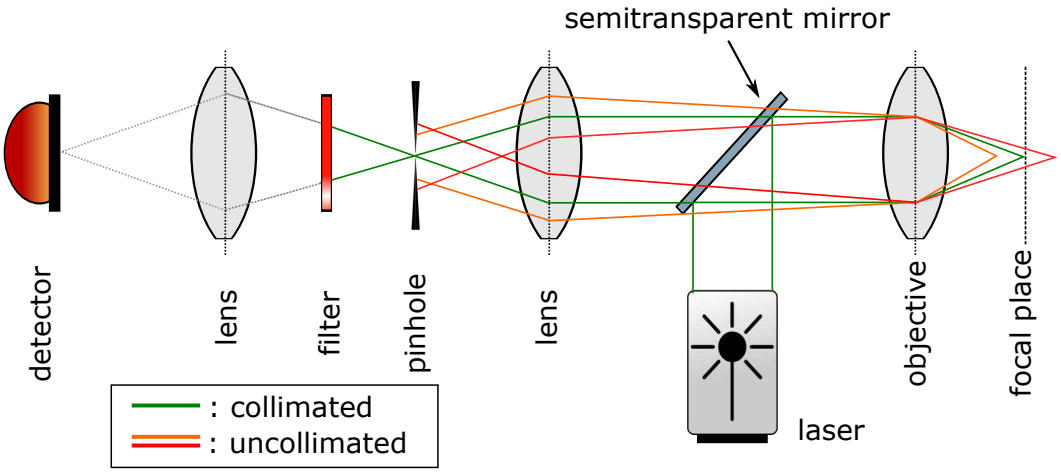

Figure 3.1. Basic principle of a epi-illuminated-confocal microscope: Function principle see text.

Multicolor-imaging As the emission wavelength for different fluorophores can be quite spread, multiple sets of detection channels can be used to discriminate their signal. This allows to visualize different parts of a sample or to co-localize different markers linked to different parts of the sample.

Spatial resolution The resolution of a typical confocal microscope as an optical imaging system is limited by diffraction. Thereby the finite focal point is often

approximated by an ellipsoid, the so called confocal volume, with a lateral and axial extension of $\Delta d \approx \lambda/(2n\sin(\alpha))$ and $\Delta z \approx \lambda/(n\sin^2(\alpha))$, respectively. Thereby α is the opening angle of the objective and n the refractive index of the medium the light is focussed into [218, 82]. Modern objectives for single molecule detection reach resolutions of $\Delta d =\sim 200\,\text{nm}$ and $\Delta z =\sim 440\,\text{nm}$ for a wavelength in the yellow to orange range. By super-resolution techniques like STORM/PALM or STED [82] the lateral resolution can even reach the nanometer scale. In STORM/PALM, emitters are turned on and off more or less deterministically and the position of individual emitters in state turned-on is determined whereas the surrounding emitters are turned off. This allows to localize a single probe with much higher precision. In the second technique mentioned, a second laser beam, which is formed into a donut-shape by an optical phase plate, the so called STED beam. The excitation beam, which in this technique is the very same as in confocal microscopy, is overlapped in the exact center of the STED beam. The STED beam is red shifted and depletes emitters within it's excitation profile by stimulated red emission. Only the fluorescence of emitters within the dark central region of the STED beam account to the signal detected. By lowering or increasing the power of the STED beam, the resolution of the microscope can be controlled.

3.1.2. (Auto-)correlation function

Besides spatial information, fluorescence carries also useful information about the fluorescent probe itself and can be used to characterize it. Therefore the fluorescence signal of an emitter is correlated with itself or another emitter. A typical correlation function used in single molecule spectroscopy is the so called $g^{(2)}(\tau)$ function describing correlation in terms of the measured intensity $I(t)$ dependent on time:

$$g^{(2)}(\tau) = \frac{\langle I(t)I(t+\tau)\rangle}{\langle I(t)I(t)\rangle} \tag{3.1}$$

Using equation (3.1), one for example can determine the number of emitters within the confocal volume.

Single photon source The fluorescence signal of a single photon emitter is caused by spontaneous emission of a single photon after an electronically excited state relaxes back to its ground state. The excited state itself has a certain lifetime being the inverse of the corresponding Einstein coefficient. As a consequence the emitter cannot emit two photons at the same time originated from the very same transition. This can also be expressed in terms of an auto-correlation function for the excited state, describing the probability to detect several photons at the same time, separated by the time interval τ. For a three level system one can define a rate equation model describing the evolution of the different state populations n_i. Whereas state 1 describes the ground state, 2 the excited state and 3 often is refereed to a metastable or shelving state. If k_{ij} is the transition rate between state i to j on finds:

$$\begin{aligned}
\dot{n}_1 &= -k_{12} \cdot n_1 - k_{13} \cdot n_1 + k_{21} \cdot n_2 + k_{31} \cdot n_3 \\
\dot{n}_2 &= -k_{21} \cdot n_2 - k_{23} \cdot n_2 + k_{12} \cdot n_1 + k_{32} \cdot n_3 \\
\dot{n}_3 &= -k_{31} \cdot n_3 - k_{32} \cdot n_3 + k_{23} \cdot n_2 + k_{13} \cdot n_1
\end{aligned} \tag{3.2}$$

If the metastable state is of different spin multiplicity as the ground and excited state, direct excitation from the ground state can be neglected. Same argument holds for exciting from the metastable into the excited state. Therefore often the assumption $k_{32} = k_{13} = 0$ is used. Reverse rates maybe not neglectable, as spin-orbit coupling between the excited and metastable state can occur. As the emitter has a certain lifetime to stay in the excited state, the overall emission rate of the emitter saturates for very high laser power (and if no stimulated emission occurs). The emission rate $R(P_{\text{opt}})$ depending on the optical pump power P_{opt} can be written as [62]

$$R(P_{\text{opt}}) = R_\infty \frac{P_{\text{opt}}}{P_{\text{sat}} + P_{\text{opt}}}. \tag{3.3}$$

Whereas R_∞ is the value of R for infinite laser excitation power and sometimes is called saturation intensity, and P_{sat} the corresponding saturation power.

Using the relations $n_1 + n_2 + n_3 = 1$ and the initial condition $n_1(0) = 1$, $n_2(0) = 0$,

$n_3(0) = 0$, one can derive an expression for the exited state. The corresponding auto-correlation has the form [135]

$$g^{(2)}(\tau) = 1 - (1 + a) \cdot \mathrm{e}^{-\frac{|\tau|}{\tau_1}} + a \cdot \mathrm{e}^{-\frac{|\tau|}{\tau_2}}. \tag{3.4}$$

With the parameters

$$\begin{aligned} \tau_{1,2} &= 2/(A \pm \sqrt{A^2 - 4B}), \\ A &= k_{12} + k_{21} + k_{23} + k_{31}, \\ B &= k_{12} \cdot k_{23} + k_{12} \cdot k_{31} + k_{21} \cdot k_{31} + k_{23} \cdot k_{31}, \\ a &= \frac{1 - \tau_2 \cdot k_{31}}{k_{31} \cdot (\tau_2 - \tau_1)}. \end{aligned} \tag{3.5}$$

For $\tau \to \infty$ the $g^{(2)}$ function converges to 1. This means that the signal is totally uncorrelated for infinite long time delay. If $g^{(2)}$ is at any time smaller then 1, this is typically called anti-bunching. For values bigger then 1 one calls this a bunching behaviour.

Multiple emitters If N emitters are monitored at the same time, each individual emitter will contribute to the auto-correlation function with the intensity I_i . The collective correlation function will then be [99]

$$g_N^{(2)}(\tau) = \frac{\sum_{i=j}^{N} \langle I_i(t) I_j(t+\tau) \rangle + \sum_{i \neq j}^{N} \langle I_i(t) I_j(t+\tau) \rangle}{\sum_i^N (\langle I_i(t) I_i(t) \rangle)}. \tag{3.6}$$

If all emitters contribute with the same signal strength and if the different emitters are uncorrelated, equation 3.6 can be written as

$$g_N^{(2)}(\tau) = \frac{N \cdot (N-1) + N \cdot g^{(2)}(\tau)}{N^2} = 1 - \frac{1}{N} + \frac{1}{N} g^{(2)}(\tau). \tag{3.7}$$

Influence of background In real experimental situations also background with the intensity $BG(t)$ (for example: laser leakage, Raman scattering, auto fluorescence of a cell tissue) contributes to the auto-correlation function. For an emitter with

the intensity $S(t)$, the measured auto correlation $c^{(2)}(\tau)$ will look like

$$c^{(2)}(\tau) = \frac{\langle (S(t) + BG(t))(S(t+\tau) + BG(t+\tau)) \rangle}{\langle (S(t) + BG(t)) \rangle^2}. \tag{3.8}$$

Assuming that $BG(t)$ is uncorrelated with $S(t)$, one can rewrite equation 3.8:

$$c^{(2)}(\tau) = \frac{g^{(2)}(\tau) \cdot \overline{S}^2 + 2 \cdot \overline{S} \cdot \overline{BG} + \overline{BG}^2}{(\overline{S} + \overline{BG})^2} \tag{3.9}$$

$c^{(2)}(\tau)$ can then be formulated as

$$c^{(2)}(\tau) = 1 - \eta^2 + \eta^2 g^{(2)}(\tau), \tag{3.10}$$

with η describing the fraction between the average signal $\overline{S}$ and the overall intensity collected $\overline{S} + \overline{BG}$:

$$\eta = \frac{\overline{S}}{\overline{S} + \overline{BG}} \tag{3.11}$$

By comparing equation 3.10 with 3.7, one may realize that both equations have the same mathematical form, making it impossible to figure out by a single measurement, if multiple emitters are monitored or a single emitter with a significant background. Therefore, if one wants to identify the number of observed emitters, the signal and background has to be determined additionally by reference measurements.

Diffusion in an open droplet Also the diffusion of fluorescent particles can be analyzed with correlation functions providing information about the typical size of the analyzed sample and even of the shape factor [150]. Approximating the confocal volume with a Gaussian beam, one can formulate the diffusion correlation function $g^{(2)}_{\text{diff}}(\tau)$ as [103]

$$g^{(2)}_{\text{diff}}(\tau) = 1 + \frac{1}{N} \left(1 + \frac{\tau}{\tau_D}\right)^{-1} \left(1 + \frac{\tau}{\epsilon^2 \tau_D}\right)^{-1/2}. \tag{3.12}$$

Whereas τ_D is the average diffusion time of N particles in the confocal detection volume and ϵ the ratio between the Rayleigh length w_z and the beam waist w_0 of a Gaussian beam.

The correlation time τ_D across and along the confocal volume is $\tau_D^{(0)} = w_0^2/4D$

$\tau_D^{(z)} = w_z^2/4D$. As w_z is bigger then w_0, $\tau_D^{(0)}$ defines the upper limit of the residual time to stay in the confocal volume with diffusion coefficient D. Using the Stokes-Einstein equation one can calculate the diffusion coefficient D for a spherical particle with hydrodynamic radius r_H to be

$$D = \frac{\mathrm{k_B}T}{6\pi\eta r_H}. \tag{3.13}$$

Whereas $\mathrm{k_B}$ is the Boltzmann constant, T the temperature and η the dynamic viscosity of the surrounding. The residual time, a particle with an hydrodynamic radius of 16 nm stays within the confocal volume is around $\sim 600\,\mu\mathrm{s}$ in water at 25 °C.

Breakdown flash In single molecule spectroscopy typically single photon counting modules are used. The most common detector for this purpose is the so called avalanche photo diode (APD). In this devices an electron avalanche effect caused by an high electric field gradient is used to amplify a single electron after an electron hole pair was created by photo-activation [106]. As sensitive as this devices are, their characteristic behavior can cause serious artifacts in the measured auto-correlation function. The weaker the detection signal, the more significant these artifacts get. The reason for this is the called breakdown flash of the APD, the photon emission caused by electron hole pair recombination after the detection is triggered [106]. As two APDs are often arranged in a Hanbury-Brown and Twiss (HBT) configuration [76], one APD will see the photons emitted by the other APD that has been triggered. In that sense one detector can trigger the detection of photons on the other detector. As the signal is highly correlated, a strong bunching behavior in $g^{(2)}$ around $\tau \sim$ ns will occur. There are several ways to tackle this problem: Typically the so called 2f-2f configuration is used: To this end the optical system mapping the pinhole onto the two detectors is just a single lens. The divergent photon flash back beam from one APD will only be fractionally detected by the second detector. To suppress the flash back further, one can also cross out the photons emitted by making the left and the right arm of the HBT detection path polarization selective [219]. Another possibility is spectral filtering by placing an additional spectral filter in front of one APD, suppressing the emission band of the

APD typically ranging from 750 nm to 900 nm [106].

instrument response function (IRF) and deconvolution The occurrence of an anti-bunching behavior also depends on the time resolution and jitter of the used setup. As the rising slope for a single emitter is dependent on the emission and excitation rate, jitter will wash out the observable dip at zero delay. If continuously exciting an emitter, the overall depth of the observed anti-bunching will decrease drastically, if the time resolution or jitter is on the order of the mentioned rates. Mathematically this behavior can be described by a convolution of the original $g^{(2)}$ with the IRF. If the IRF is known, one can simply use deconvolution theory, to recover the original $g^{(2)}$ function. Another strategies to tackle this problem, is to measure $g^{(2)}$ using pulsed excitation, leading to distinguishable peaks spaced by the repetition time of the used laser. The $g^{(2)}$ function itself is formed by a convolution integral. If accumulating the autocorrelation function of the direct laser, one can extract the IRF.
More general, the described behavior accounts for all types of acquired data, and the IRF must be characterized for the given setup.

3.2. Nanodiamonds

As this work is concentrating on nanodiamonds, their basic properties and differences to bulk diamond material are highlighted.

3.2.1. Diamond

Diamond is known to be the hardest materials existing. The reason for this lies in the high binding energies of 285.1 eV of sp^3 hybridized electron bonds between neighbor carbon atoms forming the diamond lattice [172]. Diamond has a center cubic lattice structure, is transparent (optical absorption coefficient $0.07\,cm^{-1}$) and has a very high thermal conductivity of $\approx 2000\,W\,m^{-1}\,K^{-1}$, although pure diamond is almost insulating [151]. To classify a specific piece of diamond one typically refers to the number of impurities in the diamond lattice, because they dominate its physical properties. As nitrogen is the most frequent element that can be found in diamond, it's relative amount is used for classification (see Table 3.1).

Type	Impurities	Origin
Ia	$\approx 0.1\%$ nitrogen, nitrogen cluster	98% of all natural diamonds
Ib	$\approx 0.05\%$ nitrogen, nitrogen cluster	$< 0.1\%$ in nature, includes high-pressure synthesis
IIa	few ppm nitrogen	rare in nature
IIb	less nitrogen then IIa, bor	extremely rare in nature, produced by high-pressure synthesis

Table 3.1. Classification of diamond. Adapted from [151]

3.2.2. Production of (nano)diamond

Besides natural deposits, nowadays diamond can also be created synthetically. The two main techniques allowing diamond production from nm to mm scale are the so called high-pressure-high-temperature (HPHT) and chemical vapor deposition (CVD) approach. NDs can also be produced by shock wave assisted growth or can be found in meteoroids.

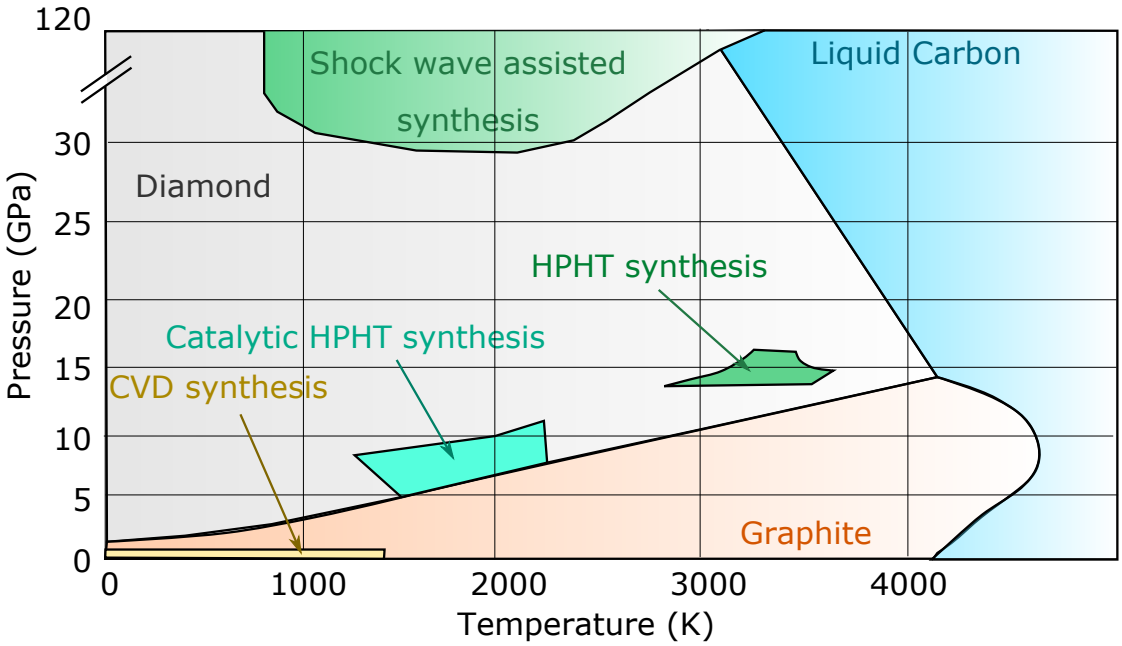

Figure 3.2. Phase diagramm of carbon. Adapted from [156]

HPHT In HPHT synthesis one mimics the condition naturally occurring deep within earth using a hydraulic molding press to transform graphitic carbon into diamond. Therefore catalysts, for example, alloys including iron, nickel, cobalt and manganese-carbide or non metallic solvents are used [1, 23]. Diamond grown *via* HPHT are of type I with 50 ppm and higher concentrations of nitrogen. But by adjusting the starting material controlled variations from several thousand to several tens of ppm are possible [1, 23, 226]. In addition high quality diamonds of type IIa and type IIb can be created by suppressing the incorporation of nitrogen using a getter like titanium, aluminum, boron, copper and germanium [1]. Typically grow conditions are shown in Figure 3.2. HPHT diamond can be fabricated in several sizes from millimeter down so some nanometer [190].

CVD During CVD synthesis diamond is grown directly on a substrate by deposition of carbon atoms that originated from a precursor like methane diluted in molecular hydrogen as vapor: Therefore the substrate is placed in an evacuated chamber and the methane/hydrogen mixture is injected. Aromatic hydrogen transforms methane into radicals by for example the chemical reaction

"$H \cdot + CH4 \rightarrow H_2 + CH_3 \cdot$". Latter, if close to the substrate, can adsorb on the surface of the substrate and chemical react with the surface creating a solid thin carbon film on top. The residual volatile hydrogen desorbs from the surface and is transported *via* convection out of the chamber. To enhance the reactivity (create more radicals) in the vicinity of the substrate, latter is heated in case of standard procedure. For diamond growth more complex variations are used to ensure the desired chemical reaction on the surface: Typically a plasma is created above the surface (plasma enhanced CVD) or hot wires are used (hot-filament CVD) to activate the vapor and increase reactivity, also creating an additional plasma. However most efficient growth of diamond is established by streaming the precursor through a plasma arc leading to more aromatic hydrogen promoting diamond deposition [35]. The initial crystal quality of the grown diamond film critically depends on the used substrate: As the diamond film on top is directly covalently bond to it, the crystal lattice constant of both has to match as good as possible. For single crystalline quality on bulk scale, diamond itself or iridium-including multilayer structures on silicon are used as the subtract [57]. For other materials like plain silicon [144] or molybdenum [199] the growth typically results in polycrystalline diamond. If the starting material was chosen wisely, the resulting crystals itself still show good property as a host material for color defects [89]. By controlling the concentration of desired dopands within the growth chamber, it is possible to introduce layers with a high density of dopands (δ-doping [139]). In addition preferential oriented growth of color centers has been demonstrated [125].

Shock-wave assisted synthesis Similar to HPHT also in shock-wave assisted synthesis high pressure and high temperature is introduced. In different to first one mentioned, explosives are used to create conditions needed in a short but intensive way. Therefore the synthesis chamber is filled with a carbon including precursor like graphite mixed with an explosive [197]. Mostly the explosive itself is used as the precursor [50]. Another variation uses an external explosive to compress the precursor in a chamber [40]. After detonation the atomic carbon condenses to a liquid phase and transforms to solid diamond resulting in nm-sized crystals with yield up 80 wt% of the final soot [66]. Depending on the used method, precursor and cooling method (wet or dry), the resulting ND size can vary between some to

several tens of nm. The size distribution typically is fairly narrow and on a similar order of the crystal size [177, 15]. In addition by using nitrogen rich explosives like trinitrotoluol (TNT) or hexogen (RDX) and mixtures the nitrogen content of diamond material can varied between some ppm to several % [177, 15]. New purification approaches allow the final product to be 99.95 % diamond crystals [126]. Finally also fluorescence from color centers could be found in this types of diamond [24, 213, 183]. Nowadays it is even possible to shrink detonation grown diamond down to 1.4 nm with a spreading of ± 0.7 nm by oxidation [191].

Extraterrestrial sources NDs can also be found in some types of meteorites having sizes between 1 nm to 10 nm [214, 178, 38, 109]. The exact growth conditions are still not known, but the most conclusive explanation is an CVD like mechanism in the atmosphere of red-giants [109, 38]. Even if this source is not a steady one far from industrial use, MNDs have been shown to be a useful work-frame in science application to evaluate stability considerations for defects in ultra small nano crystalline diamond (UNCD) [214].

3.2.3. The surface of (nano)diamond

As NDs are an interesting material for life science applications as they are non-toxic [221], also it's functionalisation for specific tasks are desirable. For example binding to specific protein or regions in a living cell is possible for some commercially available fluorescent probes. In difference to bulk diamond, the surface on NDs is more inhomogeneous. In addition, the surface of NDs typically expand to between 4 to 8 atomic layers [25]. This leads to a huge manifold of different surface groups including graphite like structures, carbonyl, carboxyl, hydroxyl and ether groups or alcohol functions [104] also depended on the procedure of ND production. After purification methods, which increase the amount of some specific surface groups, different pathways can be used to graft secondary structures on the surface of the diamond [104]. In the follow the groups and surfaces corresponding to specific functionalisation are highlighted in more detail.

Hydrogen-termination Typically atomic hydrogen terminates the surface of (nano)diamond during CVD growth as side product from precursors or molecular hydrogen used during synthesis [202]. But also post-treating in a hydrogen atmosphere at several hundred degree Celsius [220, 86, 188, 138] or using in addition a hydrogen plasma or hot-filament approach have the same effect [223]. Although diamond is a wide band gap semiconductor and almost insulating, hydrogenation of the surface have an interesting effect on the surface conduction of diamond. Oxygen related surface species lead to a low conductance of around $10 \times 10^{-14}\,\Omega^{-1}\,\mathrm{m}^{-1}$, but hydrogen bound to the diamond surface increases the surface conductance to $10 \times 10^{-8}\,\Omega^{-1}\,\mathrm{m}^{-1}$ [118]. The surface conductance itself originates from a band bending in the vicinity of the surface. Water molecules adsorbed as a thin layer on the surface of the diamond act as surface acceptor. By the chemical reaction $2H_3O^+ + 2e^- \rightleftharpoons H_2 + 2H_2O$ electrons are remove from the diamond leaving holes behind. As a consequence holes accumulate at the surface resulting in shift of the Fermi-level even below the valence band, creating a 2D hole-gas at the diamond surface [118]. Color centers in the vicinity of the surface can be discharged, if the ground state level of their current charge state configuration excite the Fermi level (see also 3.2.4, page 33).

Fluorine-termination Fluorination of the surface can be carried out by treating ND with a gas mixture of F_2/H_2 [111], or by applying a plasma with CF_4 [155]. Flour on the surface can be replaced by amine groups allowing the direct grafting of polymers with amine groups to the surface [104].

Carboxyl-group To create a homogenous distribution of Carboxyl-groups on the diamond surface, one has to treat its surface either with strong acids or air oxidation or a combination of both [104]. All techniques have in common, that the diamond itself will loose in weight (the smaller the faster [67]). But oxidative size control can also be used to increase the size homogeneity of ND [142]. As Carboxyl-groups can react with amine and alcohol groups forming stable covalent bonds, suitable polymers can be directly crafted to the diamond surface [104, 85].

Hydroxyl-group Also hydroxyl groups are interesting for further functionalisation of NDs. For example by the use of silane, grafting of peptides [8, 136] or even creating a silica shell around the ND have been demonstrated [159, 158]. Specific binding of ND to biomolecules [181, 8, 59] or the creation of more advanced sensor system in combination with color centers inside the ND [159] has been shown. To establish an efficient coverage, the most straight forward way is to reduce initial C = O groups by borane or reactive hydrides. The so called Fenton reagent allows on one hand to free the surface from carbon including functional groups and on the other hand to establish direct connections of OH radicals with the diamond surface. Also during attrition, when producing ND, a partial hydroxylation of the diamond surface can be established. Another way is photochemical hydroxylation. Typical zeta potentials of are in the range of 40 mV [104].

Grahite It's also possible to create layers of graphite on ND. For a well controlled formation of graphite layers, diamond has to be heated or irradiated for example with electrons in a vacuum chamber still containing residual oxygen. But also in a less controlled way prolonged treatment during ND attrition leads to the formation of sp^2 carbon [104]. Decorating the host ND with a graphite surface can lead to unwanted side effects for the color center NV. It has been shown that the charge state is negatively influenced [166].

Non-covalent binding As oxygen related surface groups can be dissociated in water, the surface of the ND experience a negative zeta-potential in the range of −30 meV to −50 meV. (Bio-)molecules with positive polarity (typically with amino-groups) can be adsorption. Even if an electrostatic interaction is not that strong then a covalent bond, the adsorbed material can have several connections at the same time. The diamond surface can be passivated with polymers without latter loosing their functionality. In addition the adsorbed polymers can be further chemically modified, allowing to bind other groups with more specific tasks to the surface [104]. In addition creating diamond/polymer clusters have been shown to have enhancement performance, compared to the polymer alone for example for the purpose of drug delivery or to increase material properties like the Young's modulus [104].

3.2.4. Color defects in (nano)diamond

Some impurities in diamond can form optical active defects in the visible range [225]. The reason for this is the wide band-gap of diamond with 5.5 eV [22]: If a defect provides additional levels within the band-gap that are energetically far (more then several $k_B \cdot T$) from the valence (VB) or the conduction band (CB), thermal (de)population of electrons or holes from the defect states to the CB or VB becomes unlikely. That is why such levels are sometimes also called deep level traps. Some defects having more then one defect level with in the band-gap can be optically exited and emit photons after relaxation without significant perturbation. The most prominent representatives of such color centers that are also focus of this manuscript are the so called NV and the SiV. In the following this two defects will be highlighted more closely.

The nitrogen vacancy center in diamond

The Nitrogen Vacancy Center (NV) is a point defect in the diamond lattice consisting of a single carbon substitution by nitrogen with a vacancy next to it [225]. Besides the fact that NV is a color center that can be excited and detected in the visible range, the unique electronic level structure of the negatively charged defect allows initialization and readout of the spin-sublevels just by optical means [141]. As the electron spin state of the NV is also coupled to its local environment, sensing applications for various physical quantities have been demonstrated [49, 92, 137, 203, 189, 107, 10]. Also the use as a qubit for quantum computing and various schemata for quantum processing have been shown [167]. Almost all mentioned applications are based on utilizing the ground state of NV. That will be discussed in the following.

Electronic structure As already mentioned the NV is composed of a nitrogen with a empty lattice site by side. As the Nitrogen is bound to three neighboring carbon atoms, it has two unbound electrons (lone pair electrons) that can contribute to the defect. In addition, there are three orbitals from the carbon atoms next to the vacancy, which contain one electron each. Assuming one orbital of the Nitrogen and the three orbitals of the Carbon to be sp^3 hybridized, one finds by applying

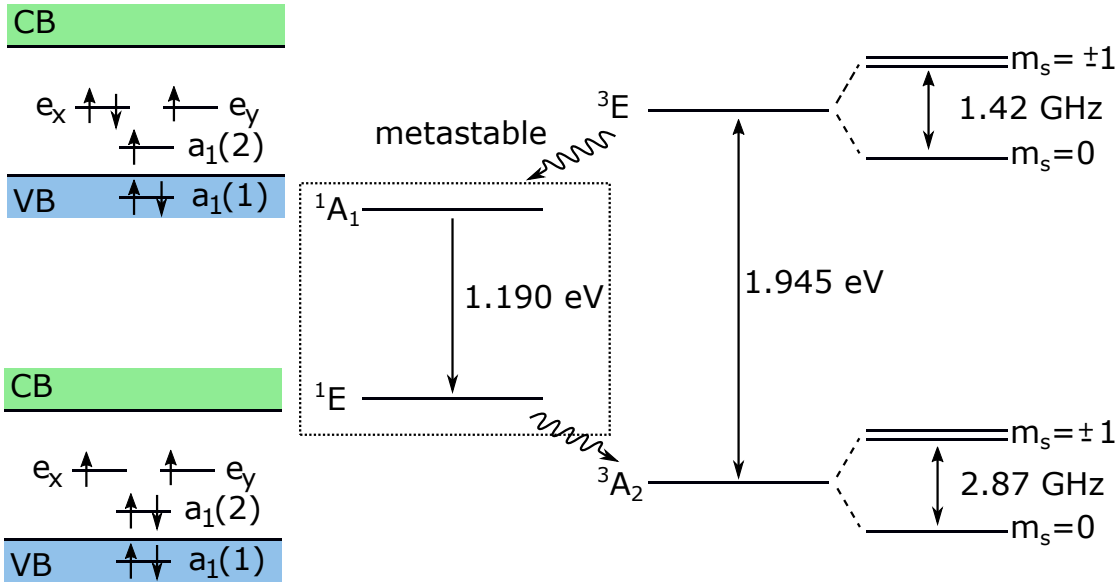

Figure 3.3. Electronic structure of the Nitrogen Vancancy center in diamond. Left: State population of electronic levels forming the NV^-. Right: State picture to describe level transitions at room temperature. For more details see text.

linear combination of atomic orbitals (LCAO) method, C_{3v} to be the point group for the individual electron molecule orbitals: The molecular orbitals are $a_1(1)$ and $a_1(2)$, being an irreducible representation (IR) of the form A_1, and two degenerated orbital state e_x and e_y. Later transform according to a two dimensional IR E. The energetic order of the orbitals is starting from the lowest: $a_1(1)$ then $a_1(2)$ and finally e_x and e_y [121, 46]. To form the NV^- an additional electron has to be captured. Typically this is suspected to originate from an electron donor like a substitutional nitrogen in the vicinity [121, 46]. After calculating the electronic configuration for the six electrons in the lowest state $a_2^2a_1^2e^2$, one finds three possible spin configurations: two singlet states: ^1E and $^1A_1$ and a triplet state $^3A_2$. In the excited state configuration $a_1^2a_1^1e^3$, a singlet $^1E'$ and a triplet ^3E is found [121, 46]. As the triplet states are lower in energy, because they have the lowest amount of unpaired electrons (Hund's rule), they form the ground (GS) and first excited state (ES) of the NV^-. ES and GS are split by the energy of $\sim 1.945\,eV$ [46]. If the NV relaxes back to the GS it can either do that directly by emitting a red photon or decay via spin-orbit coupling to a meta stable state (MS) system by

emitting an infrared photon with 1.190 eV [162]. The latter is originated from the singlet-singlet transition in the electronic lowest state that are assumed to form the former mentioned MS system [46]. Treating both singles states as one level the NV can be well descried by a three level system following equation 3.2 and 3.4. Most interesting, the coupling rates k_{ij} of NV^- are spin depended and as a consequence the adjusted spin state can be read out optically: When exciting the NV^- from the GS with the spin quantum number $m_s = \pm 1$, the probability for an inter-system crossing from the ES to MS is higher then in the case of $m_s = 0$. From MS to the GS the spin configuration $m_s = 0$ is the most preferred configuration to end in. Former one leads to a reduction of possible round trips during excitation in a given time and therefore a drop in fluorescence as the transitions MS to GS is spin forbidden and takes addition time. Later one leads to spin polarization into the GS with spin state $m_s = 0$[77].

Charge state The nitrogen vacancy can occur in several charge states. Two of them, the neutral and the negative charged configuration (see Figure 3.4) are known to fluoresce in the visible range namely. Although for the neutral nitrogen vacancy center (NV^0) it has been proposed that in principle optical read out and spin polarization like for the NV^- should be possible [63], up to now no one could make practical use of NV^0 spin system only. In addition, also a positively charged nitrogen vacancy center (NV^+) exists. Several publications give hint to its existence [70, 78, 149], but no fluorescence of NV^+ could be detected up to now. Although NV^+ still remains of interest because it could be shown, that the nuclear spin lifetime of NVs nitrogen can be extended to several seconds at room temperature [149]. Therefore the NV is first converted to NV^-, a certain nuclear spin state is adjusted and then the NV is discharged to NV^+. As the NV^+ has a singlet ground state, no direct interaction from the NV electron spin to the nitrogen nuclear spin is expected like it is the case for the NV^-.
The charge state of NV is dependent on two parameters: First one is the excitation wavelength allowing to switch to NV^0 or vise versa in a probabilistic way. In reference [11, 180] they explain this behavior by a wavelength dependent ionization and recombination process of the NV^- state. After NV^- is excited by a photon, a second photon absorbed promotes an electron from the saturated e-states to the

conduction band. If an additional electron from the conduction band is captured by the unfilled $a_1(2)$ state in an Auger process the NV will end up in the NV^0 ground

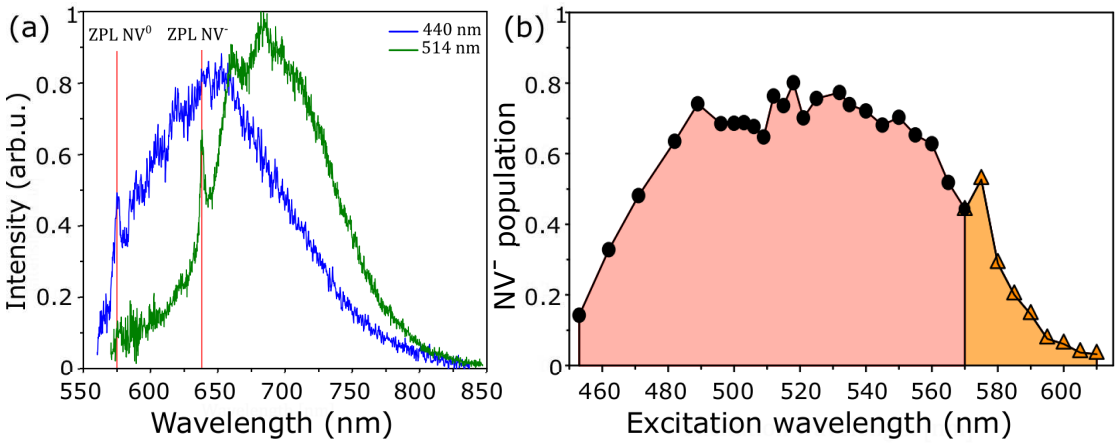

Figure 3.4. Dependence of the NV charge state for different laser excitation wavelengths.(a): The fluorescence spectra of NV^- (green) and NV^0 blue detected from the same NV center for difference excitation wavelengths.**(b):** Probability to be in NV^-. Both graphs have been adapted from [11]

state. As two photons had to be absorbed ionization is quadratically depending on the excitation power (two photon process). If the energy of the photons is high enough a linear dependence of the ionization from laser excitation power can be found. Aslam et al. [11] conducted from this results, that the NV^- ground state lies 2.6 eV below the conduction band. From similar considerations for the recombination process (NV^0 converts to NV^-), it is found that the NV^- ground state is 2.94 eV above the valence band. More interesting they could verify an interesting observation already done by [180] at liquid helium temperature: It seems that in the process of recombination to NV^-, the neutral charge state plays an important role, because excitation at the ZPL of NV^0 leads to an enhancement probability to be in NV^- state. (see Figure 3.4, island at 575 nm). After absorbing an photon an electron is promoted from the $a_1(2)$ to an e-level in the NV^0 state. After capturing an additional electron by photon absorption from $a_1(1)$ that lies deep within the valence band and therefore gets refilled quickly, the NV is in the negatively charged state. As also other impurities or charge traps can take over the role as an electron donor, the conversion from NV^0 to NV^- can still work for

excitation wavelengths below the ZPL of NV^0. A good hint that ionization of charge traps in the direct vicinity of the NV happens, is that its ZPL spectral drifts around for several tens of MHz at cryogenic temperatures [180, 161]. The charge state of NV can be very stable for several days [43]. As in reference [11, 43] the charge state was stable under dark condition, however this must not be always the case [61, 119]. In addition, charge traps can also occur if the NV is placed in close proximity to surfaces and can depend on the type of surface termination[96, 166, 60, 24]. This process can especially in NDs ($\approx 100\,\mathrm{nm}$) lead to a low NV^- to NV^0 ratio [166, 60].

The second possibility to control NV charge state is by shifting the Fermi-level.

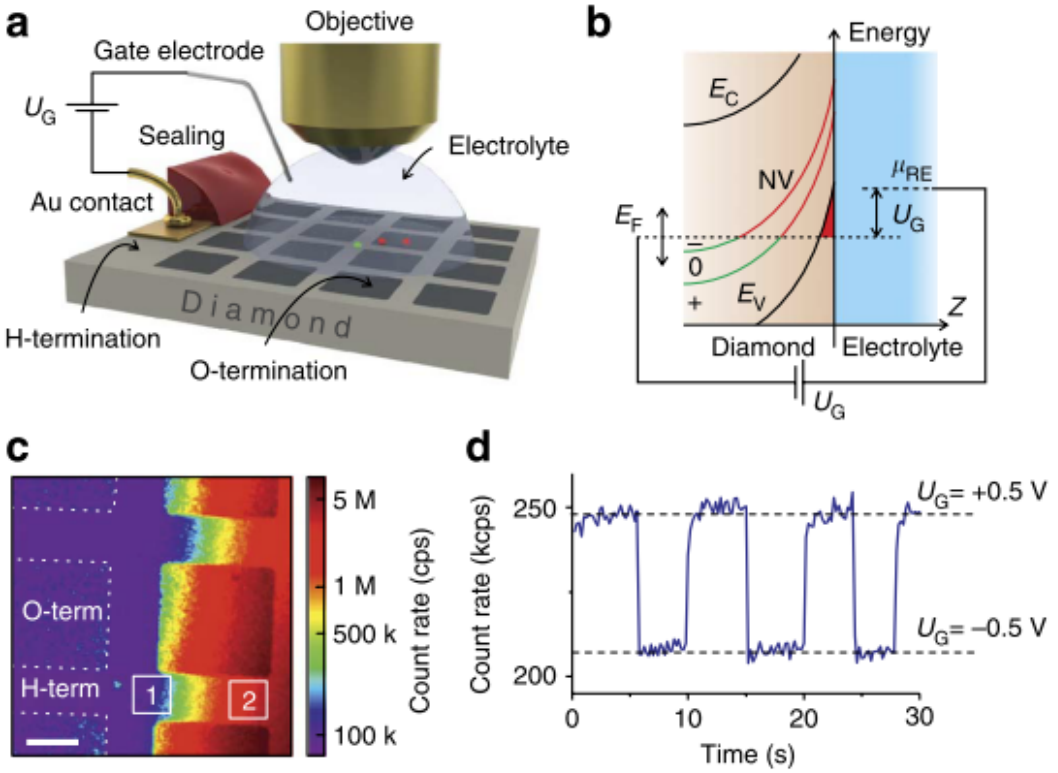

Figure 3.5. Controlling the charge state of NVs, adapted from [70]. (a): Sketch showing the setup arrangement. **(b):** Band bending model and NV ground state depending on the distance to the surface. **(c):** Confocal scan over the used sample surface, **(d)** applying two different control voltages U_G to a single NV.

If the NV sits in close proximity to a hydrogen terminated surface, the occurring band bending (see 3.2.3) leads to a downwards shifting of the Fermi-level at the

position of the NV. As a result the ground state of NV^- gets depopulated first, shifting the charge state to NV^0 and even further [78, 70]. By applying an electrical potential U_G via a gate electrode the energetic shift of the Fermi-Level close to the surface can be controlled [70, 149]. Again in small NDs ($\leq$100 nm) a charge state adjustment by shifting the Fermi-level, can be dominant because of the high surface to volume ratio [147, 145, 146].

Spin system As most results presented in this work focus on sensing with NV, its spin system shall be introduced in more detail. As already mentioned the ground state of NV^- is a triplet state and therefore a $S = 1$ spin-system. The corresponding spin Hamiltonian of NV^- H_{NV} can be expressed as

$$H_{NV} = H_D + H_{Zeeman} + H_{HF}. \tag{3.14}$$

H_D describes the spin-spin interaction of the two electrons involved and can be arrange in the form [74]

$$H_D = DS_z^2 + E(S_x^2 - S_y^2). \tag{3.15}$$

Whereas D and E in equation 3.15 are the fine structure constants of the spin system, describing the spin-spin interaction and S_j the corresponding spin operators in x,y and z-direction. D is non-zero in system with axis of threefold (or other manifold) symmetry [74]. The symmetry or spin quantization axis points along the connection of the nitrogen atom and vacancy forming the defect. In bulk diamond D is around 2.87 GHz at room temperature [4]. E occurs when there is a distortion of the C_{3v} by for example strain or an electrical field [49]. In bulk diamond E is typically neglectable small but especially in NDs, E can be of the order of several MHz [24, 122].
H_{Zeeman} describes the Zeeman interaction of the NV^- spin with an external magnetic field:

$$H_{Zeeman} = g\mu_B \sum_j^{x,y,z} B_j \cdot S_j \tag{3.16}$$

Whereas B_j is the magnetic field along the x,y,z direction, g the g-factor of NV^- and μ_B the Bohr-Magneton. For NV^- $g\mu_B$ is around 28 GHz T^{-1} [56].

H_{HF} is the hyperfine interaction between the nitrogen nuclear spin I of the NV and the NV electron spin S:

$$H_{\mathrm{HF}} = \vec{S} \cdot A \cdot \vec{I} \tag{3.17}$$

The hyperfine tensor A is written as

$$A = \begin{pmatrix} A_\perp & 0 & 0 \\ 0 & A_\perp & 0 \\ 0 & 0 & A_\parallel \end{pmatrix}. \tag{3.18}$$

$A_\parallel$ and $A_\perp$ are the axial and the non-axial hyperfine parameters encode two different types of interaction: First the isotropic Fermi contact interaction f_A and second an anisotropic interaction by considering both spins as magnetic dipols d_A [45]. f_A and d_A can be calcuated by

$$d_A = \frac{A_\parallel - A_\perp}{3}, f_A = \frac{A_\parallel + 2A_\perp}{3}. \tag{3.19}$$

Using parameters for $A_\parallel$ and $A_\perp$ in [56] one finds, that the f_A is one order of magnitude stronger than d_A for both N^{14} and N^{15}. Combining H_{D} and H_{Zeemann} and neglecting the hyperfine interaction leads to H_{NV}:

$$H_{\mathrm{NV}} = D \cdot S_z^2 + E(S_x^2 - S_y^2) + g\mu_{\mathrm{B}} \sum_j^{x,y,z} S_j \cdot B_j \tag{3.20}$$

The matrix representation of the spin operators S_j is

$$S_x = \frac{1}{\sqrt{2}} \begin{pmatrix} 0 & 1 & 0 \\ 1 & 0 & 1 \\ 0 & 1 & 0 \end{pmatrix}, S_y = \frac{\mathrm{i}}{\sqrt{2}} \begin{pmatrix} 0 & -1 & 0 \\ 1 & 0 & -1 \\ 0 & 1 & 0 \end{pmatrix}, S_z = \begin{pmatrix} 1 & 0 & 0 \\ 0 & 0 & 0 \\ 0 & 0 & -1 \end{pmatrix}. \tag{3.21}$$

Aligning the magnetic field with strength β_0 along the z-axis that is the quantization

axis, H_{NV} will have the matrix form

$$H_{\mathrm{NV}} = \begin{pmatrix} D+\beta_0 & 0 & E \\ 0 & 0 & 0 \\ E & 0 & D-\beta_0 \end{pmatrix}. \tag{3.22}$$

The Eigenenergies of the system will then be

$$E_{x/y} = D \pm \sqrt{\beta_0^2 + E^2}, E_z = 0. \tag{3.23}$$

The corresponding non-normalized Eigenvectors are

$$\begin{aligned} |X\rangle &= \frac{1}{E}(\beta_0 + \sqrt{\beta_0^2 + E^2})\,|+1\rangle + |-1\rangle\,, \\ |Y\rangle &= \frac{1}{E}(\beta_0 - \sqrt{\beta_0^2 + E^2})\,|+1\rangle + |-1\rangle\,, \\ |Z\rangle &= |0\rangle\,, \end{aligned} \tag{3.24}$$

with

$$|+1\rangle = \begin{pmatrix} 1 & 0 & 0 \end{pmatrix}, |0\rangle = \begin{pmatrix} 0 & 1 & 0 \end{pmatrix}, |-1\rangle = \begin{pmatrix} 0 & 0 & 1 \end{pmatrix}, \tag{3.25}$$

the Eigenvectors for H_{NV} with $E = 0$. In the case where $E \ll \beta_0$ the Eigenvectors are well described by the bases $|0\rangle$ and $|\pm 1\rangle$.
Interesting, when transforming the spin operators S_x, S_y and S_z into the diagonalized system with Hamiltonian $\hat{H}_{\mathrm{NV}}$, they read for $E \gg \beta_0$

$$\hat{S_x}^{\parallel} \propto \begin{pmatrix} 0 & 1 & 0 \\ 1 & 0 & 0 \\ 0 & 0 & 0 \end{pmatrix}, \hat{S}_y^{\parallel} \propto \begin{pmatrix} 0 & 0 & 0 \\ 0 & 0 & -\mathrm{i} \\ 0 & \mathrm{i} & 0 \end{pmatrix}, \hat{S}_z \propto \begin{pmatrix} 0 & 0 & -1 \\ 0 & 0 & 0 \\ -1 & 0 & 0 \end{pmatrix}, \tag{3.26}$$

and

$$\hat{H}_{\mathrm{NV}} = \begin{pmatrix} D+\sqrt{\beta_0^2 + E^2} & 0 & 0 \\ 0 & 0 & 0 \\ 0 & 0 & D-\sqrt{\beta_0^2 + E^2} \end{pmatrix}. \tag{3.27}$$

Another solution for a $\pi/2$ phase shifted modulating magnetic field leads to the

solution

$$\hat{S}_x^{\perp} \propto \begin{pmatrix} 0 & 0 & 0 \\ 0 & 0 & 1 \\ 0 & 1 & 0 \end{pmatrix}, \hat{S}_y^{\perp} \propto \begin{pmatrix} 0 & -\mathrm{i} & 0 \\ \mathrm{i} & 0 & 0 \\ 0 & 0 & 0 \end{pmatrix}, \hat{S}_z \propto \begin{pmatrix} 0 & 0 & 1 \\ 0 & 0 & 0 \\ 1 & 0 & 0 \end{pmatrix}. \tag{3.28}$$

The physical interpretation of (3.28) is that a linear modulating B-field aligned along the x-axis where strain is applied only allows transitions between the state $|X\rangle$ and $|0\rangle$, whereas fields perpendicular to the strain and the NV quantization axis only allow coupling between $|Y\rangle$ and $|0\rangle$. This is totally different to the situation in (3.21), where any linear field modulation aligned along the x or y axis will drive both transitions with equivalent strength when resonant. In contrast, if a circular rotating field (rotating in the xy-plain) is applied in the strain dominating limit, both transitions will be driven equally. Whereas in case of no strain the transition $|0\rangle$ and $|1\rangle$ can only be driven by a right hand circular and $|0\rangle$ and $|-1\rangle$ by a left hand circular rotating field. In addition, if E is much bigger or in the range of β_0, also transitions between $|X\rangle$ and $|Y\rangle$ are possible by applying a z-field.
For an arbitrary external static magnetic field H_{NV} can be expressed using spherical coordinates:

$$H_{\mathrm{NV}} = \begin{pmatrix} D + \beta_0 \cdot \cos(\theta) & \frac{\beta_0}{\sqrt{2}} \cdot \mathrm{e}^{-\mathrm{i}\cdot\varphi} \cdot \sin(\theta) & E \\ \frac{\beta_0}{\sqrt{2}} \cdot \mathrm{e}^{\mathrm{i}\cdot\varphi} \cdot \sin(\theta) & 0 & \frac{\beta_0}{\sqrt{2}} \cdot \mathrm{e}^{-\mathrm{i}\cdot\varphi} \cdot \sin(\theta) \\ E & \frac{\beta_0}{\sqrt{2}} \cdot \mathrm{e}^{\mathrm{i}\cdot\varphi} \cdot \sin(\theta) & D - \beta_0 \cdot \cos(\theta) \end{pmatrix} \tag{3.29}$$

Whereas θ is the azimuthal angle and φ the polar angle. Equation (3.29) leads to the Eigenvalue equation for the eigenvalues ϵ (see also [13]):

$$\begin{aligned} 0 &= \epsilon^3 - 2 \cdot \epsilon^2 \cdot D + \frac{D \cdot \beta_0^2}{2} + \epsilon(+D^2 - E^2 - \beta_0^2) - \frac{1}{2}\beta_0^2 \Delta_{\varphi\theta}, \\ \Delta_{\varphi\theta} &= D \cdot \cos(2\theta) - 2 \cdot E \cos(2\varphi) \cdot \sin(\theta)^2, \end{aligned} \tag{3.30}$$

allowing to calculate the strength of the external field β_0 and its orientation to the

NV^- spin quantization axis with the knowledge of D and E:

$$\begin{aligned}\beta_0 &= \sqrt{\frac{1}{3}\cdot(\omega_1^2 - \omega_1\cdot\omega_2 + \omega_2^2 - D^2 - 3E^2)},\\ \Delta_{\varphi\theta} &= \frac{-7\cdot D^3 - 4\omega_1^3 + 6\omega_1^2\cdot\omega_2 + 6\omega_1\cdot\omega_2^2 - 4\omega_2^3 + 3D(9E^2 + \omega_1^2 - \omega_1\cdot\omega_2 + \omega_2^2)}{9(D^2 + 3E^2 - \omega_1^2 + \omega_1\cdot\omega_2 - \omega_2^2)}.\end{aligned} \tag{3.31}$$

The NV^- Hamiltonian in the rotating frame To describe the spin dynamics of the NV^- it is often useful to transform the system into a reference frame rotating with the frequency corresponding to D. In typical NV experiments a linear polarized microwave field is applied. As already mentioned this allows to drive both transitions in case of $E = 0$. Assuming an external field with strength β_0 aligned along z, and a modulating field with strength β_1 within the xy-plain, H_{NV} can be formulated as:

$$H_{\mathrm{NV}} = H_{\mathrm{drift}} + u_x(t)\cdot X + u_y(t)\cdot Y. \tag{3.32}$$

H_{drift} is the drift or free evolution Hamiltonian of NV and X and Y are called the control fields along the x and y direction of the NV reference frame. Formulating the free evolution Hamiltonian and the controls leads to

$$H_{\mathrm{drift}} = \begin{pmatrix}\beta_0 + \Delta D & 0 & 0\\ 0 & 0 & 0\\ 0 & 0 & -\beta_0 + \Delta D\end{pmatrix}, X = \frac{\beta_1}{2}\begin{pmatrix}0 & 1 & 0\\ 1 & 0 & 1\\ 0 & 1 & 0\end{pmatrix}, Y = \frac{\beta_1}{2}\begin{pmatrix}0 & -\mathrm{i} & 0\\ \mathrm{i} & 0 & \mathrm{i}\\ 0 & -\mathrm{i} & 0\end{pmatrix}. \tag{3.33}$$

ΔD accounts for possible shifts in D. The coefficients in equation (3.32) $u_x(t)$ and $u_y(t)$ allow to modulate the control fields and drive transitions. If for example $u_x(t)$ follows a cosine and $u_y(t)$ a sine with frequency $\omega = \beta_0 + \Delta D$, the transition between $|0\rangle$ and $|1\rangle$ is resonantly driven. As on can see X and Y have quite some similarity with S_x and S_y. One significant difference in Y compared to S_y is, that the lower half-space has inverse phase. The reason for this is, that X and Y are a combination of two circular polarized magnetic fields rotating clock- and counterclockwise within the xy-plain. The sum of both fields results in the original linear polarized driving field.

For nanodiamonds in the limit of $E \gg \beta_0$ the corresponding Hamiltonian H_{NV} is similar:

$$H_{\mathrm{NV}} = H_{\mathrm{drift}} + [\cos(\varphi)\cdot X_{\parallel} + \sin(\varphi)\cdot X_{\perp}]\cdot u_x(t) + [\cos(\varphi)\cdot Y_{\parallel} + \sin(\varphi)\cdot Y_{\perp}]\cdot u_y(t) \quad (3.34)$$

With the free evolution Hamiltonian

$$H_{\mathrm{drift}} = \begin{pmatrix} E + \Delta D & 0 & 0 \\ 0 & 0 & 0 \\ 0 & 0 & -E + \Delta D \end{pmatrix}. \quad (3.35)$$

The corresponding control fields, if strain is aligned along the x-axis of the NV reference frame, are

$$X_{\parallel} = \frac{\beta_1}{\sqrt{2}} \begin{pmatrix} 0 & 1 & 0 \\ 1 & 0 & 0 \\ 0 & 0 & 0 \end{pmatrix}, Y_{\parallel} = \frac{\beta_1}{\sqrt{2}} \begin{pmatrix} 0 & -\mathrm{i} & 0 \\ \mathrm{i} & 0 & 0 \\ 0 & 0 & 0 \end{pmatrix}. \quad (3.36)$$

The corresponding control fields perpendicular to the strain axis are

$$X_{\perp} = \frac{\beta_1}{\sqrt{2}} \begin{pmatrix} 0 & 0 & 0 \\ 0 & 0 & 1 \\ 0 & 1 & 0 \end{pmatrix}, Y_{\perp} = \frac{\beta_1}{\sqrt{2}} \begin{pmatrix} 0 & 0 & 0 \\ 0 & 0 & \mathrm{i} \\ 0 & -\mathrm{i} & 0 \end{pmatrix}. \quad (3.37)$$

φ accounts for the rotation of the modulating magnetic field versus the strain axis within the xy-plain.

Temperature response of NV^- spin transitions. The zero field splitting D of NV^- has its origin in the spin-spin interaction of the two unpaired electrons occupying the electronic levels of the defect. D is temperature depended [34, 4, 137, 105]. The shift in D ($\delta D/\delta T$) is approximately linear at room temperature and around $\sim 70\,\mathrm{kHz\,K^{-1}}$. Interestingly, the observed shift in D cannot be explained by a simple thermal expansion model of diamond [4, 88]. Doherty et al. [44] suggested that, in addition, electron-phonon interactions have to be considered to describe the observed shift.

Optical detected magnetic resonance and spin state readout. As already mentioned the NV^- spin state can be readout by optical means. Sweeping an microwave over the resonances of NV^- results in figure 3.6(a) that shows a pulsed ODMR spectra for a Rabi amplitude of around 0.53 MHz. Therefore one performs

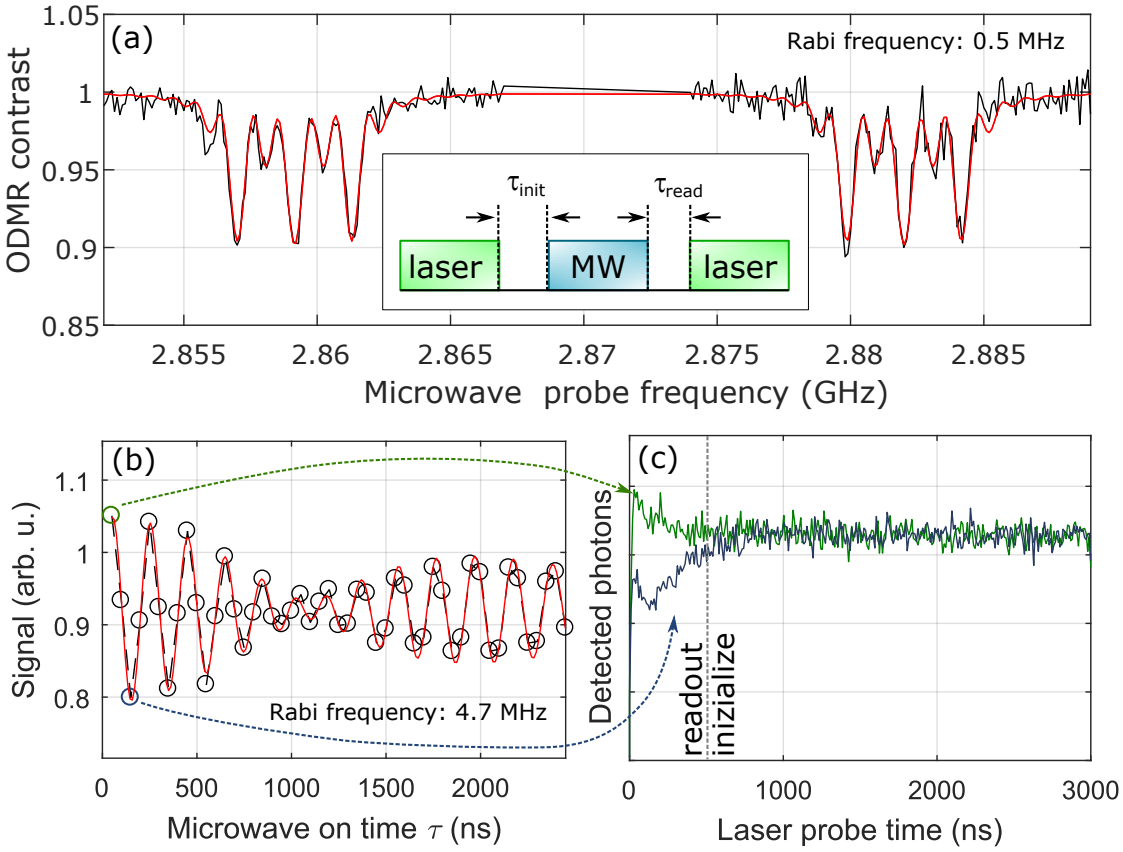

Figure 3.6. ODMR and spin state readout.(a): Pulsed ODMR spectrum for single NV at 0.53 MHz Rabi amplitude. The 3 peak structure is a consequence of the hyperfine interaction with ^{14}N that is part of the defect. The insert showed the used pulse schema the spectrum has been acquired with. (b): Rabi oscillation driven on the left center transition. The Rabi amplitude is around 4.7 MHz. (c): Zoom in into the fluorescence response for of NV^- for two different microwave pulse lengths. Also the region used for readout and initialization/normalization is marked. Different to the Rabi data, the ODMR has been normalized to 1 for better visibility.

for every frequency applied the sequence shown as an insert. First the laser is turned on and the NV^- spin state is polarized or initialized into $m_s = 0$. After turning off the laser, one waits a small time τ_{init} to let residual population in the

meta-stable relax into the ground state. Typically τ_{init} is in the range of 1000 ns. Then the microwave is turned on for a certain time, in optimum chase exactly half the Rabi frequency on resonance to apply a π-pulse. After waiting an additional small time τ_{read} ($\sim$ 200 ns) the laser is turned on again. The laser pulse itself provides, besides repolarize, the function to read out the adjusted spin state. As initial fluorescence level is defined by the adjusted spin state, the first excitation cycles will be either darker or brighter, before the fluorescence follows a steady state behavior (see figure 3.6(c), blue and green curve). The first several hundred of ns can therefore be used to readout the spin state, whereas the latter can also be used to normalize the acquired signal. For example, if one varies the microwave pulse length for a fixed frequency on resonance, one will directly see Rabi oscillations as a function of microwave pulse length (3.6(b)). In addition, the insert in figure 3.6 can be understood as the basic building block for sensing with NV^-. To perform a desired task the middle block, now being just a simple microwave pulse, can be replaced by more complex sensing schemes (see figure 3.10 for examples).

The silicon vacancy in diamond

The SiV consists - similar to the NV - out of a vacancy and one silicon atom, but arranges in a so called split-vacancy configuration (see Figure 3.7a)[68]. Also like the NV the SiV spin system can be prepared and read out optically [164, 152] at liquid helium temperature. Although the spin coherence times are limited to the nanosecond range up to know, schemas are proposed to prolong this period based on a detailed study of the involved processes [90]. An outstanding property among NV is the narrow line-width of photon emission from SiV^- down to 1 nm even at room temperature [91] in combination with 70 % of all emitted photons being within the ZPL. Also spectral diffusion is less prominent like it is the case for NV [179]. In addition SiV can even occur in very small NDs down to 1.6 nm size [212, 214]. The reason for this lies in stability considerations for the defect itself in nanometer size diamonds that is more favorable for SiV then for NV [16]. In the following paragraphs the SiV shall be explained in more detail.

Electronic structure Similar considerations like in the case of NV reveal the symmetry of SiV to be D_{3d} [68, 64, 83]. Therefore the six orbitals of the two

vacancy and 4 orbitals of the interstitial silicon are combined via LCAO. Again as NV also SiV can occur in different charge states: the neutral silicon vacancy (SiV^0) with its ZPL around 1.31 eV [42] and SiV^- with its ZPL associated with 1.682 eV [68]. The SiV^- has a doublet ground and exited state, concluded from PL and EPR studies [42] and assisted by ab initio calculations [64]. (see Figure 3.7(c)). Both individual states are double degenerated IR of E ($|e_+\rangle$ and $|e_-\rangle$ in Figure 3.7(c)). Spin-orbit coupling leads to a splitting of 0.20 meV in the ground and 1.05 meV in the excited state and results in the visible PL spectra shown in figure 3.7(b) at room temperature, and figure 3.7(d) at cryogenic conditions. Also for SiV^- spin polarization and readout has been demonstrated *via* a λ-scheme at cryogenic temperature [164]. But up to now the coherence times are limited to the nanosecond regime because of single-phonon relaxation in the ground and exited state resulting in a fast dephasing (fast flip-flops between the orbital states $|e_+\rangle$ and $|e_-\rangle$) [90]. The single photon characteristics of SiV^- are typically modeled with a three-level system including a meta-stable state [217, 135]. By ab initio methods Gali et al. [64] proposed the structure of SiV^- meta-stable emitting photons at 1.59 eV (see Figure 3.7(c), marked with *), that is pretty close to the fluorescence visible in SiV^- spectrum at 1.52 eV [134]. In addition Rogers et al. [163] found an additional state that allows efficient pumping of SiV^- (Figure 3.7(c) and (e)).

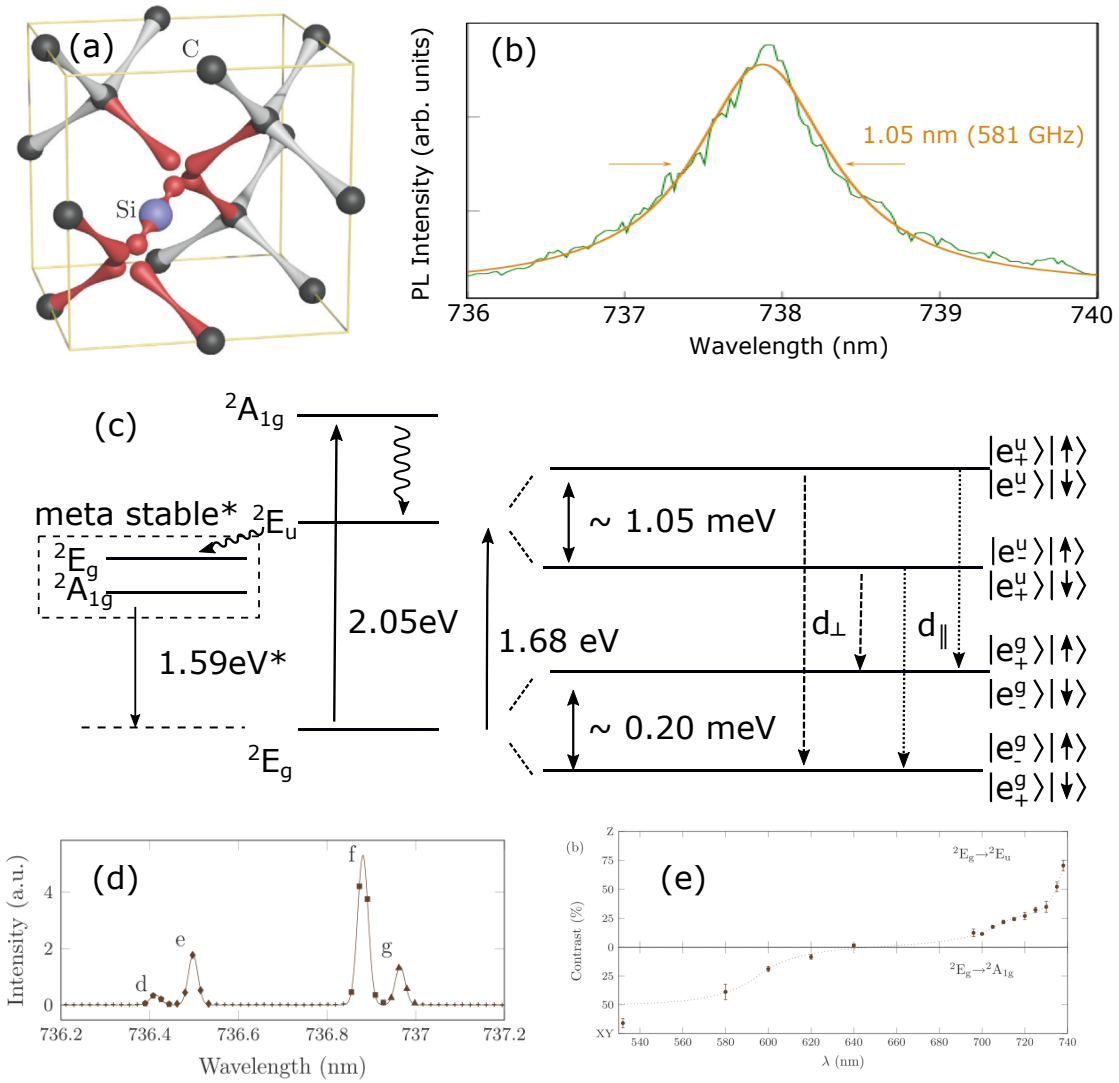

Figure 3.7. The SiV in diamond. (a): The stuctural arrangement of SiV in a split vacancy configuration.**(b):** room temperature spectrum of a single ND crystal containing several SiV adapted from [91] .**(c):** Electronic structure of the ground and exited state including the detailed structure of the involved double degenerated e-level states split by spin-orbit coupling. The dashed and dotted lines indicate the optical decay channels emitting with a dipole $d_\parallel$ parallel to the SiV axis or with a dipole $d_\perp$ perpendicular. The levels and transitions marked with * are the predicted meta stable by ab initio calculations from reference [64]. **(d):** PL spectra of the corresponding transitions in (c) whereas peaks marked with d and g correspond to $d_\perp$ and peaks marked with e and f correspond to $d_\parallel$. **(e):** photoluminescence emission (PLE) measurement on SIV excitation dipole depended on excitation wavelength. XY marks the direction perpendicular Z parallel to the SiV axis. The graph also includes the corresponding transitions involved in the excitation process (see also (c)) [163]

3.2.5. Creating color centers in (nano)diamond

As already mentioned natural diamonds typically come with a unique color depending on the concentration and type of impurities that is also depending on the growth procedure (see section 3.2.4, [225]). Besides the pure existence of a color defect, also the position of the defect to other defects is important: For example in sensing applications typically one wants to place NV as close to the surface as possible to enhance the interaction between the spin on the surface under study and NV. Or in the field of quantum information processing (QIP) where several NVs have to be entangled with also neighbor spins [48], they have to be in a certain interaction radius of NV.

Implantation The most established technique giving desired results is ion-implantation, as it allows to specifically create NV or SiV with more or less deterministic density in high vacuum. Therefore one typically accelerates Nitrogen, Silicon or molecules with a given energy towards the diamond. After penetrating the diamond surface the ion interact with the diamond lattice leading to crystal defects like vacancies. After annealing the diamond at several hundred degrees Celcius the vacancy start to diffuse. If they reach the vicinity of nitrogen or silicon they can form a NV or SiV. To enhance lateral resolution the diamond is often masked at the are where no defects are desired. Therefore for example photo-resist [187, 204], mica [129] and even the tip of an atomic force microscope (AFM) [148] has been used reaching implantation resolution of several tens of nanometer and below. The most promising technique thereby is the deterministic implantation with a Ion trap of single ions providing already a resolution of $(4.6 \pm 1.3)\,\mathrm{nm}$ resolution [175], but no result on diamond has been published so far.
As lateral extension of implantation can be controlled quite good, axial resolution is depending on implantation energy and if implanting into a crystal on the crystal orientation towards the implantation beam. As crystal have a well defined ordered lattice arrangement they provide long straight channels through the crystal. If an ion enters such a channel it can penetrate much deeper into the crystal before it collide with lattice atoms. As a consequence the axial ion distribution after implantation in stretched [204]. To suppress the so called channelingeffect

typically mono-crystalline substrate is tiled by an angle of 7° [37]. To provide high axial positions typically low energies implantation around several keV are used. But with decreasing implantation energy also the yield of creating NV drops drastically even below 1 % for below 10 keV, as the radio of created vacancies per nitrogen atom decreases [148]. If a specific density of NV is desired, one can increase the implantation dose (if not to high [208]), or co-implant with other ions like carbon or molecules [131, 55]. With increasing ion dose also the probability of creating other spin defects that alter the coherent properties increases. One of the most prominent representatives is the so called di-vacancy. By adding a p-doped layer on top of the diamond, vacancies become positively charged and the probability to form di-vacancies decreases as the two positively charged vacancies repulse each other [54]. In addition the NV formation yield increases.

Growth Besides implantation NV can also created by the addition of nitrogen gas during CVD. This allows lateral positioning in a thin layer via δ-doping [139] or even preferential alignment of NVs inside a bulk sample [125]. By intentionally introducing Silicon atoms also SiV can be created. SiV are also a common side impurity during diamond synthesis, originating from glass windows in the growth reactor. As ND are often produced via HPHT synthesis, nitrogen is already present in the diamond grain (see section 3.2.4). To enhance the concentration of optical active defect within a single grain typically high energy (MeV) proton, helium or electron irradiation is used to produce additional vacancies [81].

Thermal annealing To heal out the diamond crystal it has to be heated at least about 600 °C [6]. At such temperature the vacancy defect start to diffusion and leave the crystal via the surface. Typically annealing temperature are $T > 800\,°C$ Also the temperature used to anneal diamond material after implantation plays an important role for the quality of produced defect: Best annealing parameters for nanodiamond are 800 °C to 900 °C for 1 h to 2 h in terms of brightness [81, 185]. For diamond bulk material Naydenov et al. [130] showed that post annealing at around 1200 °C for 12 h leads to an increase of NV spin coherence times. They explain this behavior by the mobility of other spin defect also leaving the diamond crystal at higher temperature.

3.2.6. Size effects and stability of color centers

As diamond material reduces in size the surface to volume ratio increases drastically. As an interesting consequence thermodynamical calculations suggest that the preferred phase of carbon materials is size depended. Whereas for diamond particles bigger then around 5.2 nm the graphite-phase is most stable, for particles from sizes ranging from 1.9 nm to 5.2 nm diamond is more preferable [14].
In Addition, also the capability to host impurities like nitrogen or silicon decrease with size and are dependent on the surface termination, as it defines the crystallographic morphology in the surface region. Typically one compares two raw models "bucky"-diamond (diamond core sp^3-hybridized, graphite surface sp^2-hybridized) with H-terminated diamonds (core and shell have sp^3-hybridization). Placing substitution nitrogen in those model system yield that there is substation driving force toward placing Nitrogen close to the surface [15] for a 2.2 nm sized particle. In case of NV the stability in "bucky"-diamond is even less preferred at this sizes [25]. In contrast, comparable calculations for the color center SiV in the very same set of diamonds result in a high stability of this defect for hydrogenated diamonds of sizes down to 1.1 nm, and there is also sufficient experimental proof for the existence of such small fluorescent nanodiamond (fND)s [212, 16, 214]. The smallest diamond hosting NV found so far is around 5 nm [24].

Quantum confinement With reduce size of ND the particle transforms from bulk-like to quantum behavior starting at a size of 4.5 nm [22]. As a consequence also the optical band gap in diamond increases [154, 22] that can also influence the electronic transitions. In case of SiV this leads to shift of the ZPL towards the blue. Time-dependent density functional theory (TD-DFT) calculations estimated a shift of 0.03 eV for 1.8 nm and 0.12 eV for 1.1 nm sized NDs [214].

3.3. Basic principles of electron paramagnetic resonance and nuclear magnetic resonance

Most of NV sensing capacity is originated from its spin properties. In the following chapter a basic formalism is introduced to describe the theoretical background for sensing applications using NV. The spin is a characteristic property of a fundamental particle, similar to its mass, that can be described by a quantized angular momentum $\hbar \cdot \vec{S}$ having the magnetic dipole moment $\vec{\mu_s}$:

$$\vec{\mu_s} = \hbar \cdot \vec{S} \tag{3.38}$$

Whereas $\hbar$ is the reduced Planck constant and $\vec{S}$ the spin angular momentum. If the magnetic dipole $\vec{\mu_s}$ is exposed to a static magnetic field $\vec{B_0}$ it will undergo a precession following the equation

$$\hbar \frac{\vec{dS}}{dt} = \vec{\mu_s} \times \vec{B_0}. \tag{3.39}$$

As in EPR and NMR typically the response of a bulk sample is measured equation (3.39) can also be expressed in terms of the total magnetic moment $\vec{M}$ the sum of all sample spins:

$$\frac{\vec{M}}{dt} = \gamma \vec{M} \times \vec{B_0} \tag{3.40}$$

whereas γ is the gyromagnetic ratio of the particle. By transforming to spherical coordinates, one gets the characteristic precision frequency ω_L of the magnetization around the applied magnet field. ω_L is called the Larmor Precision Frequency:

$$\omega_\mathrm{L} = \gamma |\vec{B_0}| \tag{3.41}$$

3.3.1. Spins interacting with oscillating magnetic fields

In the following the static field shall be aligned along the z-axis and a second magnetic field B_1 is rotating counter clockwise with the angular velocity ω_1 in the equator of the coordinate system with the basis $\vec{e_i}$. Equation (3.40) can then be

modified as

$$\frac{d\vec{M}}{dt} = \gamma\vec{M} \times [B_0 \cdot \vec{e_z} + B_1 \cdot \cos(\omega_1 t) \cdot \vec{e_x} + B_1 \cdot \sin(\omega_1 t) \cdot \vec{e_y}]\,. \tag{3.42}$$

By transforming from the laboratory frame K into a frame K' rotating with B_1 along the z-axis, whereas B_1 shall be aligned along the x'-axis, equation (3.42) can be written as [182]

$$\begin{aligned} \frac{d\vec{M'}}{dt} &= \vec{M'} \times [(\gamma B_0 - \omega) \cdot \vec{e_{z'}} + \gamma B_1 \cdot \vec{e_{x'}}] \\ &= \vec{M'} \times [\Delta\omega \cdot \vec{e_{z'}} + \gamma B_1 \cdot \vec{e_{x'}}] \\ &= \gamma\vec{M'} \times \vec{B}_{\text{eff}}, \text{ with } \Delta\omega = \omega_{\text{L}} - \omega_1. \end{aligned} \tag{3.43}$$

$\vec{B}_{\text{eff}}$ is the effective magnetic field vector in the rotating frame. In the special case $\frac{\hbar}{\gamma}(\omega_{\text{L}} - \omega_1) \gg B_1$, which is also sometimes called the resonance condition, the influence of B_0 vanishes and the magnetic moment starts to precess only around the x'-axis. In the rotating frame picture an oscillation of the z component of the spin with the angular speed $\omega_1 = \gamma \cdot B_1$ is introduced.

3.3.2. Rabi nutations

In terms of quantum mechanics a single $1/2$ spin system with the states up $|+1/2\rangle$ and down $|-1/2\rangle$, determined by S_z, can be adopted. Such spins systems will oscillate between these two states under resonant excitation (Rabi oscillation). If the duration of excitation is chosen right one can totally invert the state population. For a more general case the population P of both states can be expressed when initially prepared in $|-1/2\rangle$ by

$$\begin{aligned} P_{|-1/2\rangle}(t) &= \frac{\omega_1^2}{\omega_1^2 + \Delta\omega^2} \cdot \cos\left(\frac{\sqrt{\omega_1^2 + \Delta\omega^2}}{2} \cdot t\right)^2, \\ P_{|+1/2\rangle}(t) &= 1 - \frac{\omega_1^2}{\omega_1^2 + \Delta\omega^2} \cdot \cos\left(\frac{\sqrt{\omega_1^2 + \Delta\omega^2}}{2} \cdot t\right)^2. \end{aligned} \tag{3.44}$$

Full inversion can only be achieved when the detuning $\Delta\omega$ from the resonance is small versus the driving strength mediated by B_1.

3.3.3. The Bloch equations

Up to now no interaction of the spins with its environment has been assumed. A first empirical deduction was performed by Bloch. Equation (3.43) can be modified as

$$\frac{d\overrightarrow{M'}}{dt} = \gamma\overrightarrow{M'} \times \vec{B}_{\text{eff}} + \begin{pmatrix} -M'_x/T_2 \\ -M'_y/T_2 \\ -(M'_z - M_0)/T_1 \end{pmatrix}. \tag{3.45}$$

Equations (3.46) are called the Bloch equations. Whereas T_1 is the spin lattice relaxation time, T_2 the coherence time and M_0 the value of M_z in thermal equilibrium typically following a Boltzmann distribution. M_0 can be approximated by

$$M_0 \approx \pi^2\hbar^2 \cdot N \cdot \omega_{\text{L}}/\text{k}_{\text{B}}T. \tag{3.46}$$

If spin polarization is possible, M_0 is no more defined by a Boltzmann distribution that describes M_0 in thermal equilibrium. In case of NV^-, M_0 can be approximated to be zero.

The choise of different time constants for the axial- $M_{x/y}$ and longitudinal magnetization M_z has its origin in the different characteristics of these quantities. From a quantum mechanical point of view the operator for S_z is related to the Eigenenergies of the system, for example for spin ½ system the states $|-1/2\rangle$ and $|+1/2\rangle$ are separated by the enery $\omega_{\text{L}}B_0$. Any state manipulation *via* a modulating field B_1 will be thermally equilibrated after longitudinal relaxation time (T_1). Especially when probing an ensemble it is often experimentally challenging to provide a sufficient homogeneous static field. But also local field inhomogeneities that for example origin from other surrounding spin species are possible. Uncertainties in the energy splitting result in a variation of Larmor precision for different parts of the ensemble. The component M_x and M_y for latter will therefore also develop

differently. Averaging over an ensemble will lead to a reduction of the components M_x and M_y over time with the time constant T_2^* that is called the free evolution time:

$$\frac{1}{T_2^*} = \frac{1}{T_2} + \gamma \Delta B_0. \tag{3.47}$$

The upper limit for T_2^*, is the coherence time T_2.
As T_1 can also be understood as the lifetime of a certain state, it defines an upper limit of the coherence time T_2. (You cannot ride a dead horse.)

3.4. Quantum mechanical description of spin systems

To explain spin dynamics it is often not sufficient to use classical descriptions. An elegant way to describe dynamics in a quantum system, described by the Hamiltonian H is called von Neumann equation [27].

3.4.1. The von Neumann equation

The von Neumann equation, that can be directly derived from the Schrödinger equation is defined as

$$\frac{d\rho}{dt} = -\mathrm{i} \cdot [H, \rho], \tag{3.48}$$

whereas ρ is the density matrix:

$$\rho(t) = \sum_{\alpha} p_\alpha \left|\Phi_\alpha(t)\right\rangle \left\langle\Phi_\alpha(t)\right| \tag{3.49}$$

Φ_α are the normalized state vectors of the system and p_α positive weights. Interestingly, the off diagonal terms of the density matrix represent the coherent evolutions of the system, whereas the diagonal terms describe the population of individual states. The evolution of a quantum system between time t_2 and t_1, can be calculated as

$$\rho(t_2) = U(t_2, t_1) \cdot \rho(t_1) \cdot U^\dagger(t_2, t_1). \tag{3.50}$$

U is the so called time evolution operator and can be formulated for a time independent H as

$$U(t_2, t_1) = \exp\left(-\mathrm{i}H(t_2 - t_1)\right). \tag{3.51}$$

Another way to formulate equation 3.48 is to define a super operator ν:

$$\nu(t_2)\rho(t_1) = U(t_2, t_1) \cdot \rho(t_1) \cdot U^{\dagger}(t_2, t_1) \tag{3.52}$$

As ν maps the density matrix at time t_1 to t_2 it is also called a "dynamic map". As the von Neumann equation only represent closed systems, dephasing can not be described.

3.4.2. Quantum Master equation

The von Neumann equation is suitable for closed systems and can describe the full dynamic of a quantum system under study. But sometimes one is only interested in a specific fraction of the system. For example the evolution of a single spin, coupled to a bath of surrounding spins. Calculating the dynamics including the bath spins can be harsch and almost impossible with nowadays computing power for increasing system size. The solution to this problem is to look only at the dynamics of the spin under study (system) without the bath (environment). Mathematically this is done by tracing out the environment. For ρ being a product state of the density matrix ρ_{s} and ρ_{e} of the system and the environment, respectively, the dynamic of the system can be described by

$$\rho_{\mathrm{s}}(t_2) = Tr_{\mathrm{e}}\left[U(t_2, t_1) \cdot [\rho_{\mathrm{s}}(t_1) \otimes \rho_{\mathrm{e}}(t_1)] \cdot U^{\dagger}(t_2, t_1)\right], \tag{3.53}$$

or:

$$\frac{d\rho_{\mathrm{s}}(t)}{dt} = -\mathrm{i} \cdot \mathrm{Tr}_{\mathrm{e}}[H, \rho]. \tag{3.54}$$

Also for the system alone it's possible to define a dynamic map describing the dynamic of the system under the influence of the environment. If the relaxation dynamics to equilibrium in the bath are much faster than the dynamics in the system one considers the bath to be Markovian (no memory effect in the bath induced by an interaction with the system) . In the case of a Markovian approximation

equation (3.54) can be explicitly expressed [27]:

$$\frac{d}{dt}\rho_{\mathrm{s}}(t) = -\mathrm{i}[\tilde{H}, \rho_{\mathrm{s}}] + \tilde{D}(\rho_{\mathrm{s}}(t)) \tag{3.55}$$

With $\tilde{D}$ called the dissipator:

$$\tilde{D}(\rho_{\mathrm{s}}) = \sum_{k,l} \gamma_{kl} \left(A_k \rho_{\mathrm{s}} {A^{\dagger}}_l - \frac{1}{2} {A^{\dagger}}_k A_l \rho_{\mathrm{s}} - \frac{1}{2} \rho_s {A^{\dagger}}_k A_l \right) \tag{3.56}$$

The operators A_k are a linear combination of a basic set of orthogonal operators defining the corresponding Liouville space of the system. In general $\tilde{H}$ must not be equal to the Hamiltonian of the system alone, and can include additional terms, introduced by the coupling of the system to the environment [27]. To calculate the evolution of a spin system, it is often more convenient to transform equation (3.55) into a matrix representation, whereas the density matrix is written as a column vector [80, 97]. The matrix representation of the generating map is then transformed by the following equation into a $n^2 \times n^2$ matrix representation with $n \times n$ being the dimension of the density matrix:

$$\tilde{\rho_s}(t_2) = \exp\left[(\tilde{\mathbf{H}} + \tilde{\mathbf{D}})(t_2 - t_1)\right] \tilde{\rho_s}(t_1) \tag{3.57}$$

As one can see in Liouville space the superoperator $L = \exp\left[(\tilde{\mathbf{H}} + \tilde{\mathbf{D}})t\right]$ describes the time evolution of the system only.

Similar to the von Neumann equation, equation (3.57) can be formulated as

$$\frac{\mathrm{d}\tilde{\rho_s}(t)}{\mathrm{d}t} = (\tilde{\mathbf{H}} + \tilde{\mathbf{D}})\tilde{\rho_s}(t). \tag{3.58}$$

Whereas $\tilde{\mathbf{L}} = \tilde{\mathbf{H}} + \tilde{\mathbf{D}}$ is the so called Liouville superoperator.

The superoperators $\tilde{\mathbf{H}}$, $\tilde{\mathbf{D}}$ and $\tilde{\rho_s}$ can be calculated *via*

$$\begin{aligned} \tilde{\rho}_{\mathrm{s}}(t) &= \mathrm{col}[\rho_{\mathrm{s}}(t)], \\ \tilde{\mathbf{H}} &= -\mathrm{i}([H]^T \otimes \mathrm{I} - \mathrm{I} \otimes H), \\ \tilde{\mathbf{D}} &= \sum_{k,l} \gamma_{kl} \left([A_k^{\dagger}]^T \otimes A_l - \frac{1}{2} [{A^{\dagger}}_k A_l]^T \otimes \mathrm{I} - \frac{1}{2} \mathrm{I} \otimes ({A^{\dagger}}_k A_l) \right). \end{aligned} \tag{3.59}$$

In case of a spin 1/2 system coupled to some environment the vectorized Markovian dissipator (3.56) can be written as [211, 7]

$$\tilde{\mathbf{D}} = \sum_{k,l} a_{kl} \left([\sigma_k]^T \otimes \sigma_l - \frac{1}{2}[\sigma_k \sigma_l]^T \otimes \mathrm{I} - \frac{1}{2}\mathrm{I} \otimes (\sigma_k \sigma_l) \right). \tag{3.60}$$

Whereas $a_{31} = a_{13} = a_{23} = a_{32} = 0$, $a_{11} = a_{22} = (2T_1)^{-1}$,$a_{33} = (T_2)^{-1} - (2T_1)^{-1}$ and $a_{12} = a_{21}^* = i(\sqrt{2}T_1)^{-1} \cdot s_{eq}$ with T_1 and T_2 being identified as the longitudinal and transverse relaxation time of the system and s_{eq} representing the population difference of states in equilibrium. In case of a spin 1/2 system σ_k are proportional to the Pauli-matrices of the spin-system [7]. Computing $\tilde{\mathbf{D}}$ yields

$$\tilde{\mathbf{D}} = \begin{pmatrix} -\frac{1+\sqrt{2}s_{eq}}{2T_1} & 0 & 0 & \frac{1-\sqrt{2}s_{eq}}{2T_1} \\ 0 & -\frac{1}{T_2} & 0 & 0 \\ 0 & 0 & -\frac{1}{T_2} & 0 \\ \frac{1+\sqrt{2}s_{eq}}{2T_1} & 0 & 0 & \frac{-1+\sqrt{2}s_{eq}}{2T_1} \end{pmatrix}. \tag{3.61}$$

As it can be seen when inserting (3.61) into equation (3.57), $\tilde{\mathbf{D}}$ acts dissipative onto the spin system (off diagonal terms of the density matix are damped with T_2, diagonal terms are equilibrating over time). Also the optimal control package "dynamo" uses equation (3.57) to optimize an open quantum system. As the equation can also be interpreted as a projection into a another state in time this method is also suitable to implement a quantum state filter when computing cooperative pulses (see section 3.4.3). Therefore one defines a projector projecting onto a desired specific state at the desired point in time. If the state at the set point is not reached the Projector will act dissipative and is "destroying coherence", that the final state cannot be reached. As the consequence dynamo tries to optimize the pulse in the desired direction.

3.4.3. Controlling Spins

In the following section the pulse schemes to manipulate the electron spin state of the NV^-, which are used in this work, are discussed. This includes simple square pulses, adiabatic passage and numerically optimized pulses utilizing optimal control

theory.

Square pulses

The most straight forward way to manipulate the state of a spin-system is to apply a constant amplitude periodically modulated magnetic field on resonance with the corresponding transition. As already mentioned in the beginning of section 3.3 Rabi nutations will establish. If the desired state is adjusted the driving field is turned off.

Adiabatic passage

In the case above a constant amplitude and resonant modulating field was applied to alter the spin state. But one can also vary amplitude and relative phase or modulate the frequency of the driving field. The most popular is the so called adiabatic passage [65]. As one can see from equation (3.43) the magnetization will always precess perpendicular to the effective applied B-field B_{eff}. If B_{eff} is changing its orientation very slowly, the spin will follow B_{eff}. If the orientation of the effective field changes much slower than the precession time of the spin, the process is called adiabatic. This can be expressed by the so called adiabaticity factor Q that describes the direct relation between precession speed around the effective B-field and its oriental change [65]:

$$Q = \frac{\omega_{\text{eff}}}{|\frac{d\phi}{dt}|}. \tag{3.62}$$

Describing the effective Larmor frequency ω_{eff} versus the change of the orientation angle ϕ of B_{eff} in the rotating frame. The larger Q is, the more efficient the applied pulse will be. In this manuscript two different adiabatic passage has been used: First is the linear chirp pulse that is equivalent to a π-pulse. Therefore the amplitude is set to a constant value and the relative detuning to resonance $\Delta\omega$ is varied in time [65]:

$$\Delta\omega(t) = 2\pi \left(f_{\text{start}} + \frac{k}{2} t \right) t \tag{3.63}$$

The sweep rate k depends on the sweep bandwidth BW and the overall pulse length T:

$$k = \frac{BW}{T} = \frac{f_{\text{end}} - f_{\text{start}}}{T} \tag{3.64}$$

Where f_{start} and f_{end} is the first and last frequency applied, respectively.
The second pulse used is the so called B_1 insensitive rotation (BIR) pulse allowing to adjust a rotation between 0 and π phase. The BIR-4 pulse is a combination of 4 so called adiabatic half passages that are subsequently applied in backward or forward direction. The first two segments already allow a phase adjustment between 0 and $\pi/2$ and is called BIR-1. This pulse is already robust against amplitude variations, but shows altering performance if the reference frame is not directly at resonance. By applying a second similar BIR-1, phase errors in the first pulse are compensated. The difference to the first BIR-1 segment is, that the phase shift introduced after the first half passage is flipped in order. Different to the linear chirp pulse also the pulse amplitude is varied. Figure 3.8 shows amplitude, phase and frequency transients of all pulses.

To construct a BIR-1 pulse the analytical approximation in reference [65] is used:

$$\begin{aligned}
\omega_1(t) &= \omega_1^{\max} \tanh\left(\frac{2\zeta}{T_p} t\right), && (0 < t < 1/2 T_p) \\
\omega_1(t) &= \omega_1^{\max} \tanh\left(\frac{2\zeta}{T_p} (T_p - t)\right), && (1/2 T_p < t < T_p) \\
\Delta\omega(t) &= \frac{BW}{2} \frac{\tan(\frac{2\kappa}{T_p}(t - 1/2 T_p))}{\tan(\kappa)}, && (0 < t < T_p).
\end{aligned} \tag{3.65}$$

To apply the driving field, $\Delta\omega$ is typically converted into a phase:

$$\begin{aligned}
\phi(t) &= \int_0^t \Delta\omega(t)\mathrm{dt}, && (0 < t < 1/2 T_p) \\
\phi(t) &= \int_0^t \Delta\omega(t)\mathrm{dt} + \Delta\phi, && (1/2 T_p < t < T_p) \\
\Delta\phi(t) &= \phi_{\text{rot}} + \pi.
\end{aligned} \tag{3.66}$$

ϕ_{rot} is a desired rotation angle one wants to apply in the Bloch sphere. As already mentioned for a BIR-4 pulse one just repeats two BIR-1 segments. The only difference is that, for the second BIR-1 segments, the phase offset $\Delta\phi(t)$ is reversed

in time. In addition as two BIR-1 pulses are applied sequenctly, the overall rotational angle is two times the set one. Optimum parameters for ζ, κ and BW has been determined to be 10, arctan(18), respectively [65].

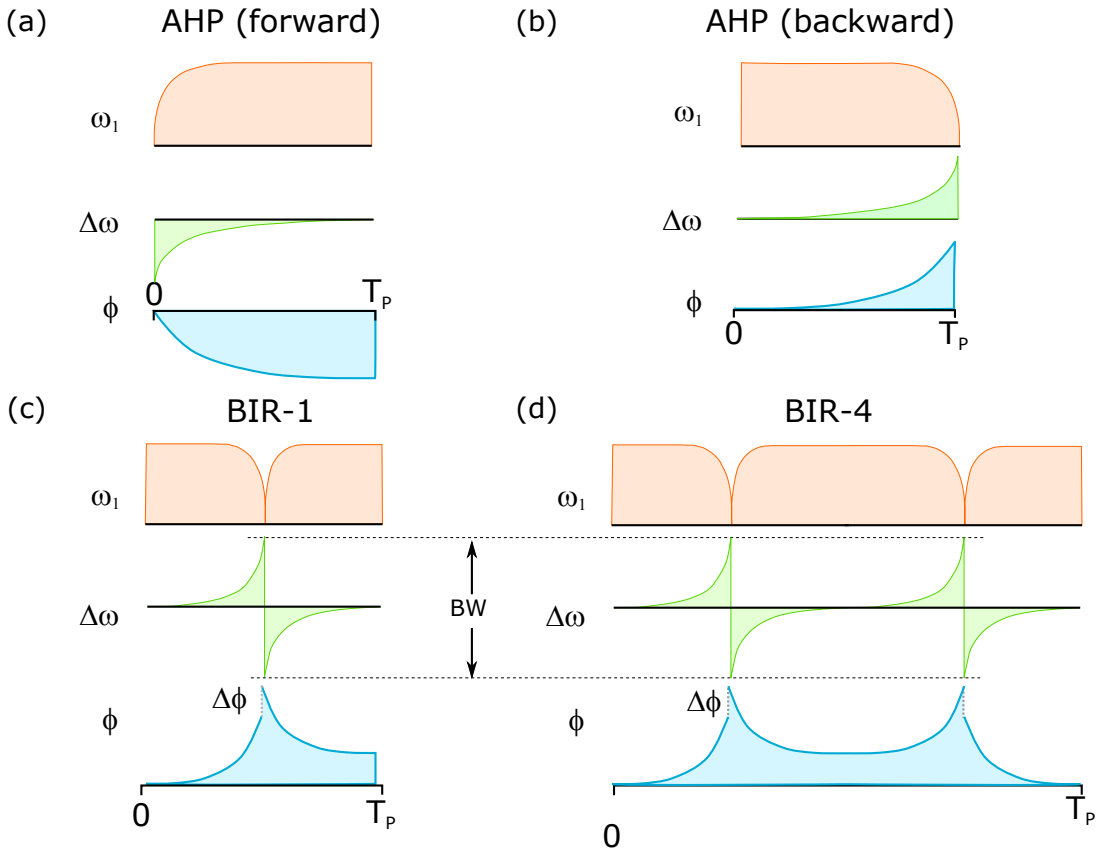

Figure 3.8. Adiabatic Passage: The BIR pulse. (a) and **(b):** Adiabatic half passage (AHF) in backward and forward direction **(c):** Construction of the BIR-1 pulse with (a) and (b). **(d):** Construction of BIR-4 pulse.

Optimal Control

Besides the already mentioned pulse schemes there is a third and even more elegant class of pulses that combines the advantages of both square pulses (very fast) and adiabatic pulses (very robust). Therefore a phase and amplitude modulated pulse is designed, which can be robust against almost every parameter in the experiment, while going clearly non-adiabatic (i.e. Q might be well below 1). The only thing

one needs (and this can also be seen as a disadvantage) is a proper description of the underlying spin system.

Gradient Ascent Pulse Engineering The most simple way to numerically calculate a desired pulse is the so called GRAPE algorithm that shall be highlighted in the following:
Starting with equation (3.4.1) (von Neumman equation) the full system evolution can be described in terms of the density matrix ρ [97]:

$$\frac{d\rho(t)}{dt} = -\mathrm{i} \cdot \left[H_{\text{drift}} + \sum_{k=1}^{m} u_k(t) H_k, \rho(t) \right] \tag{3.67}$$

With H_{drift} being the free evolution or drift Hamiltonian and H_k the control Hamiltonian describing the interaction of the system with for example an external modulating field. In case of magnetic fields, H_k is composed of the spin operators S_x, S_y and S_z. $u_k(t)$ are the amplitude at time t of this interaction and are typically called the control fields. For simple square pulses the control field would be just constant. One task might be performing a desired state transfer. To this end, one wants to find $u_k(t)$ such that the initial state $\rho(0)$ is converted into the desired final state $\rho(T) = C$. The most straightforward way is to define the performance function Φ_0 as the overlap between $\rho(T)$ and C:

$$\Phi_0 = \langle C | \rho(T) \rangle \tag{3.68}$$

With the time evolution operator U_j for a finite small time step Δt ($t = j \cdot \Delta t$,$T = N \cdot \Delta t$,$u_k^{(j)} = u_k(j \cdot \Delta t)$):

$$U_j = \exp \left[-\mathrm{i} \Delta t \left(H_{\text{drift}} + \sum_{k=1}^{m} u_k^{(j)} H_k, \right) \right] \tag{3.69}$$

Φ_0 can be formulated as

$$\Phi_0 = \left\langle \underbrace{U_{j+1}^{\dagger} \cdots U_N^{\dagger} C U_N \cdots U_{j+1}}_{\lambda_j} \, | \, \underbrace{U_j \cdots U_1 \rho_0 U_1^{\dagger} \cdots U_j^{\dagger}}_{\rho_j} \right\rangle . \tag{3.70}$$

For small time steps the change in Φ_0 depending on $u_k^{(j)}$ can be calculated [97]:

$$\frac{\partial \Phi_0}{\partial u_k^{(j)}} \approx - \langle \lambda_j | \mathrm{i}\Delta t [H_k, \rho_j] \rangle \tag{3.71}$$

Φ_0 will increase if $u_k^{(j)}$ changes like

$$u_k^{(j)} \to u_k^{(j)} + \epsilon \frac{\partial \Phi_0}{\partial u_k^{(j)}}. \tag{3.72}$$

Whereas ϵ is a sufficient small step.

To optimize the control fields the GRAPE algorithm has the following basic structure:

1. Random guess for initial $u_k^{(j)}$.
2. Calculate ρ_j starting with ρ_0 for all steps (also called forward propagation).
3. Calculate λ_j starting from C for all steps (also called backward propagation).
4. Evaluate $\frac{\partial \Phi_0}{\partial u_k^{(j)}}$ and change $u_k^{(j)}$ according to (3.72).
5. Repeat procedure within step 2 or stop if Φ_0 reaches a predefined limit.

To introduce robustness against discrete variations in for example H_{drift} ("detuning") or H_k ("transition driving strength") indicated by the parameter α_n and β_m, respectively, one can define the overall performance function Φ_{tot} [97]:

$$\Phi_{\mathrm{tot}} = \sum_{n,m} \Phi_0(\alpha_n, \beta_m) \tag{3.73}$$

Φ_{tot} and the update for the controls of the entirety of all parameters (ensemble) will then be similar to equations (3.71) and (3.72):

$$\begin{aligned} \frac{\partial \Phi_0(\alpha_n, \beta_m)}{\partial u_k^{(j)}} &\approx - \langle \lambda_j(\alpha_n) | \mathrm{i}\Delta t [H_k(\beta_m), \rho_j(\alpha_n)] \rangle \,, \\ u_k^{(j)} &\to u_k^{(j)} + \sum_{n,m} \epsilon_{n,m} \frac{\partial \Phi_0(\alpha_n, \beta_m)}{\partial u_k^{(j)}} \end{aligned} \tag{3.74}$$

Equations (3.68) and (3.69) are defined for a closed quantum system and therefore base on unitary evolutions. But similar expressions can be found based on equation (3.57). The evolution of the density matrix $\tilde{\rho}_j$ after j discrete steps is

$$\tilde{\rho}_j = L_j \cdots L_1 \tilde{\rho}_0. \tag{3.75}$$

Whereas "tilde" indicates the Louisville representation. The performance function Φ_0 reads

$$\Phi_0 = \left\langle \underbrace{L_j^\dagger \cdots L_N^\dagger \tilde{C}}_{\tilde{\lambda}_j} \,|\, \underbrace{L_j \cdots L_1 \tilde{\rho}_0}_{\tilde{\rho}_j} \right\rangle. \tag{3.76}$$

Similar to equation (3.71) one gets

$$\frac{\partial \Phi_0}{\partial u_k(j)} \approx -\left\langle \tilde{\lambda}_j | i\Delta t [\tilde{H}_k, \tilde{\rho}_j] \right\rangle. \tag{3.77}$$

As equations (3.71) and (3.77) are only first order approximations and can contain higher order terms this can lead to a slow down of the algorithm near convergence or can be limited by higher order terms. The solution to that problem is the calculation of the full gradient, where the result is used for optimization, as described in [39].

GRAPE-BFGS In former protocol the optimization of $u_k^{(j)}$ is done by maximizing the performance function Φ_0 *via* a simple first order approximation (see equation (3.72)). But also other minimization algorithm can be used to find the optimal control field. One such example is the so called BFGS [39], a quasi-Newton Algorithm that is also implemented in the "dynamo" package in combination with full gradient calculation [116].

Other optimum control algorithms Beside the already mentioned GRAPE algorithm there is also the so called "Krotov"-based approach. In different to GRAPE where the correction for single control amplitude in time is fully calculated based on present result, in the "Krotov"-approach also the control fields from former optimization step are included leading to a sequential update of the control fields [210].

Cooperative pulse design Typically sensing protocols are a composite of several state manipulation segments (see also section 3.4.4). Thereby each segment transfer a certain initial into a final state. This can be for example a $\pi/2$-pulse. If individual segments are compiled on their own for a very broad parameter range (e.g. detuning from resonance or driving amplitude variations), the desired final state maybe harsh to reach for all ensemble members at once. One way to tackle this problem is to compile the full sequence at once, allowing other segments to account for the imperfects for example in established phase made by the former segments and vise versa. As segments compensate each other they work in a cooperative fashion.
An ansatz to introduce cooperativity can be done in the frame work of open quantum systems. As already mentioned in section 3.4.2 one can replace at a desired position j, L_j with a projector that projects onto a certain state or a set of states. Thereby the projector will later define the cutting point between two pulse segments. If a certain state is not aligned at j, coherence in the modified system shall be partially remove by the projector. If the system has to be further evolved to reach a final state, which shall be pure state of the system, the algorithm is forced to set the right state at j. Thereby the projector allows some additional degreees of freedom and in principle can be understood as a quantum state filter. In the following the mechanism of cooperative pulse design after Braun et al. [26] shall be explained on the example of a simple Ramsey sequence for a two state system: Figure 3.9(a) and (b) show examples of possible state evolutions of two different drift Hamiltonian under the influence of an optimized pulse. Starting from $|0\rangle$ (1), first a superposition state between $|0\rangle$ and $|1\rangle$ (2) is established. Afterwards the system evolves back to $|0\rangle$ (3). As shown in figure 3.9(a), both states must not necessarily match in phase at (2). The used Projector P_{xy} (see figure 3.9(c)) allows the first pulse to align any phase in the equator of the Bloch sphere that is then compensated in cooperative fashion by the second pulse. To force the GRAPE algorithm to establish a superposition state at (2), P_{xy} projects onto the superposition state of $|0\rangle$ and $|1\rangle$. If the state does not match latter one the off-diagonal terms of the density matrix will be not the maximum possible what result in a reduction of this elements after applying P_{xy}. Just as an example: the pure state ρ_1 is projected by P_{xy} onto a totally mixed state. In contrast the pure state ρ_2 representing an equally populated superposition state remains untouched.

After splitting the overall compiled sequence into two pulse segments, one gets the cooperatively designed pulses.

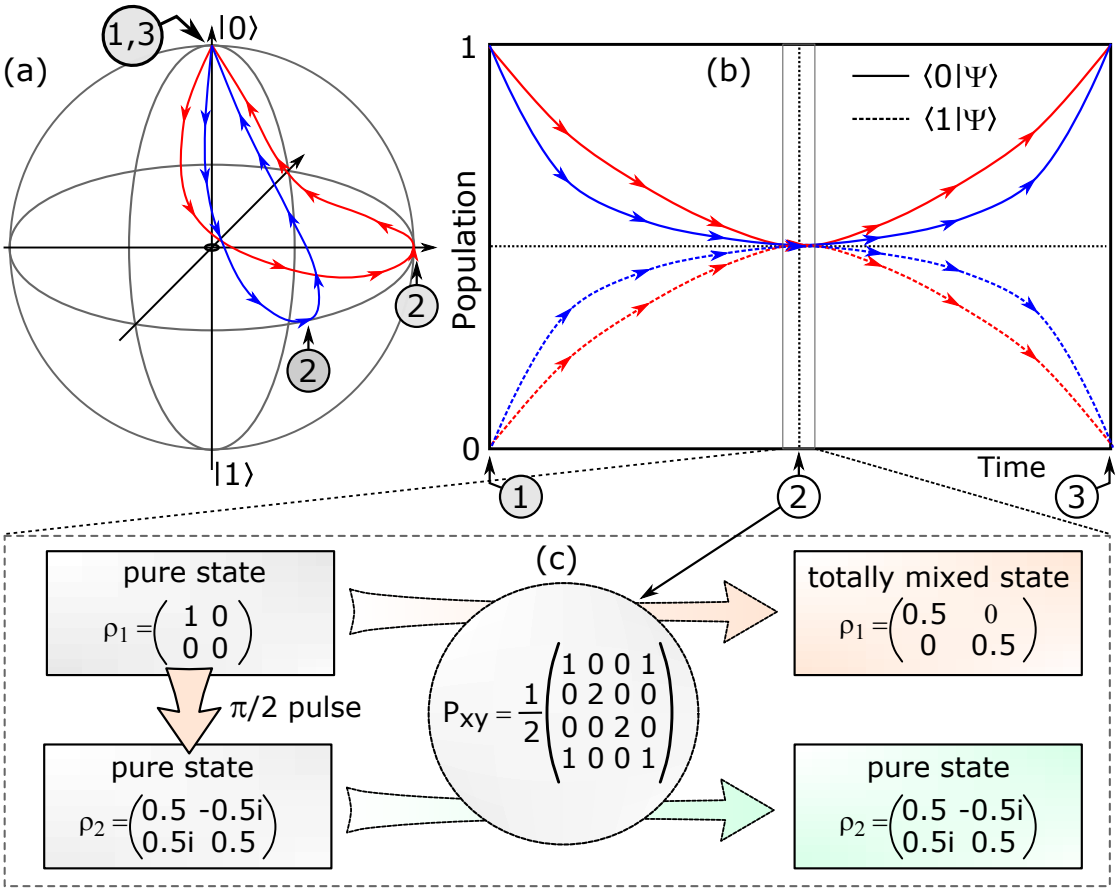

Figure 3.9. Cooperative pulse design. (a): Bloch sphere representation of two different two quantum systems evolving with the same optimum control pulse. **(b):** State evolution using the same pulses as in (a). (1), (2) and (3) present the state of the systems at the beginning after applying a $\pi/2$ pulse and after applying a second $\pi/2$-pulse. **(c):** Influence of projector P_{xy} on two different states represented by the density matrix ρ_1 and ρ_2 (right) initial. (left) after applying P_{xy}.

Similar to a two state system also for a three state system such projectors can be constructed quite easily. Equation (3.78) shows the projectors $P_{xy}^{(1)}$ and $P_{xy}^{(2)}$ enforcing an equal superposition state in case of NV between $|0\rangle$ and $|-1\rangle$, and $|0\rangle$

and $|+1\rangle$, respectively.

$$P_{xy}^{(1)} = \frac{1}{2}\begin{pmatrix} \ddots & & & \vdots & & \\ & 1 & 0 & 0 & 0 & 1 \\ & 0 & 2 & 0 & 0 & 0 \\ \cdots & 0 & 0 & 0 & 0 & 0 \\ & 0 & 0 & 0 & 2 & 0 \\ & 1 & 0 & 0 & 0 & 1 \end{pmatrix}, P_{xy}^{(2)} = \frac{1}{2}\begin{pmatrix} 1 & 0 & 0 & 0 & 1 & \\ 0 & 2 & 0 & 0 & 0 & \\ 0 & 0 & 0 & 0 & 0 & \cdots \\ 0 & 0 & 0 & 2 & 0 & \\ 1 & 0 & 0 & 0 & 1 & \\ & & \vdots & & & \ddots \end{pmatrix}. \tag{3.78}$$

In comparison to P_{xy} for the two level system, these are quite a bit special. Population is lost, if this is not only and equally distributed between the two desired states. This might sound unphysical in the first place. However, this ansatz can be justified when the NV is treated as a three level system being a subspace of a bigger Hilbert/Louville space. Whereas population is transferred into a hidden level that is not accessible.

The projectors force the optimization algorithm to depopulate the state that is not part of the superposition, which shall be aligned. This behavior presents an additional penalty when applying $P_{xy}^{(1)}$ and $P_{xy}^{(2)}$ to a state not representing the right superposition.

The projectors $P_{xy}^{(1)}$ and $P_{xy}^{(2)}$ can also be modified by an additional phase shift as shown in equations (3.79): $P_{xy}^{(1b)}$ adds a phase $\pi/2$ (e.g. $|0\rangle + |-1\rangle \rightarrow |0\rangle + \mathrm{i}\,|-1\rangle$). $P_{xy}^{(2b)}$ adds a $-\pi/2$ phase shift (e.g. $|0\rangle + |+1\rangle \rightarrow |0\rangle + -\mathrm{i}\,|+1\rangle$).

$$P_{xy}^{(1b)} = \frac{1}{2}\begin{pmatrix} \ddots & & & \vdots & & \\ & 1 & 0 & 0 & 0 & 1 \\ & 0 & 2\mathrm{i} & 0 & 0 & 0 \\ \cdots & 0 & 0 & 0 & 0 & 0 \\ & 0 & 0 & 0 & -2\mathrm{i} & 0 \\ & 1 & 0 & 0 & 0 & 1 \end{pmatrix}, P_{xy}^{(2b)} = \frac{1}{2}\begin{pmatrix} 1 & 0 & 0 & 0 & 1 & \\ 0 & 2\mathrm{i} & 0 & 0 & 0 & \\ 0 & 0 & 0 & 0 & 0 & \cdots \\ 0 & 0 & 0 & -2\mathrm{i} & 0 & \\ 1 & 0 & 0 & 0 & 1 & \\ & & \vdots & & & \ddots \end{pmatrix}. \tag{3.79}$$

3.4.4. Sensing in a coherent superposition

Sensing with the NV spin system is typically done by accumulating quantum phase in a coherent superposition state. Thereby a phase corresponding to a detuning of

resonance versus driving field is accumulated over time.

Ramsey measurement

If one sets $B_1 = 0$ in equation (3.43), the spin will experience a precession in the rotating frame picture, which scales with the detuning. If one can determine the detuning one can calculate the resonance frequency itself. Ramsey therefore proposed a scheme in 1950 [153]: Starting from the magnetization aligned along the z-axis a short pulse is applied rotating the magnetization in to the xy-plane. As such a pulse rotates M by 90° it is often referred to a "$\pi/2$-pulse". From there the magnetization will evolve corresponding to its detuning form resonance. In classical EPR or NMR this will occur as an oscillation of the magnetic field on the pick up coil. For NV one has to apply an additional $\pi/2$-pulse after a waiting interval τ (see figure 3.10(a)). This second pulse can be understood as a phase to population conversion. Depending on the accumulated phase during τ population will modulate between one or the other state participating in the corresponding transition. For a two level system (or a subspace of the NV spin system) its state evolution can be expressed as

$$|\Phi(\tau)\rangle = \frac{1}{\sqrt{2}}\left(|0\rangle + e^{i\Delta\omega\tau}\,|1\rangle\right). \tag{3.80}$$

A Ramsey measurement is often referred to free induction decay (FID) in NMR, because the amplitude of the magnetization or the state evolution is restricted by a damping with the former introduced time constant T_2^*, and therefore a measure for it.

Hahn-Echo

To measure the pure dephasing time T_2, Hahn proposed in 1960 [73] the so called Hahn-echo (HE). Therefore another pulse (180° or π-pulse) is introduced at $\tau/2$, after the first $\pi/2$-pulse, which flips the order of phase accumulation on the superposition state. In classical EPR or NMR different fractions with slightly different detunings will be refocused after an additional time $\tau/2$, resulting in signal on the pickup coils, with a damped amplitude corresponding to $\exp(-\tau/T_2)$. For

NV^- one has to apply again an additional $\pi/2$-pulse to read out the phase (see figure 3.10(b)). The corresponding state evolution in case of a two level system will then be

$$|\Phi(\tau)\rangle = \frac{1}{\sqrt{2}}\left(|0\rangle + e^{i\frac{(\Delta\omega_1-\Delta\omega_2)}{2}\tau}|1\rangle\right). \tag{3.81}$$

Any arbitrary phase $\Delta\omega_1\tau/2$ that will be accumulated during the first time interval will therefore be canceled out after the second interval with $\Delta\omega_2\tau/2$, for example if the origin for the detuning is constant during the whole sequence. Field inhomogeneities will be canceled out. On the other hand the Hahn Echo allows to measure a modulated magnetic field $B_{\mathrm{mod}}(t)$. As not only the amplitude of detuning but also the sign of $\Delta\omega$, during the second interval (after the π pulse), might change, they will not cancel out in general:

$$|\Phi(\tau)\rangle = \frac{1}{\sqrt{2}}\left(|0\rangle + e^{\mathrm{i}B_{\mathrm{rms}}\tau}|1\rangle\right) \tag{3.82}$$

B_{rms} is the root mean square of $B_{\mathrm{mod}}(t)$, if the period is matching τ.

D-Ramsey

The D-Ramsey is a scheme developed by Philipp Neumann et al [137], which allows to measure temperature with NV^-. In addition it combines the advantages of a typical Ramsey and HE by design: It is capable of measuring a phase similar to a detuning from resonance but is limited by T_2. In this scheme both NV spin transitions are used (see figure 3.10c). First a $\pi/2$-pulse is applied between the state $|0\rangle$ and $|-1\rangle$. Then after a waiting time $\tau/2$, three π pulses are applied swapping complex amplitudes of $|-1\rangle$ and $|+1\rangle$, but retaining the amplitude of $|0\rangle$. Again phase is accumulated for $\tau/2$, and an additional $\pi/2$ pulse for the transitions between $|0\rangle$ and $|1\rangle$ is performed before readout. The phase accumulated in both windows can be separated into two parts: $\Delta\omega_D \cdot \tau/2$ that is the mismatch in resonance and driving frequency due to the zero field splitting of NV, and $\Delta\omega_B \cdot \tau/2$ accounting for a detuning due to an external static (or slow enough off-resonant modulating) field. In a superposition state involving $|1\rangle$ the latter has exactly the opposite sign, if replacing $|1\rangle$ by $|-1\rangle$, and if the external field is aligned along the NV spin quantization axis. In sum only the phase $\Delta\omega_D \cdot \tau$ is accumulated.

Besides the D-Ramsey there is another scheme that was developed by Hodges et al.[84] and further modified by Toyli et al. [203] to a magnetic noise decoupling sequence. The main difference is that all three NV states are simultaneously manipulated at the very same time, by the very same pulse, creating a superposition state of all states. Therefore the Rabi driving amplitude must be ether much higher then the splitting of the transition $|0\rangle \leftrightarrow |1\rangle$ and $|0\rangle \leftrightarrow |-1\rangle$ if both transitions are pretty close, or a second microwave field resonant with the second transitions has to be applied if both transitions are well separated. The D-Ramsey needs a clear distinguishability between the two transitions like in former last case. If one transition is driven, no excitation on the other transitions shall occur.

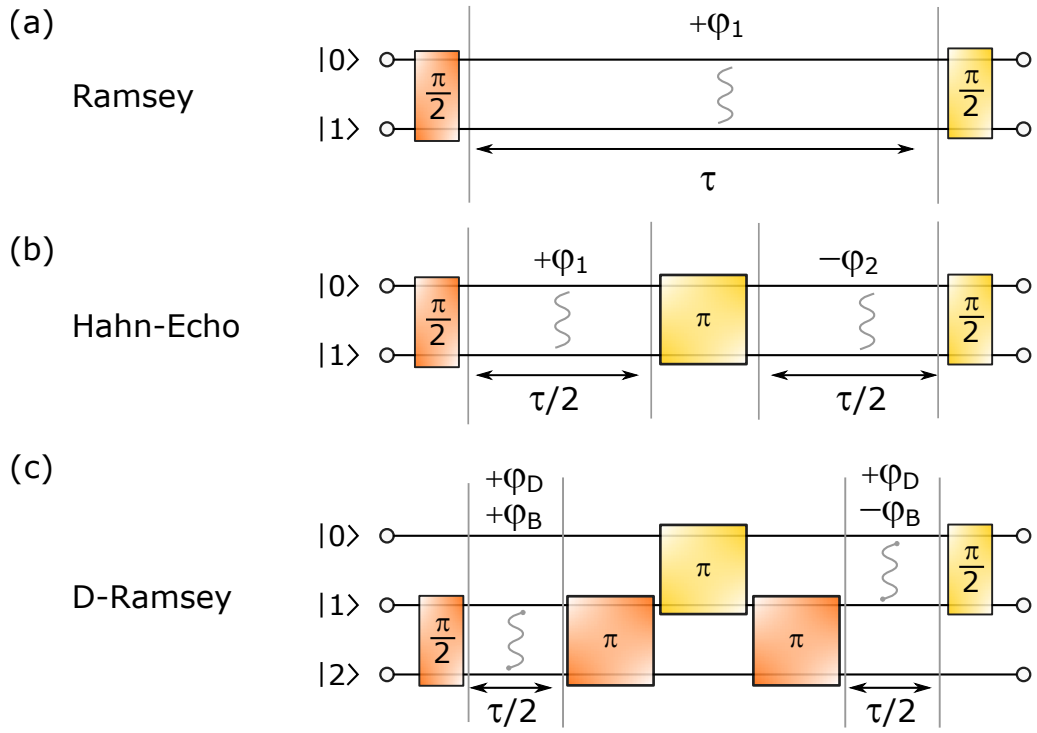

Figure 3.10. Sensing in a coherent superposition with NV. (a): Ramsey, **(b):** Hahn-Echo, **(c):** D-Ramsey

3.4.5. Noise spectroscopy

As already mentioned in section 3.3.3, page 51, spins have a finite T_1 and free evolution time (T_2^*). Besides phonon mediated relaxation processes like in case of SiV^-, this quantities are often limited by their interaction with other spins in there direct vicinity, as every spin has it's own magnetic field. As a consequence T_1 and T_2^* are altered.
In the following this interaction and the consequences on T_1 are discussed:

The average transition probability W_{km} between two (spin) states with index k and m of a quantum system can be expressed as [182]

$$W_{km} = \frac{1}{\hbar^2} \cdot \int_{-\infty}^{\infty} \mathrm{d}\tau \; G_{mk}(\tau) \cdot \exp(-i[\omega_m - \omega_k] \cdot \tau). \tag{3.83}$$

With $\omega_{m/k}$ as the characteristic angular velocity corresponding to the state m and k and $G_{mk}(\tau)$ the so called correlation function of Hamiltonian $H_1(t)$:

$$G_{mk}(\tau) = \overline{\langle m| \, H_1(t) \, |k\rangle \, \langle k| \, H_1(t+\tau) \, |m\rangle}. \tag{3.84}$$

If defining $H_1(t)$ as the Zeeman interaction of a spin (system) g with an arbitrary varying field $\vec{B}$:

$$H_1(t) = \gamma_g \hbar \cdot \sum_j^{x,y,z} B_j \cdot S_j \tag{3.85}$$

$G_{mk}(\tau)$ modifies to

$$G_{mk}(\tau) = \gamma_g^2 \hbar^2 \sum_j \sum_{j'} \langle m| \, S_j \, |k\rangle \, \langle k| \, S_{j'} \, |m\rangle \, \overline{B_j(t) B_{j'}(t+\tau)}, \tag{3.86}$$

after inserting equation (3.85) into (3.84). Whereas γ_g is the gyromagnetic ratio of the spin and B_j the field components of $\vec{B}$ in x,y and z direction.

By assuming that temporal changes in the magnetic field for different directions are independent from each other, all terms $\overline{B_j(t) B_{j'}(t+\tau)}$ in (3.86) with $j \neq j'$ have to be zero, as they are uncorrelated. The transitions probability W_{km} reads

then

$$W_{mk} = \gamma_g^2 \sum_j |\langle m| S_j |k\rangle|^2 \int_{-\infty}^{\infty} \mathrm{d}\tau \overline{B_j(t) B_{j'}(t+\tau)} \exp(-i\omega\tau). \tag{3.87}$$

If now B_j is originated by another spin of a surrounding spin bath, the term $\overline{B_j(t)B_j(t+\tau)}$ can be expressed as

$$\overline{B_j(t)B_j(t+\tau)} = \left\langle B_j^2 \right\rangle \cdot \exp(-|\tau|/\tau_c). \tag{3.88}$$

Thereby τ_c is the typical correlation time of the bath, for example its explicit spin state lifetime.
In the following a spin $S = 1$ system is considered experiencing a sufficient weak static external magnetic field. In this situation the two states $m_s = +1$ and $m_s = -1$ are almost degenerated and the rate to $m_s = 0$ and vise verse can be approximated to be equal (see figure 3.11). Having a closer look on the transition $m_s = 0$ to $m_s = +1$, $|\langle m| S_j |k\rangle|^2$ becomes

$$\begin{aligned} |\langle +1| S_x |0\rangle|^2 &= 1/2, \\ |\langle +1| S_y |0\rangle|^2 &= 1/2, \\ |\langle +1| S_z |0\rangle|^2 &= 0. \end{aligned} \tag{3.89}$$

$W_{|+1\rangle->|0\rangle}$ that is equivalent to the transitions rate κ in figure 3.11 transforms to

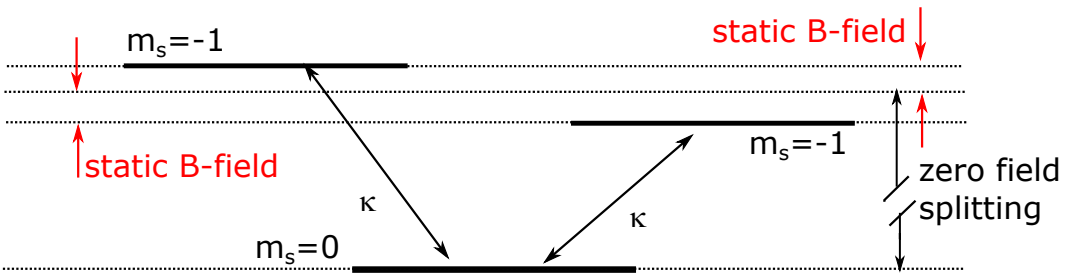

Figure 3.11. Rate mode for spin $S = 1$ system. A weak static magnetic field is applied shifting the $m_s = \pm$ levels. The shift shall be small versus the zero field splitting.

$$W_{|+1\rangle->|0\rangle} = \frac{\gamma_g^2}{2}(\langle B_x^2\rangle + \langle B_y^2\rangle) \cdot \int_{-\infty}^{\infty} \mathrm{d}\tau \exp(-|\tau|/\tau_c) \cdot \exp(-i\omega\tau). \tag{3.90}$$

After performing the Fourier transformation in equation (3.90) and substitute $\omega_m - \omega_k$ by ω one gets for κ

$$\kappa = \gamma_g^2(\langle B_x^2\rangle + \langle B_y^2\rangle) \cdot \frac{\tau_c^{-1}}{\omega^2 + \tau_c^{-2}}. \tag{3.91}$$

Even if κ is the transitions rates between different sub-levels it's not directly T_1: To explain this is more detail the rate equation model for a $S = 1$ system following figure 3.11 has to be solved for the populations p of the individual states:

$$\begin{aligned} \frac{dp_0(t)}{dt} &= -2\kappa \cdot p_0(t) + \kappa \cdot p_{-1}(t) + \kappa \cdot p_{+1}(t) \\ \frac{dp_{+1(t)}}{dt} &= +\kappa \cdot p_0(t) - \kappa \cdot p_{+1}(t) \\ \frac{dp_{-1}(t)}{dt} &= +\kappa \cdot p_0(t) - \kappa \cdot p_{-1}(t). \end{aligned} \tag{3.92}$$

For the condition $p_{+1}(0) = p_{-1}(0) = 0$ and $p_0(0) = 1$, equations (3.92) have the solution:

$$\begin{aligned} p_0(t) &= \frac{1}{3}\left[1 + 2 \cdot \exp(-3\kappa \cdot t)\right], \\ p_{+1}(t) &= \frac{1}{3}\left[1 - \exp(-3\kappa \cdot t)\right], \\ p_{-1}(t) &= \frac{1}{3}\left[1 - \exp(-3\kappa \cdot t))\right]. \end{aligned} \tag{3.93}$$

The spin relaxation time or state lifetime T_1 of the states corresponds then to $(3\kappa)^{-1}$ if all other decay channels are neglected.

More generaly T_1 is

$$T_1 = \left(\Gamma_{\mathrm{int}} + \sum_k \Gamma_{\mathrm{ext}}^{(k)}\right)^{-1}. \tag{3.94}$$

Thereby Γ_{int} is the intrinsic decay rate, which covers all intrinsic processes that are not covered by surrounding noise sources. $\Gamma_{\mathrm{ext}}^{(k)}$ is the already computed quantity

3κ, which accounts random fluctuations of a surrounding spin bath, indexed by k:

$$\Gamma_{\text{ext}}^{(k)} = 3\kappa = 3\gamma^2 \left(\langle B_{x,k}^2 \rangle + \langle B_{y,k}^2 \rangle \right) \frac{\tau_c^{(k)}}{1 + \omega_0^2 {\tau_{c,k}}^2}. \tag{3.95}$$

γ is the gyromagnetic ratio of the $S = 1$ system, ω_0 the energy splitting between the two spin states and $\tau_{c,k}$ the typical correlation time of the spin bath with index k.

To find an expression for $B_\perp^2 = \langle B_x^2 \rangle + \langle B_y^2 \rangle$, one can calculate the average field a spin bath with individual spins $\mathbf{S_j}$ placed at the distance $\mathbf{r_j}$ to the spin system produces. The magnetic field $\mathbf{B_j}$ of a single spin can be written as:

$$\mathbf{B_j} = \frac{\mu_0}{4\pi} \gamma_j \hbar \cdot \frac{1}{r_j^3} \left(\mathbf{S_j} - \frac{3(\mathbf{S_j} \cdot \mathbf{r_j}) \cdot \mathbf{r_j}}{r_j^2} \right). \tag{3.96}$$

Assuming each individual spin to be in a purely mixed state. It's density matrix ρ can be written as

$$\rho = \frac{1}{2S+1} \mathbb{1}_{2S+1}. \tag{3.97}$$

Than $B_\perp^2$ that is the sum of $B_{\perp,j}^2$ can be written as

$$\begin{aligned} B_\perp^2 &= \sum_j B_{\perp,j}^2 \\ &= \sum_j \text{Tr}[\rho B_{x,j}^2] + \text{Tr}[\rho B_{y,j}^2] \\ &= \sum_j \left(\frac{\mu_0}{4\pi} \gamma_j \hbar \right)^2 \cdot C_s \cdot \frac{2 + 3\sin^2(\alpha_j)}{r_j^6}, \end{aligned} \tag{3.98}$$

with

$$C_s = \frac{1}{2S+1} \sum_{m=-S}^{S} m^2 = \frac{S(S+1)}{3}. \tag{3.99}$$

Similar to T_1, an expression for τ_c can be found. Also τ_c can be expressed in terms of intrinsic relaxation processes Γ_{int} and for example a dipol-dipol interaction rate Γ_{dip} within the spin bath:

$$\tau_c = \left(\Gamma_{\text{int}} + \Gamma_{\text{dip}} \right)^{-1}. \tag{3.100}$$

Whereas Γ_{int} is influenced by the characteristic of the spin-species itself, the Γ_{dip}

can be estimate by calculating the average interaction frequency of a spin in the spin bath with it's surrounding: The dipolar spin-spin interaction of two spins k and l is described by the Hamiltonian:

$$H_{kl} = \left(\frac{\mu_0}{4\pi} g_k \mu_k \cdot g_l \mu_l\right) \frac{1}{r_{kl}^3} \left(S_k \cdot S_l - \frac{3(S_k \cdot r_{kl}) \cdot (S_l \cdot r_{kl})}{r_{kl}^2}\right). \tag{3.101}$$

The average interaction rate Γ_{dip} of a single spin induced by it's surrounding neighbor spins k is

$$\text{h}\Gamma_{\text{dip}} = \sqrt{\sum_{k \neq l} \langle H_{kl}^2 \rangle}. \tag{3.102}$$

Explicit calculations of $\langle H_{kl}^2 \rangle$ will be presented in section 7.2.1, page 208. h is the Planck's constant
The fraction $\frac{\tau_c^{(k)}}{1+\omega_0^2 \tau_{c,k}}$ is called the spectral density function $S(\omega)$ of the spin system. By calculating the dependence of $S(\omega)$ for both, correlation time and energy splitting, a deeper insight into the sensing capacity of noise spectroscopy is revealed: The spectral density has it's maximum value, if the correlation time of the spin bath, correspond to the inverse of the characteristic frequency of the energy splitting between the states (figure 3.12(a)). In addition, if one can vary the energy splitting of the two states one can probe the spectral density function and therefore the correlation time of surrounding spin bath (see figure 3.12(b)).

T_1 is most sensitive to noise with frequencies around the Larmor precision of probe spin system, which is in contrast to T_2. The latter is altered by any noise with frequency components up to zero. But for example by spin locking, one can filter on a specific frequency around the driving amplitude. Therefore the probe spin is prepared in a superposition state. After applying a resonant microwave (MW) along the direction of the superposition state (in terms of the Bloch sphere or rotating frame), the spin will start to precess around the applied field. Transforming two times into a rotating frame, first along B_0 or the preferred spin quantization axis, and then around B_1 will give the originally transversal relaxation time, the mathematical form of T_1 in the double rotating frame. The corresponding relaxation time is often called the spin-lattice relaxation time in the rotation frame $T_{1\rho}$ [182]. By sweeping the driving amplitude, one modifies the corresponding energy splitting of the transformed system, and the correlation time

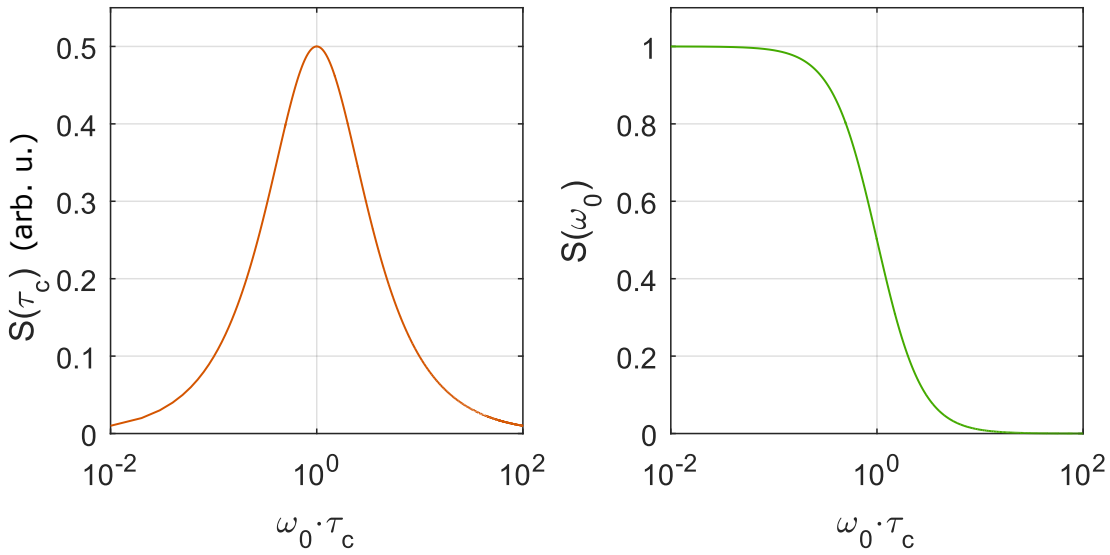

Figure 3.12. Spectral density function S: (a): S, if the correlation time of the spin bath is varied. (b): S when the energy splitting ω_0 of a spin system influenced by a spin bath with fixed correlation time τ_c is varied.

of the bath can be determined [169].

Spin bath sources in (nano)diamonds

In case of NDs there are several sources for such external spin baths that will be discussed in the following. However the discussion will focused on electron spin species:

Intrinsic defects For the production of NV decorated NDs, typically diamond crystals originated by HPHT synthesis are used. There high nitrogen content around several to hundreds of ppm reduces the needed steps for NV creation. Only vacancies have to be introduced by proton or electron irradiation. For example if one wants to find one NV in average in a 10 nm sized diamond, they need around 20 ppm nitrogen per ND, if one considers 50 % conversion efficiency and no depletion zone for NV^- at the surface of the diamond (see figure 3.13(a)). With increasing nitrogen concentration also the distance between two nitrogen and

therefore between nitrogen and later NV will decrease. As substitutional nitrogen is a paramagnetic active species [184], an influence of the nitrogen onto the NV may occur (3.13(b)).

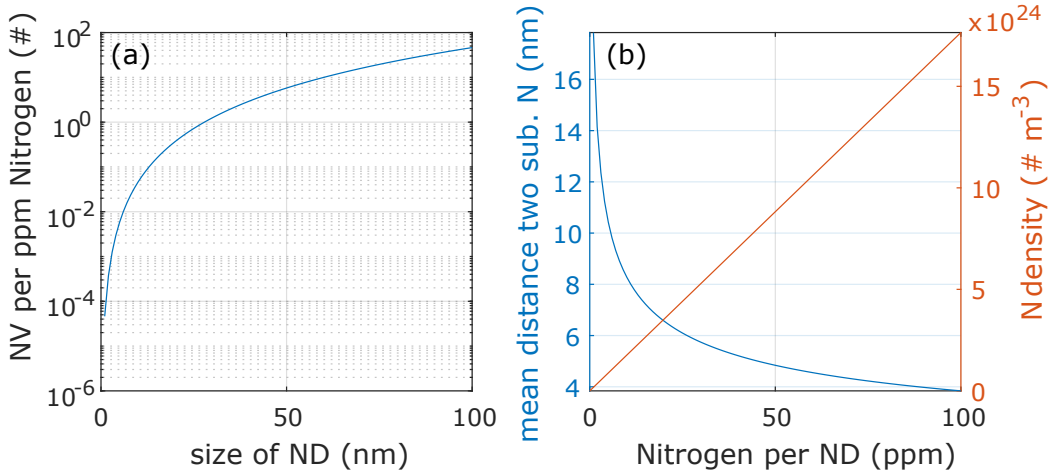

Figure 3.13. NV versus substitutional nitrogen in NDs. (a): Average concentration of NV per ND per 1 ppm substitutional nitrogen assuming a 50 % conversion efficiency. **(b):** Mean distance and overall concentration of (substitutinal) nitrogen in (nano) diamonds.

Fabrication related and surface defects Also during the production of NDs, paramagnetic spin defects are introduced by broken bonds during the milling procedure. Several groups [143, 222] report on paramagnetic spin species inside nanodiamonds. According to their model besides nitrogen, additional spins species have to be placed in a thick sub surface layer to explain their data. Also spins in thin layers have been reported directly on the surface of nano- [200, 222] and bulk diamond material [169, 165]. Thereby two types of surface spin baths have been found. One is originating from paramagnetic centers, that is again explained by dangling bonds, and second one introduced by surface phonons [169, 165].

Gd-Complex Beside the more or less naturally occurring spin species in NDs also other relaxive acting agents can be introduced. The most prominent and in clinics heavily used material is the rare earth ion gadolinium, in the triple ionized state. Packed into a complex, the originally toxic gadolinium can be used as a

contrast agent for cell tissue in magnetic resonance imaging (MRI), after injecting intravenously. Thereby the complex with with a spin $S = 7/2$ quenches the spin lattice relaxation time of surrounding protons. As one can see by comparing figure 3.14 (A) and (B) the contrast in a MRI image increases making it possible to discriminate between healthy and cancer tissue.

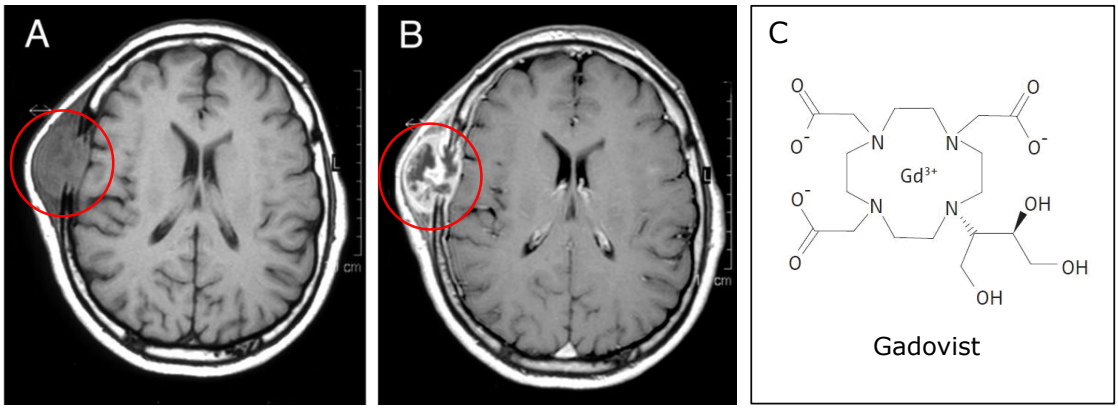

Figure 3.14. Gadolinium-Complex as a contrast agent: MRI scan of the brain of a tumor patient before **(A)** and after **(B)** the injection of the Gd-complex Gadovist shown in (C). The read cycle indicates the tumor. (A) and be (B) are taken from reference [160]

The underlying mechanism in case of T_1 is mainly dominated by dipolar interaction [32]: Thereby changes in the quantum state of Gd, or the rotation of the complex itself, leads to magnetic field fluctuations, which interact with the spin under observation (eg. protons) and increase it's relaxation rate.
Identification of the typical correlation time τ_c of a given Gd-complexes can be quite individual, as it depends on one hand on the rotation correlation time τ_R that results from self rotation of the complex and the spin lattice relaxation time of T_1^{Gd} of the complex itself. τ_R for a free complex is in the range of several tens of ps [31], but can also reach several ns, if ridgedly bound to lipids or larger compartments [98]. For the free rotating Gd-complex the rotational correlation time can be estimated by the relationship

$$\tau_R = 4\pi \frac{\eta r_{Gd}^3}{3\mathrm{k_B}T}. \tag{3.103}$$

With η being the viscosity of the environment, $\mathrm{k_B}$ the Boltzmann constant, T environmental temperature and r_{Gd} the size of the Gd-complex.

T_1^{Gd} is typically refered to modulations in the ZFS with correlation time τ_v. τ_v is caused by collisions of the complex with surrounding molecules [3]. It can be well approximated at moderate fields for some Tesla, the so called "Zeeman-limit", by applying the Redfield limit ($\tau_R \gg \tau_v$):

$$\begin{aligned} \frac{1}{T_1^{\mathrm{Gd}}} &= B\left[\frac{1}{1+\omega_0^2\tau_v^2} + \frac{4}{1+4\omega_0^2\tau_v^2}\right], \\ B &= \frac{1}{25}\Delta^2\left[4S(S+1)-3\right]\tau_v. \end{aligned} \tag{3.104}$$

With S being the overall spin quantum number of the complex, and Δ the trace of the ZFS tensor. ω_0 is the characteristic frequency that is associated with the Hamiltonian $H_0 = \hbar\omega_0 S_z$ describing the Zeaman interaction. t_c is just the inverse sum of all correlation times characterizing a different process (eg. τ_R, T_1^{Gd}, but also diffusion). As already mentioned, (3.104) is only valid in a certain range where the Zeeman splitting is larger than the ZFS of the given complex ("Zeeman"-limit). In addition the "extrem narrowing" condition has to be fulfilled ($\omega_0\tau_R \ll 1$). Violating those, corrections in the range of several tens of percent have to be applied [193]. If the external field becomes to low, the influence by the ZFS becomes dominant ("ZFS"-limit). The simple expression in equation (3.104) has to be modified, but still leads to an acceptable expression in case of T_1^{Gd} [17]:

$$\begin{aligned} \frac{1}{T_1^{\mathrm{Gd}}(B_0)} = &\frac{2}{5}a_2^2\tau_R\sum_{n=1}^{2}\left[\frac{n^2}{1+n^2\omega_0^2\tau_2^2}\right] \\ &+ \frac{44}{21}a_4^2\tau_R\sum_{n=1}^{4}\left[\frac{n^2}{1+n^2\omega_0^2\tau_4^2}\right] \\ &+ \frac{900}{91}a_6^2\tau_R\sum_{n=1}^{6}\left[\frac{n^2}{1+n^2\omega_0^2\tau_6^2}\right] \\ &+ \frac{12}{5}a_{2T}^2\acute{\tau}\left[\frac{1}{1+\omega_0^2\acute{\tau}^2} + \frac{4}{1+4\omega_0^2\acute{\tau}^2}\right]. \end{aligned} \tag{3.105}$$

And:

$$\begin{aligned} \tau_k &= \frac{\tau_R}{k(k+1)}, \qquad k = 2,4,6 \\ \frac{1}{\acute{\tau}} &= \frac{1}{\tau_2} + \frac{1}{\tau_v}. \end{aligned} \tag{3.106}$$

The parameters a_k with $k = 2, 4, 6$ describe the upcoming influence of the static ZFS, and a_{2T} the transient ZFS. a_2 and a_{2T} are often assigned with the symbols Δ_S and Δ_T, as in a lot of cases the influence of a_4 and a_6 are neglectable. Equation (3.105) reduces then to

$$\begin{aligned}\frac{1}{T_1^{\mathrm{Gd}}(B_0)} = &\frac{2}{5}a_2^2\tau_R\left[\frac{1}{1+\omega_0^2\tau_2^2}+\frac{4}{1+4\omega_0^2\tau_2^2}\right]\\ &+\frac{12}{5}a_{2T}^2\acute{\tau}\left[\frac{1}{1+\omega_0^2\acute{\tau}^2}+\frac{4}{1+4\omega_0^2\acute{\tau}^2}\right].\end{aligned} \tag{3.107}$$

Equation (3.107) has interesting consequences for the interpretation of early collected information about Gd-complexes [31]: Typically one preforms a nuclear magnetic resonance dispersion (NMRD) experiment [101] where the proton spin lattice relaxation time is monitored as a function of the applied external static magnetic field using equation (3.104). Especially in the regime where the Zeeman-term is similar or smaller in comparism to the ZFS of the Gd-Complex, this causes a systematic error in the interpretation of T_1^{Gd}. For example a detailed analysis of (3.107) showed, that for the complex Gd-DTPA the static contribution already exceeds the transient one at $B_0 \approx 0.9\,\mathrm{T}$ [17], corresponding to a proton lamor frequency of 38.3 MHz. In addition also (3.107) has it's limitation for very small B_0, as the Redfield approximation breaks down. Thus are defined by the Redfield Abragam conditions $a_2\tau_2 \ll 1$ and $\omega_0 \gg a_2^2\tau_2$, if τ_v is short [58]. As a direct consequence of the mentioned behavior, also modifying the rotation correlation time, for example by fixation, leads to an decrease in the spin lattice relaxation time of an individual Gd-complex.

The T_1 decay of a ND ensemble Equation (3.94) has to be handled with care, as it is only functional to estimate the spin lattice relaxation time T_1 of a single NV at a certain position in a ND. Experiments performed in this manuscript are almost all done on an ensemble, with various positions inside and sizes of the nanodiamond. The resulting average decay experimentally observed is not just a simple single mono Exponential, even if this will be used as an empirical estimate for T_1. In general on can calculate an average decay rate Γ_{avg}, by introducing the distribution of NV inside the ND. The resulting decay can be approximated by a

"stretched exponential" [93]:

$$I(t) = I_0 \cdot \exp(-(\Gamma_{\text{avg}} \cdot t)^{\beta}) \tag{3.108}$$

More general the decay observed can be expressed as

$$I(t) = \int_0^{\infty} R_{\beta}(\Gamma) \exp(-\Gamma \cdot t). \tag{3.109}$$

Where $R_{\beta}(\Gamma)$ is the distribution of decay rates, and is mathematically the Laplace transformation of $I(t)$. $R_{\beta}(\Gamma)$ can be decomposed into $R_{\text{int}}(\Gamma) \otimes R_{\text{env}}(\Gamma)$, whereas $R_{\text{int}}(\Gamma)$ and $R_{\text{env}}(\Gamma)$ describe the intrinsic and environmental rate distribution, respectively [18].
Figure 3.15 shows as an example the corresponding rates calculated for an ensemble of NVs in an ensemble of ND, following the size in distribution figure 7.25b. Besides

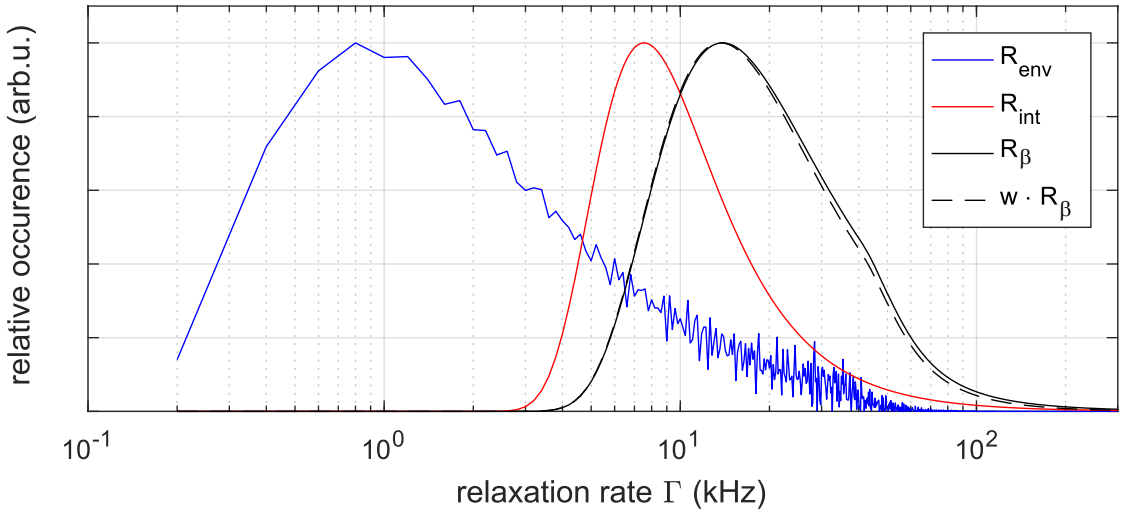

Figure 3.15. Γ distribution for ND ensemble: (blue): Simulated Γ distribution profile R_{env} for an ensemble of NV of an ensemble of different sized nanocrystal. **(red):** Intrinsic Γ distribution using equation 31 in [18]. **(black):**The convolution $R_{\beta}(\Gamma)$. **(black, dashed):** same as (black) weighted with the correction $w(\Gamma)$

the distribution of NVs in respect to the surface, also other parameters can influence the observed decay. One example is the used pulse scheme for later relaxation experiments, the linear chirp. As the pulse needs a certain time to be applied, NVs with a T_1 shorter or in the range of the pulse length with already loose spin

contrast, and therefore account less in the observed decay. The corresponding shape of $w \cdot R_\beta$ for a correction w that account for a pulse length of 2000 ns is plotted in figure 3.15.

3.5. Cells

Cells are the smallest living units of an organism. Every cell represents a structurally definable, independent and self-sustaining system (has its own metabolism). Cells proliferate, take up nutrients, can react on external and internal stimuli and are able to move if needed. One distinguishes between Prokaryotic and Eukaryotic cells. Prokaryotes are always single-cellular organism and the cells lack membrane surrounded organelles, whereas Eukaryotes are single or multicellular [19]. In figure 3.16 the main stuctural compartments of eukaryotes is pictured. As an

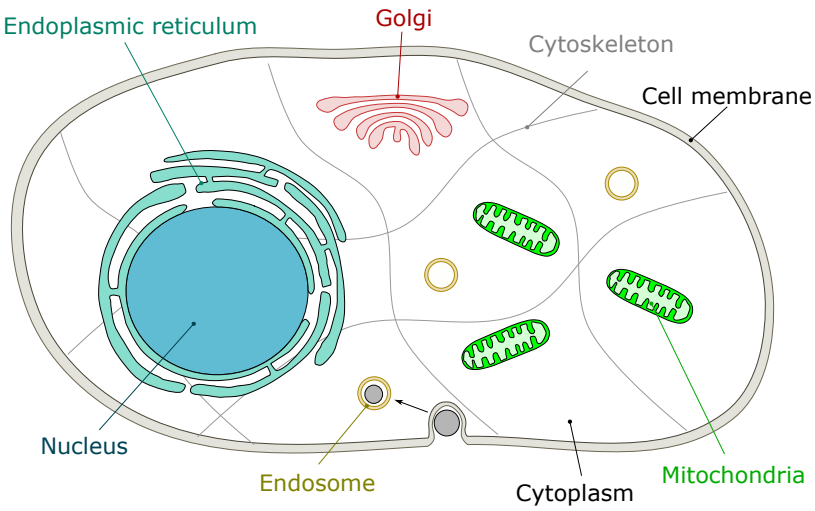

Figure 3.16. Eukaryotic cell

individual cell can be understood as a representative of tissue with the same cell type, interpreting it's response to a certain stimuli can help to interpret clinical results, or to develop drugs in a first proof of principle stage.

Cellular uptake To gather nutrients from the extracellular environment, cells have developed several mechanisms. Small hydrophobic molecules can diffuse directly across the plasma membrane. The diffusion rate is proportional to the concentration gradient and to the hydrophobicity of the molecule. Transport can also be facilitated by specific transport proteins, so called channels or carrier proteins, inserted into the plasma membrane. The first ones allow also polar

molecules or ions to pass the membrane by forming a channel.The latter ones actively transport specific molecules. If a molecule is bound, the carrier changes its conformation transporting the molecule onto the other side of the membrane and releases it. But also ion transport against a concentration gradient is possible with the help of so called ion pumps. Latter couple the transport of ions with the hydrolysis of adenosine triphosphate (ATP). This type of transport is called active transport [112].
Another class of active transport is the so called endocytosis, allowing a vital cell to uptake larger molecules, particles, cell debris or even other apoptotic cells by engulfing them. Afterwards a vesicle pinches off from the plasma membrane, the so called endosome. One distinguishes between pinocytosis that describes the process of taking up small volumes of extracellular fluid, and phagocytosis. Latter applies for specialized cells diffusing through the body liquid and taking up cell debrids and apoptotic cells.
Nanodiamonds are introduced into cells by macropinocytosis [36], a special type of pinocytosis. A plasma membrane ruffle is formed that folds back to itself and fuses with the base of the plasma membrane [110]. Nanodiamonds can escape from endosomes into the cytosol depending on their shape [36].

Cell metabolism and the respiration chain The collection of chemical processes in a cell is called metabolism. It's main purpose is to synthesize cellular building blocks like, proteins, lipids, nucleic acids or carbohydrates from metabolites. This processes are usually energy consuming and are called as anabolic reactions. In addition, to gain energy, complex nutrients are broken down to smaller metabolites. This reactions are classified as catabolic.
A lot of actively driven processes that involves specific enzymes consume ATP that contains two energy rich phosphoric anhydride bonds. During hydrolysis into phosphate and adenosine diphosphate (ADP) free enthalpy is produced. By coupling energy consuming reactions with the hydrolysis of ATP these can be driven. Typically ATP is consumed within one minute after production. Almost all ATP is produced in the cellular organelle mitochondria (see figure 3.17) that is therefore also called the power house of a cell [19]. Mitochondria are double membrane bound organelles with a size of 0.75 µm-2 µm. The inner membrane has

a lot of invaginations (cristae) making the surface of the inner membrane larger. This allows to place more protein complexes of the respiratory chain and the so called ATP synthase on the inner membrane, this ensures a high production rate of ATP, which is synthesized by latter. The number of mitochondria found in a cells, depends on the cell type. Up to 4000 can be found in hepatocytes (liver cells) [41]. The metabolites from the degradation of carbohydrates, fatty acids and amino acids are introduces into citric acid cycle, which occur in the matrix of the mitochondria. The process includes a series of oxidation and reduction reactions that end with the oxidation of a Acetyl group to CO_2. During this oxidation energy rich electrons are produced, which drive the ATP synthesis. The electrons are not directly transferred to oxygen instead NAD^+ and FAD are reduced to NADH and $FADH_2$, which afterwards transfer the electrons to the respiratory chain a set of 4 large protein complexes that are inserted into the inner mitochondrial membrane and transfer the electrons to oxygen (see figure 3.18). The electron flow within the transmembrane complexes causes an additional proton transport through the inner mitochondrial membrane. Thereby an electrochemical proton gradient between the matrix and the inter membrane space is formed. The ATP-syntase catalyses the formation of ATP from ADP and Phosphate, which is an energy consuming process. To apply this energy the ATP-synthase couples the ATP synthesis with

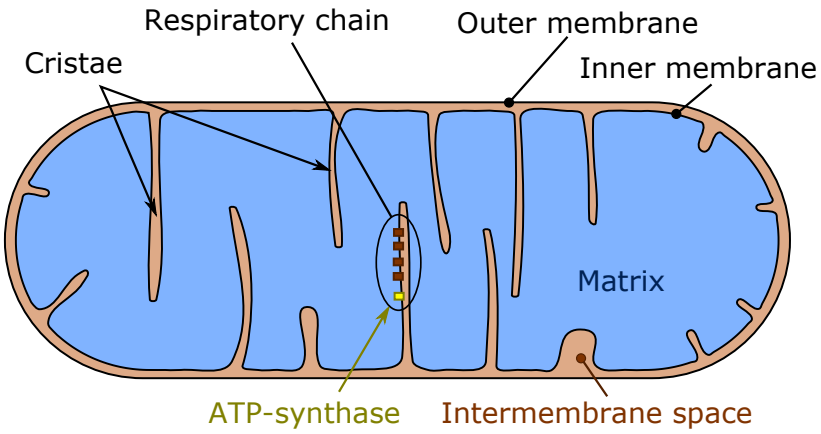

Figure 3.17. The structure of a mitochondria

the energetically favored transport of protons along the protein gradient at the inner mitochondrial membrane (protons are transported back into the matrix). During the large number of proton transport steps, some energy dissipates in form of heat. Additionally some organisms have the ability to uncouple the oxidative phosphorylation from the ATP synthesis to produce heat. One example is the so called brown fat cells, which are specialized on non-shivering thermogenesis. These cells express an uncoupling protein (Thermogenin) that forms a side way for the proton flux into the matrix. Thereby it causes a short cut: The energy from the proton gradient, which is normally used for ATP synthesis is released as heat [19]. Some chemicals like the ionophore CCCP can act in a similar way. CCCP can freely diffuse through lipid bilayers. Since the matrix of the mitochondria has a slightly higher pH then the cytosol CCCP gets deprotonated. The negative charge of the resulting CCCP anion is heavy delocalized and the weakly negative charged anion diffuse back into the cytosol. In the cytosol it gets protonated again. During many cycles of protonation and deprotonation the proton gradient is destroyed and heat is produced [186].

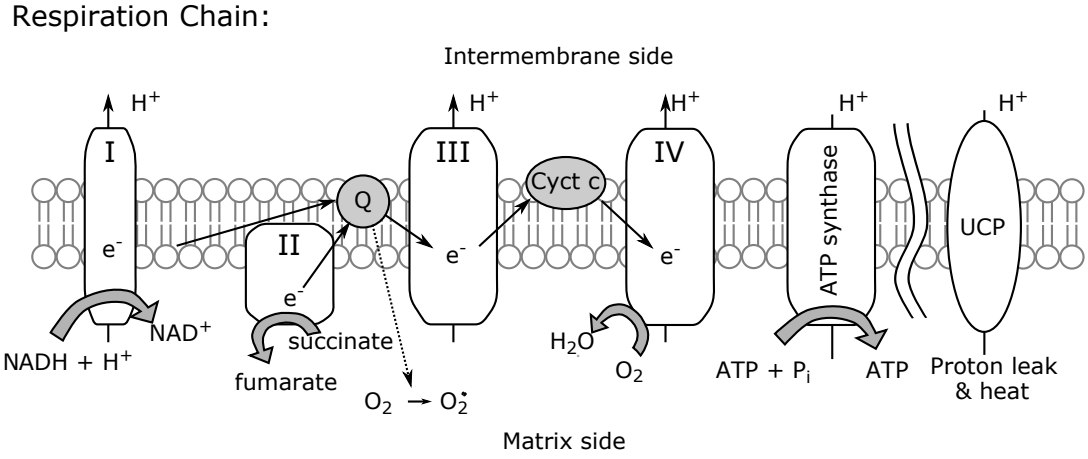

Figure 3.18. The respiration chain is highlighted.

During the process of generating ATP, reactive oxygen species (ROS) are generated as a byproduct that can damage for example deoxyribonucleic acid (DNA), oxidize lipids or aminoacids. To reduce the amount of ROS, some cells have the so called reductive pool, mainly consisting of a redox-buffer of the redox pair GSH and glutathione disulfide (GSSG). Thereby GSH is oxidized, forming GSSG.

To refill the GSH reservoir, an enzyme called the gluthatione-reductase, reduces GSSG to GSH. In living cells GSH can reach concentrations up to 10 mM [117, 114].

Diffusion in cells The motion of small ions, molecules or bigger compartments in aqueous solution can be described by the so called Fokker-Planck equation (FPE). The latter is a partial differential equation describing the probability density distribution of a particles position over time. In one dimension the probability $p(x,t)$ to find the particle at position x at time t can be written as:

$$\frac{\partial p(x,t)}{\partial t} = -\frac{\partial}{\partial x}\left[\Gamma_{\text{drift}}(x,t)p(x,t)\right] + \frac{1}{2}\frac{\partial^2}{\partial x^2}\left[\Gamma_{\text{diff}}(x,t)p(x,t)\right]. \tag{3.110}$$

Whereas the function Γ_{drift} and Γ_{diff} describe the impact of drift and diffusion, respectively. For $\Gamma_{\text{drift}} = 0$ and $\Gamma_{\text{diff}} = constant$ the solution for equation (3.110) is a normal-distribution:

$$p(x,t) = \frac{1}{\sqrt{2\pi MSD^2}} \exp\left(-\frac{x^2}{2 \cdot MSD^2}\right). \tag{3.111}$$

With the standard deviation called the mean square displacement $MSD^2 = 2Dt$. Over time the mean square displacement increases proportional to the diffusion coefficient D describing the statistical nature of particle motion.
To describe diffusion in cells the mean square displacement in d dimensions is often written as [124] :

$$MSD^2 = 2dD_\alpha t^\alpha. \tag{3.112}$$

Thereby the coefficient α describes the behavior of diffusion with the diffusion coefficient D_α. In case of Brownian motion α equals one. If α is larger than 1 the diffusion is called super-diffusion. In case of $\alpha < 1$, one speaks of sub-diffusion. As first one can be the consequence of active transport, the latter can be caused by spacial restrictions. For example the actin-filament in a cell [173] or binding to an other compartment. In general different diffusion regimes, and therefore different α values, can occur on different timescales. To identity thus, the mean square

displacement is divided by time and plot in a double logarithmic plot:

$$MSD^2/t = 2dD_\alpha t^{\alpha-1}. \tag{3.113}$$

Time regimes where the quantity MSD^2/t occurs as a flat line are dominated by Brownian motion. A increasing slope indicates super-diffusion, a decreasing slope sub-diffusion.

...

4. Molecular sized fluorescent nanodiamonds

Confocal microscopy has nowadays become a standard tool in life science to analyze living organisms and their interior. Thereby fluorescent markers allow to differentiate between different organelles or their structures within a single cell down to the nanoscale. Often dye molecules are used for this purpose, which are typically of molecular size. Dye molecules are bright, but not very photo-stable in a cellular environment [216]. Solid state probes like quantum dots do not suffer from latter limitation [21, 198] and have a core size of a few nanometers. But as *in vitro* studies demand bio-compatibility of the used probe, an outer passivation layer has to be added. Their total size increases to $\sim$ 10 nm [168, 206]. In this sense, fluorescing centers in diamond are very attractive, as their molecular orbitals participating in fluorescence are within one to two inter-atomic distances from the defect [214, 47]. In addition, diamond material was shown to be biocompatible [209, 176]. However, doping of nanodiamonds is predicted to have a size limit: Calculations have suggested, that, for example, nitrogen is thermodynamically unstable in nanodiamonds with less than 2 nm in sizes [15]. In contrast, similar considerations for SiV defects in hydrogen-passivated truncated octahedral nanodiamonds predicted stability in particles down to 1.1 nm in diameter [214].

In the following chapter the emission properties of fluorescent molecular sized nanodiamonds, originating from a meteoric source, have been analyzed *via* confocal microscopy. The MND host SiV. Thereby the used confocal setup has been tuned to maximal sensitivity for SiV^- fluorescence. At the same time the setup allows cross talk free correlation spectroscopy on the level of several thousand detected events/photons per second. Optical properties of SiV^- in MND has been probed

including PL spectra, lifetime, and average brightness at room temperature. Finally, the acquired data was compared to supplementary measurements performed by collaboration partners working on the very same sample. The results shown in this chapter, are partially published in Vlasoc et al. [214].

4.1. Setup

To detect single molecules, the sensitivity of the used setup had to be optimized to the fluorescence of SiV^- (figure 4.1). A combination of pass filters have been used to separate laser emission and background signal from SiV fluorescence. The transmission profile of all used filters are plotted in figure 4.2. The laser source is

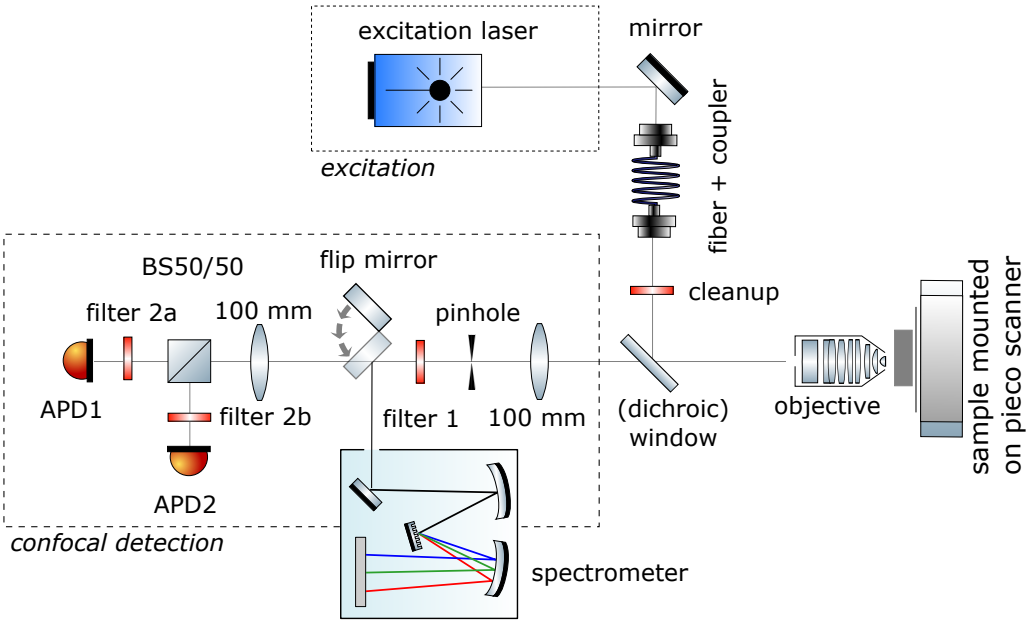

Figure 4.1. Confocal setup utilized for spectroscopic analysis of SiVs in MND.The wavelength depended transmission of the interference filters used are illustrated in figure 4.2

guided through a fiber, and cuts of wavelengths longer then 700 nm by a cleanup (SP700). Then the laser beam is deflected into the objective *via* a dichroic or a glass window. The fluorescence signal is collected by the objective and focused

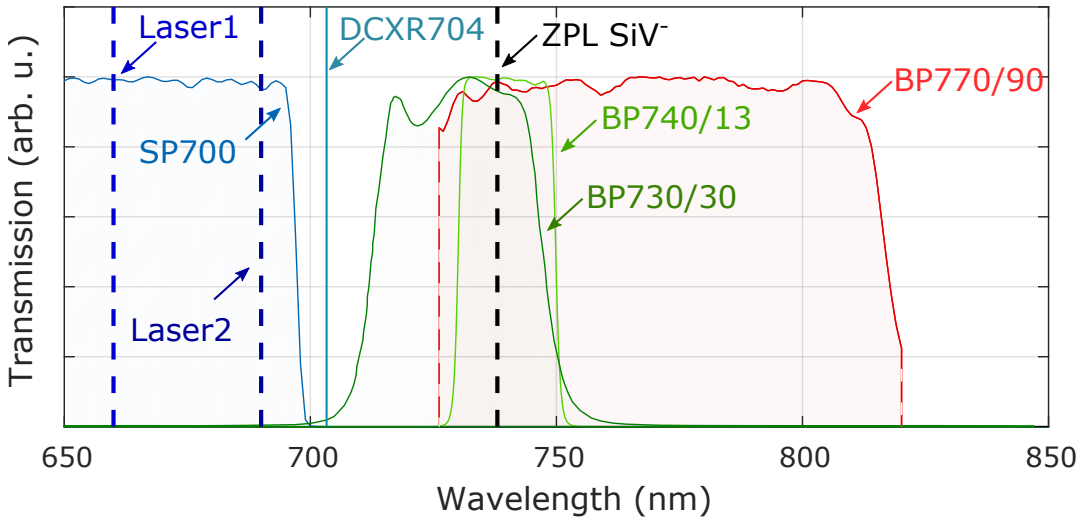

Figure 4.2. Filter setup: All filters used during following experiments together with the ZPL position of SiV^- and the laser wavelengths used."SP","LP" and "BP" mark a short pass, long pass or band pass filter, respectively. The number behind the indication letters mark the designed cutoff (LP/SP) or center frequency (BP). The second number of the bandpass notates the full width half maximum (bandwidth)

onto a pinhole, after passing the dichroic/glass window again. A first filter (filter 1) suppress laser leakage, and light is guided onto two APD in a HBT configuration. For correlation measurements each APD in equipped with an additional fluorescence filter (filter 2a and filter 2b). The detection path behind the pinhole is build up in the so called 2f-2f configuration, directly mapping the pinhole onto the APDs. In Addition, a flip mirror is placed directly after filter 1, allowing to acquire PL spectra of the position under study. Also for this a 2f-2f configuration was chosen, to focus the pinhole onto the entrance slit of the spectrometer. Two laser diodes have been used in different experiments to continuously excite SiV (center frequency 660 nm and 690 nm). For pulsed excitation a super-continuum white light source (SC400, Fianium), equipped with an accusto-optical-filter, has been used. Latter output covers a broad excitation spectrum from 610 nm to 690 nm. The pulse width of the internal master source is ≈ 5 ps. The setup is controlled *via* a custom made software written in "phyton". For more details one the used equipment see Vlasov et al. [214].

4.2. Photoluminescence spectra

To verify the existence of SiV inside the given stock material (see [214]), the stock solution has been diluted by 1 versus 99 parts of purified water, and 5 µl were drop-casted onto a plasma cleaned fused silica cover-slide. After residual water

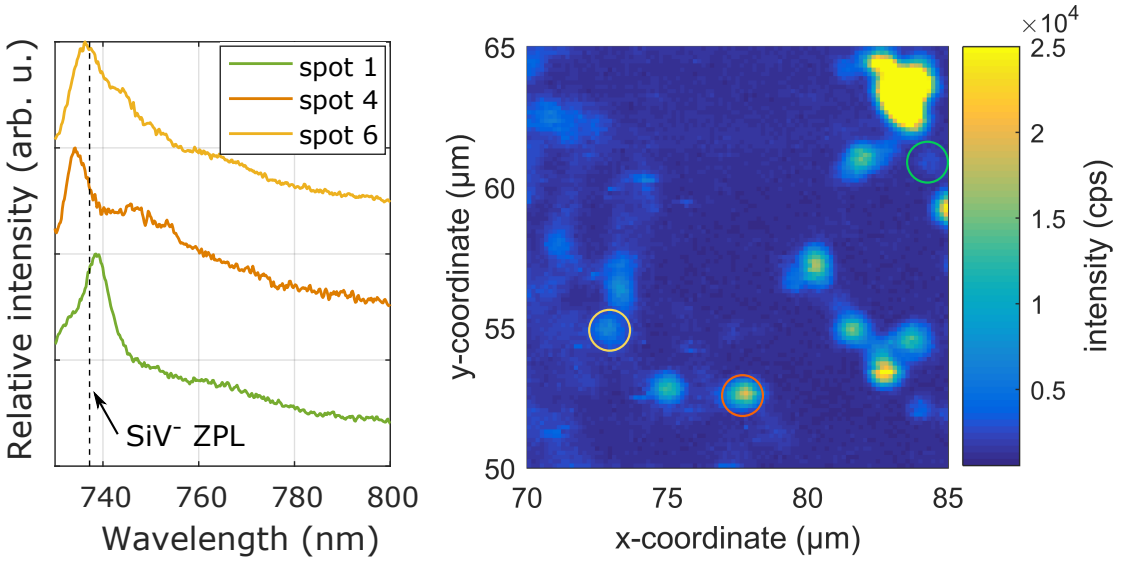

Figure 4.3. Exemplary background and transmission corrected spectra of SiV^- decorated MNDs. (a): Individual spectra of different spots shown in the confocal scan in **(b)**. The color of the cycles in (b) correspond to the spectra plotted in (a). The maximum of the confocal scan has been scaled to 2.5×10^4 cps for better visibility of dimmer fluorescent spots. Filter setting in (a) Filter 1: BP770/90. Filter setting in (b): Filter 1: BP770/90 +BP740/13, Filter 2a/b empty. In both cases a bk7-glass window was used instead of a dichroic

evaporated, a small milky ring was visible on the cover slide. It's origin has been connected to salts, used during purification process of MND material by acids. The region of interest was set next to the corner of the milky ring, and a confocal scan was performed (figure 4.3(b)) using a 690 nm diode laser. The filters used are marked in the legend of figure 4.3. The confocal scan showed dim as well as bright fluorescent spots, with an average intensity around 15 kcps, for an excitation power of 200 µW. The background signal has been well suppressed by the filter combination: On 23 different positions background signal has been determined to be around 1330 cps with a spread of 300 cps, leading to an average signal to

background ration of around 10. Then spectra have been acquired on dim an bright spots. Three examples are shown in figure 4.3(a), marked with cycles in the same color code in figure 4.3(b). Similar to other publications [135, 133], the

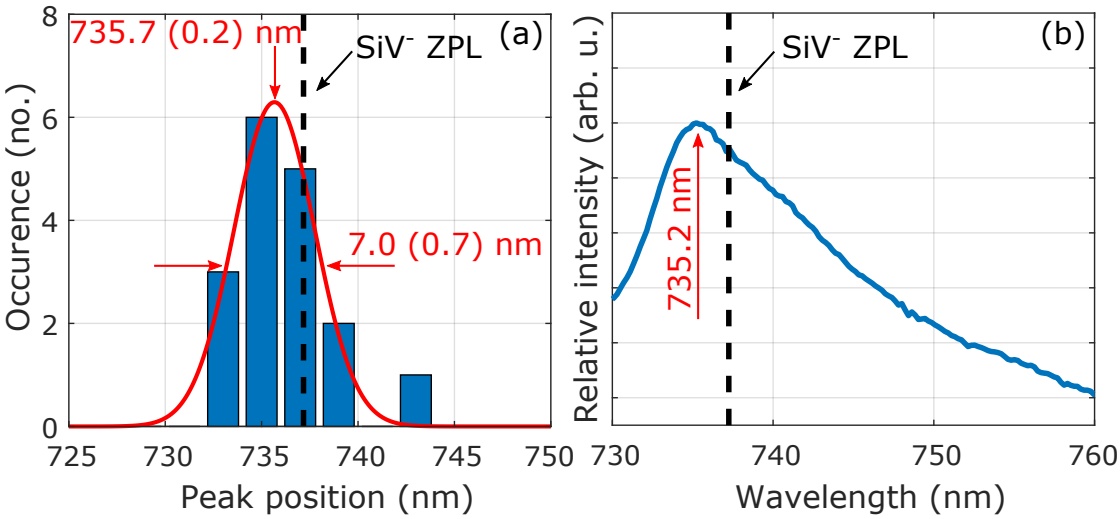

Figure 4.4. Overall shift of spectra in MND sample. (a): To estimate the shift in ZPL, a histogram of 18 spots also shown in figure 4.3(b) had been fitted to a Gaussian. The given numbers in red are the center position and the standard deviation of the Gaussian, respectively. As different spots contain different numbers of emitter, also their spectral sum is plotted in **(b)**. The estimated number of emitters participating in (b) is, based on average intensity of single emitters (compare data shown in figure 4.8 and 4.9), more then hundred. The red arrow indicate the maximum of the spectrum.

SiV^--ZPL showed a spread around several nanometers. The distribution of ZPL is plotted in 4.4(a). Fitting a Gaussian to the obtained data revealed a mean value of (735.7 ± 0.2) nm and a full-width-half-maximum (FWHM) of (7.0 ± 0.7) nm. As different spots contain different amount of emitters, also the sum of all spectra has been plotted in figure 4.4(b). The maximum of the shown average spectrum is around 735.2 nm. The spectrum was estimated to be the sum of more then hundred emitters, based on the accumulated fluorescence level measured, in combinations with results obtained for a single silicon vacancy (section 4.4.2, page 97). The average positions in both analysis show a slide blue shift in the ZPL to the literature value of 737.2 nm (correspond to 1.682 eV [68]).

4.3. Lifetime measurements

To measure the lifetime of individual fluorescent spots, one APD has been connected to a time-correlated single photon counting (TCSPC) counter card. The internal sync channel of the counting device is connected to the laser trigger output. First the IRF is measured (see figure 4.5a), to see if the IRF has to be account for by deconvolution. Fitting the first rise to a Gaussian one gets a standard deviation of 0.1 ns. In addition the right tail of the IRF was fitted to a mono exponential with a decay time of 0.5 ns. The relative amplitude of the Gaussian versus the exponential is 20. For short lifetimes (below 1 nm), jitter around 0.1 ns may already significantly contribute to the observed decay that is a convolution of lifetime and IRF. As the exponential fadeout is only 1/20 of the Gaussian, its contribution has been neglected. In addition laser leakage may cause a misinterpretation of the acquired data set. As one can see in figure 4.5a the IRF faded out with an exponential tail. Therefore the following protocol to interpret the acquired data (two examples in 4.5(c) and (d)) has been applied. The right tail was fit to a mono exponential with a fixed time shift defined by the mean value of the Gaussian fit to the raising slope. The relative amplitude of the Gaussian versus the exponential function shall not exceed a factor of around 3. This guarantees that the signal by the MND is at least 10 times larger than possible laser leaking within the first 1 ns after excitation. By fitting only the long tail 1 ns after excitation, the influence of laser leakage is additionally suppressed, as it already decades to a factor $1/e^{-2}$. Figure 4.5(b) shows the spread of lifetimes with an average of 2.1 ns and a standard deviation of 1.0 ns. Thereby deconvolution by a Gaussian profile has not been applied, as the lifetimes are in average well above 1 ns (or 20 times longer than the standard deviation of the Gaussian fitted IRF). For heteroepitaxial grown CVD diamond the SiV^- lifetime has been measured to be around 1 ns at room temperature [192]. Using the right substrate, lifetimes of 1 ns [90] to around 2.7 ns [192] has been measured. In addition the lifetime depends on the local environment on the length scale of the emitted wavelength. If its refractive index is lowered, the lifetime increases [201, 20]. Beveratos et. al. [20] found an increase of a factor of two, when changing from a diamond environment to an air/silica interface, which fits well with their theoretical model. Accounting for the different environment the

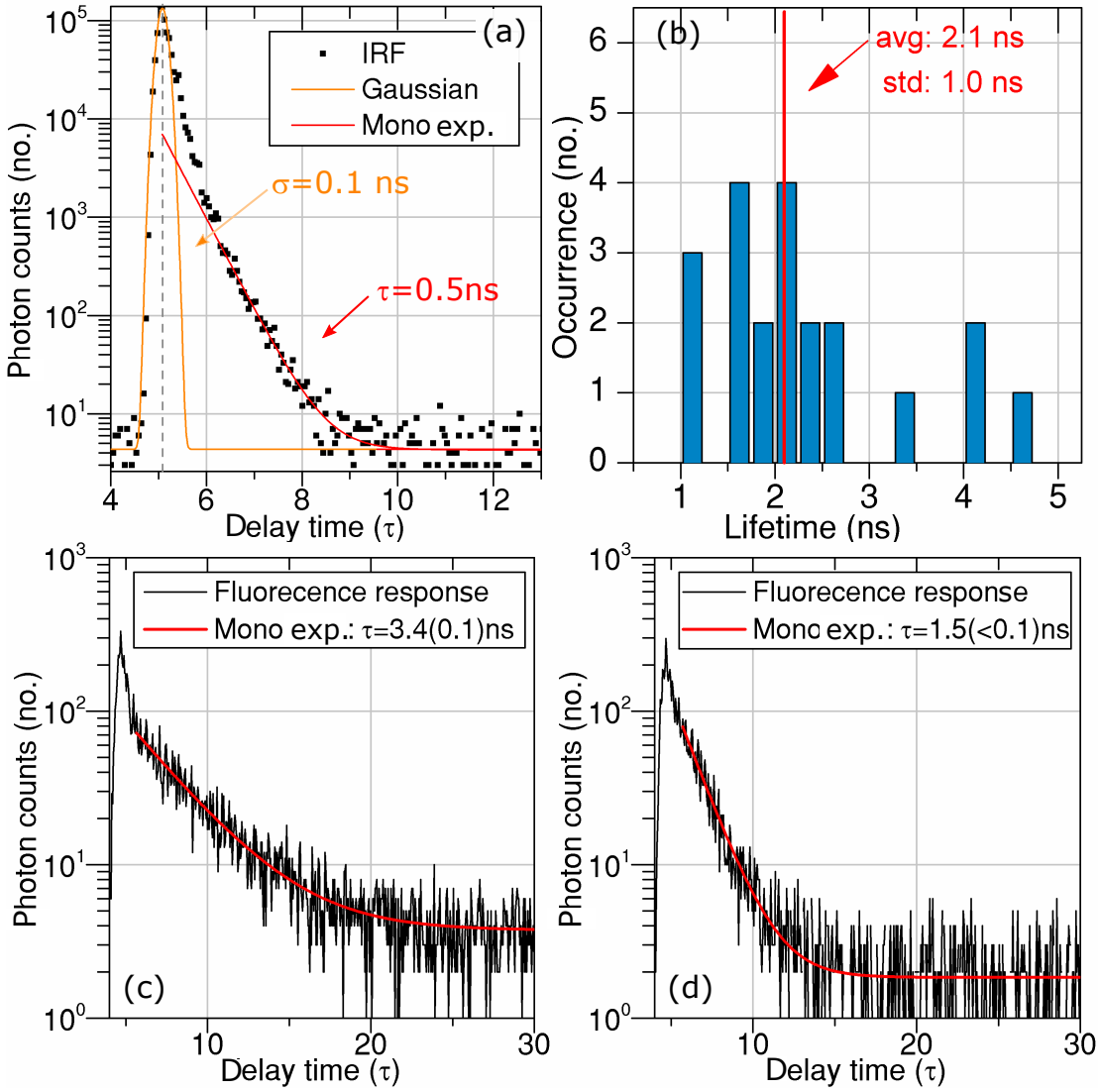

Figure 4.5. Lifetime analysis of MND sample:(a): (black): IRF of given confocal setup when detecting 5×10^4 cps acquired on background on the sample used. (red): Mono exponential fit of the pulse tail with decay constant τ. (orange): Gaussian fit with standard deviation σ. **(b):** Lifetime histogram of around 19 spots. The red colored text indicate average and standard deviation of the plotted distribution. **(c)** and **(d):** Two example for the lifetime of different spots (red) with a long and short lifetime in respect to the average value. The plots include also a mono exponential fit (red).

measured average lifetime of MND is in good agreement with reference values from literature given above.

4.4. Emission rate of SiV^- in MNDs

Next the average intensity of fluorescent spots has been analyzed to obtain informations of the average brightness of the analyzed sample. Therefore a confocal

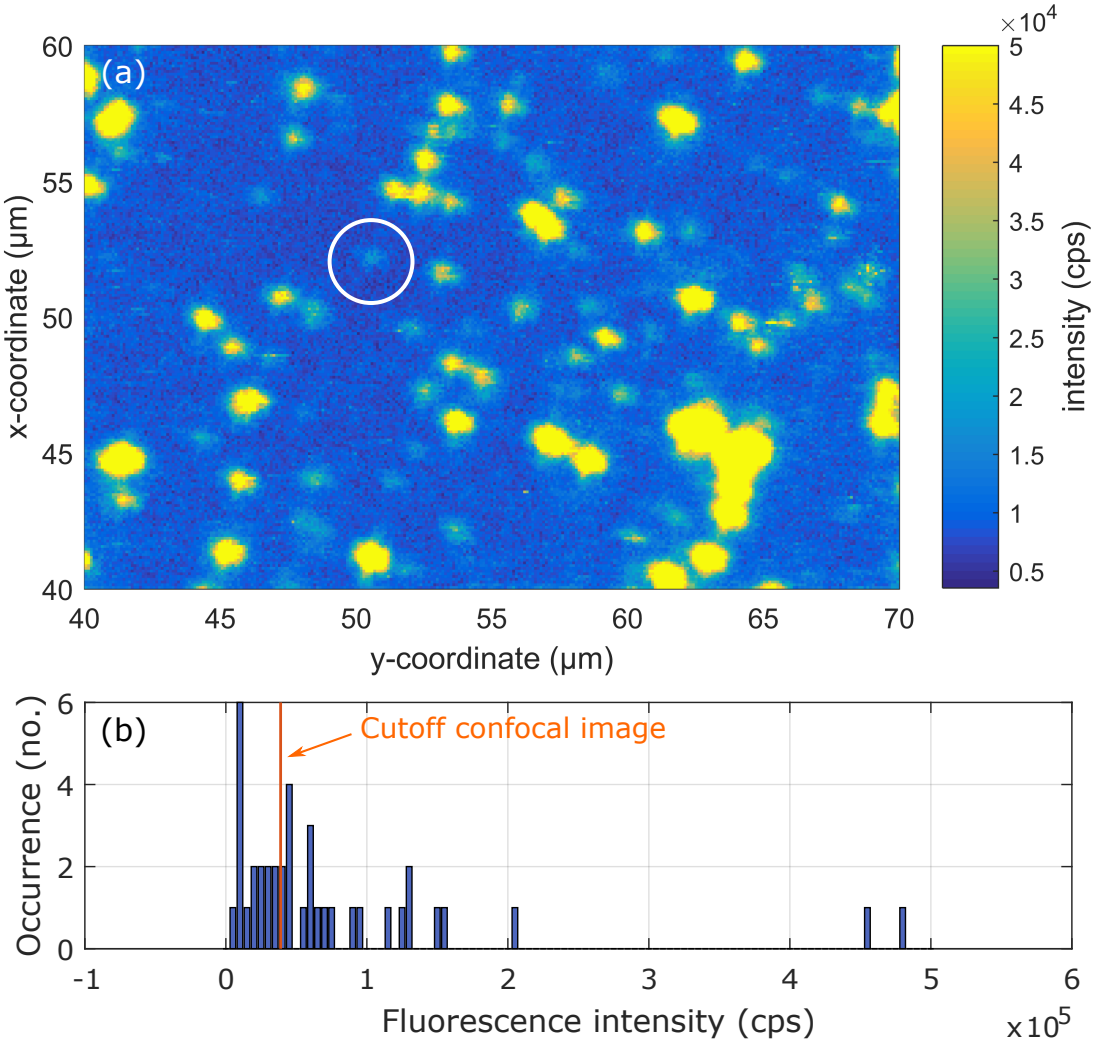

Figure 4.6. Intensity analysis of MND sample. (a:) Confocal scan of MND sample deposited on a quartz cover slide. The maximum intensity was set to $50\,\mathrm{kcps}$, to also visualize dim spots. For the scan $17\,\mathrm{mW}$ and a linear polarized excitation was chosen. The presented data shown in figure 4.9, 4.8 and 4.10 are acquired on the spot marked with a white cycle. **(b):** Background corrected intensity analysis of fluorescent spots in (a). The orange vertical line indicate the corresponding intensity cutoff of the fluorescent image in (a). Laser excitation at $660\,\mathrm{nm}$: $17\,\mathrm{mW}$

scan has been performed, preparing the setup in filter configuration 2 (Filter 1: BP770/90, Filter 2a: BP740/13, Filter2b: BP730/30, dichroic: DCXR704). The excitation laser power was set to 17 mW. Figure 4.6(a) shows the acquired confocal scan: Besides many bright spots, also some dim spots were visible. A histogram of the measured intensities is plotted in figure 4.6(b). As one can see quite a number of dim spots were present. One of the dim spot has been used to analyze its photon statistics via second order correlation to obtain the number of emitters participating in its fluorescent signal.

4.4.1. Auto-correlation and weak signals

For application as fluorescence marker the fluorescence emission rate of a single emitter is of interest, as the capability to laterally localize a fluorescent spot depends on the detected photons in the acquisition time [127]. As the detected photon flux of single emitters seems to be in the range of several kcps, the setups behavior in the low count regime has to characterized. As described on page 23 in the basics section, APDs create photons during the so called break down flash that may lead to a bunching in the acquired autocorrelation function. Figure 4.7(a) shows the measured auto-correlation function on the background of the sample already introduced. Two pronounced bunching shoulders around zero are visible, well above the noise floor (blue lines in figure correspond to $\pm 1\sigma$) in the not normalized auto-correlation function $c^2(\tau)$. Thereby filter combination 1 was used: Filter 1: BP770/90 +BP740/13,Filter 2a/b empty,dichroic: DCXR704). If changing to filter combination 2 (Filter 1: BP770/90, Filter 2a: BP740/13, Filter2b: BP730/30, dichroic: DCXR704), where every APD is equipped with it's own filter, the bunching disappears (Figure 4.7(b)). Focusing on a dim spot led to broad bunching around zero delay (Figure 4.7(c)). By zooming into the the center of the auto-correlation, 100 ns around zero delay, anti-bunching behavior is visible, whereas the artificial bunching disappeared. Therefore, filter configuration 2 has been used for correlation analysis of the dim spot. For the shown data laser excitation at 660 nm with 19 mW was applied.

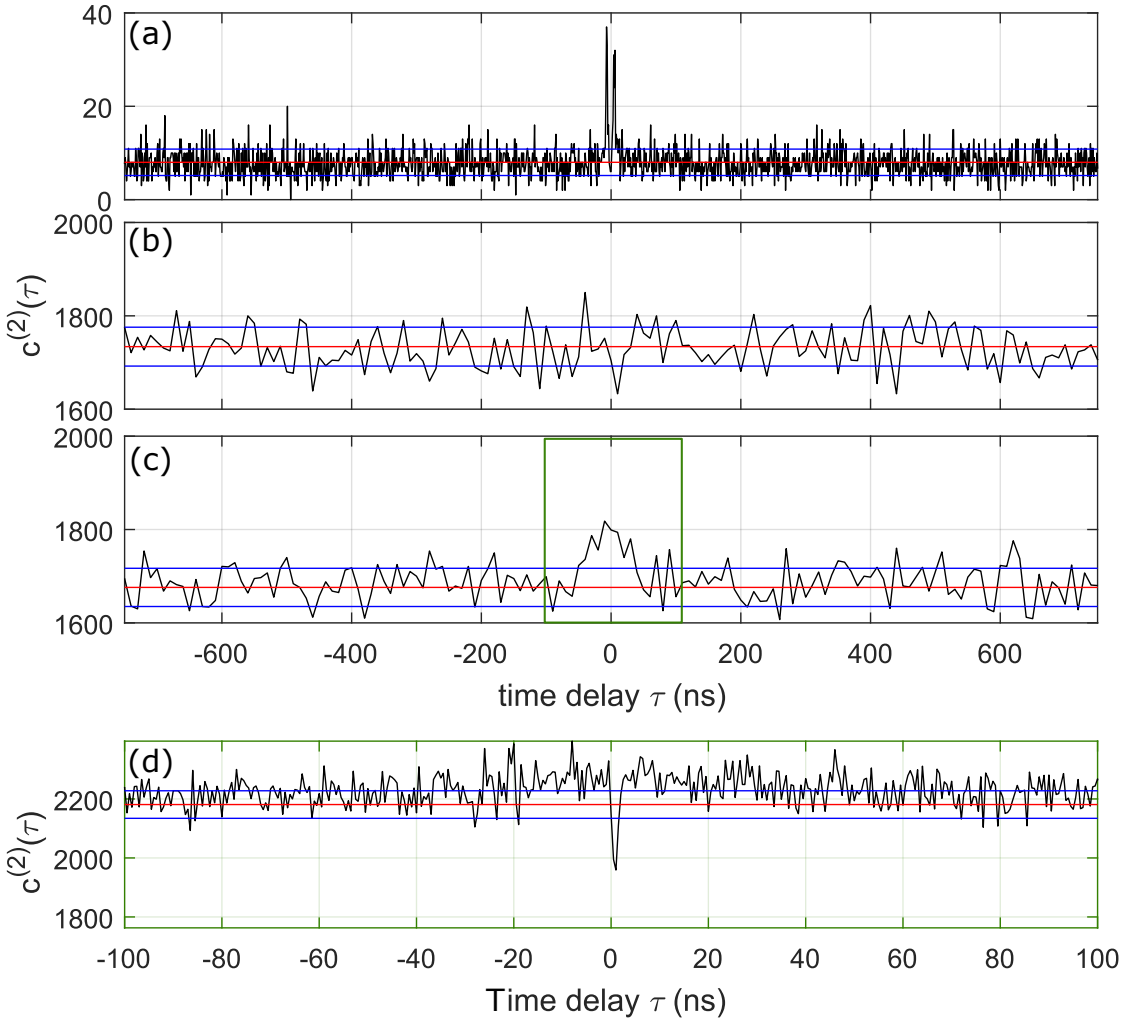

Figure 4.7. Filter setup and consequence for data acquisition, when performing an auto-correlation on weak signals. (a): Unnormalized auto-correlation function acquired on background of the sample, using filter configuration 1. **(b):** Unnormalized auto-correlation acquired on background of the sample, using filter configuration 2.**(c):** Unnormalized auto-correlation acquired on a dim spot using filter configuration 2. **(d):** Unnormalized auto-correlation with high resolution ($0.5\,\mathrm{ns}$ per bin), acquired on a dim spot, using filter configuration 2. The red line indicate the average photons per bin, the blue lines correspond to the average $\pm 1\sigma$ standard deviation.

4.4.2. Detailed analysis of single dim spot

After verifying that an acquired $g^{(2)}(\tau)$ generated reliable result, the dim spot marked with a white cycle in figure 4.7(a) was characterized. In addition, a $\lambda/4$-plate was installed between the dichroic and the objective, to create circular polarized light. As circular light can be again decomposed into two linear polarized waves with a $\pi/2$-phase shift, most homogenous excitation was expected at 660 nm for individual emitters [163]. First the PL spectra was measured (Figure 4.8(b)). The ZPL of several single SiV^- is clearly visible, where as the left peak could also be a superposition of two individual emitters. Then the saturation behavior was probed by ramping up the laser power. Using equation (3.3) leads to a saturation power of 23 mW and a saturation intensity of 38 kcps.

To measure the second order auto-correlation function for short lifetimes, the

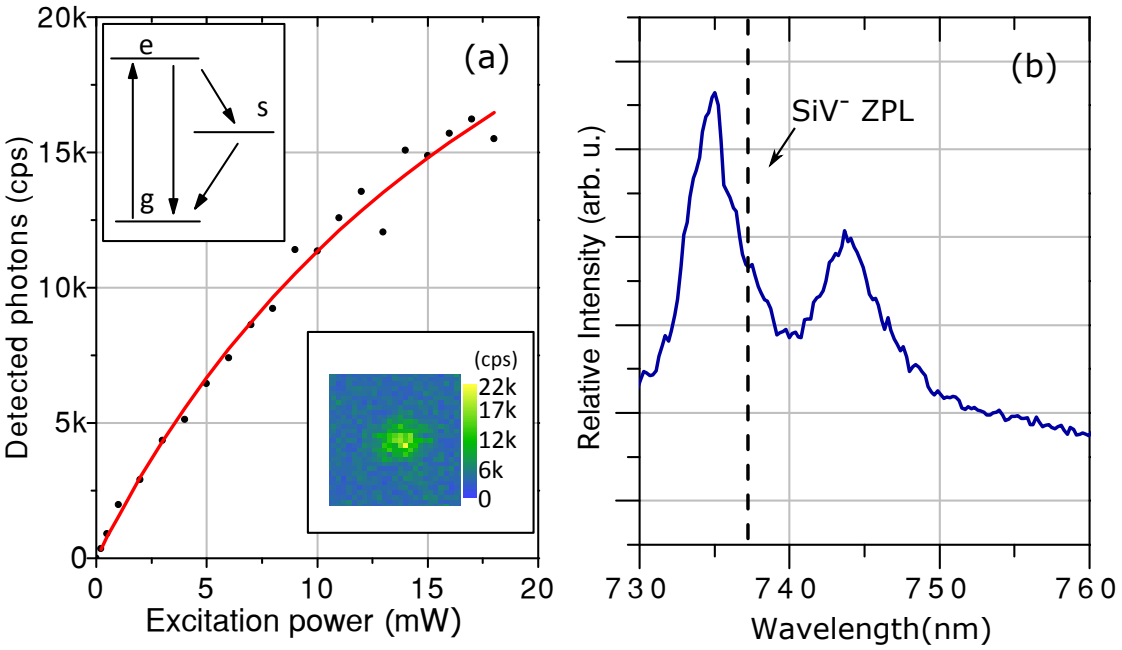

Figure 4.8. Saturation behavior and PI spectra of a dim spot. (a): Saturation curve of a dim spot, also marked in figure 4.6 with a white cycle. The insert shows the confocal image of the spot with an excitation power of 9 mW and circular excitation. **(b):** Optical PL spectra of the same spot.

pump rate should be well below the exited state lifetime, as both rates define the slope of the anti-bunching dip. In contrast low excitation rates and the connected

photon emission decrease the number of coincidences and acquisition time increases quadratically with the number of detected photons per second. As a trade off the laser power was set to around half of the saturation power to 9 mW. The accumulation time to acquire $c^{(2)}$ in figure 4.9 was ~ 14 h in total. As the laser showed long term instability, the measured $g^{(2)}$ included also long term correlations, leading to a shift over several units in the correlation value. Therefore the raw data has been re-normalized to 1 for $\tau \to \infty$. Then the re-normalized $c^{(2)}$ (or $g^{(2)}$) function has been background corrected using equation (3.9), page 22. The background was extracted by the mean count rate of a fine confocal scan in the vicinity of the spot (insert figure 4.8a). By subsequent extraction of background and emitter signal during the accumulation of $g^{(2)}$, an average background and signal was calculated. Therefore a quadratic weighting of the individual results has been chosen, to account for the quadratic dependence of the detected photon coincidences. The background corrected $g^{(2)}$ is fitted to a three state model (equation (3.4), page21) including the convolution with a Gaussian, to account for the jitter of the system. The latter has been determined to correspond to a standard deviation of 0.42 ns. To extract the jitter, $c^{(2)}(\tau)$ for the very same pulsed laser used to extract the lifetime of SiV^- was measured on background. The standard deviation for convolution was set to 0.5 ns, same as the time resolution of the measured $g^{(2)}$ function. Fitting the described model to the corrected data revealed 3 ± 1 emitters within the confocal detection volume.
Having a closer look on the photon trace of the dim spot, one realizes a blinking behavior of its fluorescence (example see figure 4.10(b) and (c) for 500 µW). The blinking can introduce additional correlations with in the measured autocorrelation function and may influence the renormalization of $g^{(2)}$ in figure 4.9. Ramping again the laser excitation power, photon time traces were accumulated. Calculating the corresponding $g^{(2)}(\tau)$ function using equation (3.1) on page 19, one sees a power dependence of the characteristic time constant in the ms regime (figure 4.10(a)). As the time constant is three orders of magnitude longer then the acquisition window used in figure 4.9, it may be visible just as an constant offset in the latter. Rescaling the data shown for the dim spot increases the fitted number of emitter to four. As individual steps within the photon time trace are visible, the trace can also be used to estimate the number of fluorescent levels included. To this end a

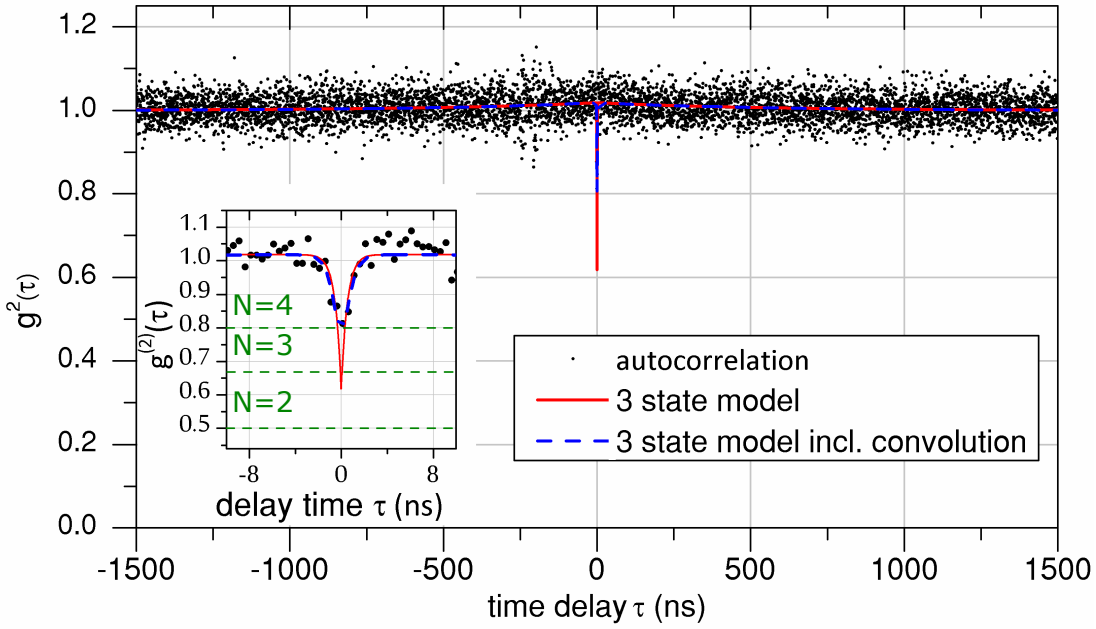

Figure 4.9. Second order auto-correlation function of a dim spot. Auto-correlation function (black) of the same spot using circular excitation and 9 mW exc. power. The insert present a zoom in to some nanosecond delay time. (red): Three state model applied to on auto-correlation function to estimate the number of emitters within the fluorescent spot. (blue): same as (red) also accounting for a jitter of 0.5 ns via convolution of the model in (red) with a Gaussian.

hidden markov model (HMM) was fit *via* maximum likelihood estimation to the trace using a Matlab scripts written by Nawid Zarrabi (see thesis,[128]). Therefore the trace was re-binned to 100 ms and fit by varying the number of fluorescent level. To construct the HMM emission the fluorescence emission of single emitters has been modeled by a Poisson distribution with each two levels. Combining the emission of several emitters results in the corresponding fluorescent level. For the joint probability transition matrix a 95 % probability to stay in a certain state has been set as a starting guess. The routine also estimates the most likely HMM emission and transition probability matrix. This has been used to recompute the fluorescence level of an individual emitter. Again the recalculated HMM emission was fed into the algorithm together with the joint probability matrix.

As maximum likelihood gives the most likely result, but does not provide a quality factor of the given fit result, the minimum number emitters needed to reconstruct

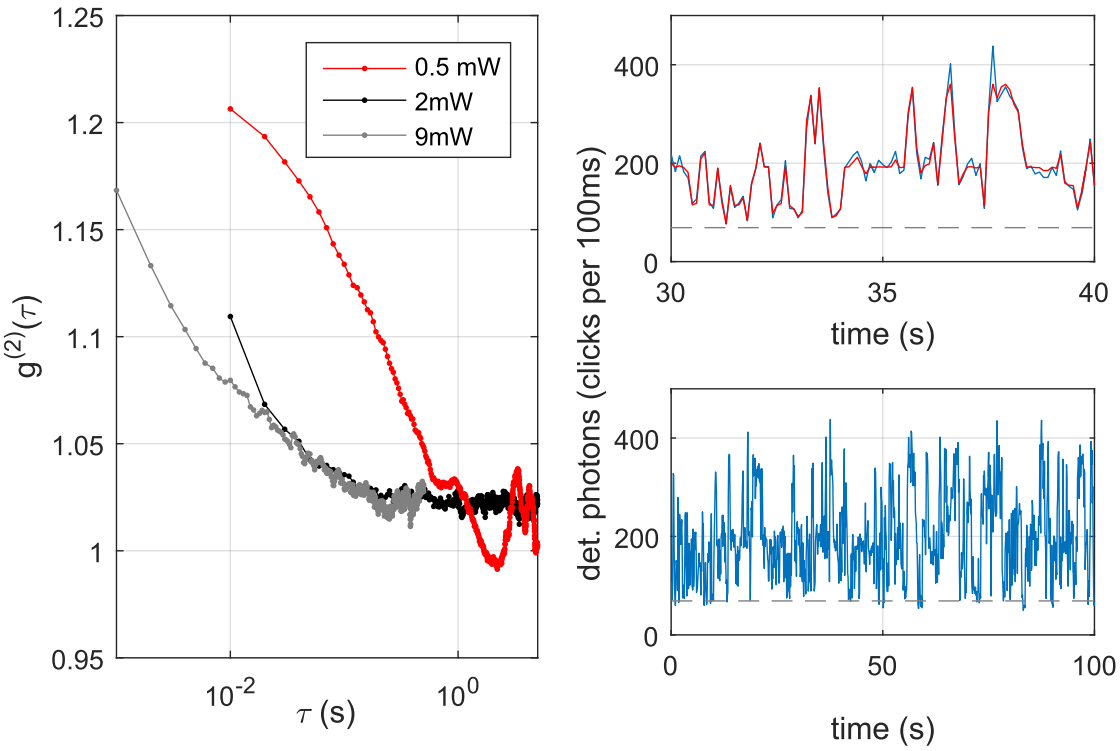

Figure 4.10. Deep analysis of single fluorescent spot. (a:) Autocorrelation function calculated from acquired photon time traces like shown in (c), for different laser excitation powers of $500\,\mu W$,$2\,mW$ and $9\,mW$ with circular excitation. **(b):** Zoom into the photon time trace, shown in **(c)**. The red line in (b) correspond to a 8 state (or 3 emitter) maximum likelihood optimized Hidden Markov model, the dashed gray line marks the minimum fluorescent level

the fluorescent level has been chosen as a benchmark. The result for assuming three emitters is plotted as a red line within figure 4.10(b). Doing the same calculations for 4 to 5 emitters results in the 2 and 7 joint states that are not populated on the main diagonal of the transition matrix, respectively. As the state with no emitter "on" was always presented, one can conclude that the trace originate from at least 3 emitters, and a 4th or 5th emitter is only partially with it's "on" state represented in the acquired trace. This should also be true for the measured auto-correlation function. Using three emitters the upper limit for the saturation intensity of a single emitter can be calculated to be 12.7 kcps. This rates are comparable to literature values for single SiV^- centers in bulk diamond [217], when accounting for the different photon collection efficiency of the different experimental configuration

[1].

4.4.3. Data from collaboration partners

To draw final conclusions also the data from collaboration partners is plotted in figure 4.11. In figure 4.11(a) the PL of MND has been compared to CVD grown diamond material. In one bulk diamond SiV have been incorporated during growth. In another diamond silicon vacancy was introduced by implantation. Also the PL of a MND ensemble shows a blue shift versus the CVD sample around 1.8 nm. As stated in theory, this can is an indication for the size of the ND. Theoretical calculations by collaboration partners indicate an increase in the ZPL energy for particle sizes between 1.1 nm and 1.8 nm of around ~ 0.1 eV [214]. To analyze this further the MND sample has been tested *via* FCS by Steffen Steinert. Using a simple diffusion model (equation (3.12)) the mean size has been estimated to be (1.6 ± 0.2) nm, when using 0.6 nm as the hydrodynamic radius of the control sample Rhodamin 6G [214]. By AC-HRTEM analysis of a fraction of the sample, an average crystal size of 1.3 nm could be verified in the analyzed region. An exemplary corresponding AC-HRTEM image is shown in (d). Thereby the dashed orange cycle marks a nanodiamond crystal with 1 nm in size. Indeed, the nanodiamonds analyzed are of molecular size.

[1] The collection efficiency of emitters deep within a diamond is restricted by total internal reflection [79], if an oil immersion or air objective is used. Whereas the emission of an emitter on an air to cover-glas interface is mainly directed into the direction of the cover-glas [53].

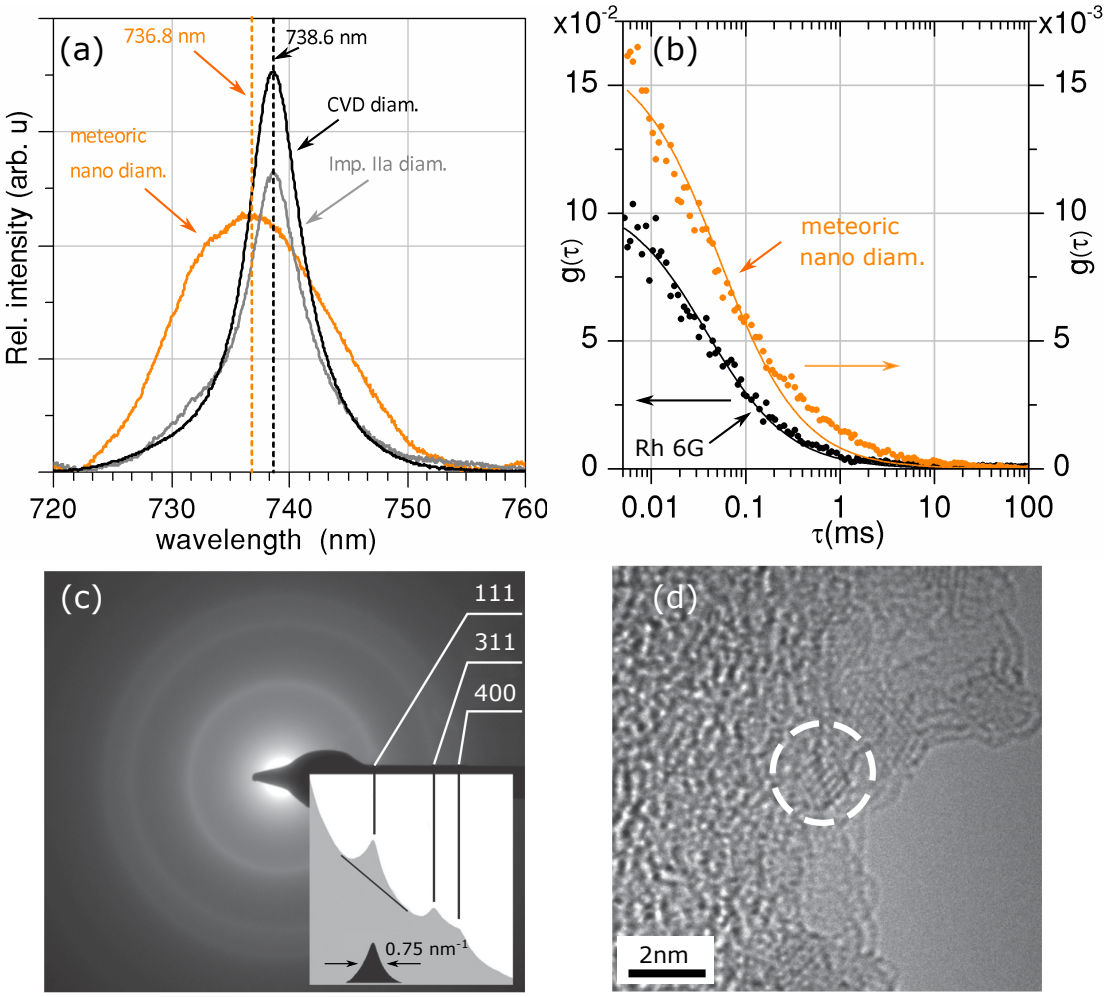

Figure 4.11. Size of MND sample. (a): Fluorescence emission spectra of different diamond samples decorated with SiV. **(b):** fluorescence correlation spectroscopy (FCS) of MND (orange) and the calibration sample (black). **(c):** high resolution transmission electron microscopy (HRTEM) analysis of MND. The electron diffraction ring pattern is evidence for the diamond crystal structure. Inset: Intensity plot profile and background subtracted peak intensity of the 111 ring. **(d):** aberration corrected high resolution transmission electron microscopy (AC-HRTEM) image of nanodiamond grain. The diamond marked with a orange cycle is around 1 nm. Data in (a), (c) and (d) were acquired by cooperation partner, see author contribution in [214]. (b) was measured by Steffen Steinert (also see [214])

4.5. Summary, Conclusion and Outlook

Molecular sized MND decorated with SiV have been spectroscopically analyzed on single emitter level. The measured optical lifetime of 2.1 ns in average (spread: 1 ns) and spectra correspond well to literature values in polycrystalline synthetic nanodiamond. In addition the spectral positions of the ZFS is shifted towards the blue, which is in good agreement with observations made by collaboration partners performed on the very same sample in a powder sample. Theoretical calculations performed by collaboration partners suggest, that the observed shift is a consequence of a quantum confinement effect opening the band-gap of nanodiamonds, which results in a shift of the SiV fluorescent levels. Then an individual spot containing a few emitters has been analyzed. The obtained spectra shows two clear distinguishable peaks around the SiV^- ZPL. Using signal autocorrelation, it has been estimated, that 3 ± 1 emitters are located within the confocal detection volume. In addition, the analyzed spot showed a blinking behavior. The blinking behavior was analyzed by the fluorescent time trace *via* a Hidden Markov model. The latter suggests 3 emitters within the detection volume. The saturation intensity of a single emitter has been estimated to be 12.7 kcps, which is comparable to values in literature. The saturation power around 23 mW.
Although the analyzed SiVs in MNDs showed a blinking behavior, its long term stability is maintained. Similar behavior has been observed for NV^- in ND of 5 nm size [24]. As blinking is one of the mandatory requirements to enable super resolution spectroscopy like STORM or PALM, ultra small nanodiamonds decorated with SiV could serve as a suitable platform. As the defects are highly localized, restricted by the overall size of the diamond, even multiple emitters within a ND will not negatively effect localization precision.
In current study meteoric nanodiamonds have been used, however, the supply is highly limited. Nowadays development in nanodiamond production allow the creation of 1.4 nm sized nanodiamonds with a fairly narrow spread of 0.7 nm using shock-wave-assisted synthesis [191]. As diamond material is non-toxic, together with the various possibilities for chemical modifications of diamond surfaces, fluorescent nanodiamonds may serve as a suitable targeting agent for living cells in future.

5. CW nano thermometry in living cells

The effect of thermogenesis is one of the most common observations in human life. Physical exertion often leads to sweating, exposure to extreme coldness to shivering. One being on diat often feels colder and has a slightly lower body temperature as energy uptake is reduced. Thereby thermogenesis is regulated by the brain, but heating or reducing the body temperature is accomplished on the cellular level [113, 94]. During the past decades intensive attempts have been made to measure the heat produced by a single cell. Several macroscopic probes were developed: For example a vibrating silica stick is changing its resonance frequency by temperature changes of the cell [87], or a thin thermocouple element that is stuck into the cell [215]. As macroscopic probes offer solid measurement schemes, they do not provide the resolution needed to monitor local differences with sub-cellular resolution. For example, heat production accomplished by special organelles like mitochondria cannot be resolved. Therefore fluorescent/phosphorescent probes were developed monitoring changes in the properties of emission of (genetically encoded) organic dyes or inorganic probes [28]. To name a few example: Fluorescent lifetime [140], spectral shifts [100], overall change in the emission strength [69] or other quantities that correlate with temperature [51]. Temperature differences measured by fluorescent means inside living cells have been determined to be around several to tens degree Celsius. However, that result is in contrast to established theory, as shown by Baffou et. al. [12]. After solving the heat equation for a spherical particle, he and coworkers found that temperature must be several orders of magnitude lower, if energy inside the cell is continuously consumed over several seconds to minutes to produce heat. They concluded that at least the fluorescent probes show artificial induced temperature readout, and even if some publications provide

sufficient controls, they behave manifold depended inside living cells.
As the NV is able to measure temperature with a sensitivity of $\sim 100\,\mathrm{mK}/\sqrt{\mathrm{Hz}}$ [137, 105] and (nano)diamonds are non-toxic [176, 209], one may think about using nanodiamonds as a temperature sensor within a living cell to sense variations in this quantity. However, up to now only external heat sources have been probed inside cells [105]. To this end a cwODMR based method was developed, allowing temperature sensing utilizing ND hosting an ensemble of NVs. To insert nanodiamonds into living cells (HepG2, a human liver cancer cell line), the mechanism endocytosis is utilized (see section A.3 and 3.5). As the used particles have sharp edges, they can escape the endosomes and accumulate inside the cytosol [36]. To verify closest proximity to mitochondria the particles are surface modified with triphenylphosphine (TPP) (section A.4). In addition cells are labeled with a fluorophore that specifically accumulates within the mitochondria of living cells. The fluorescent label allows to co-localize fluorescent ND with mitochondria and verifies close proximity from the beginning, when sensing temperature changes. To introduce changes in local heat production, the ionophore CCCP is used that short-cuts the inner membrane potential of mitochondria, resulting in additional heat dissipation.

5.1. Experimental setup

To measured temperature inside living cells after preparation, the setup shown in figure 5.1 was utilized. Orange laser light was power stabilized *via* an acusto optical modulator (AOM). Therefore the latter was controlled within a feedback loop, consisting of a photo-diode and a PID-controller. The orange laser was combined with a blue laser and guided into a photonic crystal (PC) fiber. A bk7-window deflected light onto the objective. Thereby the orange laser excited NV^-, and the blue laser "MitoTracker-Green" (Thermo), a fluorophore staining the mitochondria of living cells.

The emission of NV and the MitoTracker-Green was collected by the objective, passed the bk7-window and was detected with 3 APDs. The first set of APDs detected mainly the fluorescence of NV, the last one the signal of MitoTracker-Green. To suppress leaking light from the lasers, two long-pass (LP647, Razor

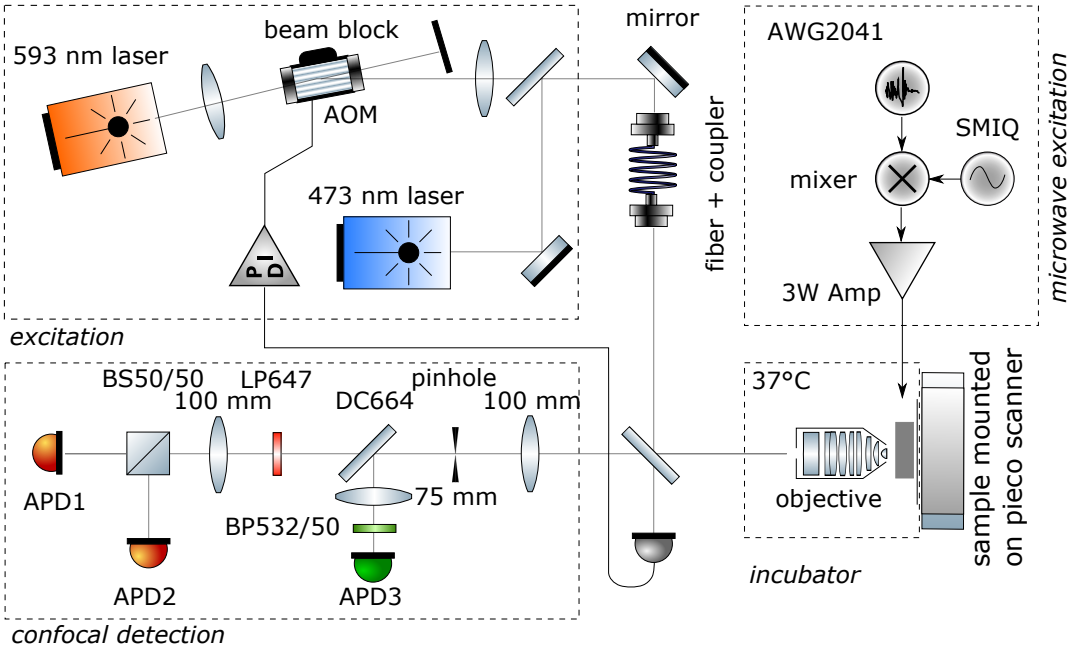

Figure 5.1. Setup cw nano thermometry

Edge, Semrock; LP575) in case of NV, and one Bandpass (ET535/30m, Chorma) in case of MitoTracker has been used. To manipulate the NV spin system one arbitrary waveform generator (AWG) (AWG2041) was connected to a mixer (ZX05-C60LH-S+,mini-circuits). The local oscillator input was connected to a frequency source (SMIQ03B, Rohde&Schwarz). The microwave leaving the mixer was then guided through a microwave switch (ZASWA-2-50DR+,mini-circuits) allowing to additionally suppress microwave excitation, if needed. After the switch a 3 W amplifier (ZVE-3W- 83+, mini-circuits) amplified the microwave excitation and coupled latter into the sample. For microwave radiation an omega micro-structure was used. To create the observation chamber, a cover-glass holding the micro-structure was glued to a microwave printed circuit board (PCB)-board and connected. Then a spectroscopic cell culture dish, without its cover-slide, was glued on top with epoxy. The connection between dish and the cover-slide was sealed with polydimethylsiloxane (PDMS), to ensure that the cell culture has no have direct contact with the epoxy. As the micro-structure was made out of copper, the structure was applied on the other side of the cover slide to ensure that cells did not

touch with the copper. As the omega had a radius of $\sim 500\,\mu m$ and has been much bigger then the thickness of the cover slide (70 µm to 170 µm), the magnetic field on both sides of the cover slide is similar. To monitor the temperature of the sample, a thermistor was directly put into the dish in contact with the used medium. In addition the temperature could be controlled, using a incubator system (Objective heater system: tempcontroller mini, Recon; Sample heater system: tempcontroller 37, Recon). The incubator also allowed to flush the chamber with a 5 % CO_2 atmosphere. To detect fluorescence an oil immersion objective (UPlanFL 100x NA 1.3,Olympus) was used. All experiments performed on living cells, have been done with the initial settings 37 °C and 5 % CO_2. The laser power for orange was set to $\sim 2\,\mu W$ and for blue $\sim 400\,nW$, if not stated differently. To control the experimental setup, a custom written software in the program language "python" was used.

5.2. Control experiments

To ensure that an observed temperature change is caused by the living cell itself, several control experiments had to be performed. First the nanodiamonds were characterized, to find there specific temperature response (shift if ZFS D). Then the TPP modification done by Zhiqin Chu had to be characterized on it's capability to bind to mitochondria. Then one had to confirm that the cell viability is not negatively influenced by the laser or microwave. As one wanted to measure the temperature increase after CCCP stimulation, a proper concentration of CCCP had to be found, that did not influence cell viability, but still leads to depolarization of the mitochondrial membrane potential.

5.2.1. Sample characterization

The characteristics of ND exhibit a wide range of tune-ability on parameters like NV density, size and surface modification. For continuous wave (cw) nano thermometry one wants to maximize the signal to noise ratio (SNR). Therefore edged diamonds with a high density of NVs have been chosen as starting material [34]. In the following the temperature depended shift in the fine structure constant has been

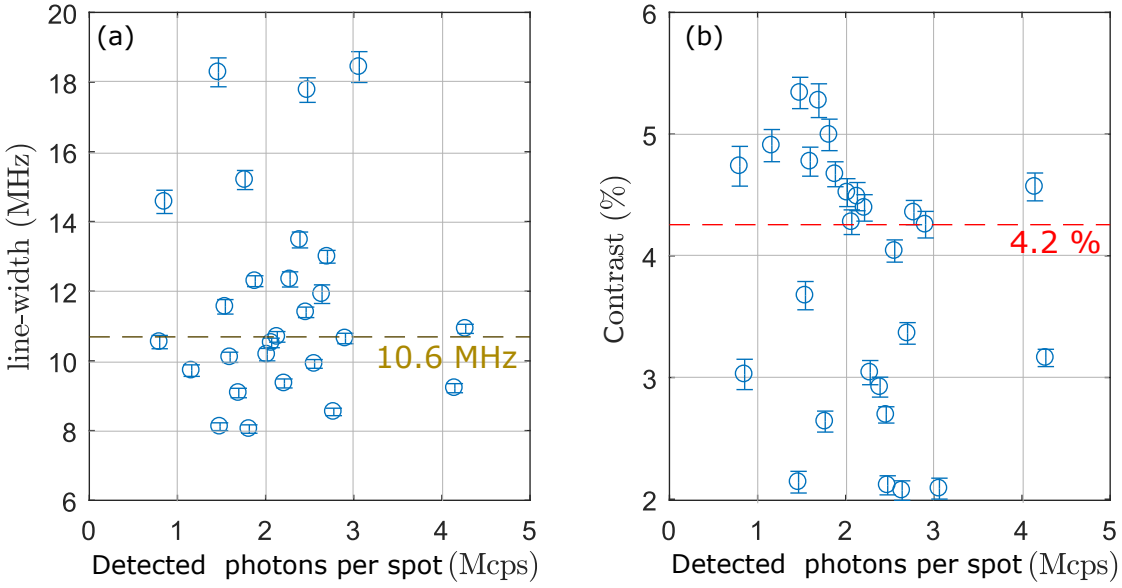

Figure 5.2. ND-TPP: contrast and linewidth. (a): linewidth and **(b):** contrast of the EPRsignature of NV measured by ODMR dependent on photon count rate extracted on the fluorescent spots presented in figure 5.3. Dashed lines represent the corresponding median value

characterized for the specific sample used, after modifying with TPP (see appendix A.4) for modification protocol by Zhiqin Chu).

Therefore a chamber for cell studies (see section setup) was incubated with $20\,\mu g\,ml^{-1}$ ND-TPP solution in 50 mM 4-(2-hydroxyethyl)-1-piperazineethanesulfonic acid (HEPES) buffer at pH 7.4. After waiting for 10 min, the solution was removed and replaced by 4 ml of the very same buffer. A small fraction of ND-TPP adsorbed on the surface (see figure 5.3(a)). Then a thermistor was directly placed within the solution as reference. To estimate the temperature dependent drift of the zero field splitting $^{\Delta D}/_{\Delta T}$, one acquired fine sweeped ODMR spectra for different temperatures of the incubator system, ranging from around 23 °C to 35 °C. After extracting the relative shift of the EPR lines as plotted in figure 5.3(c) and (d), the average shift of all spots has been extracted to be $(79 \pm 1)\,kHz\,K^{-1}$. In addition the relative intensity of single fluorescent spots could be extracted (figure 5.3(b)): With a lower threshold of 500 kcps, the median intensity of all fluorescent spots was around 1.6 Mcps, excited by 1.5 µW orange laser light. As ODMR contrast and linewidth define the

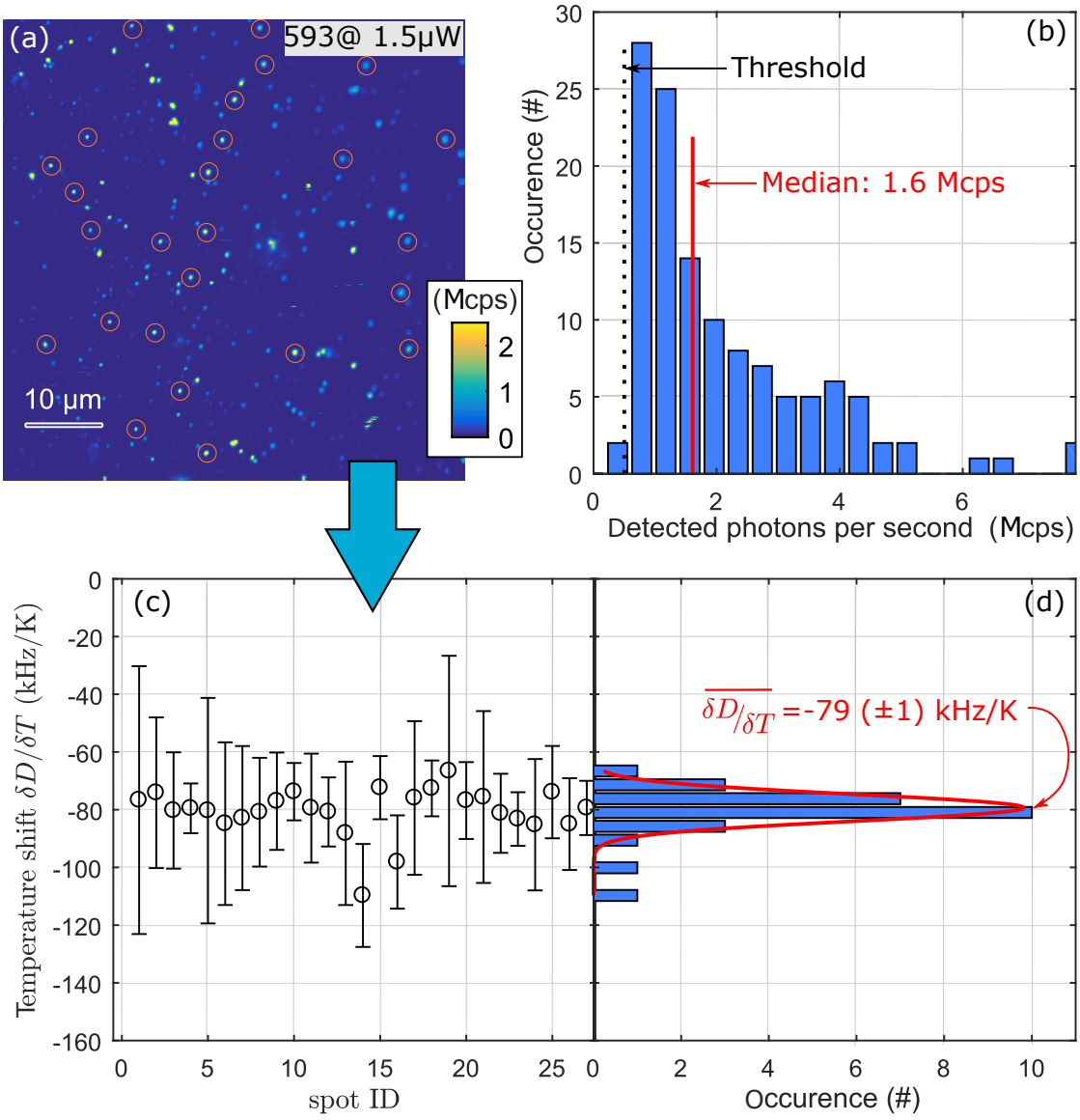

Figure 5.3. ND sample used for cw nano thermometry. (a): Thresholded confocal scan of ND-TPP, adsorbed on a cover glass of the sample chamber used for cell experiments. The sample is covered with buffer. All spots marked with orange cycles are analyzed further in (c) and (d). **(b):** Intensity distribution of all the shown spots in (a). The black dashed line marks the threshold used to extracted the median intensity (red solid line) of analyzed spots. **(c):** Temperature shift coefficient $^{\Delta D}/_{\Delta T}$ of the zero field splitting D for all spots marked in (a). **(d):** histogram of (c) including a Gaussian fit (red) to extract an average temperature shift.

later temperature sensitivity in a given experiment, also these parameters were extracted (figure 5.2(a) and (b)). The median for contrast and linewidth is 4.2 % and 11.6 MHz, respectively. Interestingly there seemed to be no tendency of contrast and linewidth in connection with the fluorescence strength, so that only dim or bright spots gave rise to higher ODMR contrast or smaller linewidth.

5.2.2. Binding of ND-TPP to mitochondria

As NDs should be located close to mitochondria, selective targeting is desired. Therefore nanodiamonds have been modified with TPP to target mitochondria (see appendix A.4, page 227) and incorporated into living cells via endocytosis (see appendix A.3, page 227). After staining mitochondria with MitoTracker-Green, the as prepared sample has been analyzed using the above described setup. Nanodiamonds showing close proximity with mitochondria have been identified by co-localization of NV with "MitoTracker" fluorescence. One example of such a confocal scan is shown in figure 5.4(a). After a suitable NV was found, its position has been traced. Therefore the scanner of the setup was moved along a small cycle in x and y direction with radius 50 nm. By correlating the fluorescence signal of NV with the position on the cycle, a position correction was calculated. By monitoring the fluorescence of a second cycle shifted by 100 nm in z-direction, a 3D correction of the scanner versus the ND could be applied. An example for the resulting trajectory has been plotted in figure 5.4(b). As cells and it's organelles could move during observation, the trajectory includes a drift term besides diffusion. Applying singular value decomposition (SVD) the axis of drift can be determined. Then the mean square displacement (MSD) was calculated perpendicular to the drift axis and fit to a 2D diffusion model introduced in equation (3.112). Same procedure has been repeated for ND without TPP modification (bare-ND). The resulting diffusion coefficient D versus the diffusion parameter α is shown in figure 5.4(d). As one can see, the diffusion coefficient for unmodified ND has been similar to the modified nanodiamonds, but a clear difference in α is visible. As α is a measure of the diffusion behavior and a smaller value indicate a more hindered diffusion, one may conclude that modified nanodiamonds have a higher tendency to be hindered in diffusion by temporally binding of ND-TPP at the surface of a mitochondria.

To gather further inside into the diffusion behavior of modified nanodiamonds,

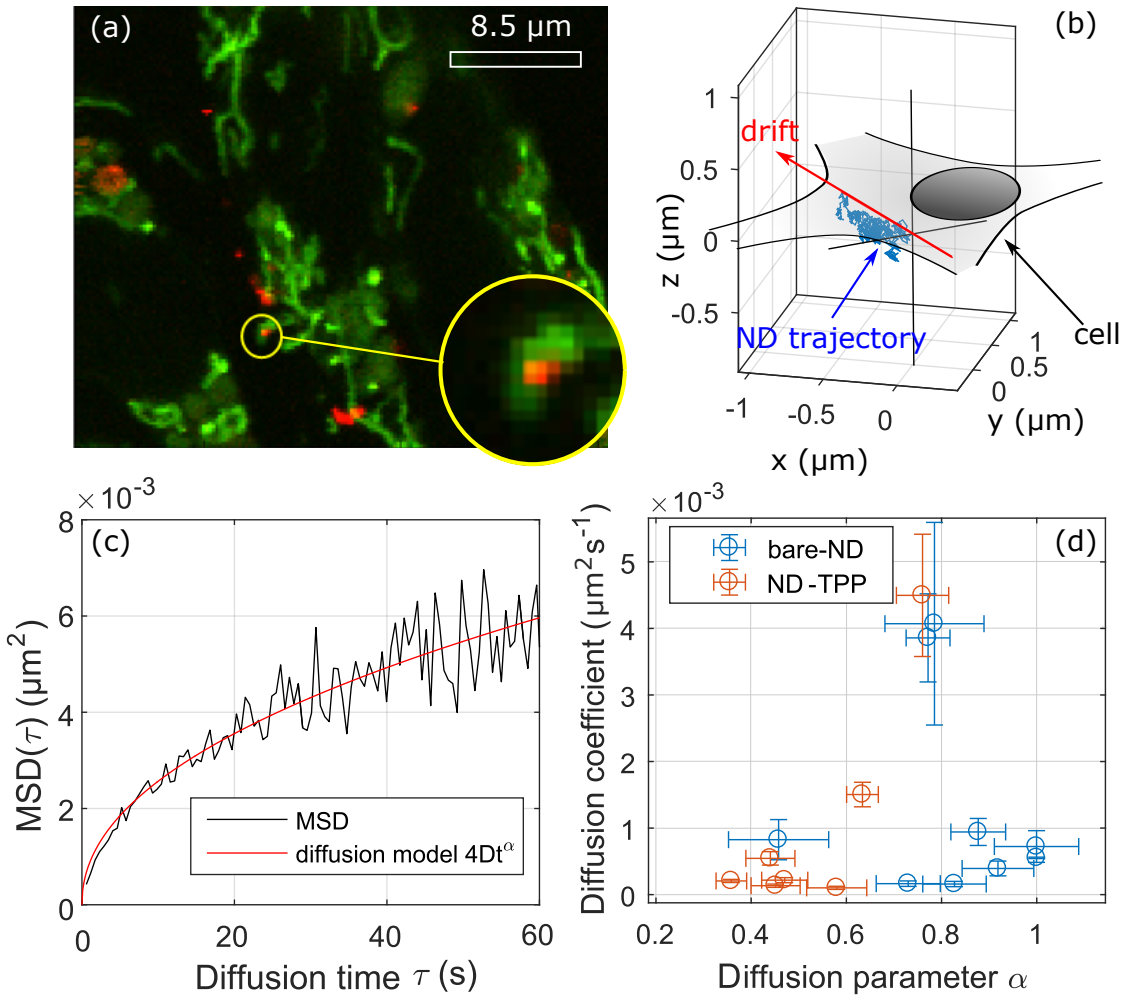

Figure 5.4. Diffusion analysis of bare ND versus ND-TPP: (a): Typical confocal scan showing in green stained mitochondria and in red NV fluorescence. The yellow cycle represent the zoom into one off the analyzed nanodiamond.**(b):** The diamond is contentiously traced for more then 10 min. As drifts can occur during measurement, the acquired trajectory is analyzed via SVD to determine the direction of directed motion. **(c):** Aligning the z-coordinate along the drift axis, the x and y components can be analyzed by a two diffusion model with the parameter α. Whereas α describes the type of diffusion. **(d):** Diffusion coefficient versus diffusion parameter α for bare ND (blue) and ND-TPP (red).

the MSD divided by the diffusion time was plotted versus the diffusion time τ in a double logarithmic plot. If α is 1, a straight horizontal line will show in the

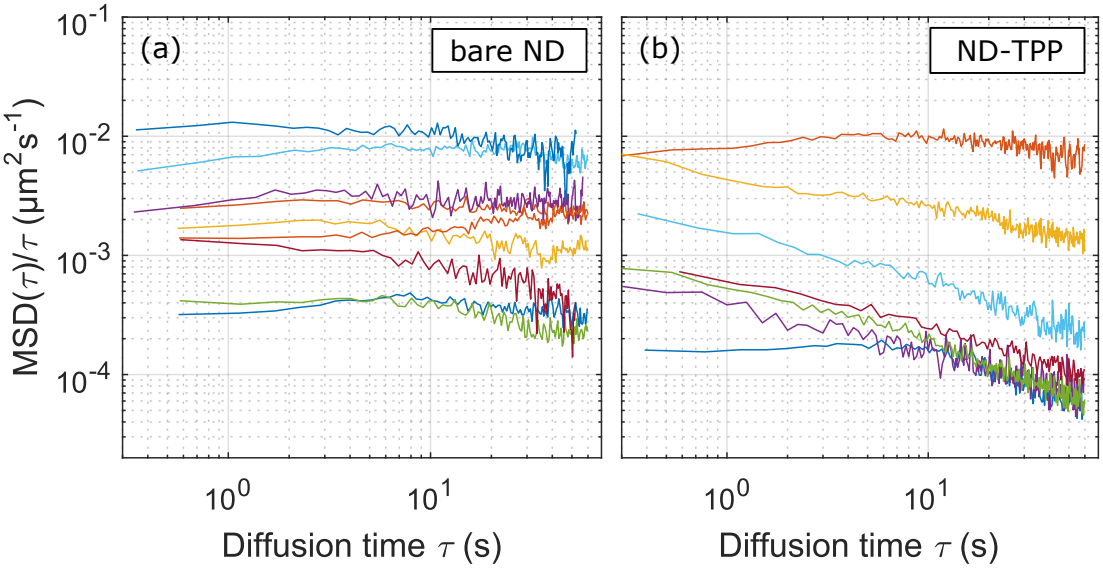

Figure 5.5. Diffusion analysis of bare ND versus ND-TPP. MSD divided by diffusion time versus diffusion time for (a) bare NDs and (b) ND-TPP .

plot (Brownian motion). An increase or decrease indicates anomalous diffusion. The advantage of visualizing the acquired data in such away, is that one is able to identify different values of α for different time regimes. Doing so, for example one can identified free and hindered diffusion on different time scales [195]. As figure 5.5 reveals, a slide decrease of the quantity MSD/τ with increasing τ for bare nanodiamonds, it's decreasing slope is much more pronounced for ND-TPP. In both cases some examples showed partially a positive slope, that may result form uncompensated drift components during SVD procedure. Besides the different α, no big difference in the behavior of the quantity MSD/τ and the diffusion coefficient was observable. Therefore incorporation of ND inside mitochondria, like it has been observed for silica particle [120], is expected to be less likely then just a temporal sticking to mitochondria. As this would mean that nanodiamonds prefer to be close to the surface of mitochondria, this is still sufficient result for the given overall task.

5.2.3. Cell viability: Influence of laser irradiation

As laser light was used to probe the fluorescence of NV the question arises, if the cell viability was influenced during irradiation. To this end a batch of cells had been irradiated with green light at a laser power of 30 µW for 2 min. In real experimental situation usually a laser power an order of magnitude lower is used. In terms of irradiation dose this correspond to around 20 min to 30 min for later experiments. To verify experimental comparability HepG2 cells had been incubated prepared as described in appendix A.3 (see figure 5.6(a)). After irradiation (figure 5.6(b)) cells were stained with Calcein, a non fluorescent organic dye that turns into a green fluorescent dye after being enzymatically cleaved in living cells. As can bee seen from figure 5.6(d) there was no significant difference in cell viability, between irradiated and untreated cells.
The presented experiment also allows to estimate the probability of a cell being alive in a given experiment after a certain time. From the the acquisition of figure 5.6(a) to 5.6(d) the measurement time in the experimental incubator already reaches around 1.5 h but still cell viability reaches as a lower limit around 90 %.

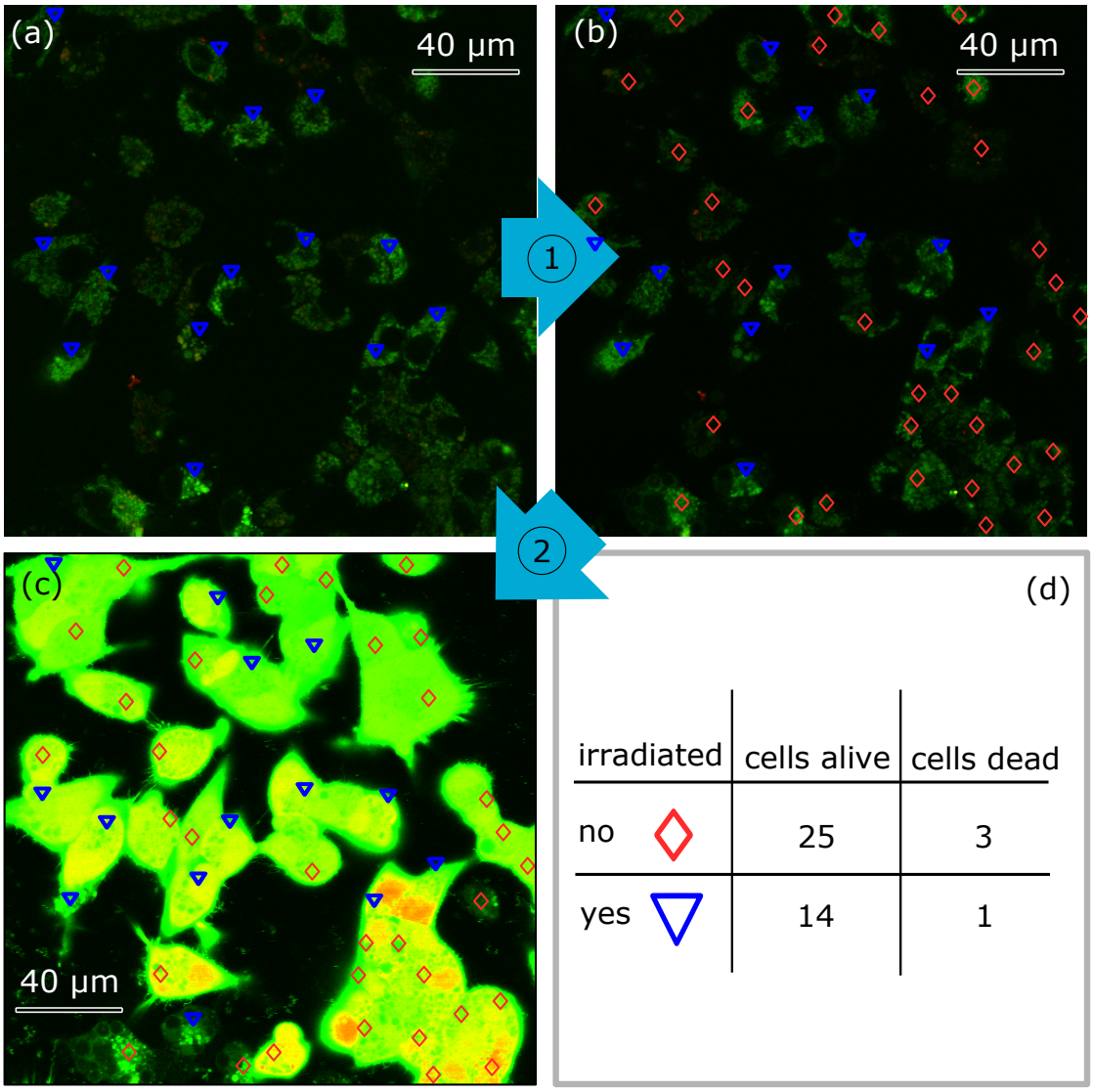

Figure 5.6. Cell viability: influence of laser irradiation. (a): confocal scan of HepG2 cells before laser irradiation. **(b):** Same region of interest as (a) after laser irradiation. **(c):** Same region of interest after Calcein staining. **(d):** Statistics of cell viability in case of no additional irradiation (red diamonds) and additional laser irradiation (blue triangles).Arrow (1) indicated before and after laser irradiation. Arrow (2) indicates before and after staining with Calcein

5.2.4. Cell viability: Influence of CCCP

In current experiment CCCP is used to uncouple the electron transport chain from the oxidative phosphorylation. To find a conditions for cell stimuli without influencing the cell viability, a MTT-assay was performed. Therefore cells were incubated with the dye MTT (3-(4,5-dimethylthiazol-2-yl)-2,5-diphenyltetrazolium bromide) after stimuli with different concentrations of CCCP. If cells are alive the yellow colored MTT is reduced to blue-violet Formazan. By measuring the absorption at 570 nm after a fixed time, one can calculate the cell activity by comparing to a reference without stimulation. For more details see appendix A.6.

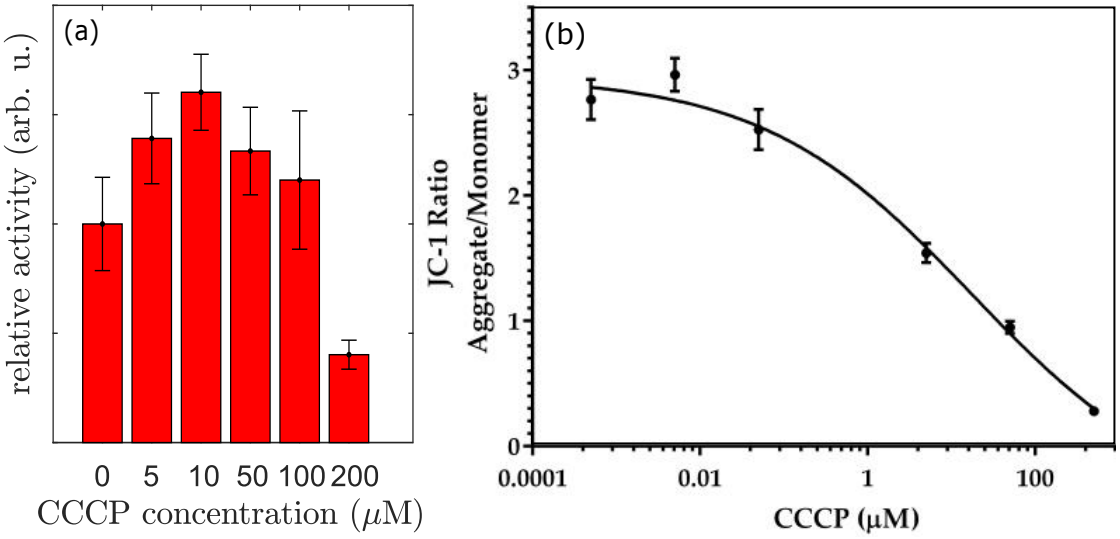

Figure 5.7. Cell viability: cell line.(a): MTT assay. **(b):** State of membrane potential using the fluorophore JC-1. Graph has been taken from reference [2].

As shown in figure 5.7(a) a clear drop at 200 µM is visible. In addition, in figure 5.7(b) the result from [2] has been plotted. There the fluorophore JC-1 was used to probe the mitochondrial membrane potential. JC-1 is a cationic dye, which in low concentrations shows a green fluorescence. It accumulates in the mitochondria depending on its membrane potential and forms in high concentration aggregates which show a red fluorescence. By plotting orange versus green fluorescence, one can verify the decrease in the mitochondrial membrane potential that seems to develop already for concentrations around 1 µM CCCP. To induce a possible temperature

change typically a concentration of 20 µM was used in the following experiments.

5.3. CW nano thermometry

As laser light and microwaves can be absorbed by aqueous solution like cell culture medium, its capability to introduce artificial heating has to be analyzed. To this end, also characteristic quantities like pH and ion concentration that modulate the absorption behavior of a liquid solution has to be considered, especially for microwave excitation. In addition, the method to measure temperature has to be characterized on its sensitivity in a cellular enviroment.
Afterwards, heat production within living stimulated cells can be analyzed considering all the above mentioned issues.

5.3.1. Robustness of CW nano thermometry

In the following section the robustness of nano thermometry is discussed. This includes environmental influences like pH changes or changes in ionic strength of the used buffer solution, influences by external magnetic fields and artificial heating by the measurement process itself.

Influence of laser irradiation on temperature measurements

As light can be absorbed by matter, the laser used for probing NV can act as a potential local heat source. Thus the influence of local laser heating as function of irradiated laser power has been analyzed. Therefore an additional second green laser with a wavelength of 532 nm with powers up to 100 mW has been installed as heat source generator. The orange (593 nm operating at 1 µW) laser was used, as in cellular experiments, to probe the temperature (see figure 5.8(a)) by monitoring the change in the zero field splitting, via an ODMR spectrum. As huge variations in excitation strength of the NV can lead to changes is the observed ODMR sweep, direct excitation by the green laser was avoided. Therefore the distance between the heating green laser to the orange probe laser was tuned in the focal plane *via* a 2-axis galvo-system. Then the temperature increase for different distances and laser power excitation strengths were measured (see Figure 5.8(c)). To extract the

temperature generated at the center of the green laser, the heat equation was solved in the stationary case. The confocal excitation volume was modeled, for reason of simplification, with a spherical normal distribution scaling with the absorbed Power P_{abs}. The spacial extension σ_c of the focused beam was directly extracted from wide-field images acquired by a CCD camera (Figure 5.8(b)). The heat source density for a stationary case $p(r)$ reads then

$$p(r) = \frac{P_{\text{abs}}}{\sqrt{8\pi^3}\sigma_c^3} \cdot e^{-\frac{r^2}{2\sigma_c^2}}. \tag{5.1}$$

Inserting equation (5.1) into the stationary heat equation after transforming into spherical coordinates leads to:

$$-\kappa \frac{1}{r}\frac{\partial^2}{\partial^2 r}\left(r \cdot T(r)\right) = \frac{P_{\text{abs}}}{\sqrt{8\pi^3}\sigma_c^3} \cdot e^{-\frac{r^2}{2\sigma_c^2}}. \tag{5.2}$$

Thereby angular dependencies for the temperature distribution $T(r)$ has been dropped. κ is the thermal conductance. Equation (5.2) has the analytical solution

$$T(r) = T(\infty) + \frac{P_{\text{abs}}}{4\pi\kappa r} \cdot \text{Erf}\left[\frac{r}{\sqrt{2}\sigma_c}\right]. \tag{5.3}$$

In a real experimental situation, or when modeling the laser beam as a Gaussian beam, absorption and therefore heat generation, not only happens in the vicinity of the heat source. As the beam penetrated all the way through the position of focus and as the opening angle of the used objective are rather big (around 60 to 70°), almost all the medium in the vicinity of the spots is partially heated. To empirically account for the latter, a temperature increase linear with laser power P_{laser} scaling temperature increase was added, and equation (5.3) reads as

$$\Delta T(r, P_{\text{laser}}) \approx +\frac{\alpha_{\text{abs}} \cdot P_{\text{laser}}}{4\pi\kappa r} \cdot \text{Erf}\left[\frac{r}{\sqrt{2}\sigma_c}\right] + \beta_{\text{abs}} \cdot P_{\text{laser}}. \tag{5.4}$$

Using equation (5.4) one can estimate the coefficients α_{abs} and β_{abs}, whereas α_{abs} is dimensionless not to be mistaken as the absorption coefficient. Introducing the series expansion of the error-function, the temperature increase at zero radius can

be expressed as

$$\Delta T(r=0, P_{\text{laser}}) \approx \underbrace{\left(\frac{\alpha_{\text{abs}}}{\sqrt{8 \cdot \pi^3} \sigma_c \kappa} + \beta_{\text{abs}} \right)}_{\delta T / \delta P} \cdot P_{\text{laser}}. \tag{5.5}$$

Fitting equation (5.4) to the obtained data sets, shown in figure 5.8(c), resulted in $\delta T/\delta P$ equals $(0.8 \pm 0.2)\,\mathrm{K\,mW^{-1}}$. α_{abs} was determined to be on the order of 10^{-3}, when assuming κ to be $0.608\,\mathrm{W\,m^{-1}\,K^{-1}}$. In cellular experiments typically laser excitations around several µW are used, laser heating itself is therefore neglectable.

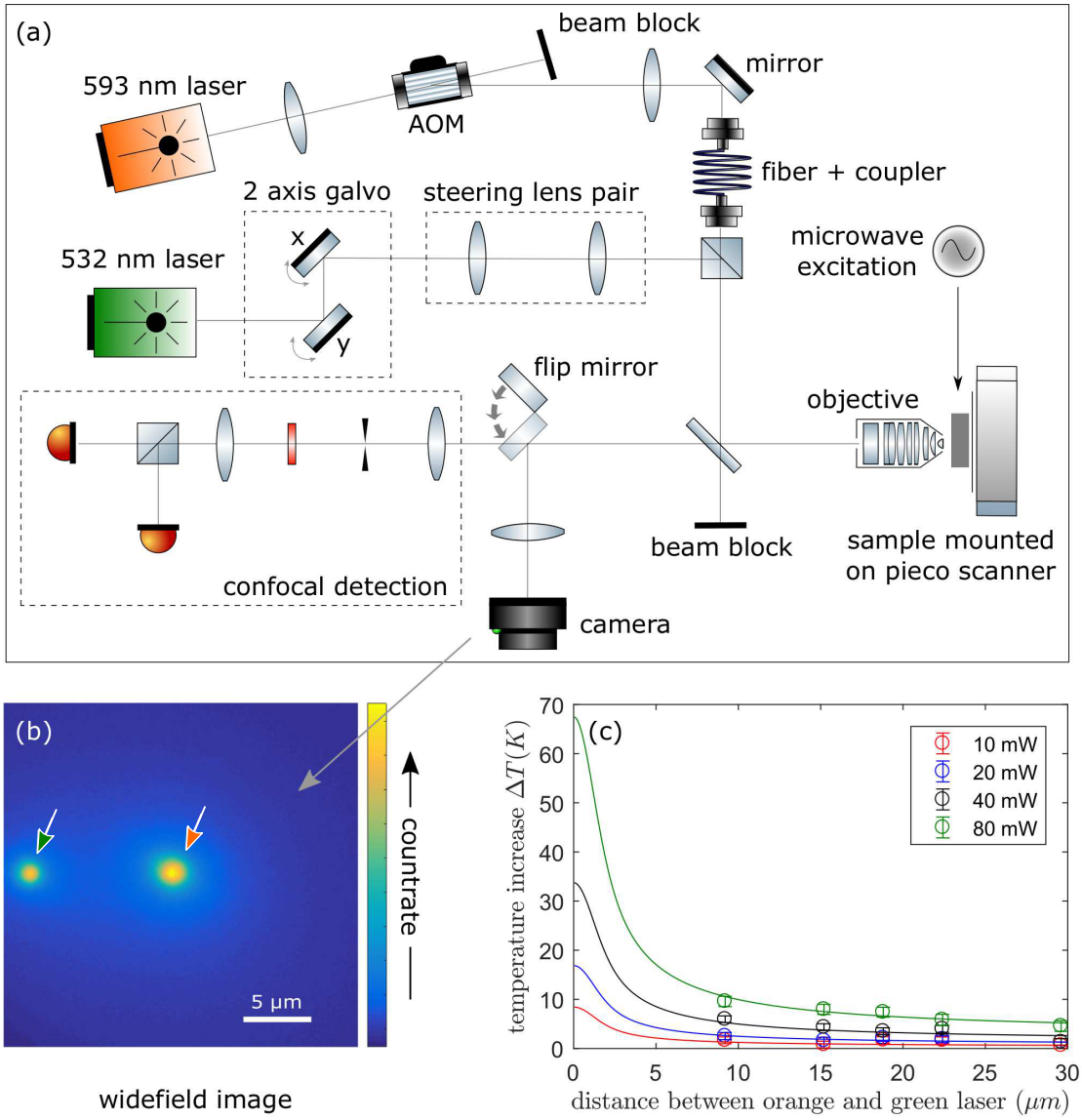

Figure 5.8. Influence of laser irradiation during nano thermometry (a): Experimental setup used to probe the influence of laser heating. The setup itself is a slide modification of the typical used one, adding a second green laser that position can be controlled in the focal plane of the objective via a 2-axis galvo system in combination with 2 steering lenses. **(b):** Wide-field image showing the two confocal spots of the heat generating green laser (green arrow) and the orange laser (orange arrow) for temperature probing. **(c):** Temperature increase dependent on different laser powers from $10\,\mathrm{mW}$ (red) to $80\,\mathrm{mW}$ (green) and the corresponding fit result using equation (5.4).

Influence of the external magnetic field on nano thermometry

The nitrogen vacancy center is sensitive to magnetic fields, and the shift of the EPR lines is depending on the orientation of the NV spin quantization axis to the applied magnetic field [13]. When changing the angle between the NV axis and the external magnetic field, this will lead to a shift of the two ODMR transitions in the same or opposite direction. Although no artificial external magnetic field is applied, the earth magnetic field around half a Gauss is always present. Considering that NDs can tumble inside live cells, slow angular changes are expectable [122] and may lead to an artificial temperature drift.
One can numerically solve the NV spin Hamiltonian under the influence of an external static magnetic field B_0 (see figure 5.9(a)) for the most prominent angular alignments ($\theta = 0, \pi/2$ and $\varphi = 0, \pi/2$). Figure 5.9(b) and (c) show the response of the NV spin transitions for an external field of 10 G, when varying the polar angle θ. The plots also include the position of the transitions without and with an additional strain induced zero field splitting E around 5 MHz, which was aligned along the x-axis of the NV^- reference frame. As in case of strain the position of the transitions is also dependent on the azimuthal angle φ (see equation (3.30)), both conditions are plotted. For B_0 being in the equator of the NV reference frame, the splitting between the two transitions is minimal, as if the magnet field would hardly be present. The smaller the angle θ, the more the splitting between the two resonances enlarges. Interestingly, in first situation the center of mass between the two transitions do not meet at the zero field splitting D. The situation is similar for $E = 5$ MHz. A closer analysis on the central shift and the opening of the splitting for fixed angles and varying B_0 is shown in figure 5.9 (d) an (e), respectively. For simplification only the solution for $E = 5$ MHz is plotted. The central shift of the EPR lines is around 5 kHz for the most unfavorable polar angle $\theta = \pi/2$ (see figure 5.9 (e)). This correspond to a temperature shift of $\approx$10 mK for $B_0 < 1$ G. The maximum opening of the EPR transitions changes around 1.5 MHz (see Figure 5.9 (d)). As the opening is naturally canceled with the term $f_1 - f_2$ by the used "two point"-method (see equation (5.6)), it will have an minor effect on temperature measurement. Considering that the NDs used in current study contain hundreds of NV centers in clusters of several NVs containing four possible orientations, the

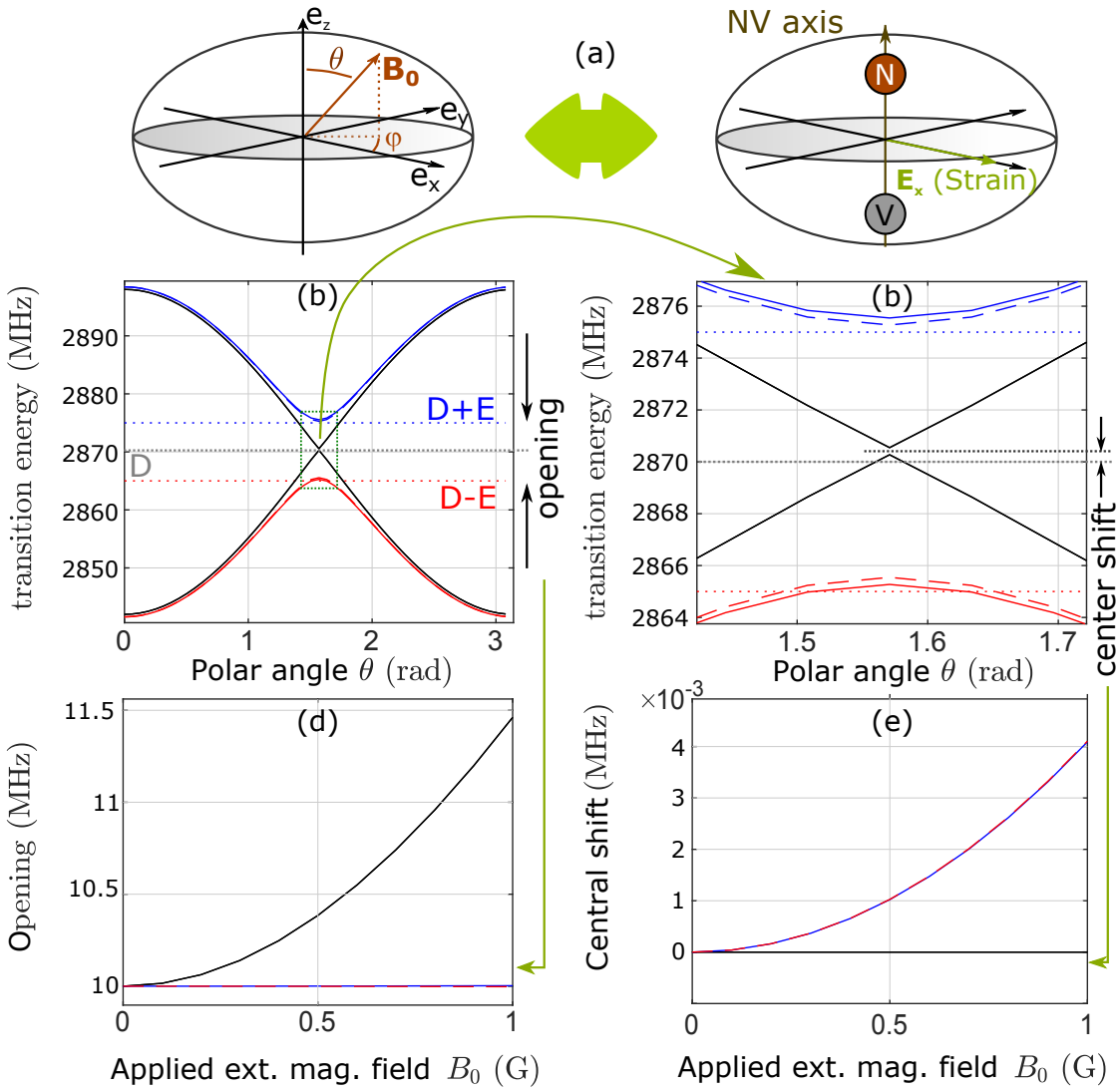

Figure 5.9. Influence of magnetic field on NV transition. (a): Sketch showing the magnetic field (left) and the NV reference frame in spherical coordinates (right). (b) Simulation showing the NV spin transitions for $E = 5\,\mathrm{MHz}$ in red and blue depending on the polar angle θ for a static field of $10\,\mathrm{G}$. The smaller θ the more the gap between the two transitions opens. The black lines indicate their behavior for $E = 0\,\mathrm{MHz}$. Horizontal lines indicate the corresponding transition energies for no magnetic field present. **(c)** Zoom into the inner region of **(b):** Solid lines stand for an azimuthal angle $\varphi = 0$, dashed lines for $\varphi = \pi/2$. One also can see that the transitions are shifted simultaneously upwards for an polar angle of $\pi/2$ if the magnetic field is present. **(d):** Opening of the transitions gap for different θ angles. (black): $\theta = 0, \varphi = 0, \pi/2$,(blue): $\theta = \pi/2, \varphi = 0$,(red): $\theta = \pi/2, \varphi = \pi/2$. **(e):** Simultaneous shift of both transitions into the same direction. (black): $\theta = 0, \varphi = 0, \pi/2$,(blue): $\theta = \pi/2, \varphi = 0$,(red): $\theta = \pi/2, \varphi = \pi/2$.

shift in the same direction will be further reduced. Therefore, the error introduced by magnetic fields is neglected.

Influence of microwave heating

To measure the temperature with NV, its spin transitions have to be excited *via* microwave irradiation. As water has a reasonable absorption cross-section at 2.87 GHz [30], significant heating is expected, if to much microwave power is used. To check the influence of microwave heating another microwave source (SMIQ2) has been added that is driven off resonant to the NV spin transition at 3 GHz. The influence of microwave irradiation was then compared with cell culture medium and air, by replacing the solvent in the used chamber system (see Figure 5.10(a) and section 5, page 105). The output of SMIQ2 was modulated between on and off. Figure 5.10(d) shows an example if 1 W were applied *via* SMIQ2. The temperature measured locally by NV thermometry was similar to the temperature measured by an external thermistor that was placed in the cell medium. The local temperature, increase induced by SMIQ2, has been extracted and plotted in Figure 5.10(c). A linear regression reveals the power depended temperature increase in case of cell-medium to be $(5.8 \pm 0.5)\,\mathrm{K/W}$, and for just air $(3.6 \pm 0.7)\,\mathrm{K/W}$, respectively. Typically cell experiments are performed with microwave powers around 80 mW. This corresponds to a temperature increase of 0.5 K. Indeed, a similar but lower increase in temperature was observed at the beginning of each cellular experiment (see section 5.15, page 138). The question arises if this could be treated as a global temperature increase, as already indicated by the measured temperature of the thermistor, and therefore could be considered as offset. To this end the heat dissipated by the microwave was calculated:
If 1 W microwave power would be fully absorbed by the solution a temperature increase, caused by the used omega coil, would be around 3000 K, if the energy is dissipated in a volume of $0.16\,\mathrm{mm}^3$ (coil volume:$r = 500 \times 10^{-6}\,\mathrm{m}$, $h = 200 \times 10^{-6}\,\mathrm{m}$, using equation (2) in [12]). A temperature increase in the order of $\sim 10\,\mathrm{K}$ was measured. This lead to a relative absorption of the micro-structure around 3.3 per mile and a power density of $2\,\mathrm{MW\,m^{-3}}$, within the volume of the coil structure, with a typical microwave driving power around 80 mW. Calculating the

power dissipation within the volume of a cell results in 5 pW ($r = 10 \times 10^{-6}$ m, $h = 10 \times 10^{-6}$ m). Even if the cell exhibit a strong absorption, the extinction coefficient within the cell must be more then 6 orders of magnitude higher then the surrounding medium to see a local temperature increase of around 1 K. This seems to be unrealistic, as long as no special absorbers are introduced into the cell. Therefore the temperature increase induced by microwave absorption was treated as a simple offset, on a scale much larger as the cell volume. Therefore, in real temperature measurement one waited, until the system reached an plateau before starting the desired experiment. In a second step the upper limit for the change in temperature by rapidly increasing the ionic strength of the surrounding medium was estimated from 0 M to 2 M. First the absorption of the sample chamber was measured as a function of ionic strength of the given solution, using a spectrum analyzer (MS710A, Anritzsu) for 3 GHz and the frequency range from 2.84 GHz to 2.91 GHz (NV band). Therefore the difference between input and output port sketched in figure 5.11(a) was calculated, also considering reflection on the input by impedance mismatching (detailed schema and used solutions see appendix A.1.2). Thereby the blue colored data set in figure 5.11(b) represents the resulting relative absorption of the chamber at 3 GHz, and red the average of the NV band. With increasing ionic strength also the absorption of the chamber increases and is higher compared to the reference value for just air, indicated by the horizontal lines. The used cell culture media had an ionic strength of 150 mM, the ratio of absorption between air and this specific setting is 1.8 for 3 GHz and 1.2 for the NV band. This means that the presented analysis above with two microwaves sources at the same time gives an upper limit for the expectable temperature increase, and explains why in real experiments the measured temperature increase at the beginning of the experiment is lower. Furthermore the temperature increase for different ionic strengths is directly measured locally with one microwave source whereas 0 M is set as the reference point (figure 5.11(c)). The temperature increased by around 1 K, if the ionic strength was ramped up from zero to one molar concentration. Furthermore the measured dependence reassembles a similar behavior like already seen in figure 5.11(b), suggesting that NV temperature readout itself is not affect by the environment. More like, the microwave absorption increases with rising ionic strength. From the analysis about this also allows to conclude that very

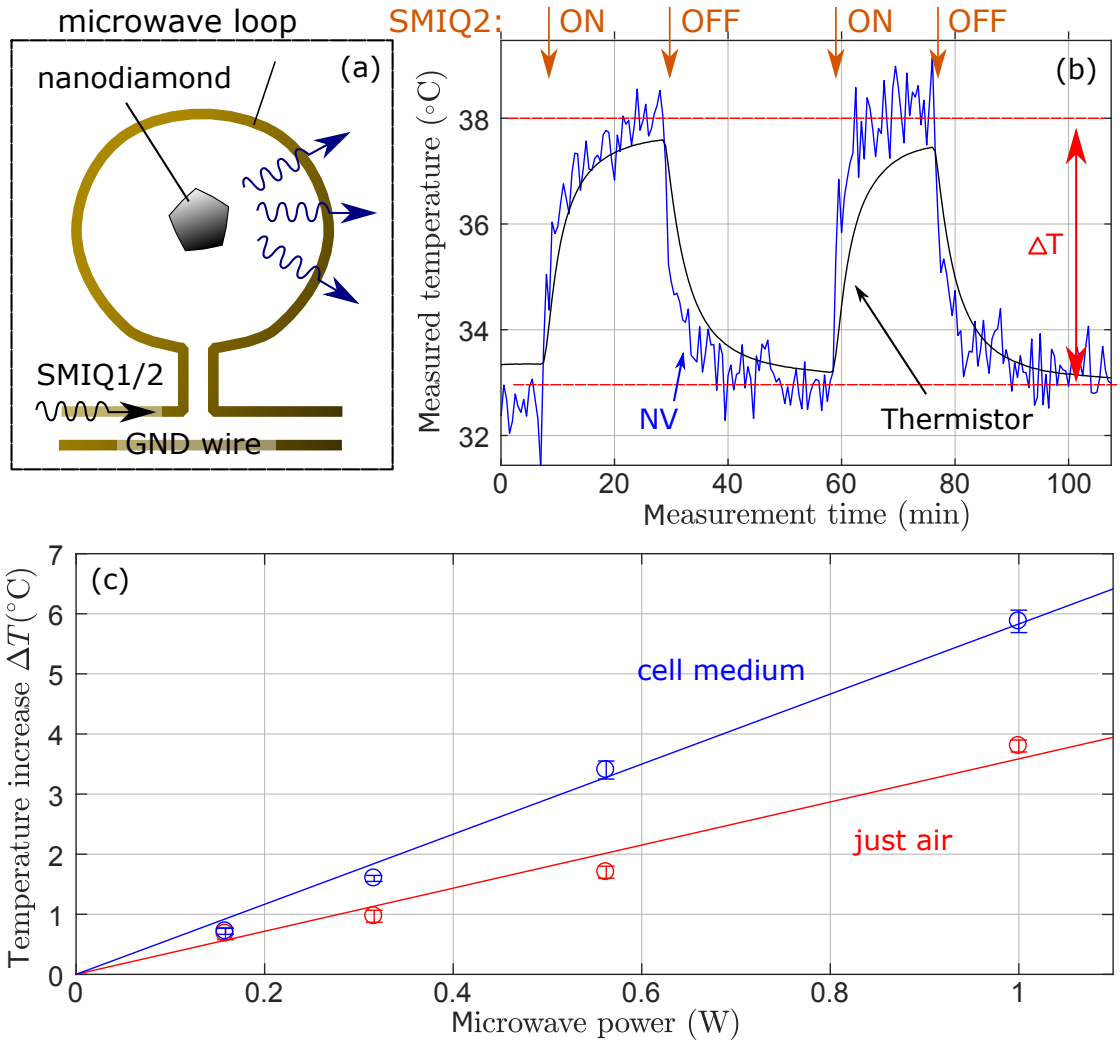

Figure 5.10. Influence of microwave irradiation on temperature measurement. **(a):** Microwave coil used to excite the NVs inside the ND with SMIQ1. SMIQ2 was used to generate heat. **(b):** Temperature change ΔT, when applying $1\,\mathrm{W}$ at $3\,\mathrm{GHz}$ using SMIQ2, whereas (blue) indicates the measured temperature via NV and (black) the control thermistor placed in the medium. **(c):** Relative temperature increase measured with NV for just air (red) and cell medium (blue). Also the linear regressions for each case has been plotted.

local and even very drastic changes in the ionic strength within the cell will not be observable. The composition of the used solutions can be found in appendix A.1.3.

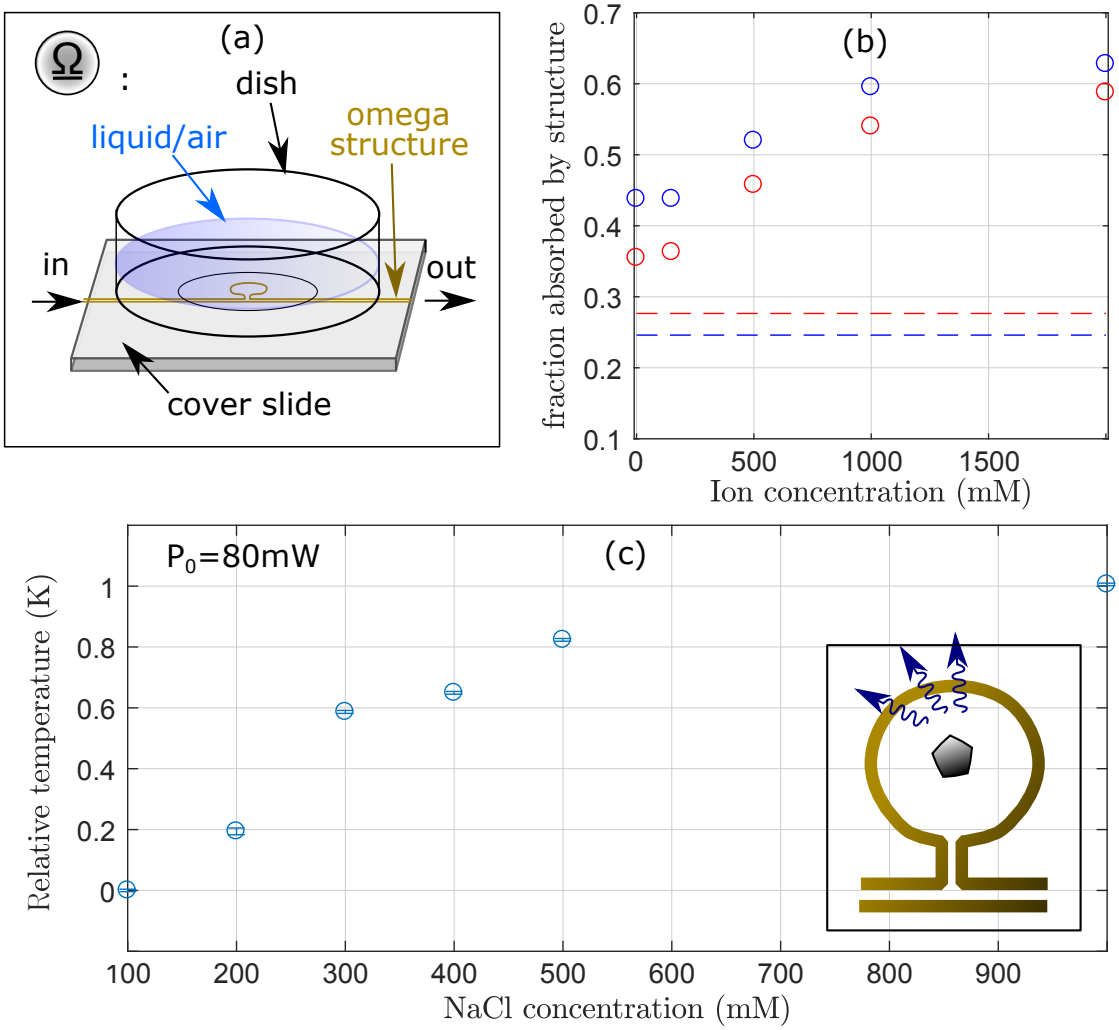

Figure 5.11. Influence of microwave irradiation on temperature measurement. **(a):** Temperature change when applying a second off resonant microwave to the sample at 3 GHz with 1 W power. **(b):** Relative absorption of microwave structure using a spectrum analyzer. (blue): 3 GHz, (red): NV resonance band. The absorption had been normalized to the bare structure exposed to air. One can see that the relative absorption is increasing when increasing the ion concentration on top of the microstructure. **(c):** Relative change in temperature, depending on the ionic strength of the solutions measured with NV.

Influence of pH on cw nano thermometry

When a ND enters a cell *via* endocytosis, the pH of it's local environment undergo several changes: The cell medium has as a pH of 7.4. Endosomes have an pH up to $\sim$ 4.8. After escaping an endosome, a ND ends up in the cytrosol with pH $\sim$ 7.4. Thereby one may ask, how robust the used "two point"-method is against changes in pH. Therefore several NDs have been analyzed, fixed on a cover-glass

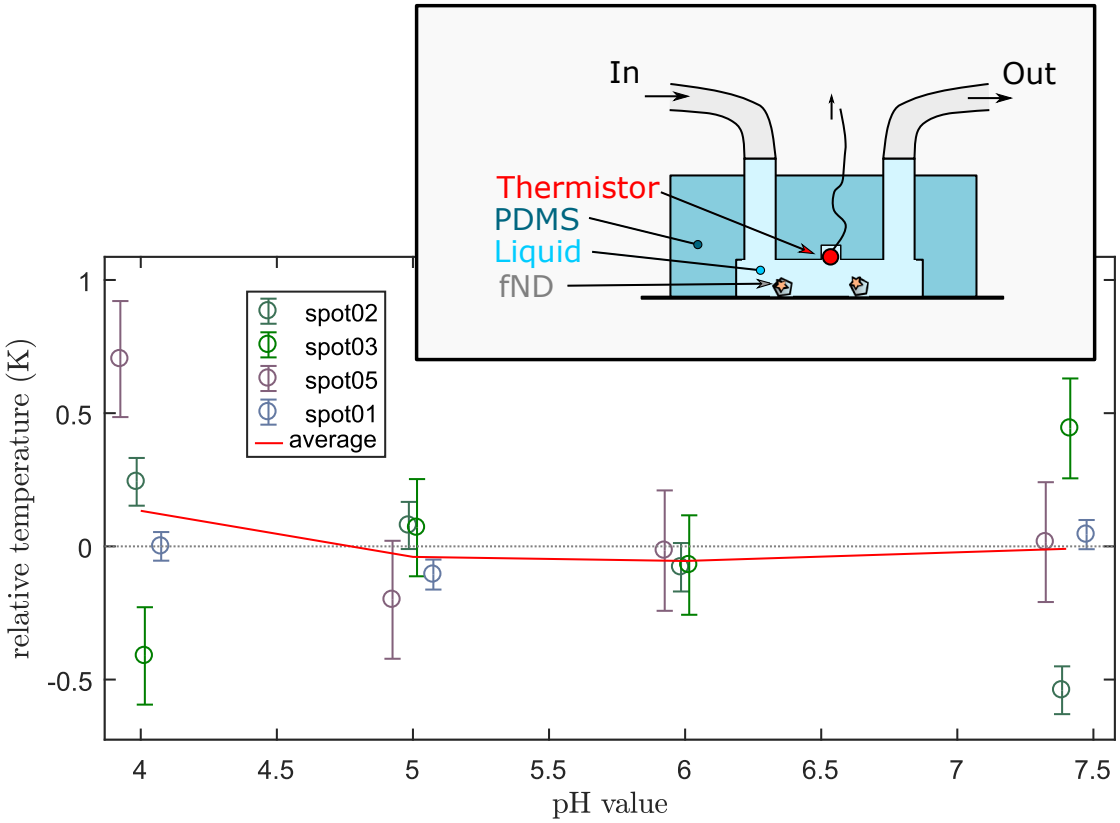

Figure 5.12. Influence of pH on cw nano thermometry: Temperature read out for different spots with "two point"-method (cycles) and their average (red line). The upper insert shows a sketch of the used sample chamber.

in a microfluidic device (see sketch in figure 5.12). In addition, the chamber also hosted a thermistor, which was in contact with solution to monitor changes in the environmental temperature. Especially as the overall run time of the experiment exceeded 5 h. To introduce NDs into the chamber system, particles where suspended in a 50 mM HEPES buffer pH 7.4. After injection and waiting until the particles

were adsorbed on the cover-glass, the chamber was flushed with a special buffer, including a mixture of Citric Acid and Sodium Phosphate. The used buffer system can be tuned in a wide pH range by keeping the overall ionic strength constant [123]. As shown in figure 5.12, individual particles seemed to show a dependence on pH that is not uniform or has a general tendency. Taking the average for all spots as an estimate (see figure 5.12, red line), the maximum expectable error in temperature reading is below 0.2 K for a unfavorable change in pH. From a different perspective, to be on the save side, one has to wait until NDs have arrived in the cytrosol. Therefore one typically waits 24 h after incubation with nanodiamonds before starting a temperature sensing experiment (see appendix A.3) .

5.3.2. The monitor function r

As stated in theory, the crystal field constant D of the NV spin is temperature dependent [34, 4, 137, 105], showing a shift $^{\delta D}/_{\delta T}$ of the ESR lines around $\sim 70\,\mathrm{kHz\,K^{-1}}$ under ambient conditions. To monitor this shift, the function r has been used:

$$r = \frac{S_{f_1} - S_{f_2}}{S_{f_1} + S_{f_2}} \tag{5.6}$$

Where S_{f_1} and S_{f_2} are the fluorescence level positioned at the tail of the left and right wings of left and right ODMR transition. To derive an expression for r, the signal S of the individual EPR transitions are modeled by a single Lorentzian line shape:

$$S(\Delta f) = 1 - c \cdot \gamma_L \cdot \frac{\gamma_L}{4 \cdot \Delta f^2 + \gamma_L^2} \tag{5.7}$$

With c as the ODMR contrast and γ_L the Lorentzian FWHM of the resonance. In typical experiments the chosen frequencies were set to the most sensitive points $S(\pm\Delta f)$ on the right and the left flank of the acquired ODMR spectrum (see figure 5.15(b)). This is for a Lorentzian line profile the case, when the second derivative is zero $S''(\pm\Delta f) = 0$: Using the first order Taylor expansion for S_{f_1} and S_{f_2}, one

obtains

$$\begin{aligned} S_{f_1}(\Delta T) &= (1-\frac{3}{4}c)\cdot\frac{N}{2} - \frac{3\cdot\sqrt{3}}{4}\cdot\frac{c}{\gamma_L}\cdot\frac{N}{2}\cdot {}^{\delta D}/_{\delta T}\Delta T, \\ S_{f_2}(\Delta T) &= (1-\frac{3}{4}c)\cdot\frac{N}{2} + \frac{3\cdot\sqrt{3}}{4}\cdot\frac{c}{\gamma_L}\cdot\frac{N}{2}\cdot {}^{\delta D}/_{\delta T}\Delta T. \end{aligned} \tag{5.8}$$

Whereas the acquired photons N are equally split on the fluorescence emitted at f_1 and f_2. Inserting equation (5.8) into (5.6) leads to the temperature dependent monitor function r:

$$r(\Delta T, c, \gamma_L) = -\frac{3\sqrt{3}\cdot c}{(4-3c)\gamma_L}\cdot({}^{\delta D}/_{\delta T}\cdot\Delta T) \tag{5.9}$$

Equation (5.9) allow to calculate the change of Temperature ΔT *via* r, if the other parameters are known:

$$\Delta T = -\frac{(4-3c)\gamma_L}{3\sqrt{3}\cdot c\cdot {}^{\delta D}/_{\delta T}}\cdot r \tag{5.10}$$

The monitor functions r: linear approximation versus exact expression

As the monitor function r is derived by introducing a Taylor expansion, one may ask on which scales this approximation keeps valid, because leaving the linear range can also have an impact on the sensitivity reachable during temperature readout. One can also calculate an exact solution of r, namely r_a. To this end S_{f_1} and S_{f_2} have to be replaced by $S(\Delta\omega_- + {}^{\delta D}/_{\delta T}\Delta T)$ and $S(\Delta\omega_+ + {}^{\delta D}/_{\delta T}\Delta T)$:

$$r_a(\Delta T, \gamma_L, c) = -\frac{3\sqrt{3}\cdot c\cdot\gamma_L^3}{(4-3c)\cdot\gamma_L^4 + 3(4-3c)\gamma_L^2({}^{\delta D}/_{\delta T}\Delta T)^2 + 36({}^{\delta D}/_{\delta T}\Delta T)^4}\cdot {}^{\delta D}/_{\delta T}\Delta T \tag{5.11}$$

By substituting ${}^{\delta D}/_{\delta T}\Delta T$ with $\gamma_L\cdot\tau_\gamma$, where τ_γ is a scaling factor describing a relative displacement in scales of γ_L, equation (5.11) becomes

$$r_a(\Delta T, \gamma_L, c) = -\frac{3\sqrt{3}\cdot c\cdot\gamma_L^3}{(4-3c)\cdot\gamma_L^4 + 3(4-3c)\gamma_L^4\cdot\tau_\gamma^2 + 36\gamma_L^4\cdot\tau^4}\cdot {}^{\delta D}/_{\delta T}\Delta T. \tag{5.12}$$

Equation (5.12) is converging into equation (5.9) for small shifts versus the linewidth

($\tau_\gamma \ll 1$). Now the relative change of the monitor function r to its exact form is calculated:

$$\frac{\Delta r}{r} = \frac{r - r_a}{r} \tag{5.13}$$

With a line width of $\approx 8\,\mathrm{MHz}$ and a temperature caused shift of $0.8\,\mathrm{MHz}$ ($0.1\gamma_L \approx 10\,\mathrm{K}$ shift), the sensitivity will only be altered by $3\,\%$. In the range used ($\sim 10\,\mathrm{K}$) therefore no significant loss in sensitivity or non linearities are expectable.

The monitor functions r: influence of changing contrast and linewidth

As linewidth and contrast may change during a running experiment, the error introduced has to be estimated. The monitor function r can also be written as

$$r(\Delta T, c, \gamma_L) = -\frac{3\sqrt{3}\cdot c}{(4-3c)\gamma_L} \cdot ({}^{\delta D}/_{\delta T} \cdot \Delta T + \Delta f). \tag{5.14}$$

In equation (5.14), ${}^{\delta D}/_{\delta T} \cdot \Delta T$ has been replaced by ${}^{\delta D}/_{\delta T} \cdot \Delta T + \Delta f$ accounting for a little offset Δf from the optimum set point $S_{f_1} = S_{f_2}$. To calculate the influence of changes in contrast c by δc, one calculates using equation (5.14)

$$r(0, c + \delta c, \gamma_L) = r(\Delta T, c, \gamma_L). \tag{5.15}$$

And resolve equation (5.15) to ΔT, which gives the error in temperature reading $\Delta T_{error}(\delta c)$:

$$\Delta T_{\mathrm{err}}(\delta c) = \frac{4\delta c \Delta f}{c(4 - 3(c + \delta c)) \cdot {}^{\delta D}/_{\delta T}} \tag{5.16}$$

The very same can be done for finding the error introduced by changing the linewidth γ_L by $\delta\gamma_L$:

$$\Delta T_{\mathrm{err}}(\delta\gamma_L) = -\frac{\delta\gamma_L \Delta f}{{}^{\delta D}/_{\delta T}(\gamma_L + \delta\gamma_L)} \tag{5.17}$$

For variations of some percent both equations reduce for its absolute values to

$$\begin{aligned} \Delta T_{\mathrm{err}} &= \Delta f \cdot {}^{\delta D}/_{\delta T}{}^{-1} \cdot \Delta_{\mathrm{err}} \\ &= \frac{10[mK]}{[K][\%]}. \end{aligned} \tag{5.18}$$

Thereby equations (5.18) and (5.17) are expressed in terms of relative changes $\Delta_{\text{err}} = \frac{\delta c}{c}$ or $\Delta_{\text{err}} = \frac{\delta \gamma_L}{\gamma_L}$, respectively.
Each percent change in contrast and linewidth lead for each centigrade away from the optimum set point to an additional error of 10 mK. Whereas, if contrast and linewidth change in the same direction with the same amount, their shift will compensate each other.
To mimic this behaviour, the laser intensity used to excite a small fixed ND cluster was varied (see figure 5.13a) during reading out a fine sweeped cwODMR spectrum. As contrast and linewidth of a cwODMR spectrum can also be a function of laser power excitation [52].Then the measured linewidth and contrast for left and right transitions have been extracted, and its relative change calculated (figure 5.13(b)). In a second step the experiment has been repeated with the "two point"-approach, resulting in the the monitor function r shown in figure 5.13(c) and the corresponding temperature read out. Therefore equation (5.10) has been used with the averaging contrast ($c = 7.3\,\%$) and linewidth ($\gamma_L = 13.3\,\text{MHz}$) of left and right transition. ${}^{\delta D}/_{\delta T}$ has been set to $70\,\text{kHz}\,\text{K}^{-1}$. The errors are plotted in figure 5.13(d). As one can see, the calculated overall error ΔT_{err} is quite small in comparison to the calculated change in temperature shown in figure 5.13(c). The reason for this lies within the assumption of having equal linewidth and contrast on both left and right transition. If this is not the case, already a small offset can occur in the beginning that changes different to the presented calculations. To ensure that overall laser excitation did not change during an experiment, the laser has been stabilized with a PID-loop. In addition, the frequency dependent microwave output of the amplifier has been corrected by applying an amplitude correction for a certain frequency of the AWG.

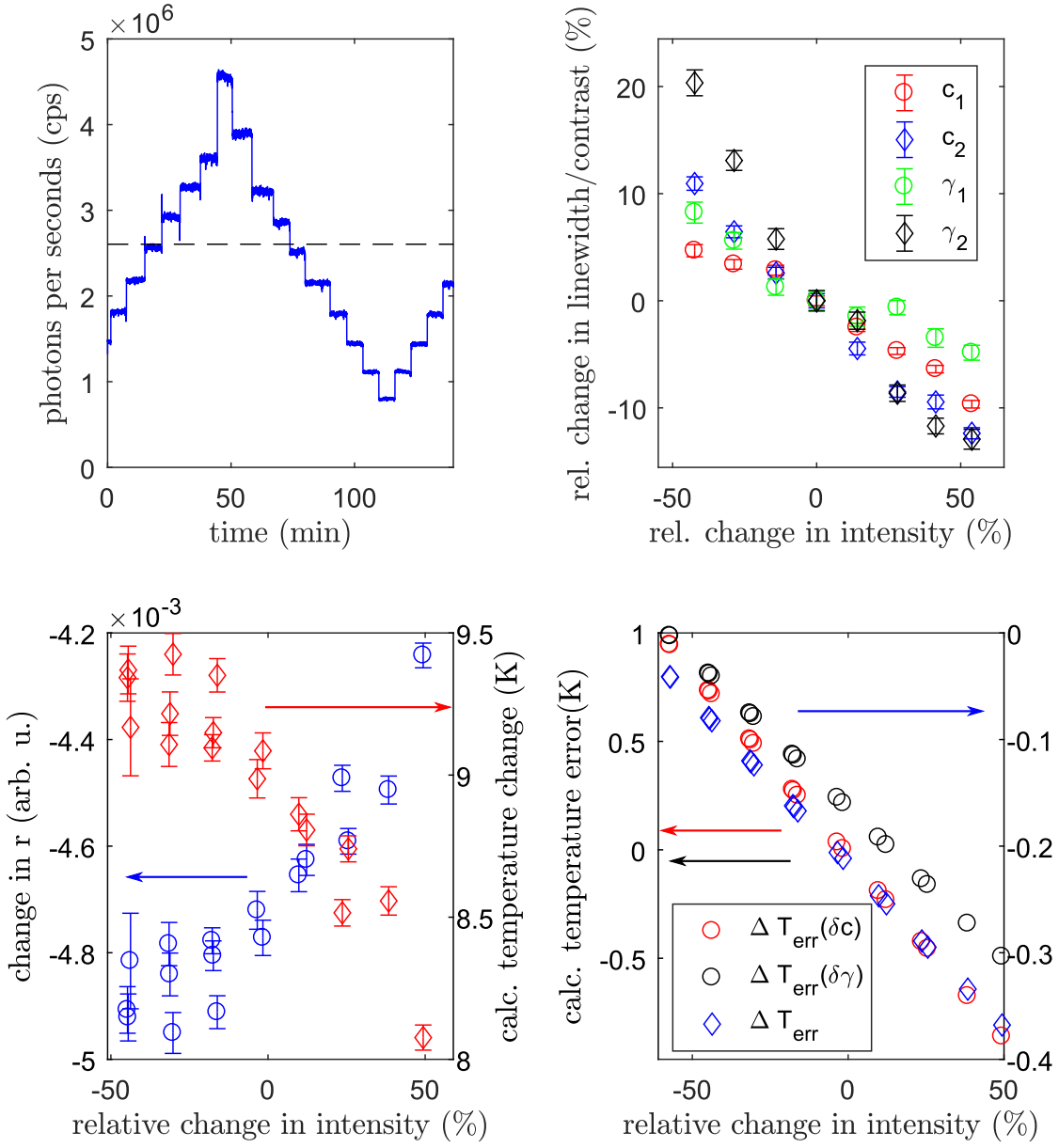

Figure 5.13. Monitor function r depending on contrast and linewidth. (a): measured photon flux of a fixed ND cluster when modulating the excitation intensity. The dashed line indicates the reference level to calculate the relative change of intensity in the following graphs. **(b):** Relative change of linewidth γ and contrast c depending on the relative change of collected photons. Index one and two stand for fitting the data set with two Lorentzian functions. **(c):** measured monitor function r (blue) and calculated temperature (red). **(d):** Calculated error for the individual changes of contrast(red), linewidth (black) and the corresponding overall error (blue).

The monitor functions r: background and signal fluctuations

In the following the effect of changes in the fluorescence level due to changes in signal and background on the monitor function r has been analyzed. Therefore, the monitor function was modified:

$$r' = \frac{g_1(\Delta T, t) - g_2(\Delta T, t)}{g_1(\Delta T, t) + g_2(\Delta T, t)} \tag{5.19}$$

To account for a background the photon flux Θ_{BG} and $\alpha(t)$ that shall describe changes in the detected photon signal $\Theta_N (= N/t)$ during the time interval t is introduced:

$$g_i(\Delta T, t) = \alpha(t) \cdot S_{f_i}(\Delta T, t) + \Theta_{\mathrm{BG}} \cdot t \tag{5.20}$$

The monitor function can be rewritten:

$$r' = -\frac{3\sqrt{3}c}{\gamma_L} \cdot \frac{\alpha(t)\Theta_N}{8 \cdot \Theta_{BG} + (4 - 3c) \cdot \alpha(t)\Theta_N} \cdot {}^{\delta D}/_{\delta T} \cdot \Delta T \tag{5.21}$$

By replace Θ_N with $\tau \cdot \Theta_{\mathrm{BG}}$, equation (5.21) can also be written as

$$r' = -\frac{3\sqrt{3}c}{\gamma_L} \frac{\alpha(t)\tau}{8 + (4 - 3c) \cdot \alpha(t)\tau} {}^{\delta D}/_{\delta T} \cdot \Delta T. \tag{5.22}$$

Whereas τ is the relative signal strength versus background. The term $\alpha \cdot \tau$ can also be understand as the signal to background ratio (SBR). To calculate the relative error of r' one use $\Theta_N = \tau \cdot \Theta_{\mathrm{BG}}$ after partial differentiation:

$$\begin{aligned}
\Delta r' &= \frac{\delta r'}{\delta \Theta_{\mathrm{BG}}} \Delta \Theta_{\mathrm{BG}} \\
&= 8 \frac{3\sqrt{3}c}{\gamma_L} \frac{\alpha \Theta_N}{(8 \cdot \Theta_{\mathrm{BG}} + (4 - 3c) \cdot \alpha \Theta_N)^2} {}^{\delta D}/_{\delta T} \cdot \Delta T \Delta \Theta_{\mathrm{BG}} \\
&= \frac{8}{8 + (4 - 3c) \cdot \alpha(t) \cdot \tau} \cdot \frac{1}{\Theta_{\mathrm{BG}}} \left(\frac{3\sqrt{3}c}{\gamma_L} \cdot \frac{\alpha\tau}{8 + (4 - 3c) \cdot \alpha\tau} \cdot {}^{\delta D}/_{\delta T} \cdot \Delta T \right) \Delta \Theta_{\mathrm{BG}}, \\
\frac{\Delta r'}{r'} &= \frac{8}{8 + (4 - 3c) \cdot \alpha(t) \cdot \tau} \cdot \frac{\Delta \Theta_{\mathrm{BG}}}{\Theta_{\mathrm{BG}}}
\end{aligned} \tag{5.23}$$

With a SBR around thousand, the relative error accumulated on the monitor function r is on the order of per mill, even for changes of 100 % in background. In fact, fluorescence change during temperature measurement mainly comes from the ND itself, rather than any other background fluorescence. In this sense, only the movement of a ND spot (translational and rotational motion) may affect the measurement result. Similarly one can calculated the error introduced by fluorescence fluctuation:

$$\begin{aligned}\Delta r' &= \frac{\delta r}{\delta \alpha}\Delta\alpha \\ &= -8\frac{3\sqrt{3}c}{\gamma_L}\frac{\tau}{(8+(4-3c)\cdot\alpha\tau)^2\cdot\alpha\tau}\delta D/\delta T\Delta T\Delta\alpha \\ &= \frac{8}{8+(4-3c)\cdot\alpha\tau}r'\frac{\Delta\alpha}{\alpha}, \\ \frac{\Delta r'}{r'} &= \frac{8}{8+(4-3c)\cdot\alpha\tau}\frac{\Delta\alpha}{\alpha}.\end{aligned} \tag{5.24}$$

With a SBR around thousand and a fluctuation around 5 % (controlled by 3D particle tracking), the calculated error of the monitor function is on order of $1e^{-5}$, and therefore has been neglected.

The monitor functions r: reducing thr error by integral correction

As discussed in section 5.3.2, the error in temperature reading increases depending on the offset to the optimum set point where the fluorescence level S_{f_1} equals S_{f_2}. If temperature increases or decreases, one will inevitably drift from the original position, with the consequence, that the measurement error will increase. An easy way to tackle this problem, is to shift f_1 and f_2 and thereby equalize S_{f_1} and S_{f_2} again. Technically this can be done by an active feedback loop, using the difference in f_1 and f_2 as the direct error signal, to compute the desired shift in f_1 and f_2. In the performed experiments an software based integral-correction (I-correction) has been implemented. The temperature readout can be formulated as

$$\Delta T(t) = -\frac{(4-3c)\gamma_L}{3\sqrt{3}\cdot c\cdot {}^{\delta D}/_{\delta T}}\cdot r_I(t) + \frac{\Delta f_I(t)}{{}^{\delta D}/_{\delta T}}. \tag{5.25}$$

Whereas $f_I(t)$ is the the correction of f_1 and f_2, respectively, and r_I the monitor function, when applying the I-correction.

The monitor function r: a shot noise limited measurement

Up to now all introduced error sources are more or less suppressible by experimental control, but there is also a fundamental limit for the sensitivity of a measurement, introduced by the photon statistics of the fluorescence signal collected for readout. To estimate the sensitivity $\delta T_{\min}$ of a given experiment the noise-power equivalent was calculated:

$$\delta T_{\min} = \frac{\sigma_s}{{}^{dS}/_{d\Delta T}} \tag{5.26}$$

Where σ_s is the standard deviation of a fluorescence signal (N photons per detection interval) and ${}^{dS}/_{d\Delta T}$ is the first derivative of $S_{f_{1/2}}$. $T_{\min}$ reads after inserting equation (5.8) into (5.26):

$$\delta T_{\min} = \frac{4}{3 \cdot \sqrt{3}} \cdot \frac{1}{\sqrt{N}} \cdot \frac{\gamma_L}{c} \cdot {}^{\delta D}/_{\delta T}{}^{-1} \tag{5.27}$$

Considering the used nanodiamonds (see section 5.2.1) have a minimum linewidth of 8 MHz, a maximum contrast around 5 % , and a photon count rate $S_{f_1} + S_{f_2}$ that can reach ~ 5 Mcps, a sensitivity of $\delta T_{min} \approx 0.7\,\mathrm{K}\sqrt{\mathrm{Hz}^{-1}}$ can be achieved. For a 30 s integration time, the typical time interval used, finally a sensitivity (uncertainty) ≈ 0.15 K is reachable.

As already mentioned the movement of NDs inside the cell can also cause intensity fluctuations. These do not add to σ_s, if one can ensure that the intensity fluctuations, originated from movement of the particle, happen on a longer time scale than the actual read out of S_{f_1} and S_{f_2}. To ensure the latter, the readout was alternated in the millisecond range between the two frequencies f_1 and f_2. This led to a correlated change between the two fluorescent levels, as can be seen in figure 5.14: The example shows heavy fluctuations as a function time (figure 5.14(a)). If one plots the change from time step to step indexed by t_k and t_{k+1}, one gets a huge variation of 34k counts (figure 5.14(b)), but the difference between the two traces with the same time step t_k is much smaller (2k counts, see figure 5.14(c)) and obeys the expected shot noise of 2k counts. In this sense using the very same α in equation (5.20) for the signal measured on both frequencies is also justified.

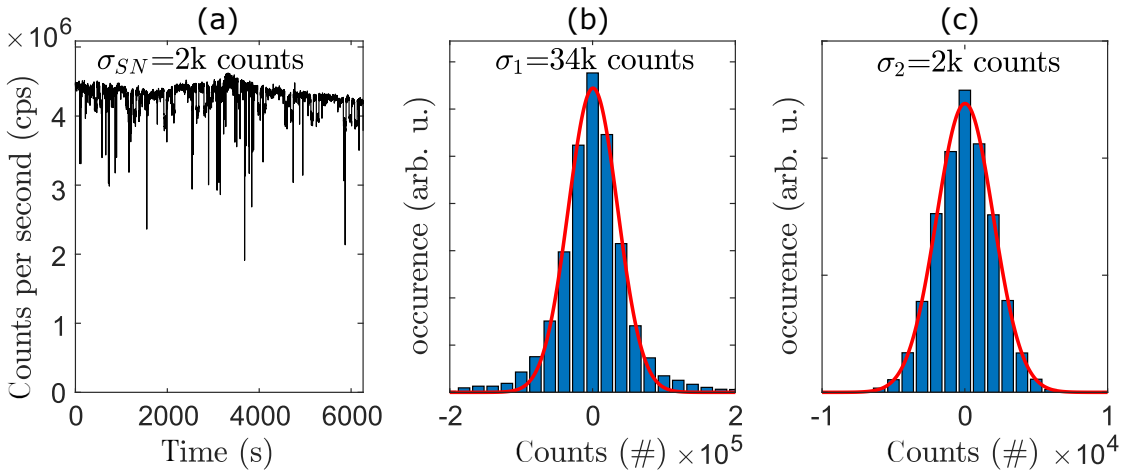

Figure 5.14. The monitor function r is shot noise limited. (a) shows the sum of measured intensities at frequency f_1 and f_2 during temperature read out. σ_{SN} gives the expected shot noise. **(b):** Histogram of the fluctuations within the trace, by plotting the difference between $S(t_k) = S_{f_1}(t_k) + S_{f_2}(t_k)$ and $S(t_{k+1}) = S_{f_1}(t_{k+1}) + S_{f_2}(t_{k+1})$. **(c):** Histogram of plotting the difference between $S_{f_1}(t_k)$ and $S_{f_2}(t_k)$. Red lines in (b) and (c) are Gaussian fits, the corresponding standard deviations $\sigma_{1,2}$ are plotted as well.

The monitor function r: overall error in cw thermometry

The overall error of an individual measurement is

$$\Delta T_{\mathrm{err}} = \sqrt{(\Delta T_{\mathrm{SN}})^2 + (\Delta T_{\delta c \delta \gamma_L})^2 + (\Delta T_{\mathrm{fit}})^2 + (\Delta T_{\delta \mathrm{BG}})^2 + (\Delta T_{\delta \alpha})^2 + (\Delta T_{B_0})^2} \tag{5.28}$$

ΔT_{SN} is the error instructed by shot noise and is calculated from the photon flux, and by measuring a fine sweep cwODMR before staring the actual stimulation experiment. The latter is also used to calculate $\Delta T_{\delta c \delta \gamma_L}$, the accumulative errors introduced by changes in contrast and linewidth. To calculate $\Delta T_{\delta c \delta \gamma_L}$ it was assumed, that if the detected photon emission from NVs change by $\sim 50\,\%$, contrast and linewidth change by $\sim 10\,\%$ (see figure 5.13(b)). ΔT_{fit} is the error accounting for the uncertainty, when determining the temperature change $\Delta T(r)$ from experimental data (see also the next section 5.3.3). $\Delta T_{\delta \mathrm{BG}}$ and $\Delta T_{\delta \alpha}$ are the errors introduced by variations in the background and count rate and ΔT_{B_0} is the error introduced by the tumbling of the nanodiamond. The latter three are neglected based on former analysis.

5.3.3. Protocol to measure temperature in cells with the "two point"-method

First, cells are incubated within a homemade dish (see section 5.1, page 106) with TPP modified NDs and the mitochondria are marked with "MitoTracker Green". The detailed procedure for the ND modification, incorporation of ND and cell preparation and stimulation with CCCP is shown in appendix A.4, A.3 and A.5, respectively.
To measure the temperature in cells with the the "two point"-method a calibration of the monitor function r has to be done for each individual measurement. In the following the protocol is discussed as visualized in figure 5.15: In a first step one co-localize the fluorescence of ND with stained mitochondria in a cell by fluorescence. Then ODMR is probed on a proper target. If the observed characteristics of the give target is satisfying the expectations (contrast in the range of 5 % or higher, linewidth around 8 MHz or lower, fluorescence is stable in average within 5 %) the temperature measurement is started. A temperature measurement itself is divided in five phases. Phase 1: In the beginning one waits around 10 min until the system is in thermal equilibrium, as there is a certain microwave heating expectable (see section 5.3.1). During that time the I-correction is already turned on (see page 134). Phase 2: Now the I-correction is turned off, and f_1 and f_2 are shifted simultaneously up and down in frequency to characterize the change of the monitor function versus a frequency shift. The extracted response allow to calculate the frequency shift induced by temperature via the monitor function. Then the I-correction is turned on again (Phase 3). After waiting for around 10 min, typically 20 µM CCCP is injected to induce mitochondrial stimulation (Phase 4). To ensure that CCCP addition has minimal influence on the temperature inside the chamber, the CCCP containing solution is pre-load in a flexible tube, placed within the incubator system. One end of the tube is directly within the petri dish. By applying small air pressure at the other end of the tube, CCCP is introduced into the cell culture dish. In a last step (phase 5) the temperature of the incubator is modulated to correlate the shift in frequency of the zero field splitting with the temperature in the cell culture medium that is monitored by a thermistor. Both, Phase 2 and Phase 5 are used to calculate the temperature shift $\Delta T(t)$ introducing the uncertainty

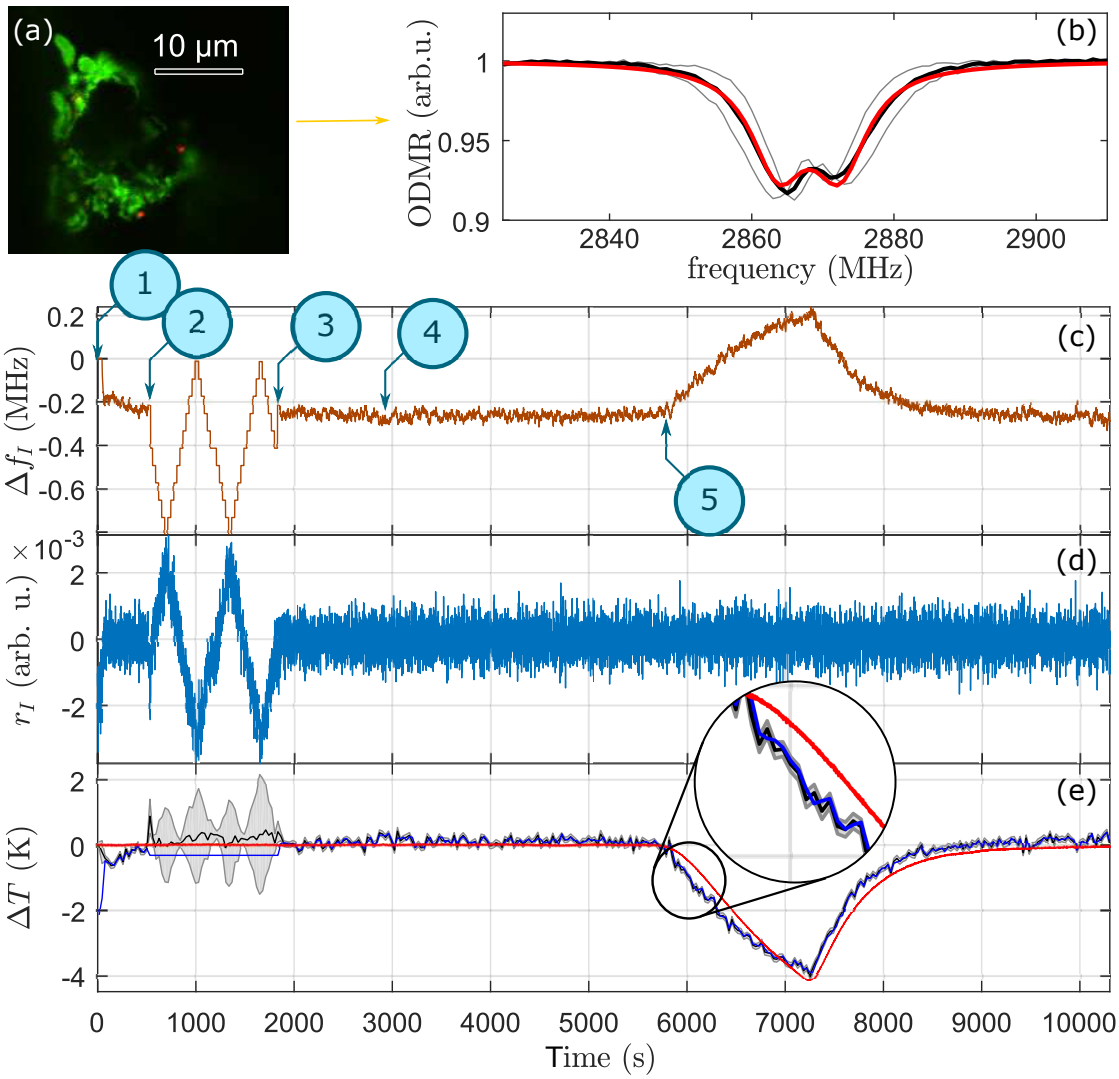

Figure 5.15. Protocol to perform a temperature measurement inside a living cell. (a): Confocal scan allowing to co-localize the fluorescence of ND (red color) with mitochondria (green color). **(b):** cwODMR of a proper NV decorated ND that could be co-localized with the stained mitochondria. The plot shows the backward and forward sweeps during frequency sweeping, the average of both (black) and double Lorentzian fit (red). **(c):** Relative frequency shift of f_1 and f_2. Also marked are the five phases during temperature sensing. See text for more explanation. **(d):** Corresponding monitor function r as described in equation (5.25). **(e):** Calculated temperature (black) with error (gray area), the corresponding temperature if only the I-correction had been used (blue), and the output of the control thermistor in the sample chamber (red).

ΔT_{fit}. Interestingly, during Phase 2 the error is huge. The main reason is the error component $\Delta T_{\delta c \delta \gamma_L}$ that dominates the overall uncertainty, as $S(f_1)$ and $S(f_2)$ are not leveled out by the I-correction. When the I-correction is turned on the error decreases and the overall error is dominated by shot noise.

5.3.4. CW nano thermometry in living HepG2 cells: CCCP stimulation

The protocol established above has been repeated several times. Individual results for temperature readout before and after CCCP stimulation are shown in appendix A.2. The average of all performed measurements are shown in figure 5.16. No clear increase in temperature after stimulation (green vertical line) is visible, like this has been the case for other studies. Interestingly the calculated error was

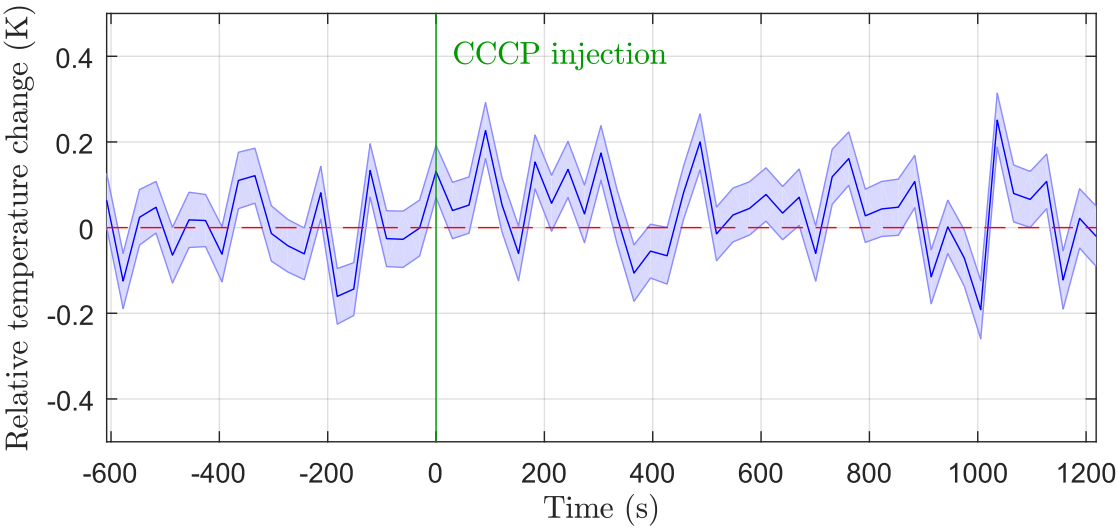

Figure 5.16. Average temperature before and after CCCP stimulation of living cells. The green line indicates the point in time, when CCCP was injected. Blue area indicates the overall error. Read dashed line indicates the average temperature before CCCP injection. Binning:30 s.

smaller then the fluctuations visible. That can also be seen for individual data set in appendix A.2. One may ask, what the origin of this could be. As the cell is in direct contact with the cover-glas that was in contact with the heated objective *via* a thin immersion oil layer, the seen temperature fluctuations maybe originated

form the regulation circuit of the objective heater itself. As the thermistor is in solution, which is mainly heated by the sample heater unit, thermistor temperature and the measured temperature by the NV may slightly differ for changes induced by the objective heater.

5.4. Summary, Conclusion and Outlook

The sensing capabilities of NV defects for temperature measurement inside living HepG2 cells have been exermined. To monitor the temperature in the vicinity of mitochondria, nanodiamonds have been conjugated with TPP. The modification with TPP shall enable targeting to mitochondria. Analyzing the diffusion of TPP modified ND suggest a more sticky behavior to mitochondria within the cell then for unmodified nanodiamonds. By stimulating the cell *via* the ionophore CCCP, an uncoupler of the oxidative phosphorylation has been introduced. Stimulation with CCCP dissipates the MMP but does not reduce cell viability within the concentration. During this procedure heat shall be produced. To measure the resulting temperatur increase, a center of mass approach has been developed, which based on monitoring two points at the flanks of left and right ODMR transition of a NV ensemble. In addition, a feedback loop locks the frequency of the main microwave source onto the ZFS of the NV spin system. The calculated sensitivity of the given ND sample is $700\,\mathrm{mK}/\sqrt{\mathrm{Hz}}$ and is mainly limited by shot noise. To exclude influences from the experimental apparatus on the measured temperature, several control experiments have been performed: Cell viability under the influence of laser illumination has been checked: Cells exposed to laser light do not show a significant difference to the control without intense exposure. For NV thermometry microwaves have to be applied to the sample. Increasing the ionic strength within the sample chamber leads to heating during the application of microwave. The measured temperature shift suggested, that local changes in the ionic strength cannot lead to measurable temperature changes on the micro- or nano-scale, and can be treated as a global temperature increase.
Comparable experimental work in literature show an increase of several Kelvin over several minutes after the stimulation of single cells. In this work no change in temperature has been observed by averaging over 9 individual measurements

within an uncertainty of 0.1 K for a time resolution of 30 s. These findings are consistent with classical calculations considering the overall energy stored within a single living cell.
As CW thermometry provides a simple tool to measure temperature, it suffers from some drawbacks. As one measures the center of mass of a broad EPR spectra, small asymmetries in the ODMR spectra can lead to shifts that are not induced by temperature. Therefore the used experimental setup has to be well characterized. In addition precise temperature readout has a limited bandwidth of $\sim$ 1 Hz in the presented case. Fast changes in temperature, typically expected at the nano scale are hard to resolve. A solution for latter problem is achieved by using robust pulsed methods to readout the NV^- spin system and to extract temperature. That solution will be presented and discussed in the following section.

6. Robust-pulsed nano thermometry

In the former section cw ODMR was used to analyze temperature changes in living HepG2 cells after CCCP stimulation. No temperature increase could be observed in average. This is consistent with theoretical considerations, as up-scaling cells to the amount needed to form a living organism would result in temperature increases far beyond normal body temperature [12]. The former does not exclude that the characteristic of temperature fluctuation may change during stimulation. For example, Inomata et al. [87] observed a characteristic change of heat generation from a burst like to a continuous increasing behavior after stimulating brownian fat cells with norepinephrine. The observation can be explained by the measurement chamber design and the system response: As the change in the resonance frequency of a silica stick around $\sim 840\,\mathrm{kHz}$ is probed, this also defines the upper bandwidth (time resolution) that one can achieve with the developed technique. As heat dissipation of the used measurement chamber is much lower, compared to single cells in cell culture media, a constant temperature increase will be visible. Interestingly, a technique called stimulated echo, which was developed for NMR, allows the detection of fast correlation. The temporal resolution is theoretically limited by the time one needs to manipulate the spins under study. Applications of this technique using the NV^- has been shown in various experiments [107, 224]. The probe scheme can be understood as two sensing blocks, which are separated by a correlation interval. The sensing block itself can be, for example, a simple Ramsey scheme, which probes the frequency shift of the applied microwave frequency versus resonance. By correlating the first sensing block with the second one, one can extract the average relative shift of resonance or its direction for a certain time, defined by the correlation interval. But in principle, one can characterize every quantity that is detectable by a proper design sensing block. The only limitation is, that the change has to occur on the time scale of the

spin lattice relaxation time of NV^-. In terms of a D-Ramsey this would be the relative change in temperature.
As in cellular environment NDs can tumble, probing spin dynamics of NV must be robust against such changes. To this end a new method has been developed to enable temperature sensing on the nanoscale based on optimal control theory. To develop the sensing block that is the focus of this work, the basis pulse scheme by Neumann et al. [137] has been chosen. In the following paragraph the theoretical requirements for such a pulse are developed and its limits are exploited. Afterwards the new developed scheme is compared to other pulse control schemes like adiabatic passage and square pulses. In the end the method is tested for different NVs in bulk material, fixed ND and rotating NDs.

6.1. Designing a Cooperative Optimal Control D-Ramsey Pulse

Figure 6.1 shows the basic pulse scheme of a D-Ramsey pulse sequence. Thereby all electronic spin sublevels of NV^- are used: First a superposition between $|0\rangle$ and $|1\rangle$ is created. After phase accumulation in a first evolution interval, the population is transferred to the sublevels $|0\rangle$ and $|-1\rangle$ *via* three transition selective π-pulses. After a second evolution interval, and an additional $\pi/2$-pulse the state evolution is read out. (See also section 3.4.4, page 66 for a detailed explanation). It is of prime importance for the functionality of the D-Ramsey sequence that the complex amplitude of the $|0\rangle$ state remains on $|0\rangle$, whereas the amplitudes of $|-1\rangle$ and $|+1\rangle$ are swapped.

The full pulse train can be separated into three individual segments with different functionality: 'seg1': initialize sensing, 'seg2': modify system to be sensitive to the center of gravity of both transitions. 'seg3': phase to state translator. To achieve this, three building blocks and the quantum state filter method by Braun et al. [26] is used (see also 62). First, the dynamics of a single NV has been simulated. Therefore the system was defined as described in equation (3.32) on page 40. The shift introduced by an external magnetic field has been set to 5 MHz, resulting in a splitting of 10 MHz for the EPR transitions. In addition,"dynamo"

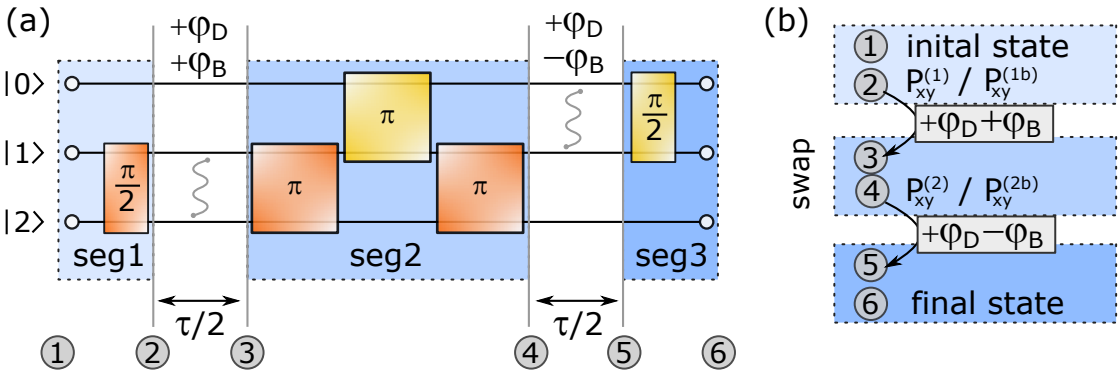

Figure 6.1. Schematic representation of D-Ramsey. (a): D-Ramsey as designed by Philipp Neumann et al. [137]. In addition, the translation into a cooperative pulse design is depicted by blue boxes consisting out of three pulse segments: seg1, seg2 and seg3. **(b):** Requirements for a cooperative pulse to force a D-Ramsey like behavior. (1): Initial state must be fixed. (2): The Projector $P_{xy}^{(1)/(1b)}$ forces the superposition state between $|1\rangle$ and $|2\rangle$, equivalent to a $\pi/2$-pulse. Between (3) and (4): The pulse must shuffle the populations to fit the projector $P_{xy}^{(2)/(2b)}$ and therefore adjusts a superposition state between $|0\rangle$ and $|1\rangle$. Within (5) to (6): The pulse evolves the quantum system into the predefined final state

shall optimize the pulse response for three different configuration that resample the hyperfine structure of ^{14}N. Therefore additional magnetic shifts with 0 MHz and ±2.16 MHz are introduced. To see how phase accumulates during the evolution interval, a detuning $\delta\omega = 0.2$ MHz is introduced. Therefore $\delta\omega \cdot S_z^2$ is added to the Hamiltonian. Doing so, one would expect only a single harmonic modulation between state $|0\rangle$ and $|+1\rangle$ with a period of 5 µs matching the adjusted detuning, when varying the time of the evolution intervals.

From a first naive view one could think that the Projectors $P_{xy}^{(1)}$ and $P_{xy}^{(2)}$ (see page 66 for definition) would already be enough to achieve the desired task, as they force the projection onto the corresponding superposition state and do not have restrictions on the overall phase accumulated during a possible sensing period. Simulating the state dynamics of the model NV$^-$ for different evolution intervals reveal, that only if the period matches a multiple of π ($2\pi = 5$ µs), the final state is reached as desired. As shown in figure 6.2(a), in all other cases the pulse fails. As can be seen in the FFT of the evolution of $|0\rangle$ in figure 6.2(b), frequency components between 1 MHz and 4 MHz occure. The origin of this behavior can be seen in the fact, that

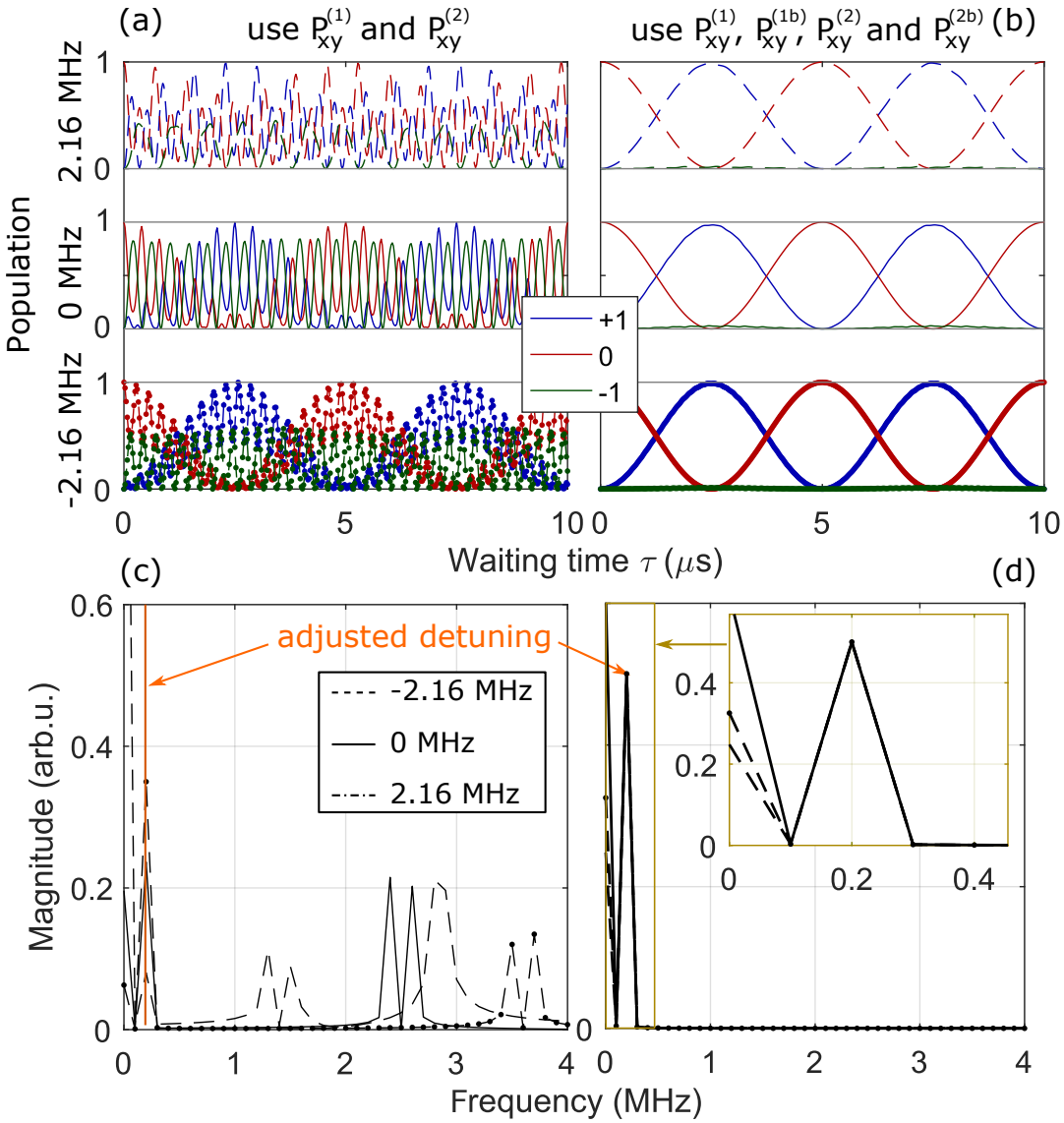

Figure 6.2. Simulated evolution of Coop-D-Ramsey for different projector combinations : (a): Evolution for NV spin states with and without ^{15}N hyperfine when applying a Coop-D-Ramsey. Only Projector $P_{xy}^{(1)}$ and $P_{xy}^{(2)}$ are used to compile the pulse. **(b):** Compilation includes an additional mirrored ensemble applying $P_{xy}^{(1b)}$ and $P_{xy}^{(2b)}$ instead of $P_{xy}^{(1)}$ and $P_{xy}^{(2)}$. **(c):** fast fourier transformation (FFT) of the $|0\rangle$ population shown in (a) with and without hyperfine. **(d):** FFT of the $|0\rangle$ population shown in (b) with and without hyperfine. In (c) and (d) also the adjusted detuning from the zero field splitting is drawn by an orange line. Both pulses have been optimized to a Frobenius norm error (FNE) $\sim 5 \times 10^{-3}$.

the pulse is compiled for a fixed evolution interval $\tau/2 = 0$. In a real experiment, as in the performed simulations, the relative phase accumulated during these intervals will also vary, and "dynamo" is not sensitive to this case. Therefore one has to introduce another condition to force "dynamo" to also include phase shifts during the evolution interval. To this end, a second mirror system is introduced, utilizing the projector pair $P_{xy}^{(1b)}$ and $P_{xy}^{(2b)}$. The difference in the projector with index (b) is that in the first one, an additional $+\pi/2$ shift is introduced, whereas in the second a $-\pi/2$. Optimal control has to optimize both systems (original and mirror). As one can see in figure 6.2(b), a clear oscillation between state $|0\rangle$ and $|+1\rangle$ is visible with a period of 0.2 MHz. The additional frequency components between 1 MHz and 4 MHz disappeared (see figure 6.2(d)). The projectors $P_{xy}^{(1b)}$ and $P_{xy}^{(2b)}$ are only one solution to solve the problem. One could add an $\pi/2$ phase shift in $P_{xy}^{(2)}$ and change the final state of the mirror ensemble to the state $|+1\rangle$, but this would require modifications of "dynamo".

6.2. Simulations

Having the right recipe at hand to compute an Coop-D-Ramsey pulse, one desires to know the parameter range such a pulse has to be optimized for. If different quantum systems must be forced to behave in the same way, one would expect in worst case a prolongation of the pulse in time with increasing number of systems. The entirety of this systems will be called 'ensemble' in the following.
Two different subsets within the ensemble are considered: First one is the variation of the free evolution Hamiltonian by symmetrical shifts around the ZFS introduced by $\Delta\omega \cdot \mathrm{S_z}$ (Zeeman term) and center of mass shifts by $\Delta\omega \cdot \mathrm{S_z^2}$ (temperature shift). The second subset considers the variation in the control field Hamiltonian. To simplify computation, only the control fields with the spin operators S_x and S_y are considered. If an additional ZFS E is introduced, the transformation of S_z leads to a coupling of the new eigenstates $|X\rangle$ and $|Y\rangle$ (see equation (3.24), page 38). Again this has been dropped for simplification, as is requires modifications on the package "dynamo". Even if S_z is not considered, following simulation and experimental data show a sufficient match.

6.2.1. Optimizing an Cooperative Optimal Control D-Ramsey Pulse

As a first approximation, one wants to find the requirements a pulse has to fulfill in terms of the possible variation of the control field. If a transition between two states is driven, a minimum strength for a fixed time is needed to fulfill a desired state adjustment. For example, if one has only limited time τ_p and wants to perform a π-rotation, at least a driving strength (Rabi amplitude) of $\frac{1}{2\tau_p}$ is needed. The latter also depends on the relative orientation of the NV versus the actual control field vector $\overrightarrow{B_1}$ [1]. Therefore not for all orientations the desired state can be adjusted in τ_p.
For example, if the spin quantization axis of a NV is tilted around 45° to $\overrightarrow{B_1}$, its transitions will be driven by a factor of $1/\sqrt{2}$ slower, in comparison to an NV having it's spin quantization axis perpendicular to $\overrightarrow{B_1}$. If one wants "dynamo" to generate a control field that is also suitable to perform a Coop-D-Ramsey for the tilted NV, one has to include an ensemble with a relative driving amplitude $1/\sqrt{2}$ smaller than the reference amplitude. In the following analysis, the lowest relative driving amplitude one wants to account for, is called the "relative lower amplitude limit". All orientations in between with a Rabi amplitude bigger then "relative lower amplitude limit" are called the "addressable fraction". Thereby an "addressable fraction" of 1 means that all orientations can be addressed.
To get an overview, what the consequences for an arbitrary oriented NV versus the driving field vector are, the control field vector is projected onto the equator of the NV reference frame (figure 6.3(c)). The control field is assumed to be linearly polarized, matching the experimental configuration. The calculated x and y components, B_x and B_y, are then used to calculate the addressable fraction of NV for the polar angle θ. In case of no strain, the relative lower amplitude limit is referenced to the maximum Rabi amplitude one will have for $\theta = \pi/2$. By comparing equation (3.32) to (3.33) with (3.34) to (3.37), one can see, that in case of strain this correspond to a azimuthal angle φ of $\pi/4$, which has been chosen as

[1] The control field Hamiltonian H_1 is defined as $H_1 = u_x(t)\cdot\gamma B_x S_x + u_y(t)\cdot\gamma B_y S_y + u_z(t)\cdot\gamma B_z S_z$. $\overrightarrow{B_1} = (B_x, B_y, B_z)$ is the vector direction of the control field. Linear or circular microwave excitation is controlled by the choice of $u_i(t)$.

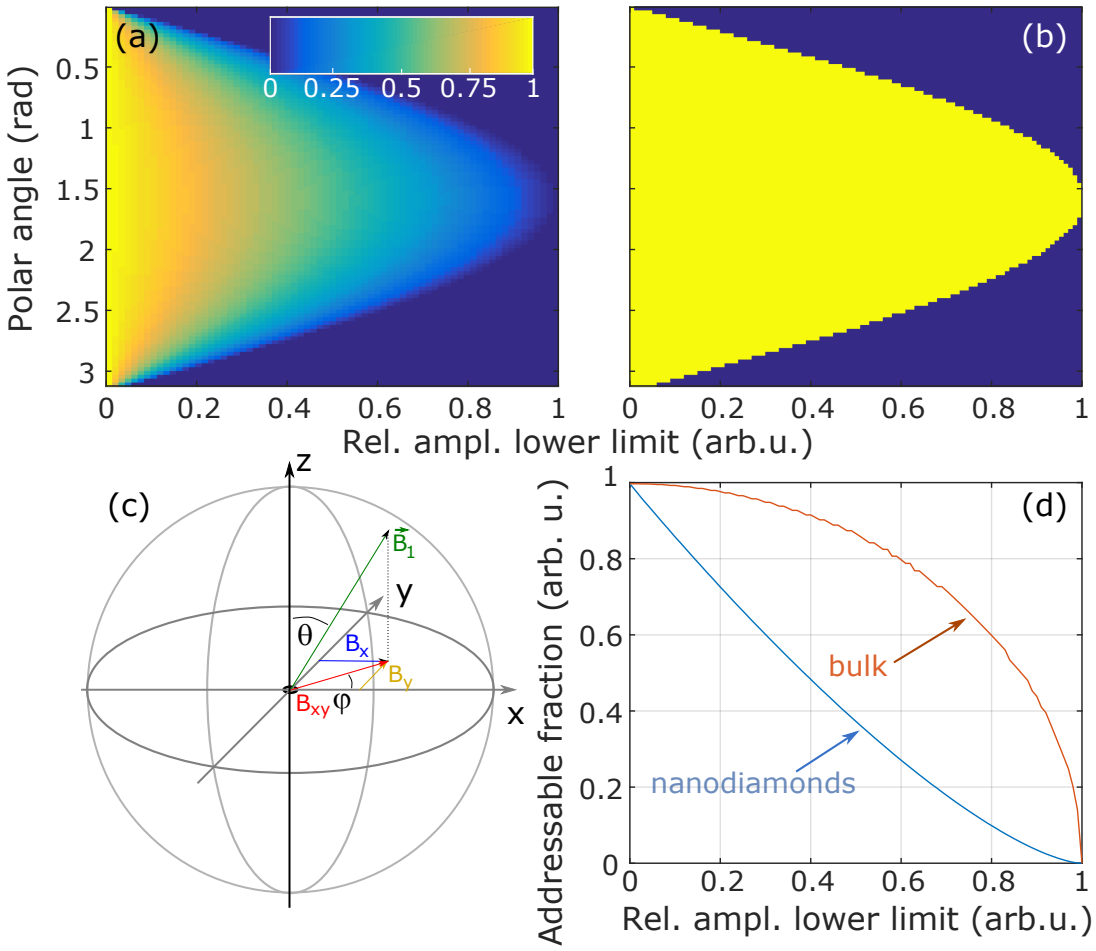

Figure 6.3. Addressable fraction of an ensemble versus B_1 field orientation: (a): Addressable fraction of NVs dependent on the polar angle θ and the lower amplitude limit. The polar angle is set between the $\vec{B_1}$ direction and the quantization axis of NV aligned along the z-axis. (b): same as (a) for a NV in bulk diamond **(c):** Model used to calculate (a) and (b). A strain field giving rise to the zero field parameter E points along the x-direction. To calculate the fraction of NVs that are addressable by the designed pulse only the projection onto the equator has been used. The relative lower amplitude limit for x and y direction had been set to the same values. **(d):** Average addressable fraction of NV for bulk and nanodiamond case when averaging over the polar angle θ. Whereas for a ND B_x and B_y have to meet the lower limit condition, in the bulk case only B_{xy} has to satisfy this requirement. (d) can be seen as the lower guaranteed fraction one can address by the designed optimal control pulse.

the reference for latter case. The additional dependence on the azimuthal angle φ leads to a further restriction for the stained case: If B_x increases for a certain φ, B_y has to decrease, therefore both have to fulfill the relative lower amplitude limit at the same time.
Varying the polar angle and calculating the addressable fraction of NV that can be driven by the relative lower amplitude limit, results in figure 6.3(a) and (b) for strained ($E \neq 0$) and un-strained case ($E = 0$), respectively. The lower the amplitude limit, the higher the reachable fraction of possible orientations in both cases. Averaging over all possible polar angles results in figure 6.3(d). As one can see in the un-strained case (bulk) with a driving amplitude of 0.8, already around 60 % of all possible orientations are covered. This is unproportionally harder for the strained case (nanodiamond): The minimum amplitude one has to address is around 0.4 (more precise 0.38) to address at least 50 % of all orientations and around 0.3 to drive at least 60 %. The situation for $E \neq 0$ case would change to bulk like behavior, if a circular microwave excitation would have be chosen. The amplitude of B_x and B_y would become independent of φ, as $\overrightarrow{B_1}$ can be separated into two equally strong linear polarized waves along x and y direction. As this requires an advanced design of the used microwave structure [5], this approach was discarded.

In a next step the consequences of amplitude scaling was calculated for different types of ensembles, by simulating its spin dynamics *via* "dynamo". To this end three different ensemble have been assumed. First one accounts only for the electronic transitions of NV^-. Second one accounts also for the hyperfine of ^{14}N by adding magnetic shift terms of $0, \pm 2.16\,\mathrm{MHz}$ to the parameter space of the ensemble. And last one, also includes an additional magnetic shift of all transitions with $\pm 40\,\mathrm{kHz}$. In addition, three different amplitude limiting parameters have been chosen: 0.9, 0.8 and 0.3. Experimentally quite some effort is connected to the determination of the z component of $\overrightarrow{B_1}$. Therefore the amplitude limit has been also expanded to higher amplitudes, as possible tumbling of a ND may increase B_{xy}: The range in which a pulse shall be optimized is set to 0.9 to 1.1, 0.8 to 1.2 and 0.3 to 1.3. As a measure of success the Frobenius norm error (FNE) is used describing the discrepancy between the desired and adjusted state in terms of the Frobenius norm. The final optimization results are plotted in figure 6.4. The FNE has been plotted

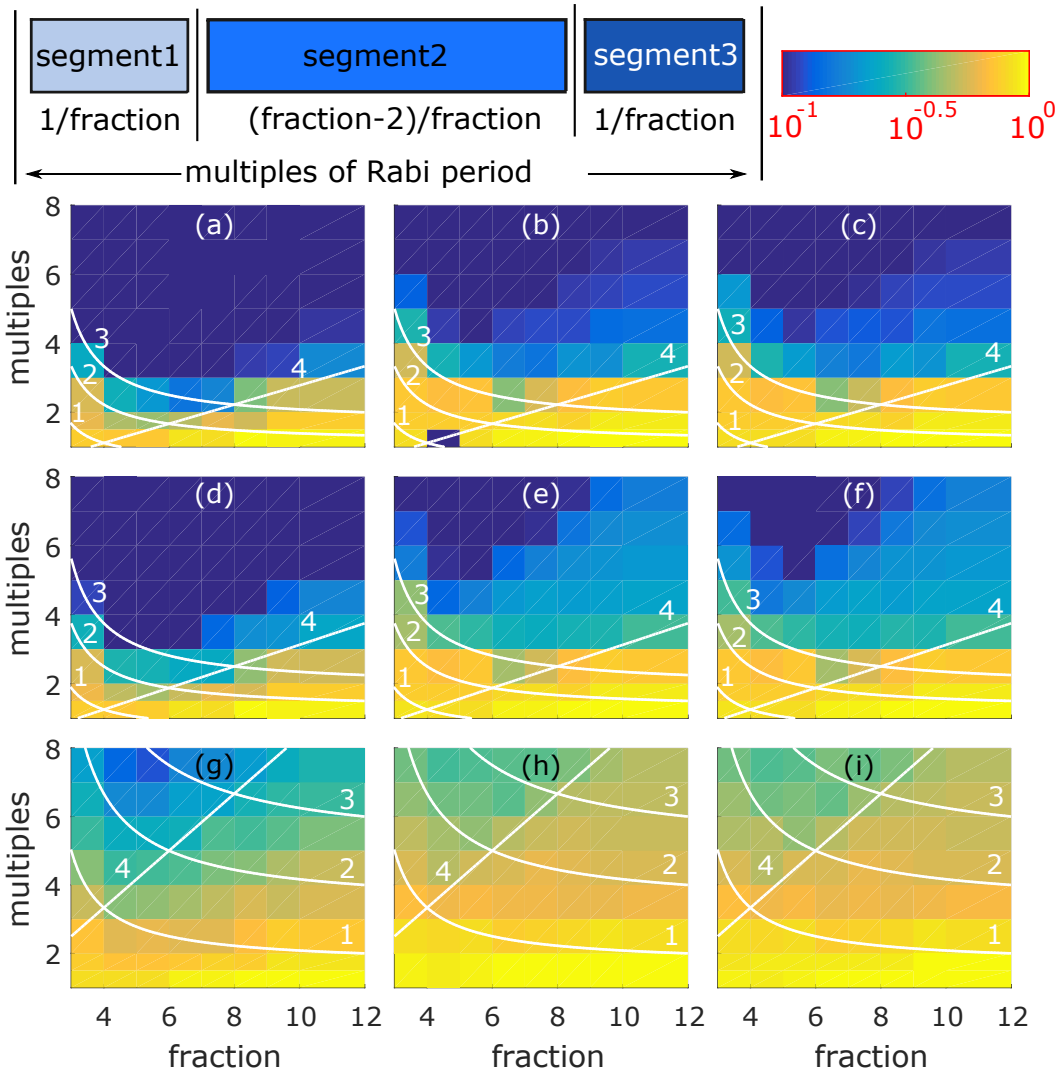

Figure 6.4. Optimization of Coop-D-Ramsey pulse parameters: (a): NV electron spin only. **(b):** Adding ^{14}N Hyperfine lines as a magnetic detuning. **(c):** Adding $\pm 40\,\mathrm{kHz}$ to account for ^{13}C hyperfine. The amplitude in (a), (b) and (c) is allowed to vary between 0.9 to 1.1 of the set Rabi frequency. **(d)**, **(e)** and **(f)**: same as (a), (b) and (c) allowing the amplitude to vary form 0.8 to 1.2. **(g)**, **(h)** and **(i)**: same as (a), (b) and (c) allowing the amplitude to vary form 0.3 to 1.3. The upper left sketch illustrates the meaning of "fraction" and "multiples". White lines show the limit: **(1)**: Segment2 is minimum 0.5 Rabi oscillations long. **(2):** Segment2, 1 Rabi oscillation. **(3):** Segment2, 1.5 Rabi oscillations. **(4):** Segment1/3: minimum 1/4 Rabi oscillations. The reference is the lowest Rabi frequency allowed in the system.

varying two parameters. The overall time, described in terms of "multiples" of the Rabi period, and the relative time for each segment, expressed in "fractions". For a fraction of 3, segment 1,2 and 3 are of equal length. For a fraction of 8 the segments have the same length as the original sequence defined by Neumann et al. [137]. As the task of the first pulse segment is to adjust a superpositions state starting from the initial state being the eigenstate $|0\rangle$ of the spin system, their length must be at least 1/4 of the maximum Rabi period within the system that shall be considered. Same hold for the third segment in the figurative sense. The white line marked with the index (4) in figure 6.4 indicates the positions where this limit is reached. In addition, three other white lines with the index (1), (2) and (3) are marked. As in the second segment in the original pulse sequence three π-pulses are placed, the minimum time one has to spend has to be at least 1.5 of the minimum inverse Rabi frequency (index (3)) in case of using square pulses. As numerical optimization allows to address several transitions at the same time, the minimum time needed can be shorter. Therefore also the condition 0.5 and 1 times the inverse Rabi frequency are plotted with index (1) and (2). As one can see in figure 6.4, with increasing complexity also the sequence has to be prolonged to minimize the FNE. Interestingly there seems to be a valley bordered by the lines with index (2) and (4). The meeting point of both lines is at a fraction of 6 that will be used for further calculations.

To find an estimate on the minimum pulse length needed, the three introduced ensemble have been optimized for different relative amplitude windows, with a fixed fraction, set to six. In the beginning a Coop-D-Ramsey sequence with a length of 2 multiple is calculated for a relative lower and upper amplitude limit of 1. The final error between the adjusted and the desired state in terms of a Frobenius norm (FNE) that shall be reached, shall be equal to or below 0.1. If "dynamo" cannot optimize the sequence within 600 iterations, its pulse length is increased by 0.5 multiples (if pulse length ≥ 4 multiples, the pulse length is increased by 1 multiple) and a new sequence is compiled. If the calculated Coop-D-Ramsey has a FNE below or equal to 0.1, the relative amplitude range ,"dynamo" shall optimize for, is increased and a new sequence is compiled with the same pulse length. Repeating this for the different types of ensemble, which has been introduced before, results in figure 6.5. The absolute driving amplitude was set to 3 MHz. The resolution

of the amplitude parameter space that was added to the ensemble is 0.1 (for example: 0.8, 0.9, 1.0 for a relative lower and upper amplitude limit of 0.8 and 1.0, respectively). As one can see in figure 6.5, with increasing amplitude tolerance, the overall length of the pulse increases. If not only the electronic transitions are considered (blue), the pulse must be additionally prolonged: Adding the hyperfine splitting by ^{14}N (green), the pulse length almost doubles. Adding an additional

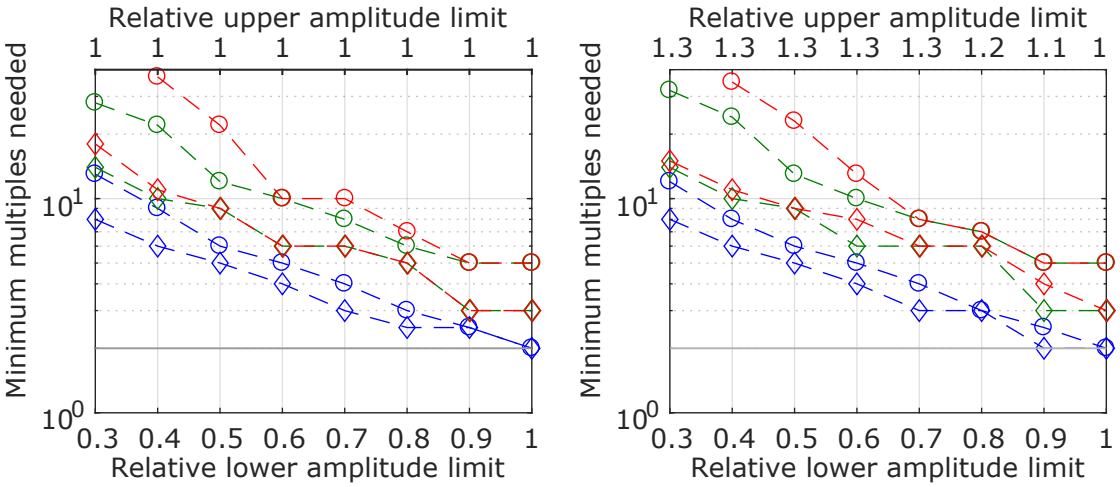

Figure 6.5. Minimum pulse length for Coop-D-Ramsey. (a): Minimum pulse length for different scenario to reach a FNE below 0.1: (blue): Only the NV electronic transitions are considered. (green): Include ^{14}N hyperfine lines as a static magnetic field $(0, \pm 2.16\,\mathrm{MHz})$ to the parameter space of the ensemble. (red): Include in addition ^{13}C hyperfine as a static magnetic field $(\pm 40\,\mathrm{kHz})$. Lower and upper axis label show the range within the amplitude scaling was optimized for. The vertical gray line marks the minimum pulse length needed by a square pulse. (diamonds): No detuning is introduced. (circles): Detuning is introduced from $-0.2\,\mathrm{MHz}$ to $0.2\,\mathrm{MHz}$ in 3 steps.

hyperfine splitting of $\pm 40\,\mathrm{kHz}$ (red) only slightly enlarges the sequence length. Increasing the complexity even further by considering also detuning (circles) in D $(0, \pm 0.2\,\mathrm{MHz})$, the Coop-D-Ramsey has to be prolongs again versus no detuning (diamonds). Interestingly, shifting the upper amplitude limit has no significant influence (compare figure 6.5 (a) and (b)).

In summary, if one wants to cover a relative lower amplitude limit 0.4 (50 % of all orientations in ensemble), the optimized pulse must be at least around 6 to 9 multiples long. Considering hyperfine splitting, around 10 to 24 multiples are needed. Adding an additional weekly coupled spin, 11 to 37 multiples should be

applied. However, one has to realize, that all pulses were only optimized for 600 iteration steps. Especially for a broad range of amplitude parameters this does not mean, that the sequence is fully optimized. Therefore the presented analysis has to be understood as an estimate. In addition, experimental analysis will show that the pulse performes even at a broader bandwidth that the amplitude limit and detuning originally set (see section 6.3).

Increasing computation speed As stated in the theory section, the used projectors $P_{xy}^{(1,1b)}$ and $P_{xy}^{(2,2b)}$ also remove population, when they are applied on a density matrix not presenting the right superposition state (for definition see equations (3.78) and (3.79)). However, the projectors provide an additional penalty as they force "dynamo" to depopulate the state, which is not part of the superposition the projectors project onto. As a result compilation speed is increased during the optimization of a Coop-D-Ramsey pulse. To demonstrate this, three different sets of ensembles have been optimized for random initial guesses of the control field amplitudes $u_x(t)$ and $u_y(t)$. All ensembles include magnetic shifts of $0, \pm 2.166\,\mathrm{MHz}$ and have a relative lower and upper amplitude limit of 0.8 and 1.2 (5 steps), respectively. The first ensemble (ensemble 1) is compiled with an overall length of 6 multiples (Rabi periods). For the second ensemble (ensemble 2) the overall length was increased to 8 multiples. The last ensemble (ensemble 3) is 7 multiples long and additional shifts in the ZFS D have been introduced $(0, \pm 0.2\,\mathrm{MHz})$. The fraction for all ensembles is set to 6.
Now, for each ensemble a Coop-D-Ramsey pulse is generated with a random staring guess of $u_x(t)$ and $u_y(t)$. To optimize the pulse, two different sets of projectors are used. The first set of projectors are the already introduced $P_{xy}^{(1,1b)}$ and $P_{xy}^{(2,2b)}$ (set 1). Also the second set of projectors project onto a superposition state in the corresponding subspace, but preserve the overall population (set 2). The projectors can be found in the appendix (equations (B.1) and (B.2)). After optimizing each ensembles for 300 iterations one gets figure 6.6. Figure 6.6(a) to (c) show the iterative optimization by "dynamo" for several random guesses of the control field amplitude. For all three ensembles the FNE starts with a lower value, when using set 1 instead of set 2. This would mean that set 1 already provides from beginning a better pulse. As in each run the same starting guess for set 1 and set 2 has

been chosen, the reduction of the FNE must be a consequence of the removal of population by set 1. After several tens of iterations the FNE for the different

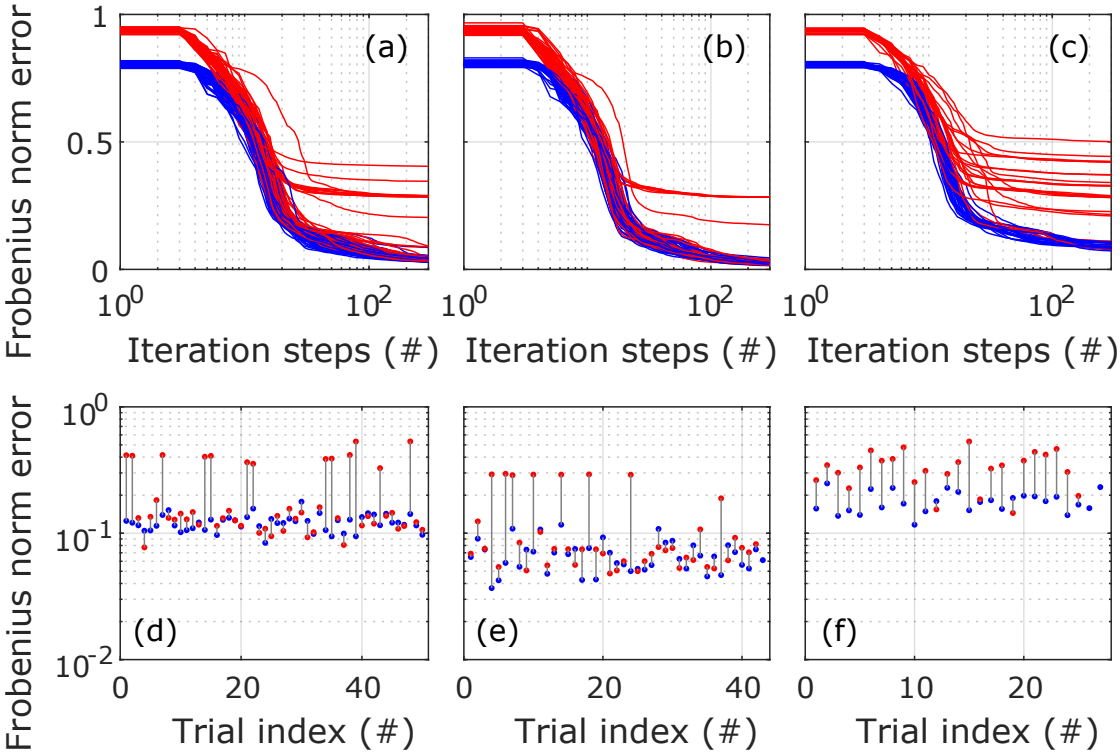

Figure 6.6. Comparing different sets of projectors. (a): FNE of ensemble 1 plotted over the iteration steps during optimization for different starting guess of $u_x(t)$ and $u_y(t)$. For compilation the projectors $P_{xy}^{(1,1b)}$ and $P_{xy}^{(2,2b)}$ (blue) and the $P_{xy}^{(1',1'b)}$ and $P_{xy}^{(2',2'b)}$ (red) have been used. **(b)** and **(c)** are the equivalent compilations for the ensemble 2 and 3, respectively. **(d)**, **(e)** and **(f)**: Recalculated FNE between adjusted and desired state for different starting guesses for the ensembles shown in (a), (b) and (c) after 300 iterations. To calculate the FNE the projectors $P^{(1'',1''b)}$ and $P^{(2'',2''b)}$ have been used. For more details see text.

sets seem to follow the same behavior. However, the FNE of set 2 saturates early for higher values than set 1. That this is not just an artifact introduced by the removal of population, can be seen in figure 6.6(d) to (e). There the FNE has been recalculated after 300 steps for the data shown in figure 6.6(a) to (c) using a third set of operators, namely $P^{(1'',1''b)}$ and $P^{(2'',2''b)}$ (set 3, for definition see equations (B.3) and (B.4) in the appendix). Set 3 does not project onto a certain state, like this is the case for the other ones, but reduces as a penalty the coherence in the

quantum system, if the latter is not aligned in the desired superpositions state. As one can see in figure 6.6(d) to (e), the FNE of set 1 is comparable or smaller then this is the case for set 2. Therefore the projectors $P_{xy}^{(1,1b)}$ and $P_{xy}^{(2,2b)}$ provide an additional penalty to optimize Coop-D-Ramsey pulses faster.

6.2.2. Comparison to other pulse schemes

With increasing complexity of the ensemble to optimize for, also the overall length of the pulse itself increases. The question arises why not to used simple square pulses or maybe just some other pulse types like adiabatic sweeps to adjust a certain state. This shall be discussed in the following.

Square pulses To this end, the D-Ramsey scheme has been simulated within the kernel of "dynamo" using square pulse. To set realistic parameters that are reasonable for temperature measurement, a bulk like system has been simulated with a line splitting of 20 MHz, also including the ^{14}N hyperfine line as an magnetic shift of the electronic transitions. Averaging over all hyperfine lines reveal figure 6.7. Therefore the simulated D-Ramsey has been fit to a simple sine function and the oscillation frequency and amplitude has been extracted. As shown in figure 6.7(a) the maximum signal one can get for a Rabi driving amplitude of 4 MHz is 40 %. Varying amplitude and detuning to D results in loss of signal amplitude. Especially for amplitude variations a second phenomena appears: As with reducing pulse power also the error in adjusting the desired state increases, the pulse scheme tends to lose its capability to act as a D-Ramsey. As a result the occurring oscillation, originated from varying the evolution interval between the segments, does not correspond to the detuning to D anymore (figure 6.7(d)).

Increasing the microwave power in the beginning first results in being more robust against detuning, but later leads to losses in signal contrast. This may be counter intuitive in the first place, but can be understood quite easily, if one keeps in mind that both EPR lines are just split by 20 MHz. With increasing microwave power one looses the capability to selectively drive the left or right EPR transitions, resulting in a lowering of the signal contrast. One could also think about applying a higher external magnetic field, but this could lead to a center of mass shift of the

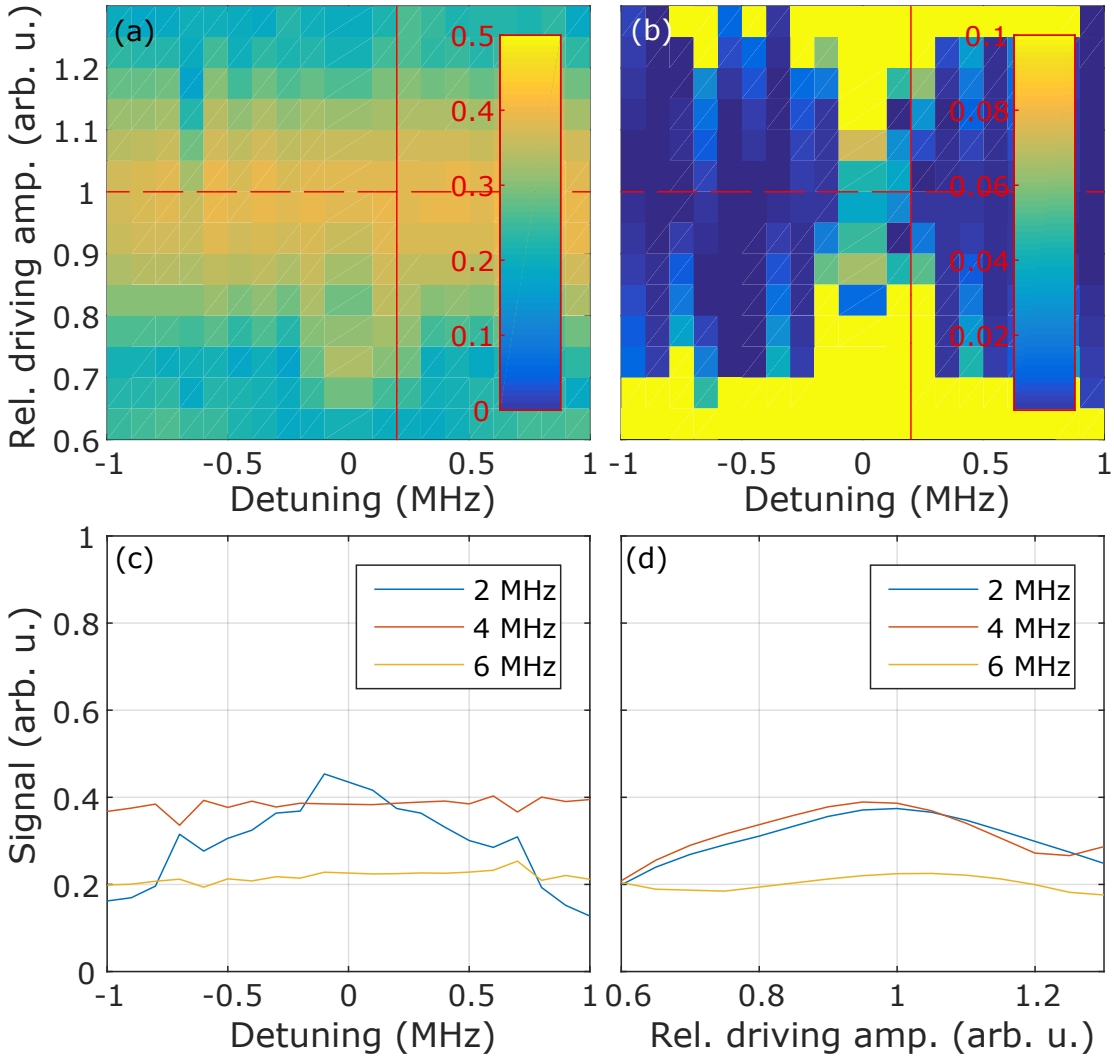

Figure 6.7. Signal amplitude of D-Ramsey using square pulses (a): Signal amplitude depending on relative Rabi driving amplitude and detuning for an absolute Rabi frequency of $4\,\mathrm{MHz}$ **(b):** Relative error of measured detuning versus set detuning. **(c)** and **(d):** Signal amplitude along the line cut marked in (a) and (b) for different absolute Rabi driving amplitudes marked in the legend. EPR line splitting had been set to $20\,\mathrm{MHz}$.

EPR lines, if the relative orientation of the NV changes (see also section 5.9, page 122). All in all the D-Ramsey works within an amplitude variation range of 0.8 to 1.2, but not outside that interval. For well separated EPR lines the ratio 0.8 to 1.2 should be independent of the used microwave power. Comparing this range to figure 6.3(d) by rescaling it to experimentally observed Rabi, the possible fraction one could address for $E = 0$ is more then 70 % of all NV orientations. But in case of strain just around 20 % can be addressed.

Adiabatic passage: BIR pulses Similar to the latter paragraph also an adiabatic pulse, namely the BIR4 pulse, has been tested for its capabilities. State control is achieved by slowly changing the effective magnetic field B_{eff} in the rotating frame. The latter can be achieved by detuning from resonance or changing the amplitude of the driving field. For the BIR4 pulse that is constructed as described in theory on page 57, three parameters define the success of a certain spin state adjustment: First parameter is the available maximum Rabi amplitude one must drive the system, which defines the maximum x and y component of B_{eff}. Second, the sweep bandwidth used to control the z-component of B_{eff}. And last, the overall pulse length, allowing to control, how fast B_{eff} changes. Varying all this quantities results in figure 6.8 when applying a π-pulse on the transition $|0\rangle \leftrightarrow |1\rangle$. Every single plot shows the FNE between desired and adjusted state, depending on the maximum Rabi amplitude available and the sweep bandwidth. From left to right the overall pulse length is varied. For weak static external magnetic fields, the line splitting between the transitions $|0\rangle \leftrightarrow |1\rangle$ and $|0\rangle \leftrightarrow |-1\rangle$ may be even smaller than the sweep bandwidth. A BIR4 pulse, used to drive one transition, may also affect the other transition. Therefore also the line splitting is varied from top to bottom. At a pulse length of 8 µs a remarkable insensitivity to the Rabi frequency is observable for line splittings bigger then 10 MHz. In that sense the BIR pulse behaves as expected. As BIR4 has to fulfill the adiabatic condition, also the adiabaticity is plotted within the last row. As expected, increasing the overall length of the pulse result in a reduction of the FNE, and the adiabaticity increases. But also the line splitting influences the success of adjusting the desired state: For a line splitting of 10 MHz the FNE around 0.5 indicates, that the desired state is not reached at all in almost all cases. For a line splitting of 20 MHz only low Rabi amplitudes result

in good results (or a small FNE). The adiabatictiy is therefore insufficient to fully determine, if a state is well adjusted or not that is in total contrast to the linear chirp pulse used in section 7.

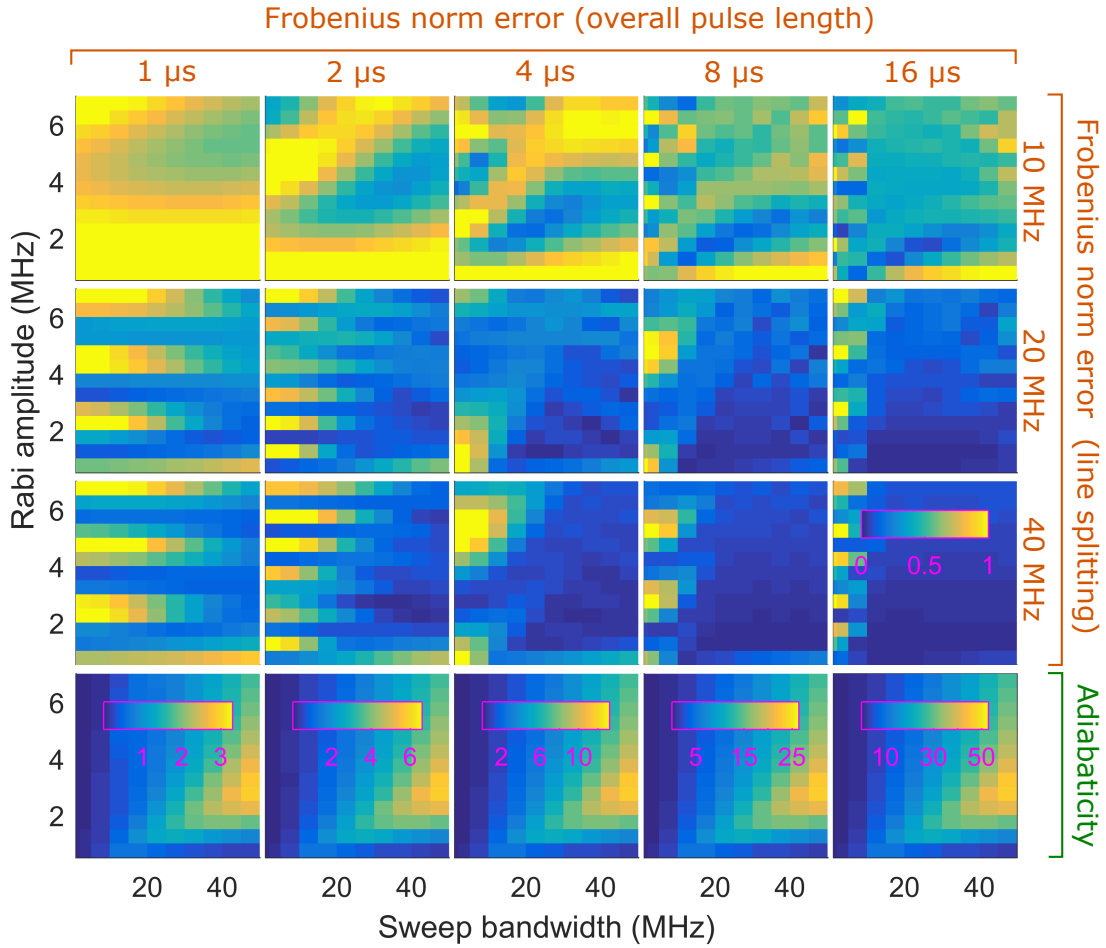

Figure 6.8. Optimizing pulse parameters for BIR4. From left to right: The overall pulse length is varied. From Top to Bottom: Splitting of EPR transitions is varied. Lower line: minimum adiabaticity of the BIR4 pulse.

For nanodiamonds typically a line splitting from some few to several tens MHz is expected. For further analysis a line splitting of 20 MHz was used, still representing a reasonable parameter choice[1]. To understand how the BIR4 pulse responds to detuning from resonance, the corresponding shift was introduced in the Hamiltonian. Figure 6.9 shows the result for varying the detuning and the maximum Rabi driving

[1]This would correspond to a $E = 10\,\mathrm{MHz}$ if the splitting is introduced by strain.

amplitude. Again from left to right the pulse length was increased. From top to bottom now the sweep bandwidth has been plotted. Similar to former result the FNE decreases with increasing pulse length. Again, for a pulse length of 8 µs the result for small detunings starts to become independent of the applied maximum Rabi frequency. Varying the sweep bandwidth seems to have minor effect, but increasing the detuning leads to a continuously increasing error in state adjustment. For a hyperfine splitting of 2.16 MHz the pulse fails.

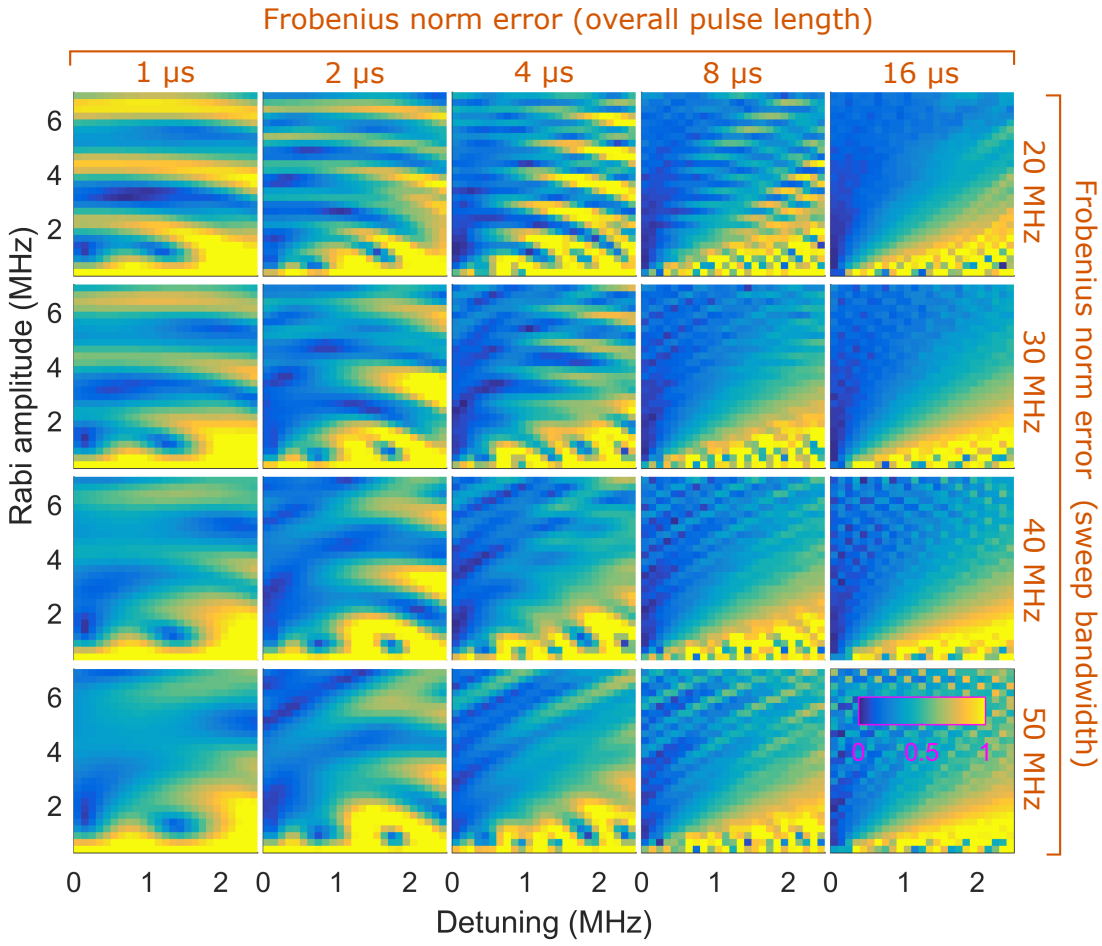

Figure 6.9. Optimizing pulse parameters for BIR4. The plots show the FNE for different BIR4 pulse parameters. From left to right: The overall pulse length is varied. From Top to Bottom: Sweep bandwidth is varied. EPR line splitting has been set to 20 MHz.

Nevertheless a D-Ramsey utilizing a BIR4 pulse has been simulated with same

parameter choice as in the case of square pulses. The result is plotted in figure

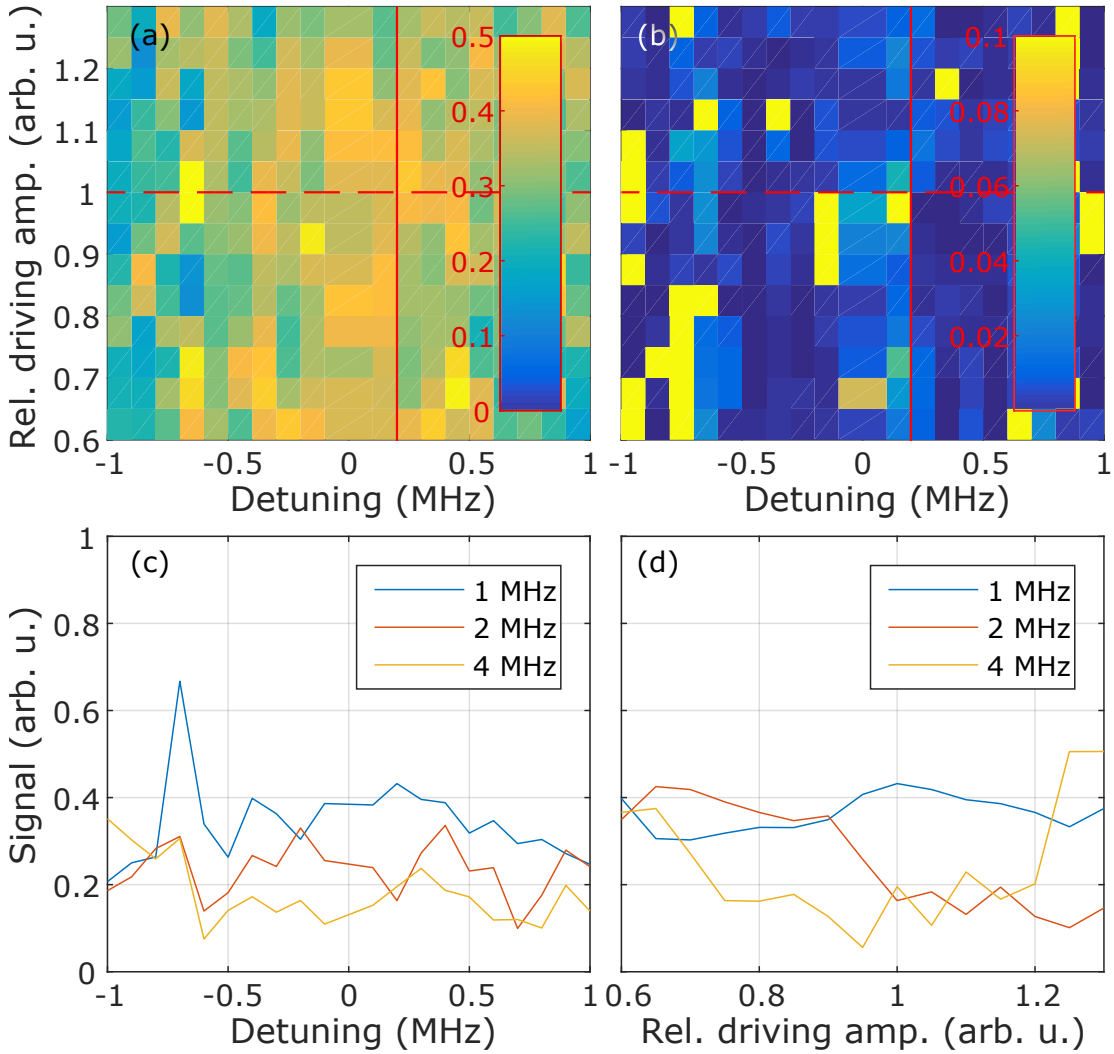

Figure 6.10. Signal amplitude of D-Ramsey using BIR4 pulses (a): Signal amplitude depending on relative Rabi driving amplitude and detuning for an absolute Rabi frequency of 1 MHz **(b):** Relative error of measured detuning versus set detuning. **(c)** and **(d):** Signal amplitude along the line cut marked in (a) and (b) for different absolute Rabi driving amplitudes marked in the legend.

6.10. For the simulation, a bandwidth of 25 MHz and an overall pulse length of 40 µs (5 times 8 µs) has been used. Similar to the square pulse only a contrast of around 40 % is reached. But the pulse scheme itself seems to be much more robust against amplitude variations. Also the read out error of the measured detuning is

smaller over a wider range of tuning parameters. Again with increasing maximum Rabi driving amplitude the overall signal contrast got worse. Also the overall pulse length is significantly higher then in case of square pulses. As one will see later the designed optimal control pulse scheme reduces the overall pulse length needed to almost a tenth and simultaneously increase the signal contrast by a factor of two.

6.3. Experiments

To test the performance of the Coop-D-Ramsey several scenarios have been chosen. First an NV^- in bulk diamond exposed to a weak external magnetic field B_0 is tested. Then an NV^- in a ND is probed within the limit $\beta_0 \ll E$. After fully compensating the external magnetic field, a NV^- in a NV rotating in an agarose matrix is tested and the temperature drift is measured.

6.3.1. Setup

To test the Coop-D-Ramsey a confocal setup as described in figure 6.11 is used. Green laser light is modulated with an AOM, filtered by a cleanup (BP532/50) and guided into a PC fiber. A dichroic mirror with a cutoff at 664 nm deflect light onto the objective. The emission of single emitters pass the dichroic and is detected again with two APDs in a HBT configuration. To suppress leaking light from the laser a long-pass (LP647) is used. To manipulate the NV spin system two AWGs (AWG2041) working in Master/Slave mode are connected to the I and Q channel of an IQMixer (IMOH-01-458,Pulsar Microwave). The IQ inputs of the mixer have an operational bandwidth from DC to 500 MHz with a maximum of −10 dBm input power. The local oscillator input is connected to a frequency source (SMIQ03B, Rohde&Schwarz) and has a bandwidth of 2 GHz to 4 GHz at 10 dBm. The IQ mixer is connected to a microwave switch (ZASWA-2-50DR+,mini-circuits) allowing to additionally suppress microwave excitation. After the switch the microwave excitation is amplified by a 16W amplifier (ZHL-16W- 43+, mini-circuits) that is directly connected to the sample. For bulk NVs and fixed ND a simple copper wire, for rotating ND a micro omega structure with a diameter of 500 µm is used. To monitor the temperature of the sample a thermistor was connected to the sample

holder. The setup is fully controlled *via* custom made software programs written in "python".

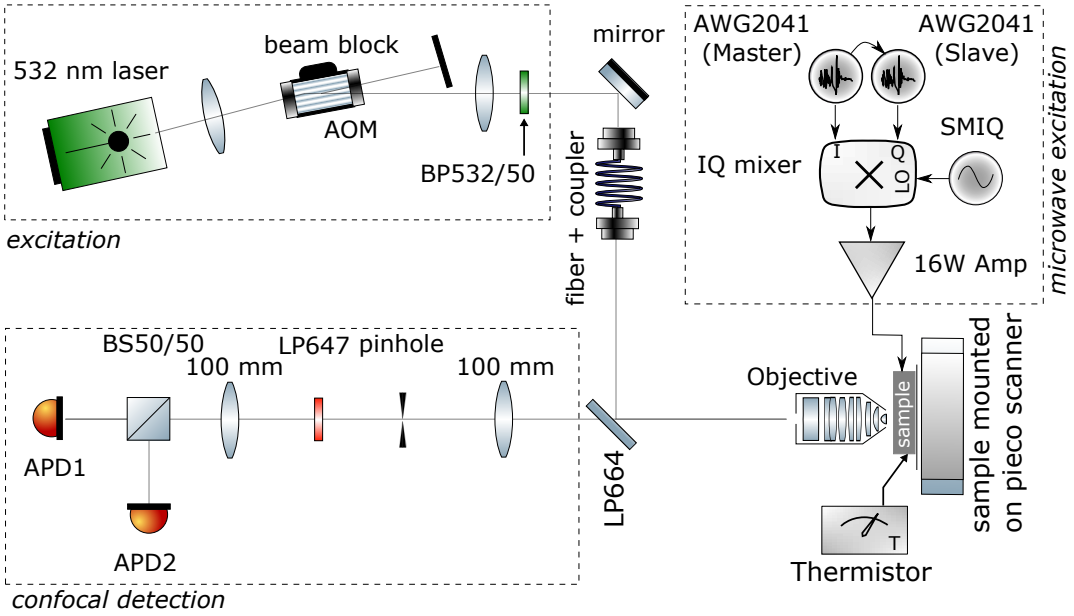

Figure 6.11. Setup: Basic experimental configuration for NV pulsed nano thermometry.

Frequency response and non-linearity in microwave excitation Both microwave sources and other microwave components can only operate in a certain parameter range. Exiting these limits have to be handled with care, as failure free operation can not be guaranteed. Typical parameter ranges are given, for example environmental/device temperature and frequency depended amplitude and phase response.

Depending on the design, real devices show a (reproducible) discrepancy from their ideal design, if the used parameters are in the guaranteed parameter range. This can be for example output saturation or phase shifts for a certain frequency near the bandwidth (BW) of a MW amplifier or other components like the used frequency mixer, switches or microwave sources. As the used AWG can only provide a sampling rate of $1\,\mathrm{GSpl\,s^{-1}}$ (10^9 sample per second), one can typically

expect a bandwidth of 100 MHz. As for a simple MW pulse (only a microwave field with a single frequency is applied at the same time) phase shifts and amplitude damping often play a minor role. But those can have a dramatic impact on optimal control pulses: The control fields of such pulses are often very complex and have to be modulated during one pulse ($\sim 2\,\mu s$) within a time interval of 20 ns. This can lead to high frequency components within a single pulse. Figure 6.12 shows the frequency response of the used AWG in a Bode-diagram for a peak-to-peak amplitude of 0.2 V. As one can see the amplitude slightly decreases and the phase shifts, the higher the generated frequency gets. For frequencies about 100 MHz the phase starts to oscillate. In addition, one can see that both AWGs seem to have slightly different amplitude damping. The consequences for an optimal control pulse are plotted in figure 6.13 showing in (a) the magnitude and (b) the phase for different frequency components of an typical optimal control pulse are visible.

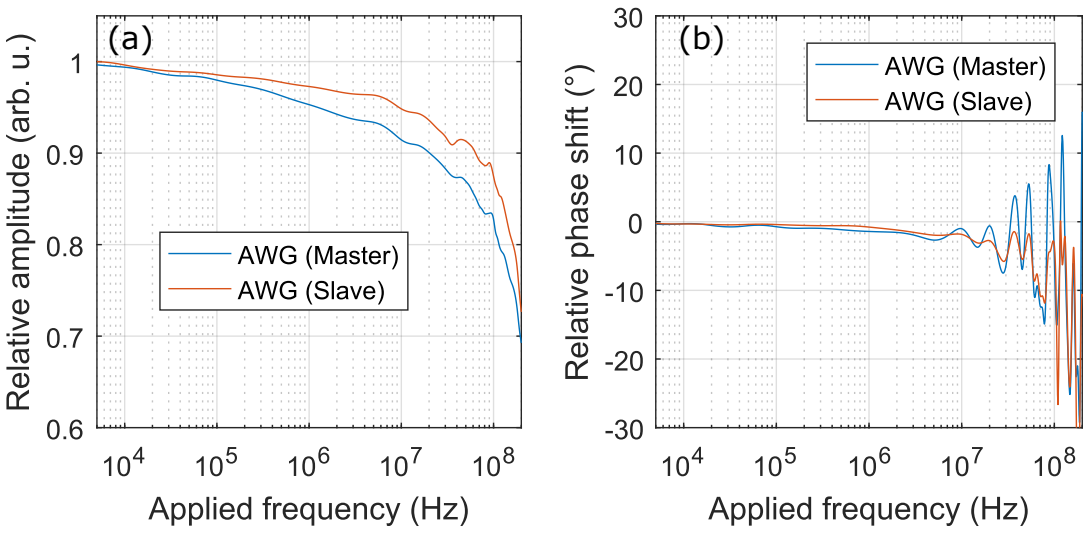

Figure 6.12. Bode diagram of the used AWG AWG2041: (a) Amplitude and **(b)** phase response depending on the applied output frequency. The output was set to peak-to-peal amplitude of 0.2 V verifying that the AWG is not saturating.

To calculate the expected AWG output $S_O(\omega)$ the generated sequence $S(\omega)$ was multiplied with the instrument response function (IRF) $\widehat{IRF}(\omega)$ in Fourier space. In principle this also allows to correct the AWG output, by applying the inverse of the IRF onto the calculated sequence before uploading onto the AWG. But as later results show good agreement between experiment and simulation, one dropped the

implementation of phase and amplitude correction.

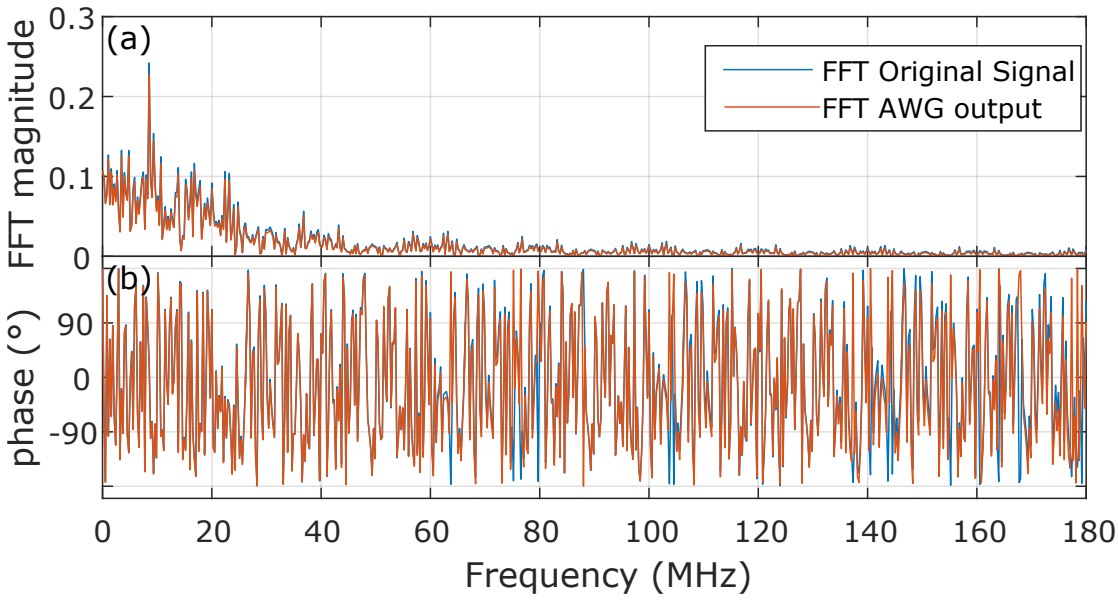

Figure 6.13. FFT magnitude and phase plot of a Optimal Control pulse: (a) Magnitude and **(b)** phase plotted versus frequency before (blue) and after (red) applying the signal response shown in figure 6.12.

.

6.3.2. Coop-D-Ramsey: single NV in bulk diamond

As a first test system, a bulk NV^- was modeled in "dynamo" using the description in equations (3.32) and (3.33). Therefore a weak external magnetic field was applied leading to a splitting of (10.3 ± 0.1) MHz of the electronic spin transitions. Figure 6.14(b) shows the corresponding pulsed ODMR spectrum using a driving strength of (1.2 ± 0.1) MHz, also to resolve the ^{14}N hyperfine lines. The maximum Rabi frequency one can drive on left and right transitions was measured to be (4.6 ± 0.1) MHz (figure 6.14(a)). This value was used to fix the maximum amplitude allowed in "dynamo". The pulse shall still work for an amplitude variation from 0.7 to 1.3. Also the hyperfine transitions of ^{14}N were considered as a magnetic detuning. In addition, a variation in D from 0.0 MHz to a maximum of 0.2 MHz has been allowed. To satisfy the shape of the pulsed ODMR and additional hyperfine interaction with a spin 1/2 (splitting (0.44 ± 0.03) MHz) was introduced. For pulse

compilation the latter was dropped, as the ensemble to calculate already exited 126 entries for a overall pulse length of 3 µs (35 ns binning). The pulse sequence was optimized until the FNE, the error between adjusted and desired state in terms of the Frobenius norm was below 0.1 (final FNE: 0.072). To characterize the

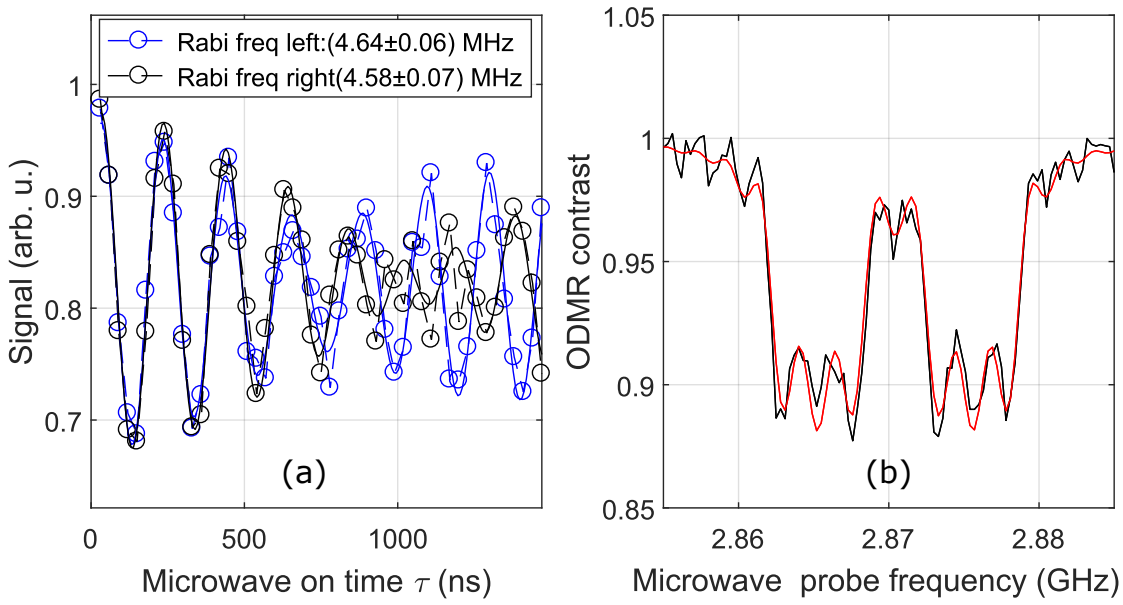

Figure 6.14. Characterization of single NV (a): Rabi oscillation on right (black) and left (blue) center peak marked in (b) with dashed vertical lines to determine the driving amplitude. **(b:)** Pulsed ODMR (gray) of single NV with a driving amplitude around 1 MHz. The fit includes also a ^{13}C like hyperfine splitting in addition to ^{14}N.

performance of the calculated Coop-D-Ramsey, the relative amplitude of the AWGs was varied to simulate rotational changes. To simulate a shift in temperature the local oscillator (carrier) was slightly detuned. As the pulse is compiled for a certain reference frame, slight changes in the carrier frequency has the same effect than changing the zero field splitting D. As the measured signal is the fluorescence response of NV, one has to renormalize the acquired data assuming that the dark state corresponds to $|+1\rangle$ and the bright state to $|0\rangle$ of the NV ground state spin Hamiltonian. Therefore a spin contrast measurement (corresponding to a T_1 measurement) was performed, to estimate the maximum Signal contrast accessible for the given NV (see figure 6.14(a), gray line). Measuring T_1 with no microwave pulse reveals the fluorescent state of $|0\rangle$. Inverting the spin state from $|0\rangle$ to $|\pm\rangle$

before readout reveals the fluorescent level of the latter. For spin inversion a linear chirp was used (see also figure 7.4 on page 184 for more details). The acquired data sets were then renormalized and fitted to a corresponding model, to extract the signal strength, plotted in figure 6.14(c) and (d) in red color. The Hahn-Echo fits best to a Gaussian decay with a signal of 0.60 ± 0.01 and a decay constant of $(41.7 \pm 7.5)\,\mu s$. To estimate the signal of the Coop-D-Ramsey, the data was fitted to sinusoidal function. As one wants to know, if the performed experiment fits to

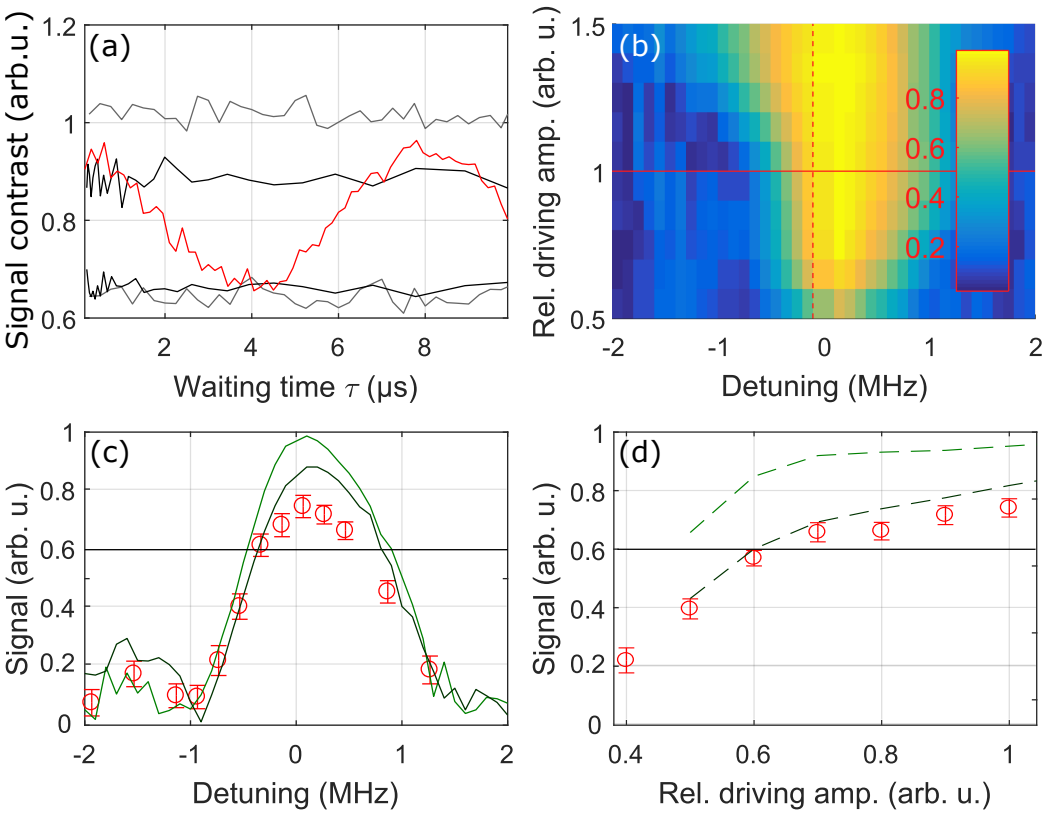

Figure 6.15. Coop-D-Ramsey performed on single NV in bulk:(a): Different pulsed measurements: T_1 (gray), Hahn Echo T_2 (black), Coop-D-Ramsey (red) correction for the best measurement. **(b):** Simulated signal contrast. The red solid and dashed line mark the parameter region where the measurement contrast had been determined also experimentally. **(c) and (d):** Acquired signal contrast (red) re-normalized by the T_1 measurement measured along the red lines in (c). The black line indicates the signal from HE result. The green solid and dashed line are extracted from (b). The dark green solid and dashed line are the signal if an additional ^{13}C hyperfine interaction of $100\,kHz$ is introduced.

the theoretically modeled system, the as compiled pulse was tested using the kernel of "dynamo" for the same condition as set in the experiment. Varying relative amplitude and detuning results in figure 6.15(b), if considering only the hyperfine stucture of ^{14}N. The red vertical and horizontal lines of (b) are also plotted in (c) and (d) as green lines for comparison. In addition, dark green line in (c) and (d) are plotted, corresponding to the result one would expect, if also an additional ^{13}C is coupled to the NV^-. Especially the latter agrees well with the collected data. The simulated signal shows an interesting behavior: With increased amplitude the pulse seems to work even better, as the tolerance against detuning increases. This is conclusive as the pulse was also compiled for higher driving amplitudes. With increasing driving strength of a transition, the pulse gets more insensitive to not being exactly resonant to a transition, "dynamo" has to take that into account. As a consequence the bandwidth in detuning increases with increasing driving strength. The range in which the pulse has been compiled for amplitude and detuning is suitable high, if one sets a threshold for the minimum signal one wants to collect. For example for minimum signal strength of 50 %, the magnetic field or frequency detuning is allowed to vary within a range of 1 MHz for relative amplitudes between 0.7 to 1.5. In addition, as the Hahn Echo provides the raw model for constructing a D-Ramsey sequence, one cannot expect a better contrast for a D-Ramsey performed with a square pulse, than a Hahn-Echo measurement can provide. As the Hahn-Echo has been acquired with best fitting parameters for one transition. The Coop-D-Ramsey has almost double the tolerance range for amplitude ranges, with always almost double the contrast then one can expect for the same conditions using square or BIR4 pulses (compare to figure 6.7 and 6.10).

6.3.3. Coop-D-Ramsey: single NV in a fixed ND

Similar to bulk also NV in nanodiamonds has been tested. Therefore the magnetic field was compensated using several differently oriented NVs in bulk diamond. Fitting the cwODMR to Lorenzian lines reveal a hyperfine splitting of 0.4 MHz but with almost 100 % error (see figure 6.16) . But using this value when fitting the measured Rabi oszillation give reasonable good match with (2.11 ± 0.01) MHz on the left transition and (1.65 ± 0.01) MHz on the right one. The difference in driving

strength can not be explained by the frequency depended damping of the AWG that should be for the set carrier at 2.81 GHz result in a ratio of 0.96. In addition,

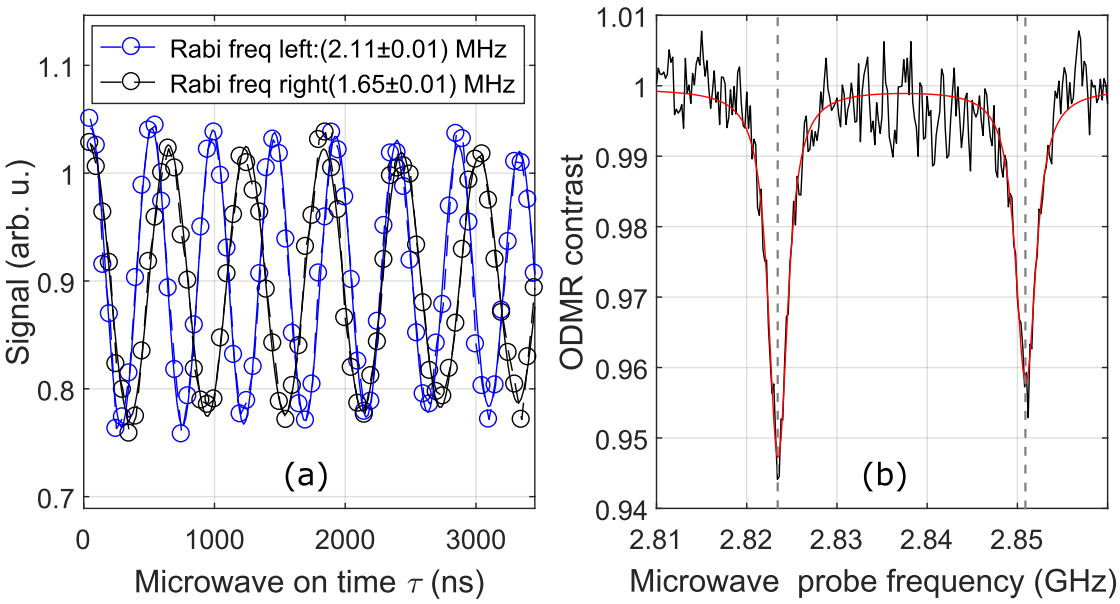

Figure 6.16. Characterization of single NV (a): Rabi oscillations on the right (black) and left (blue) center peak marked in (b) with dashed vertical lines to determine the driving amplitude. **(b:)** cwODMR (black) of a single NV^-. Lorenzian fit (red) including 6 lines (see also text). The fits in (a) and (b) include a ^{14}N hyperfine splitting around 400 kHz.

the reduced hyperfine splitting is a strong indication for a dominant ZFS E. On basis of the given hyperfine splitting the upper limit for the residual magnetic field is around 0.4 G. With a splitting of 27.4 MHz (E=(13.7 ± 0.1) MHz) the condition $E \gg \beta_0$ is well satisfied, allowing to use the model defined in equations (3.35) to (3.37). The optimal control pulse has been optimized for an amplitude scaling from from 0.9 to 1.1, allowing a shift in D from 0 MHz to 0.3 MHz. The overall pulse length was 3000 ns with a sampling of 10 ns. A FNE of 0.06 was reached. Nevertheless, if again setting the threshold to 50% of the overall signal one still get a bandwidth of 1 MHz in detuning. Even if the amplitude tolerance was set from 0.9 to 1.1, the pulse performs well within an amplitude range of 0.8 to 1.3.

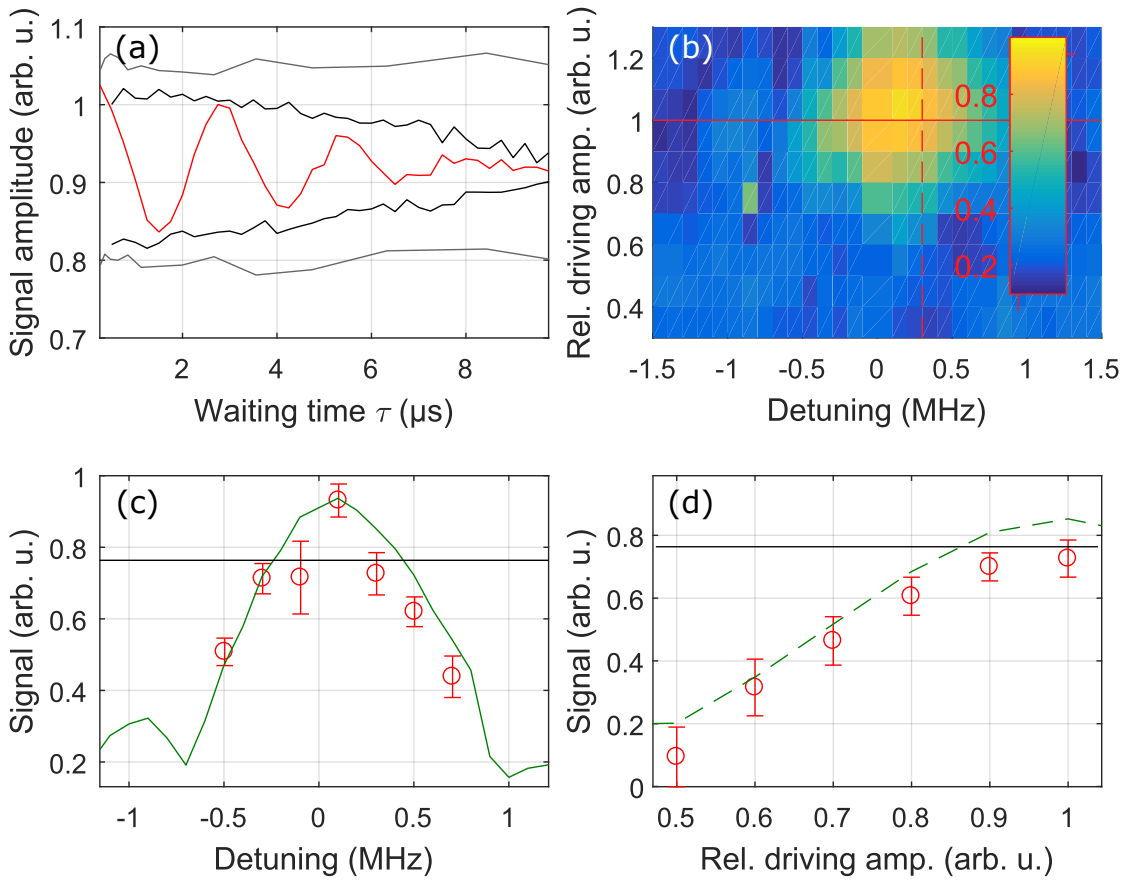

Figure 6.17. Coop-D-Ramsey performed on single NV in a ND: (a): Different pulsed measurements: T_1 (gray), Hahn Echo T_2 (black), Coop-D-Ramsey (red) IRF for the best measurement. **(b):** Simulated signal contrast. The red solid and dashed line mark the parameter region where the measurement contrast had been determined also experimentally. **(c) and(d):** Acquired and re-normalized signal contrast measured along the red lines in (c). The black line indicates the signal from HE result. The green solid and dashed line are extracted from (b) including a $^{14}\mathrm{N}$ hyperfine interaction of $400\,\mathrm{kHz}$. For renormalization a T_1 measurement was used.

6.3.4. Coop-D-Ramsey: single NV in a rotating ND

To test the performance of the Coop-D-Ramsey for an even more complex situation, 25 µl of ND stock solution ("M19-S11c", SN: AA00M7, Diamond Nanotechnologies Inc.) have been mixed with 25 mg agarose (target concentration 5 wt%, Agarose Typ 1-A A0169, Sigma) in 475 µl purified and deionized water. After heating the mixture for 30 min at 90 °C, the sample is put into a spectroscopic cell culture dish, whereas the observation glass has been replaced by a micro-structure hosting an omega structure with a ring diameter of 500 µm for microwave excitation. After filling additional water into the cell culture dish to prevent the agarose matrix to dry out, the cap of the dish is sealed with para-film to prevent water evaporation.

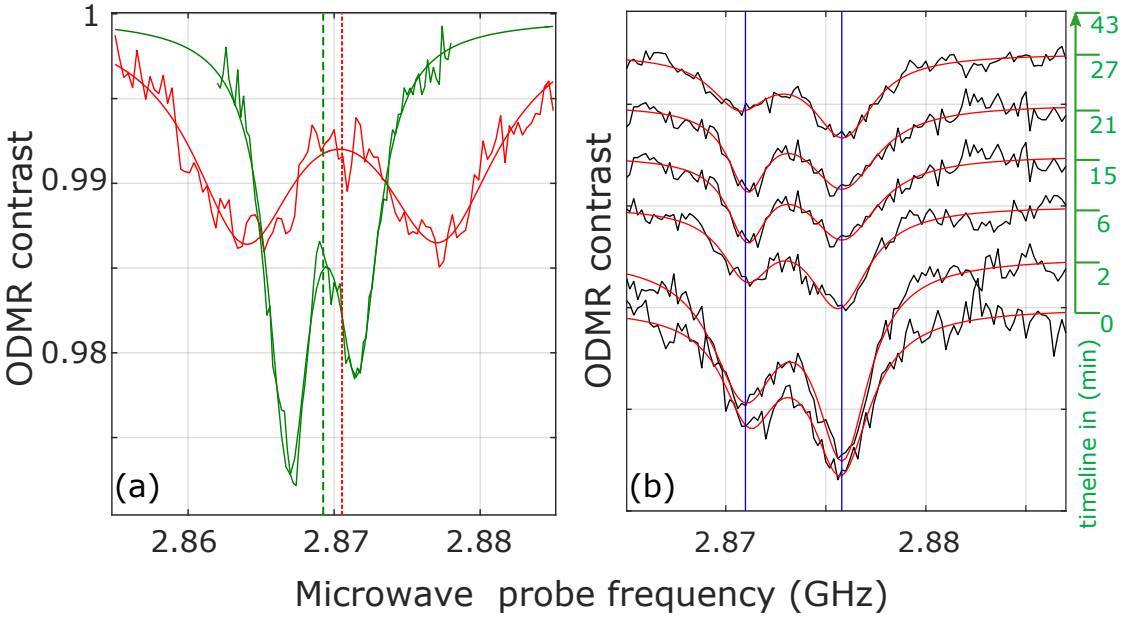

Figure 6.18. Compensation of external magnetic fields. (a): ODMR of a ND containing several NVs. The line splitting reduces from (13.3 ± 0.9) MHz to (4.7 ± 0.2) MHz. The center shifts from (2870.5 ± 0.4) MHz to (2869.3 ± 0.1) MHz **(b):** ODMR of single rotating ND measured over time. Time intervals are given in green on the left side of the plot. Individual ODMR measurements are vertically stacked for better visibility.

Advanced magnetic field compensation A magnetic field perpendicular to the NV spin quantization axis shifts of the ODMR lines into the same direction. One

may mistake the rotation of a ND as a temperature shift. Therefore the external magnetic field has to be compensated as good as possible. To this end, the sample has been mounted on a stage equiped with three coils, having a diameter from 8 cm to 9 cm. The coils were arranged in a way, that the magnetic field of all three coils was aligned almost perpendicular to each other. The configuration allows to compensate a residual field in arbitrary direction within some few Gauss. Afterwards a cwODMR spectrum of a ND containing multiple NVs was acquired. With the coils just turned off, one measured the red spectrum shown in figure 6.18(a). The left and the right transitions have been fit to a simple double Lorentzian to extract the line splitting and the center of all transitions. After compensating the residual magnetic field by continuously optimizing the ODMR spectrum to shift to lower frequencies and thinning of the left and right transitions, one got as a result the green line, shown in the very same figure. The line splitting was reduced from (13.3 ± 0.9) MHz to (4.7 ± 0.2) MHz. The center shifted from (2870.5 ± 0.4) MHz to (2869.3 ± 0.1) MHz. Estimating the original field that has been compensated, lead to (2.2 ± 0.2) G on basis of equation (3.31). With the compensated field a single NV was searched and the ODMR spectrum was probed several times over time. As one can see in 6.18(b) the overall shape of the measured ODMR spectra changed it's shape drastically over time. But the position of left and right transitions show no significant change to the average value plotted as blue lines.

Testing Coop-D-Ramsey on single slowly rotating NV Similar to former analysis, a single NV in a rotating ND has been pre-characterized before performing the Coop-D-Ramsey scheme. To verify that only a single NV is monitored, $g^{(2)}$ has been measured: Figure 6.19(a) shows the result in case of background correction. The anti-bunching at $\tau = 0$ drops well below 0.5, indicating the detected photons originate from a single emitter. Probing the ODMR spectrum revealed figure 6.19(b) for a Rabi amplitude around 0.7 MHz. Fitting the acquired data with 6-fold Lorentzian fit, revealed a hyperfine splitting of (0.67 ± 0.37) MHz. By halving again the microwave driving strength a hyperfine splitting of (0.68 ± 0.10) MHz was calculated. Assuming the residual splitting to be originated from the ZFS E, a hyperfine splitting of (0.81 ± 0.30) MHz is calculated. To cover the hyperfine lines the hyperfine ensemble includes the values 0.00 MHz, ± 0.65 MHz and ± 1.3 MHz as

magnetic shifts. As one desired to measure temperature, the resolution in possible detunings was set from 0 MHz to 0.3 MHz in five steps. A relative amplitude variation of 0.7 to 1.3 in 0.1 steps was introduced for an absolute driving amplitude of 4 MHz. The pulse was optimized until a FNE, describing the discrepancy between adjusted and desired state in terms of the Frobenius norm, of 0.12 was reached. The calculated overall error is a bit about the aim of 0.1, but as the pulse already had to be prolonged to 4000 ns (16 multiples of Rabi period, with 50 ns resolution), this has to be understood as a tradeoff between pulse length and precision. To

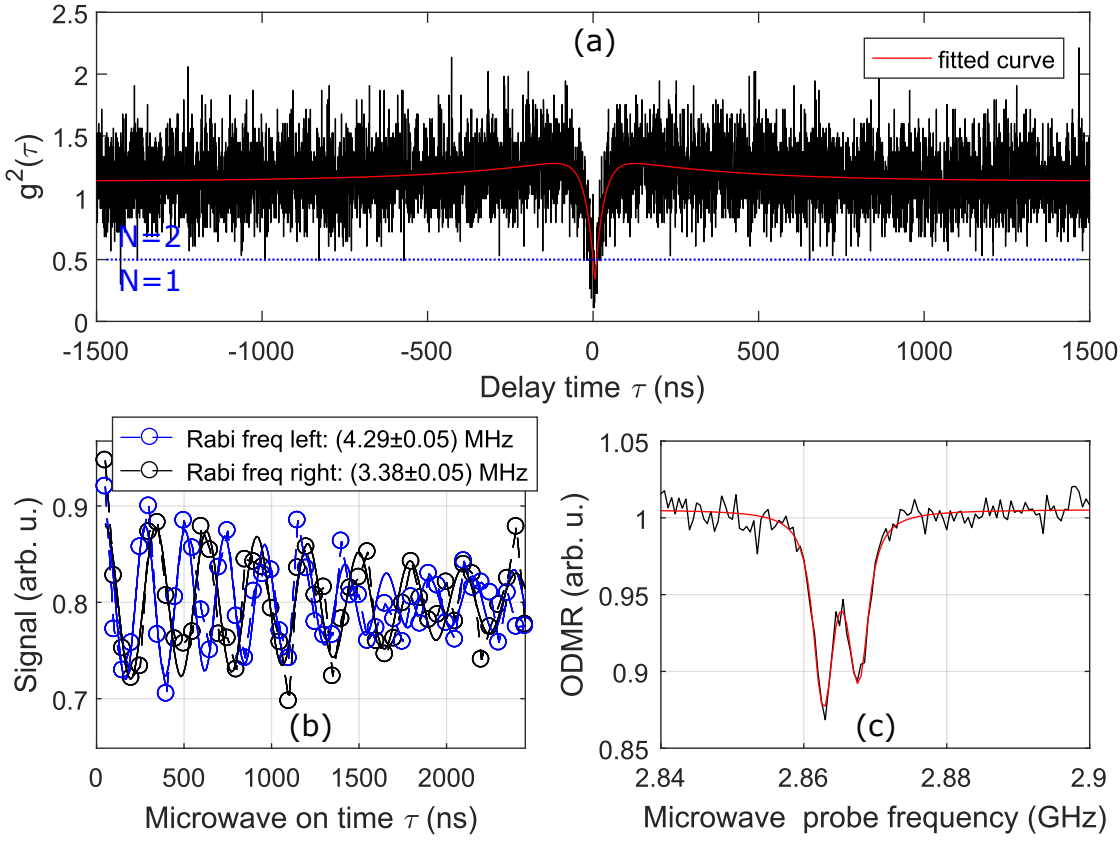

Figure 6.19. Characterization of a single NV in a rotating ND (a): Background corrected $g^{(2)}(\tau)$ function (black) with 3 model state fit (red). $N = 1.4(\pm 0.2)$. **(b):** Rabi ozillation on right (black) and left (blue) peak in (c). **(c):** cwODMR (black) of single NV. Lorenzian fit (red) including 6 lines (see also text). The fits in (b) and (c) include a ^{14}N hyperfine splitting around 700 kHz that is reduced because of E. Rabi oscillations are show as the normalized spin signal contrast.

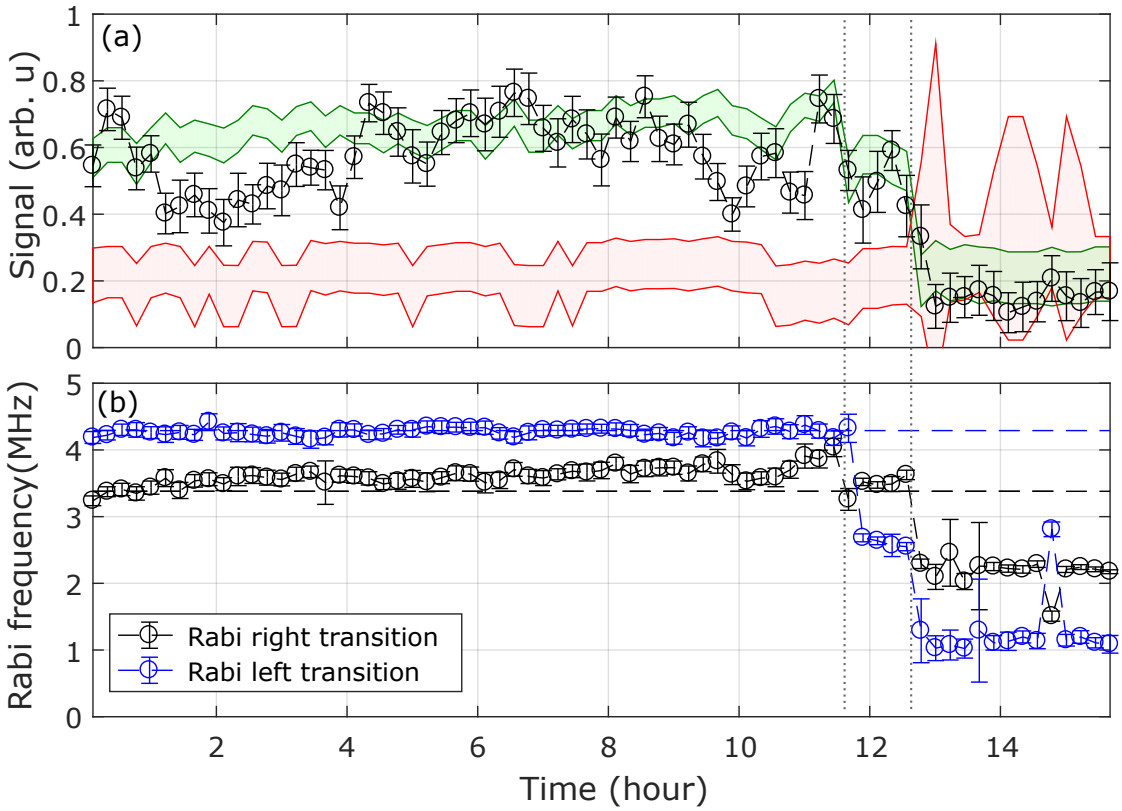

Figure 6.20. Analysis of Coop-D-Ramsey for a rotating ND. (a): A Signal contrast of 1 means maximum spin contrast. Simulated contrast for Coop-D-Ramsey (green) and D-Ramsey (red) using the measured Rabi frequencies as input parameters. **(b):** Rabi frequency of left and right transition, extracted by a 3 state model fit. Blue dashed lines indicate the initial Rabi frequency of individual transitions. Grey dotted lines indicate a rapid change in the transitions driving amplitude.

identify changes in the relative driving strengths of both transitions, the overall sequence contained, beside the Coop-D-Ramsey, a Rabi measurement on left and right transition. Later ones are used to calculate the maximum signal contrast by fitting both transitions to a three state Rabi oscillation model. Figure 6.20 shows the signal amplitude and measured Rabi frequencies over time. In addition, the expectable contrast simulated is plotted in red. As one can see almost a contrast of 80 % is reached. More interestingly around 11 h after starting the measurement, a drastic change in left and right driving strength occurs, but the signal contrast shows only slight variations. After 12.5 h the signal contrast drops again drastically

as the orientation of the ND becomes unfavored to excite both transitions. The predicted signal amplitude (green area) corresponded well to the measured value. In addition the signal contrast one would have if using a D-Ramesy, was plotted as red area. To compute the shown result, the Rabi amplitudes measured in the beginning has been chosen. For low Rabi amplitudes (after $\sim 12\,\mathrm{h}$) the red area expanded dramatically. The reason for latter is a result of an increasing confidence interval when fitting the simulated pulse response. Analyzing the measured detuning result

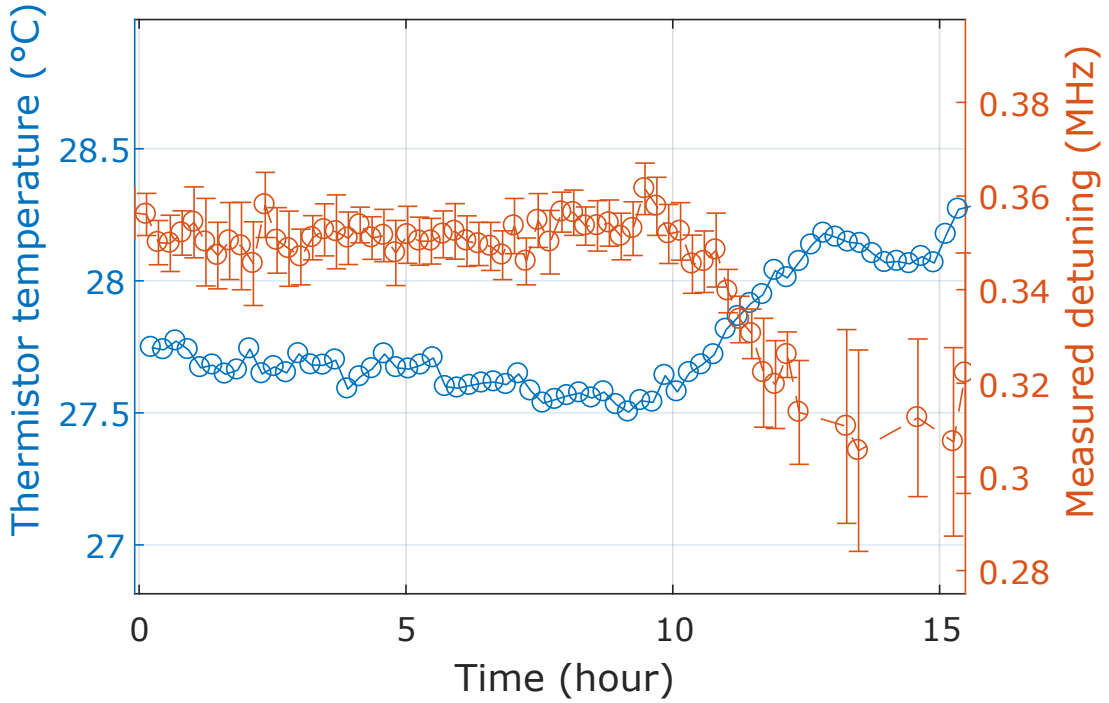

Figure 6.21. Temperature measurement using a Coop-D-Ramsey. (red): Measured detuning using a Coop-D-Ramsey. **(blue):** Temperature reference using a thermistor.

in figure 6.21. The calculated shift in D per Kelvin is 60 kHz what is in good agreement with literature values [137, 4].

6.4. Summary, Conclusion and Outlook

A new scheme for robust pulsed nano-thermometry was developed based on the so called D-Ramsey scheme. To this end optimal control theory was applied. To optimize the compiled microwave pulses to a desired functionality, the package "dynamo" developed by Ville Bergholm and Shai Machnes has been used. "Dynamo" utilizing the so called GRAPE-BFGS method. In addition, "dynamo" allows a cooperative pulse design by applying quantum state filters at a desired position in time. Therefore the explicit spin Hamiltonian of NV was formulated. After designing the necessary quantum state filters, the optimum parameter range for the Coop-D-Ramsey has been identified. This includes the relative time for each individual cooperative pulse segment that form the Coop-D-Ramsey scheme. The shortest pulses are generated, when the center pulse segment is four time larger then the first and the last segment. With the optimized parameters, pulses have been tested on fixed NVs in bulk diamond and nanodiamonds. Nanodiamonds have been fixed transversely in a 5 % agarose matrix, and the performance of a Coop-D-Ramsey has been tested under slow rotation of the ND. A maximum signal contrast of almost 80 % has been reached for the fixed NVs. In case of the slowly rotating ND, the Coop-D-Ramsey outperformed the square pulse by a factor of almost 3. The monitored shift in the ZFS D correlated well with the change in the reference temperature measured by a thermistor.
Simulating the evolution of a D-Ramsey (square pulses) for a model NV in bulk diamond yields to a signal contrast of around 40 %, for comparable conditions set in the experiment. Similar results have been obtained for the adiabatic pulse scheme BIR4. Using BIR4 pulses instead of square pulses increase the robustness of a D-Ramsey scheme. However, the time to apply a BIR4-D-Ramsey, had to be extended to several tens of microseconds to accomplish reasonable results. For a successful application of the Coop-D-Ramsey sensing scheme, $\sim 4\,\mu s$ are necessary for a Rabi driving amplitude of $\sim 4\,MHz$. In theory this allows to sense changes in temperature close to the megahertz regime.
Having this new tool at hand, one can sense temperature changes in complex environments, such as living cells. In addition, the high temporal bandwidth of the Coop-D-Ramsey scheme, close to megahertz, may allow in future precise sensing of

temperature fluctuations.

7. Chemical sensing

Similar to temperature sensing, also for chemical quantities like oxygen, GSH and pH, sensor systems have been developed based on fluorescent probes. Again, changes in emission properties are monitored: For example photon up-conversion [9], spectral shift [71], overall intensity [194, 75] and other properties [171, 115]. Also the charge state of NV in nanodiamonds has been shown to be responsive to changes in pH after surface modification [145]. As the developed sensor is in principle sensitive to any kind of ion species close to the surface, it is not selective. To overcome this limitation, the capacities of an already established hybrid system has been enhanced to a modular sensor platform [159]. To this end, NV decorated nanodiamonds are used [157], they are later utilized as a readout bus of the sensor state. After the surface of the nanodiamond was modified with a sub-nanometer sized silica shell, the polymer poly[(2-hydroxypropyl)methacrylamide] (HPMA) can be directly grown on the surface by a "grafted from" approach [158, 132, 159]. A Gadolinium (III)-complex is attached to the polymer via a cleavable or non cleavable linker (Figure 7.1). The Gd(III)-complex is creating a stochastically fluctuating magnetic field that can be sensed by NV^- *via* spin state lifetime relaxometry [200, 95]. Therefore the NV center is initialized into the spin sublevels $m_s = 0$, after a characteristic time, depending on the distance and amount of Gd(III)-complex in the direct vicinity of the nitrogen vacancy center, the spin state will equilibrate in a superposition by the presence magnetic field noise. If the Gadolinium(III)-complex is released after cleavage of the linker, the extracted spin state lifetime of the NV^- will increase. Thereby the cleavage rate will be a measure of the quantity, which is studied.

In this work two different kinds of sensors have been quantified. One is capable to measure pH, and the other one measures the presence of a reducing agent. (see Figure 7.2). In addition, two control samples, one with a Gd(III)-complex,

but without a cleavable linker (sample: ND-HPMA-Gd), and one without any Gd(III)-complex (sample: ND-HPMA), have been used for calibration. All chemical modifications have been done by Jitka Neburkova and coworkers (for more details see ref [159]).

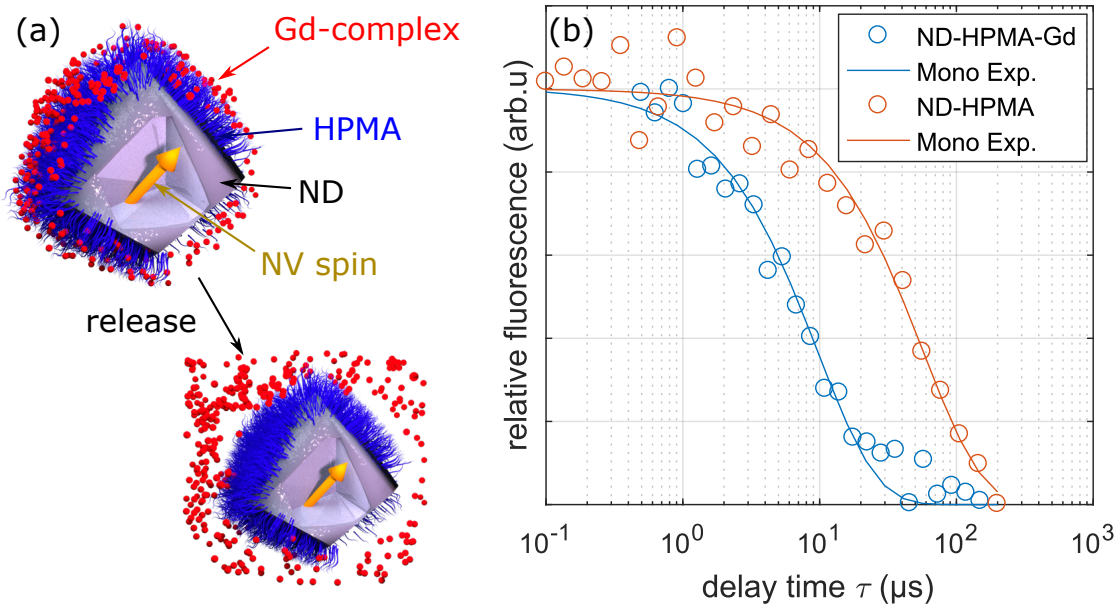

Figure 7.1. Chemical sensing with NV in ND. (a): By reading out the spin lattice relaxation time of NV^{-}, the concentration of surrounding Gd(III)-complexes is probed. The latter are linked via a cleavable linker to the co-polymer HPMA. If the linker is cut, the Gd(III)-complex is released. **(b):** Probing the spin lattice relaxation time of two control samples with (ND-HPMA-Gd) and without (ND-HPMA) Gd(III)-complexes attached to it.

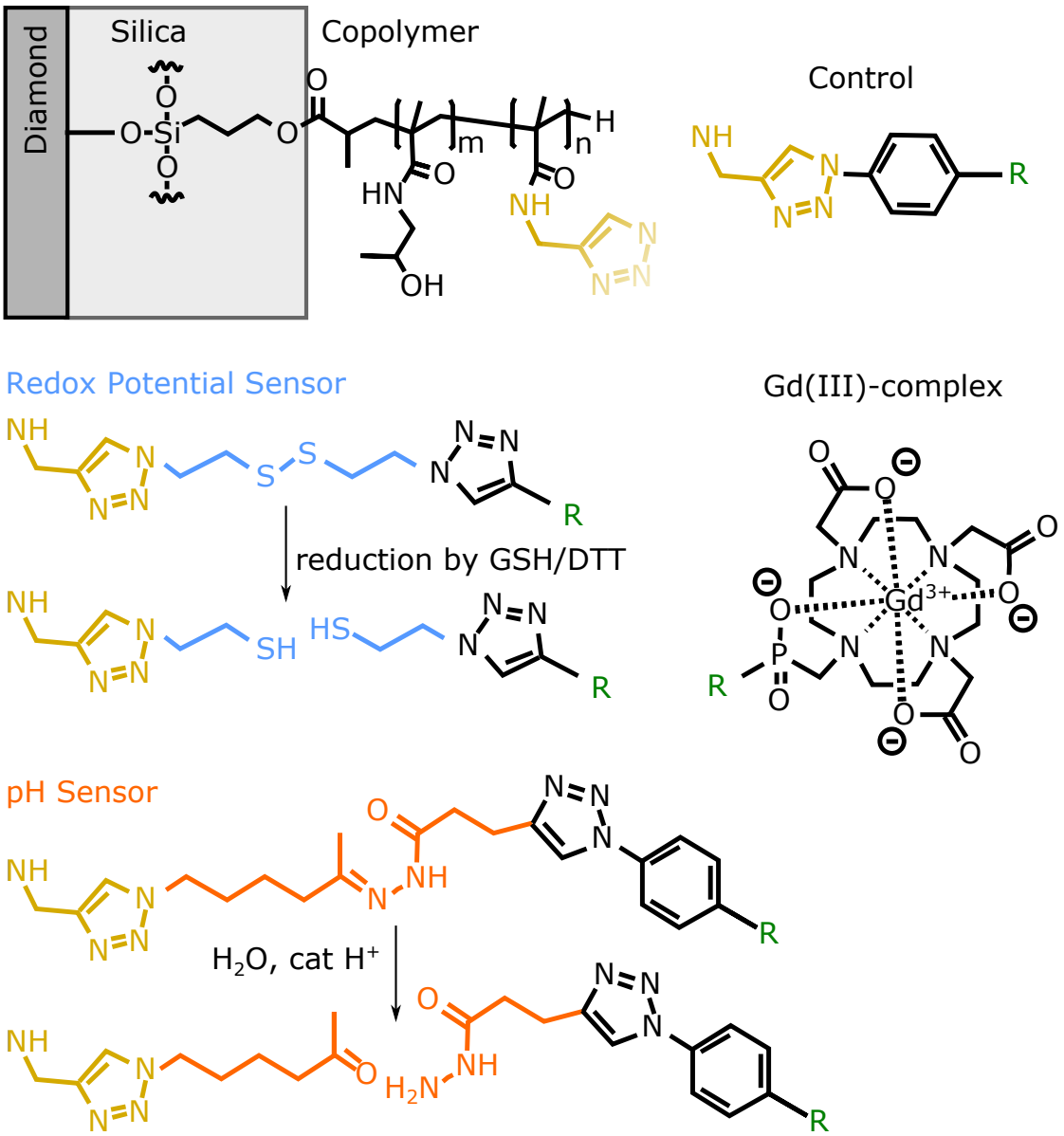

Figure 7.2. Overview of chemical sensor species. The upper left sketch shows a schematic drawing of the ND surface with a silica shell that host the co-polymer HPMA. One of the free morities can be modified with a linker unit connecting the polymer with the Gd(III)-complex. Two different sensor units have been tested throughout this work. First one is a pH sensitive linker (orange) and second the redox potential sensor (light blue).

Setup for chemical sensing. To test different samples, a confocal setup as described in figure 7.3 was used. Green laser light is modulated via an AOM, filtered by bandpass (cleanup, BP532/50) and guided into a PC fiber. A dichroic mirror with a nominal cutoff at 664 nm, or and bk7-window, deflect light onto the objective. The emission of NVs pass the dichroic mirror and is detected again

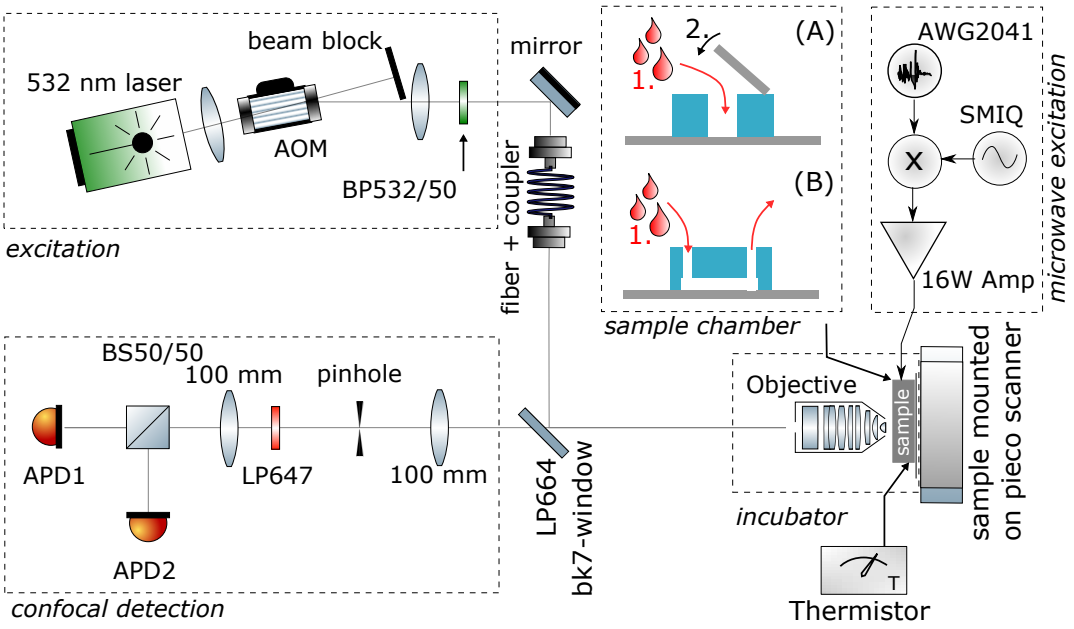

Figure 7.3. Experimental setup for chemical sensor species. For further information see text.

with two APDs in a HBT configuration. To suppress leaking light from the laser a long-pass filter (LP647, Razor Edge, Semrock) is used. To manipulate the NV spin system one AWG (AWG2041) is connected to a mixer (ZX05-C60LH-S+,mini-circuits). The local oscillator input is connected to a frequency source (SMIQ03B, Rohde&Schwarz). The mixer is then connected to a microwave switch (ZASWA-2-50DR+,mini-circuits) allowing to additionally suppress microwave excitation. After the switch the microwave excitation is amplified by a 16 W amplifier (ZHL-16W-43+, mini-circuits) that is directly connected to the sample. For bulk NVs and fixed ND a simple copper wire stretched over a cover glass is used. To test the pH dependence of individual fixed crystals, the sample is injected into a PDMS

chamber (figure 7.3, sample chamber configuration (B)). The latter has been glued with epoxy to the modified cover slide. To monitor the sample in an open droplet, a simpler design is used (figure 7.3, sample chamber configuration (A)). A PDMS block with a hole in the middle has been glued to the modified cover-slide to form a chamber with approximate 150 µl volume. The upper side of the chamber has been sealed with another cover slide after sample injection. To monitor the temperature of the sample, a thermistor is connected to the sample holder. In addition, the temperature can be controlled using a incubator system (Objective heater system: tempcontroller mini, Recon; Sample heater system: tempcontroller 37, Recon). For measurements in an open droplet a water immersion objective (UPlanApo 60x NA 1.2, Olympus) and in all other cases an oil immersion objective (UPlanFL 100x NA 1.3, Olympus) is used. The setup is fully controlled *via* custom made software programs written in "python".

7.1. Experimental characterization of hybrid sensor platform

In the following section the main experimental results are summaries. First the used pulse scheme, a chirp pulse, was analyzed for its robustness and was compared to theoretical simulations. Then the introduced hybrid sensor system has been characterized.

7.1.1. Experimental determination of robustness in spin inversion utilizing linear chirp pulses.

In principle, measuring T_1 is simple and could be implemented in already existing commercial devices by minor modification, because only light modulation in the nanosecond range is required. As the fluorescence of the NV^- can also hold information on its charge state, one has to apply a second control that requires microwave excitation [72]. Therefore one inverts the population of the spin state sublevels using a π-pulse. By comparing the control with the sequence without the π- pulse, one can extract the spin state. To introduce a spin inversion, an adiabatic

passage in form of a simple chirp pulse was used. This pulse type is robust against resonance detuning and changes in the microwave driving power [65] (see figure 7.4.). As one can see in figure 7.5(b), the probability to flip the spin state of a NV^- in bulk diamond is reasonable high, as long as the chirp pulse is sweeped over the resonance. (The maximum contrast reachable is around 30 % at room temperature). As a result the bandwidth of the pulse is roughly the frequency sweep band. Therefore the sweep width will now be called the bandwidth of the linear chirp pulse. In comparison, the square π-pulse perform less optimal. The resonant Rabi frequency used is this experiment is around 2.5 MHz. The sweep rate for the former cases is $20\,\mathrm{kHz\,ns^{-1}}$. Figure 7.5 suggest, that as long as the

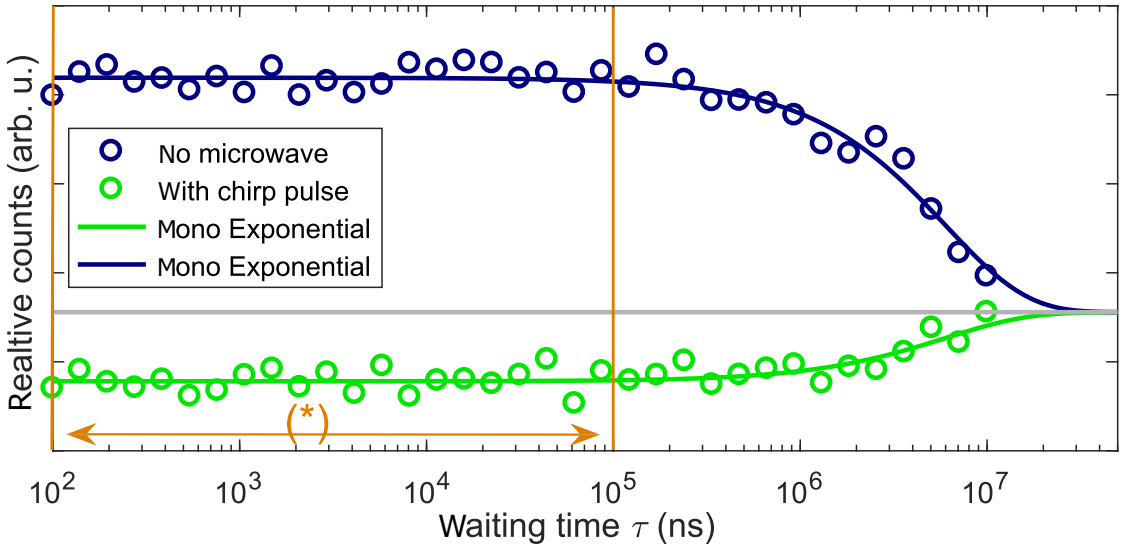

Figure 7.4. T_1 measurement utilizing a linear chirp pulse. A typical T_1 measurement for a NV in bulk diamond is shown. (blue) and (green) cycles represent data acquired with and without an additional linear chirp pulse before readout, respectively. The measured decay curves are fit to a mono Exponential decay (solid lines) revealing a T_1 of around 6 ms, for the analyzed NV. The area marked with a star (100 ns to 100 µs) had been used to extract the contrast shown in figure 7.6.

transition, which shall be driven, is well within the sweep bandwidth of the chirp, full spin inversion is provided.

In addition, one has to fulfill the adiabatic condition, meaning that in the rotating frame the sweep speed or the angular change of the effective magnetic field must be slow versus Larmor precision of the spin. As depicted in figure 7.6, the contrast

of a typical T_1 time reduces drastically, if the sweep speed is set to high, or if the MW driving amplitude (Rabi amplitude) is set to low. The sweep bandwidth was set 100 MHz to the left resonance about 25 MHz apart form the sweep starting frequency.

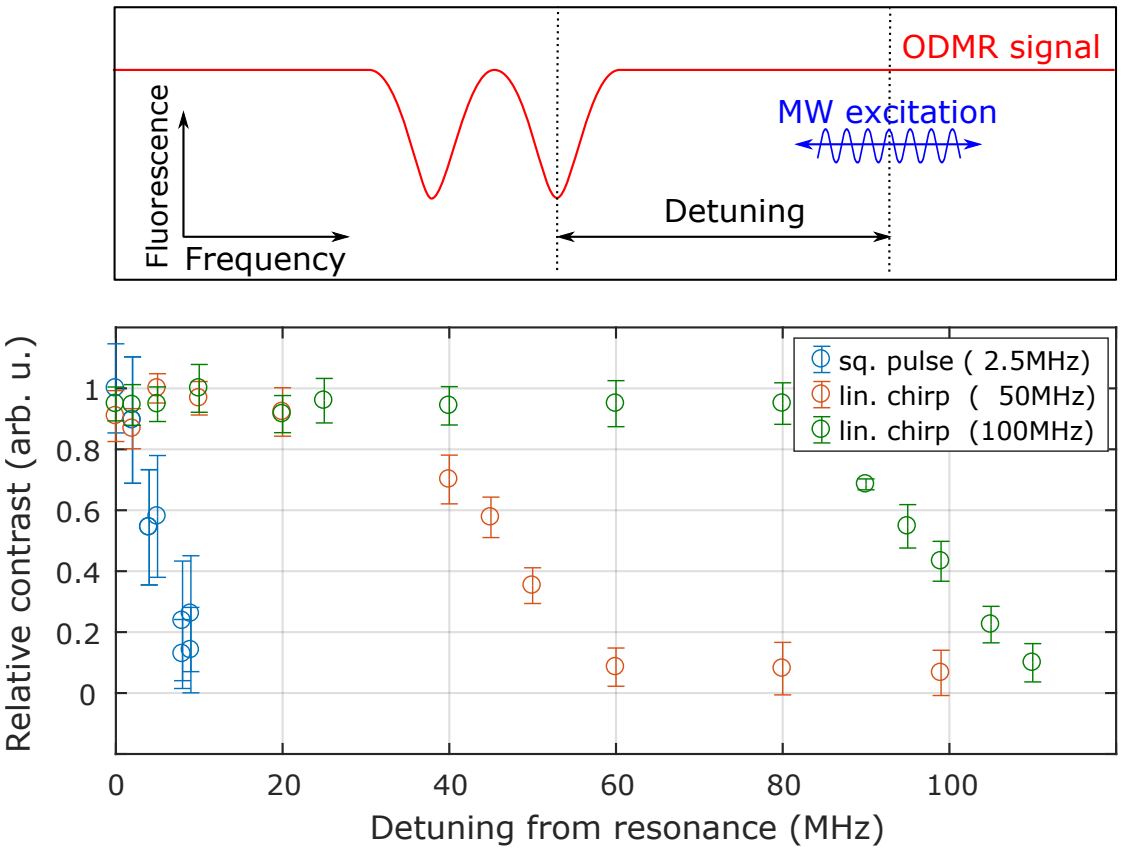

Figure 7.5. Comparing excitation bandwidth of linear chirp vs. square pulse: The **(upper graph)** schematically shows the experimental procedure to probe the bandwidth of different pulse schemes. In the **(lower panel)** the experimental results for the T_1 contrast are plotted for a square pulse using a typical microwave power corresponding to a Rabi amplitude of 2.5 MHz and two linear chirp pulses using the same power with a sweep width of 50 MHz and 100 MHz , respectively. The sweep rate for the chirp pulses was around $20\,\mathrm{kHz\,ns^{-1}}$.

In case of nanodiamonds one always has to deal with a stochastic orientions of NV. In addition, nanodiamonds, if used in a cellular environment, tent to tumble [122]. Up to now square pulses have been used on fixed NV in bulk diamond with well aligned pulse length and power, to perform maximum spin inversion with a

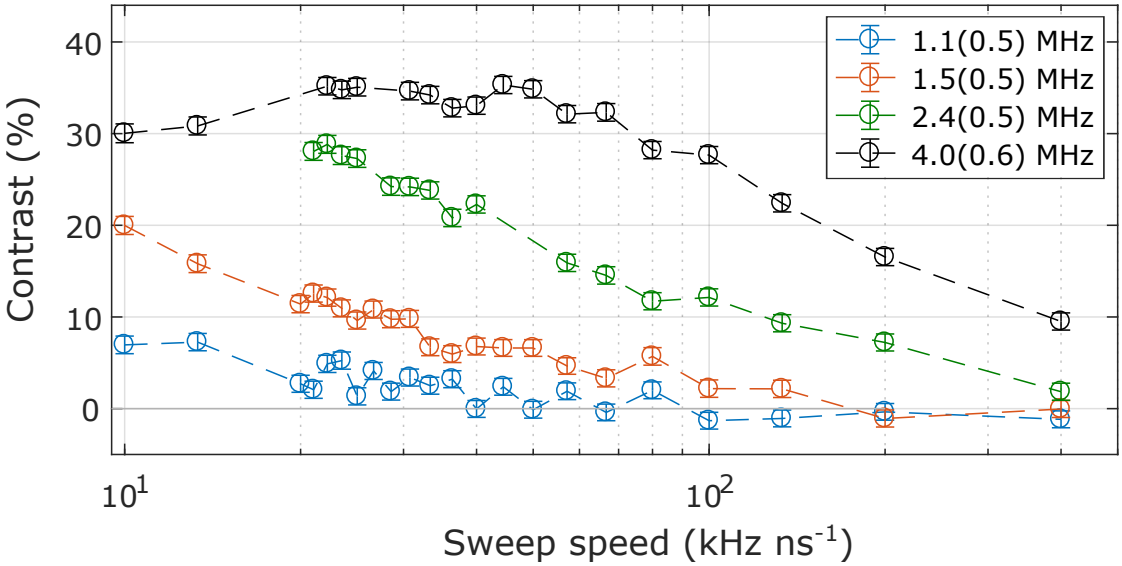

Figure 7.6. Performance of linear chirp pulse versus sweep speed. Sweep speed for different microwave powers. The legend indicates the extracted Rabi frequencies. To extract the T_1 contrast the area marked with a star (100 ns to 100 µs) in figure 7.4 has been used to extract the contrast.

π-pulse. In an ensemble this is only possible to a certain degree, as the amplitude of the driving field for a transition, is depending on the NV spin quantization axis relative to the driving field vector. In an ensemble this means that only a fraction of the spins can be manipulated as desired. The consequence is, that one looses spin contrast in a T_1 measurement, if microwave pulses have to be used. To quantify this behavior the sample ND-HPMA was drop-casted on a cover slide and dried out forming big clusters. The estimated number of NV per confocal spot was around several hundreds of emitters, based on the measured fluorescence level. Figure 7.7(a) shows an typical ODMR of the analyzed cluster. In addition, in figure 7.7(b) and 7.7(c) the linewidth and signal contrast of the ODMR lines are plotted as a function of microwave and laser power. As the contrast continuously drops, the linewidth of the two transitions seem to saturate around 12 MHz to 14 MHz, depending on the used laser power. HE measurements of the very same well dispersed ND sample, has been carried out, resulting in an average transverse relaxation time (T_2) time around 0.9 µs (see figure 7.13(b)) for single to few NVs. This is a typical value for NDs [201, 108, 205]. The natural line width of a single

ODMR line is expected to be in the range of several hundreds of kilohertz to megahertz regime, but not in the range of several tens of megahertz. Therefore the observed line broadening in attributed to be a characteristic of the spread in the ensemble. Differences in the zero field splitting parameter E [24, 122] from NV to NV and also a residual magnetic field like the earths magnetic field can be the origin of this splitting. Repeating the measurement in bulk diamond for different driving strengths and sweep speeds resulted in the data shown in figure 7.7(d). As expected, the square pulse (purple line) showed reduced spin contrast compared to the chirp pulse. But again with decreasing driving power, expressed in the effective Rabi frequency for the ensemble, the contrast of the T_1 measurement drops. The faster the sweep speed, the earlier this drop appears for the chirp pulse. Again the sweep bandwidth was set to 100 MHz starting around 25 MHz from the center of both peaks.

For estimating the sensitivity enhancement when using chirp pulses, the quantity enhancement factor EF was defined. Thereby EF describes the relative power noise equivalent for a measurement performed with a linear chirp versus a square pulse:

$$EF = \frac{c_{\text{chirp}}}{c_{\text{sqr}}} \cdot \sqrt{\frac{t_{\text{sqr}}}{t_{\text{chirp}}}} \tag{7.1}$$

With c_{chirp} and c_{sqr} being the T_1 contrast and t_{chirp} and t_{sqr} the overall sequence length of a given measurement. As one can see in figure 7.8, the chirp pulse almost always performs better then the square pulse, in the case of an ensemble. For a sufficient low sweep speed of around 40 kHz ns^{-1}, an enhancement of two is achieved. As EF can also be understood as a gain in sensitivity, one can conclude that an experiment performed on an ensemble with a chirp pulse is twice as sensitive in comparison to a square pulse. In addition, the broad acceptance range of the driving amplitude reduces the need for a careful calibration before starting an experiment.

As the linear chirp pulse belongs to the class of adiabatic passages, also the adiabaticiy factor Q, quantifying the performance of a sufficient inversion in the spin states, is of interest. Based on the measured Rabi frequency and the sweep speed, Q was calculated using equation (3.62) and plotted in figure 7.9. The contrast dropped to a factor of 1/2 around a Q factor of 2. In later experiments

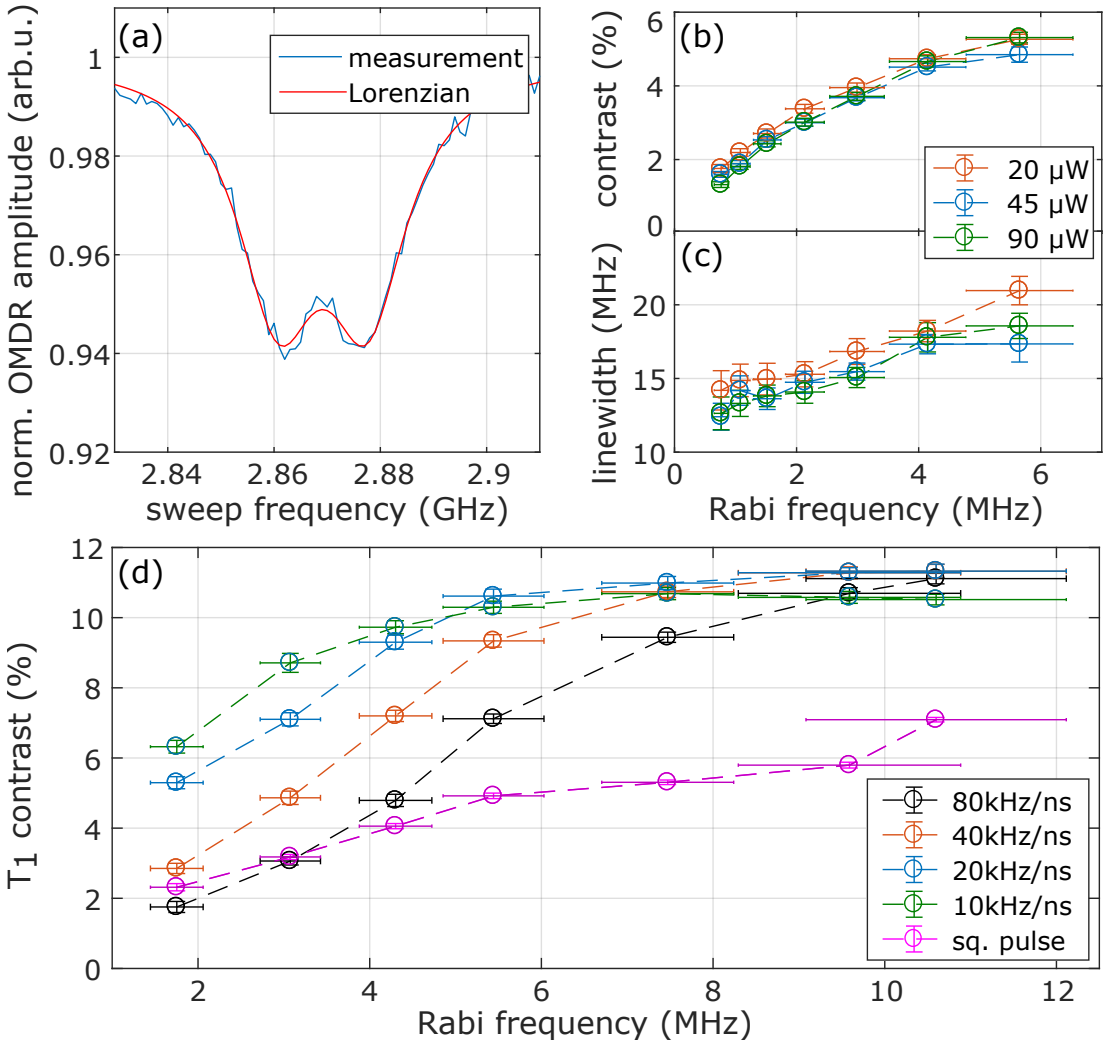

Figure 7.7. Microwave power dependence of measurement contrast using a linear chirp pulse: (a): normalized ODMR spectra of a dense ND ensemble containing more then several hundreds of NVs of the sample ND-HPMA-Gd dried on a cover slide. A excitation laser power of $20\,\mu\mathrm{W}$ with $4.3\,\mathrm{MHz}$ MW driving strength (Rabi amplitude) has been applied. **(b)** and **(c)**: extracted Lorentzian linewidth and contrast of ODMR signal like shown in (a) varying the laser and MW excitation strength. **(d)**: extracted contrast of a T1 contrast applying the same procedure as in Figure 7.4, for different sweep rates with a typical sweep bandwidth of $100\,\mathrm{MHz}$.

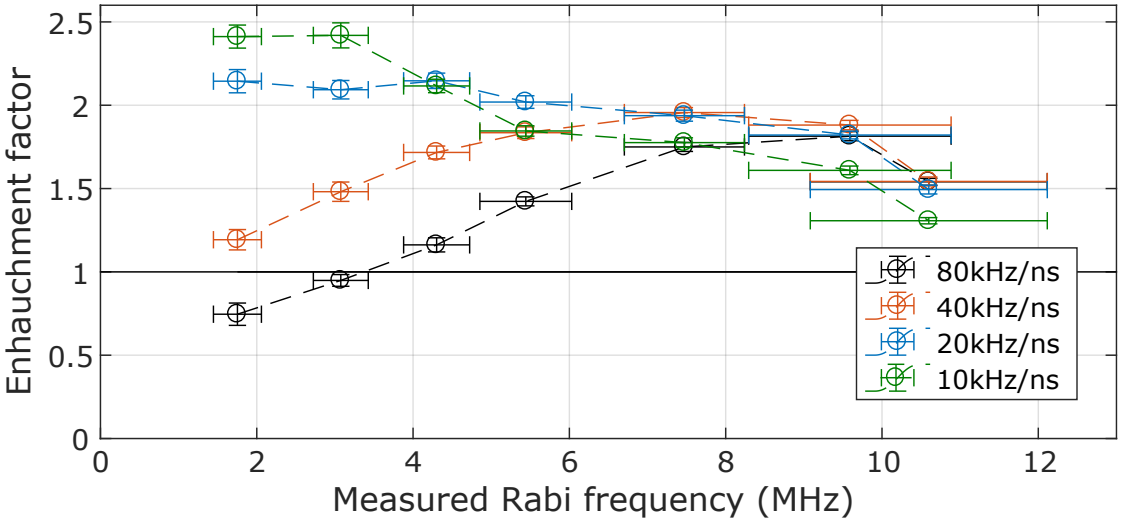

Figure 7.8. Relative enhancement in sensitivity using chirp pulse vs square pulse. Based on figure 7.7(d) the expectable enhancement in sensitivity had been calculated. See equation (3.62), 56 for calculation.

the Q, based on a contrast estimate, has been between 1.5 and 10.

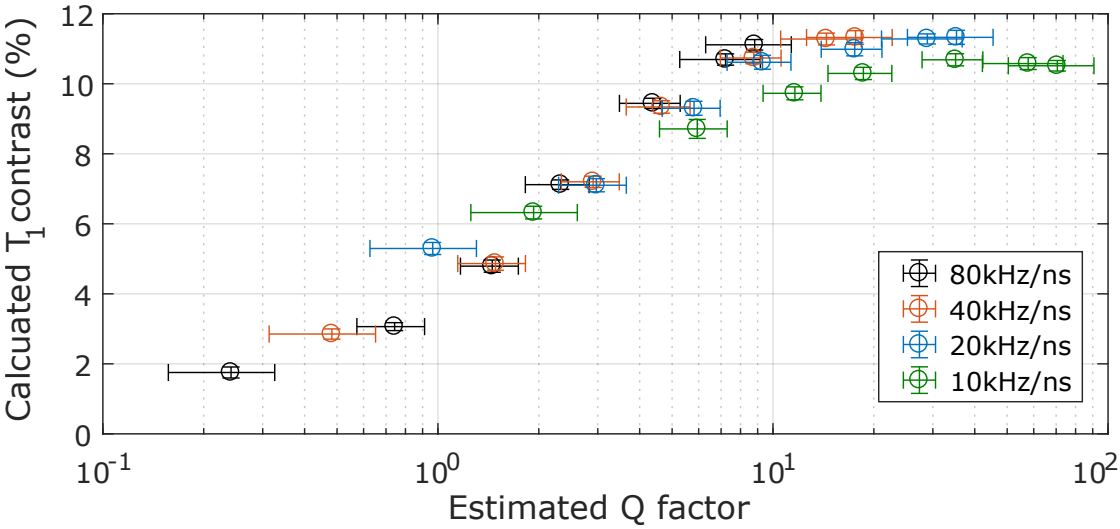

Figure 7.9. Adiabicity factor Q. Based on figure 7.7(d) also Q has been calculated for different sweep speeds (see legend).

7.1.2. Theoretical determination of robustness in spin inversion utilizing linear chirp pulse.

To analyze the behavior of a chirp pulse acting on NV^- spin sublevels, its state evolution is simulated by numerically solving the von Neumann equation:

$$i\hbar\frac{\partial\rho}{\partial t} = [H, \rho] \tag{7.2}$$

Equation (7.2) can be solve numerically using the "*ode*45"-function in "Matlab", which utilizes a numerical ordinary differential equation solver based on a fourth order "Runge-Kutta" algorithm. For the driving field B_1 a linearly polarized MW

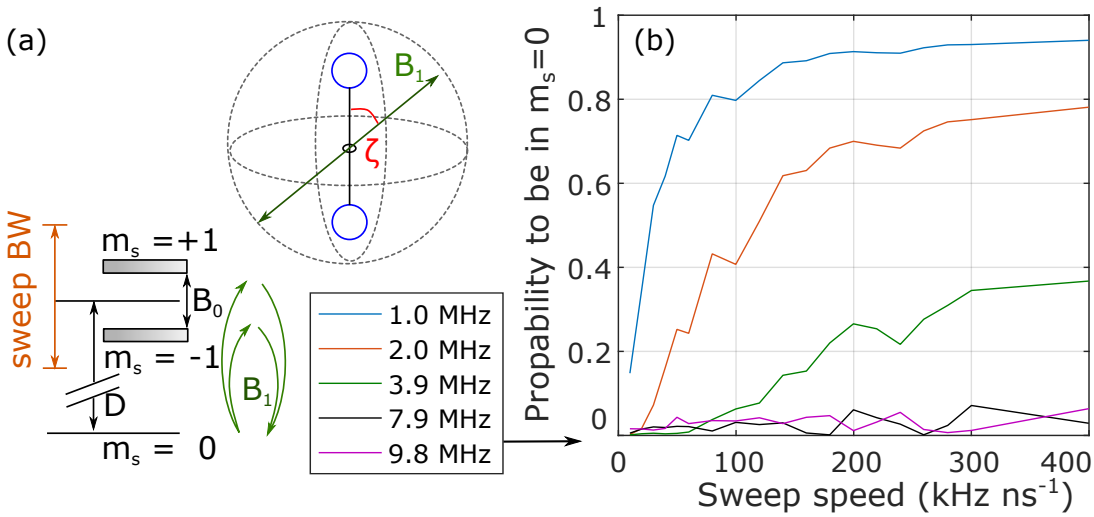

Figure 7.10. Simulation: Robustness of linear chirp pulse vs. square pulse. (a): Sketch of the performed simulation: The MW excitation B_1 is turned along the polar angle ζ using the Hamiltonian in section 3.2.4 equation (3.15). **(b):** Simulating the probability to be in $m_s = 0$ for different MW driving strengths dependent on the sweep band width for $\zeta = \pi/2$.

excitation along the xy-plane of the NV reference frame is assumed (see figure 7.10), while its z-component are neglected for simplification. The desired broadening and splitting of the EPR transitions is treated as a Zeeman-term, which would be introduced by a magnetic field aligned along the NV quantization axis. Both transitions are split by 16 MHz similar to the splitting visible in figure 7.7(a). The

zero field parameter E is set to zero. In this scenario only the angular dependence of the microwave excitation field versus the NV quantization axis with angle ζ is relevant. The broadening introduced shall be inhomogeneous, i. e. is modeled as a Gaussian distribution. Similar to the experimental results, in the following simulations the population of $m_s = 0$ as the bright state of NV has been plotted, as this is also probed in real experiment [1]. Following the experimental procedure, the chirp pulse with a band width of 100 MHz was swept in the simulation as well, starting 25 MHz away from the centers of both resonance peaks. In a first step no broadening of the EPR lines was assumed.

First, ζ is set to $\pi/2$, the state evolution with a chirp pulse was simulated and the final population in $m_s = 0$ was examined. Similar to figure 7.6, an increase of the sweep speed and altering the driving strength (Rabi amplitude) results in a reduction of spin population inversion.

In a next step the sweep rate was fixed to 40 kHz ns^{-1} and the spin system was simulated for different polar angle ζ and varying amplitude of the driving field (see figure 7.11). The simulation was repeated for an inhomogeneous line broadening of 3 MHz. Both calculations have been repeated for a simple square pulse. The needed length for the π-pulse is extracted from an ensemble-like average Rabi oscillation plot of all polar angles ζ. Interestingly, no line broadening (0 MHz) results in a better performance of the square pulse for almost all angles. Only if the driving power is set to values above $\sim$ 8 MHz, the chirp pulse is better (fig. 7.11(a) versus 7.11(b)). This behavior changes if a broadening of 3 MHz is introduced[2] (fig. 7.11(c) versus 7.11(d)). Again, repeating all the mentioned calculations for different line broadenings and averaging over all possible angular orientations ζ, one can extract the enhancement by a chirp pulse versus the square pulse (see figure 7.12). Interestingly, the chirp pulse doesn't seem to be effected by the broadening of the EPR lines at all. Again a very broad acceptance range in terms of the driving field strength is visible. Taking the linewidth extracted from cwODMR in figure 7.7 of 12 MHz for a Gaussian one would get a standard deviation of 5.1 MHz.

[1] Note: a high probability to be in $m_s = 0$ means a low inversion efficiency.
[2] Note: The broadening given in this section is given in standard-deviations.

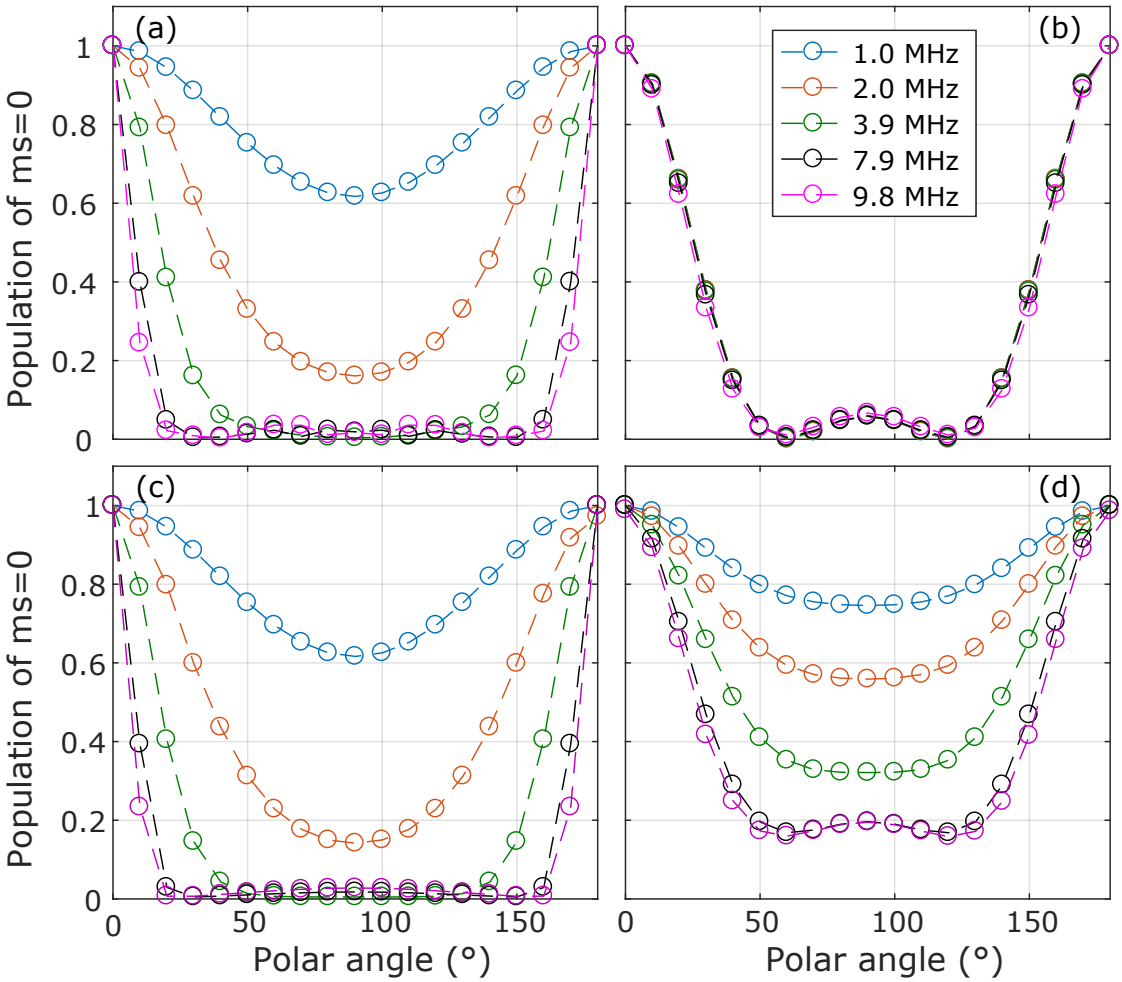

Figure 7.11. Simulation: Robustness of linear chirp pulse vs. square pulse (angular dependence). (a): linear chirp pulse with fixed sweep speed $40\,\mathrm{kHz\,ns^{-1}}$ for different MW driving strengths depending on the polar angle ζ. For a $0\,\mathrm{MHz}$ inhomogeneous broadened EPR line. **(b):** same as (a) but for a square pulse. **(c):** same as (a) but for an inhomogeneous broadened line of $3\,\mathrm{MHz}$. **(d):** same as (b) for inhomogeneous broadened line with a standard deviation of $3\,\mathrm{MHz}$.

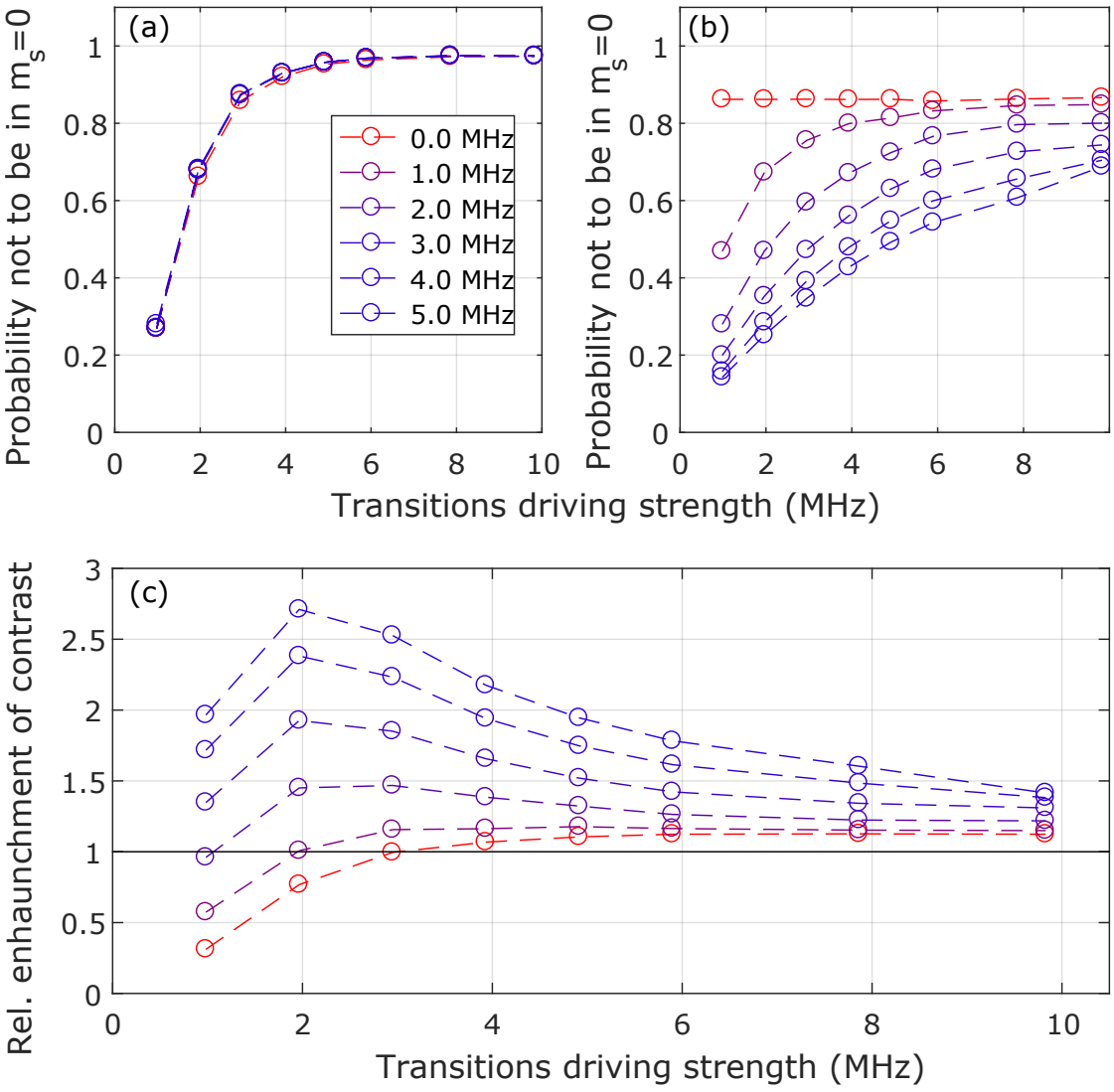

Figure 7.12. Simulation: Average performance of chirp pulse versus driving strength: (a): for a chirp pulse assuming different line broadenings as standard deviations are given in the legend. **(b):** same as (a) for a square pulse. **(c):** Enhancement of chirp pulses versus square pulses. **(c)** was calculated by taking the probability **not to be** in $m_s = 0$ for the chirp pulse divided by the result obtained for a square pulse.

Comparison between simulated and experimental results. The behavior of the theoretically determined enhancement (figure 7.12(c)) has a slightly different shape than the experimentally determined curve (figure 7.8, sweep speed 40 kHz).However, they show in principle the same behavior with an enhancement factor or two for a experimentally determined inhomogeneous broadening of around 12 MHz FWHM. In both cases the linear chirp has a very broad acceptance range in driving field amplitudes (Rabi amplitude), and simulations confirm that the chirp pulse is unaffected by inhomogeneous broadening in comparison to a square pulse, which is affected by latter.

7.1.3. Characterization of Control Samples ND-HPMA and ND-HPMA-Gd

In the following section the two control samples ND-HPMA (no Gd(III)-complex) and ND-HPMA-Gd (non-cleavable linker) are characterized for their basic optical and spin properties. In preparation, the samples were well dispersed and spin coated on a cover-slide. Then T_1 was measured in buffer solution with different pH and also varying GSH concentrations. To this end, the sample was measured in a droplet, which was placed in a PDMS chamber. Buffer solutions were prepared by Andrea Zappe. For details see appendix C.1. For examining the pH dependence, buffer system 1 was used.

Basic properties

First the sample ND-HPMA, the control sample without any Gd(III)-complexes attached to the polymer, has been spin-coated on a cover slide. A confocal scan is shown in figure 7.13(a). Every spot marked in figure 7.13(a), has been analyzed using the autocorrelation $g^{(2)}(\tau)$ to determine the number of emitters within the confocal spot. An average of 3.5 particles per spot has been determined. All spots showing a clear ODMR signature have been measured for T_1 and T_2 (see figure 7.13(c)/(d)). T_1 is spreading between tens of microseconds to almost a millisecond for 13 analyzed spots. The average is 444 µs. T_2 was in average 0.9 µs, spreading from 400 ns to 1.6 µs.
The second reference sample, ND-HPMA-Gd, was prepared and gauged in the very

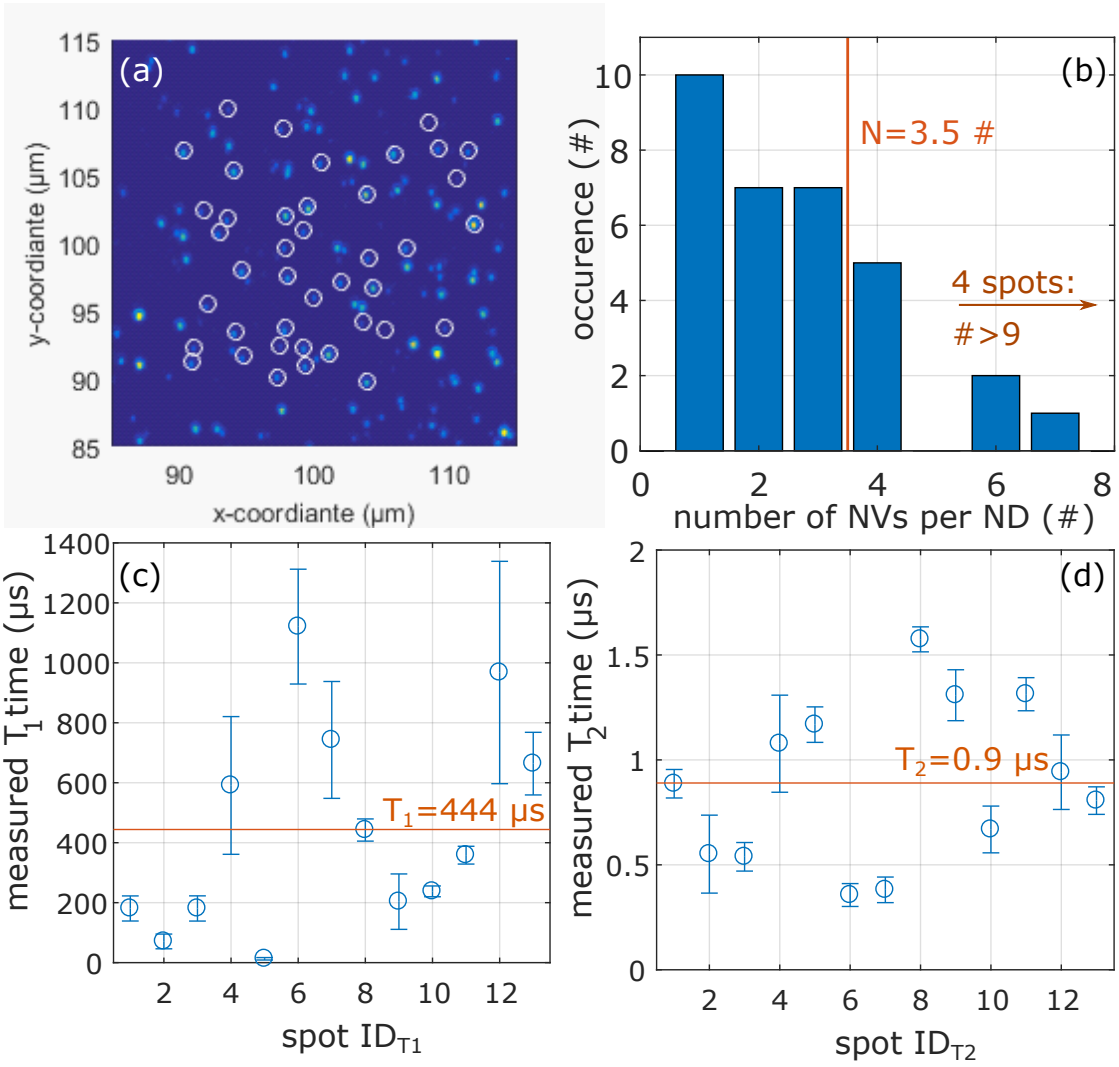

Figure 7.13. Characterization of ND-HPMA. (a): Confocal scan of sample ND-HPMA, the data has been scaled to $2\,\mathrm{Mcps}$ maximum (yellow). The white cycles indicate the analyzed spots. **(b):** Statistical distribution of NVs per ND of the analyzed spots in (a). **(c):** T_1 analysis of spots in (a) using a linear chirp. **(d):** T_2 analysis of spots in (a) via Hahn Echo. The orange text and markers in (b,c,d) indicate the corresponding average values measured. Errors bars are given as $95\,\%$ confidential interval.

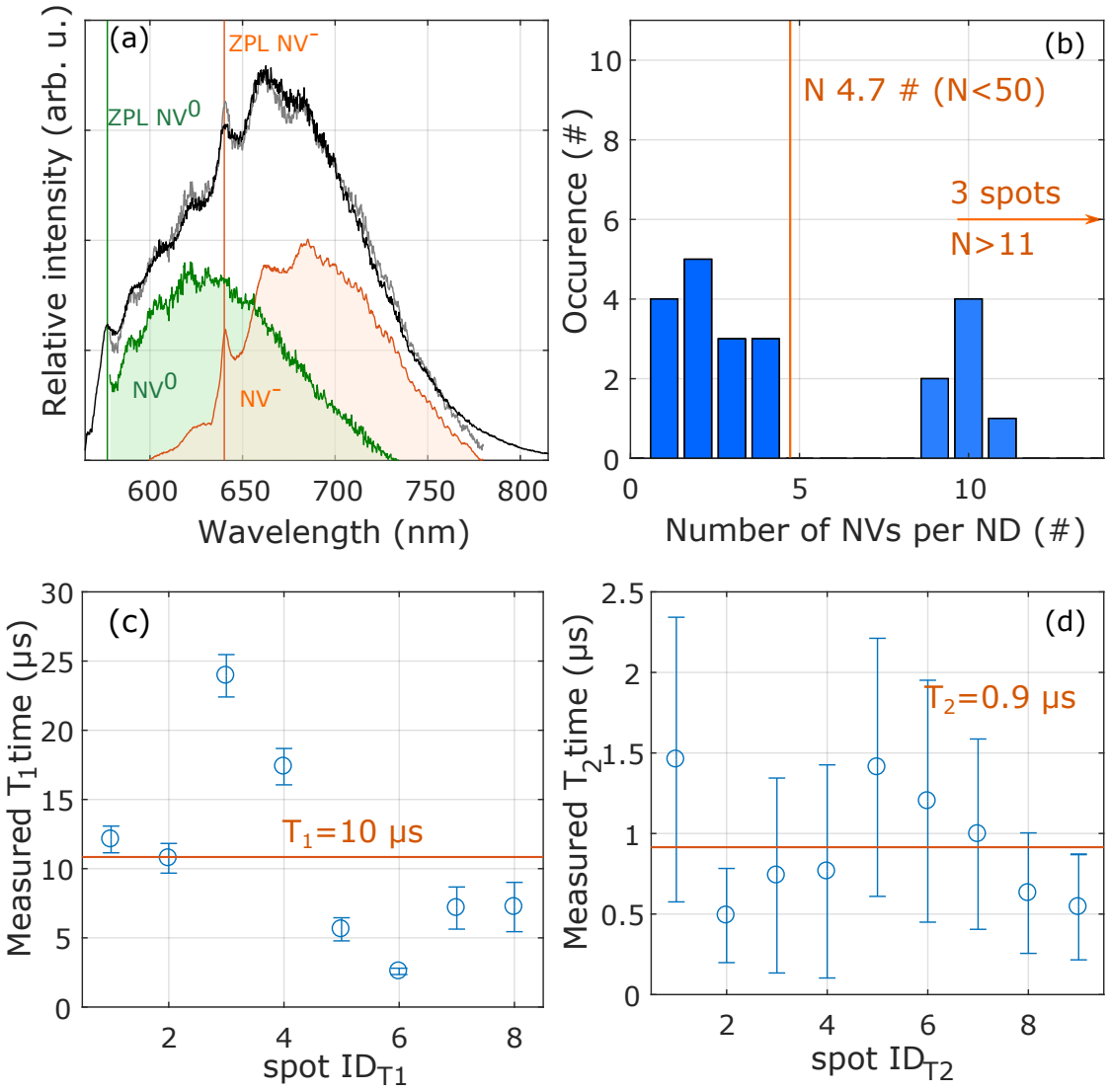

Figure 7.14. Characterization of ND-HPMA-Gd: (a): Average fluorescence spectra of the given sample. The ZPL of NV^- (orange) and NV^0 (green) have been highlighted. In addition, the spectrum has been fit to the sum of two corresponding raw spectra (gray), extracted from bulk diamond. The ratio between NV^- to NV^0 spectra (orange) and (green) is around one by one. **(b):** Statistical distribution of NVs per ND of the analyzed fluorescent spots in (a). **(c):** T_1 analysis of spots in (a) using a linear chirp. **(d):** T_2 analysis of spots in (a) by a Hahn Echo. The orange text and markers in (b,c,d) mark the corresponding average values measured. Errors bars are given as $95\,\%$ confidential interval.

same procedure as ND-HPMA. The average number of NVs per ND is 4.7. T_1 is much shorter (10 µs), and in presence of the Gd(III)-complex, the largest measured T_1 time has been 24 µs for 8 spots analyzed. The corresponding T_2 are similar to the result obtained for ND-HPMA, but the contrast of the HE is much weaker, visible in the increasing error bars.
In addition, the fluorescent spectra of the sample ND-HPMA-Gd was measured, showing both, NV^- and NV^0 fluorescence with a ratio around one to one. The observed NV^0 to NV^- balance is typically for nanodiamonds [81]. In the performed experiments the fluorescence of NV is cut off around 650 nm. The detected residual fluorescence consists out of 1 part NV^0 and 2 part NV^- fluorescence. As a consequence, one will see already a decrease in contrast of the ODMR signal to $\sim 20\,\%$ compared to $\sim 30\,\%$ for NVs in bulk diamond. The reference spectra for NV^- has been extracted from single NVs in bulk diamond, whereas in case of NV^0, NVs in bulk diamond close to a surface, which was terminated with hydrogen, has been used.

Response of control samples to different pH values

In a next step both samples have been mixed by 1 part to 9 parts buffer solution with different pH. 30 µl of the mixture has been placed in a PDMS chamber and their individual T_1 time was monitored for 1 h. Figure 7.15 shows an experimental summary for different solution with different pH values. Data shown are an average of at least three individual measurements using the very same conditions. To extract T_1, a mono exponential function was fitted to the acquired data. Besides slight variations in the average T_1 times, which are plotted in the very same figure as well, the polymer and the Gd(III)-complex were stable over the pH ranges tested.

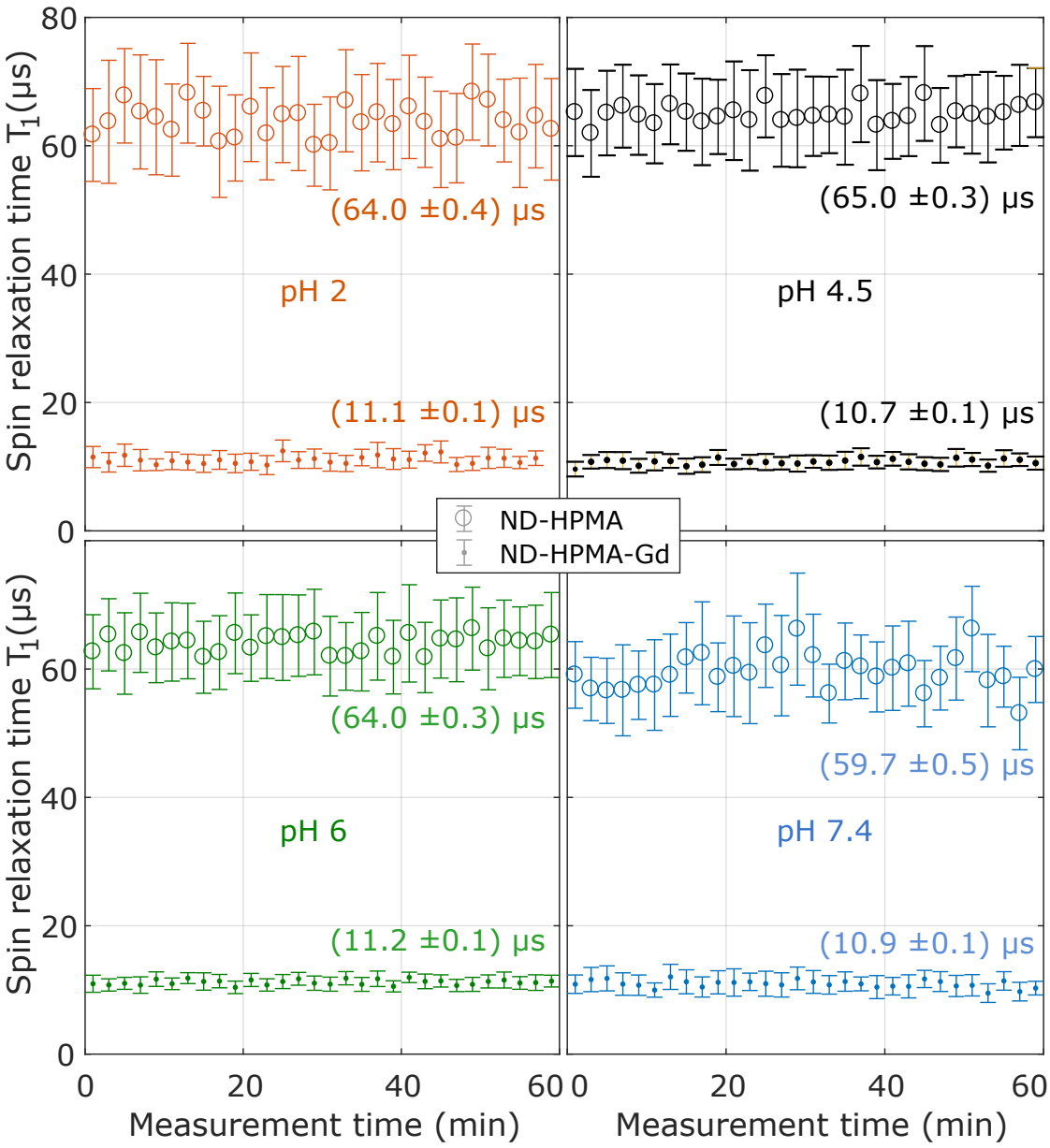

Figure 7.15. pH response of control sample ND-HPMA and ND-HPMA-Gd: pH 2 (red), pH 4.5(black), pH 6 (green), pH 7.4 (blue). All buffers are from buffer system 1 (see appendix C.1).

Response of control samples to different Glutathione concentrations

Additionally, all samples have been tested for changes in T_1, when glutathione (GSH), a reducing agent typically present in cells, was added during the experiment. Again, sample and buffer solution were mixed in a 1:9 ratio. This time using a 50 mM tris(hydroxymethyl)aminomethane (TRIS) buffer, adjusted to pH 8.5 (see appendix C.2, page 233). After 20 min a GSH containing solution was added, prepared with the very same buffer, increasing the relative concentration within the sample volume to 1 mM, 5 mM and 10 mM GSH, respectively. The injection time is marked as zero time in figure 7.16. No significant influence of GSH has been observed after 40 minutes. All presented data have been averaged over at least two and more data sets. All measurements have been performed within an incubator system set to 37 °C.

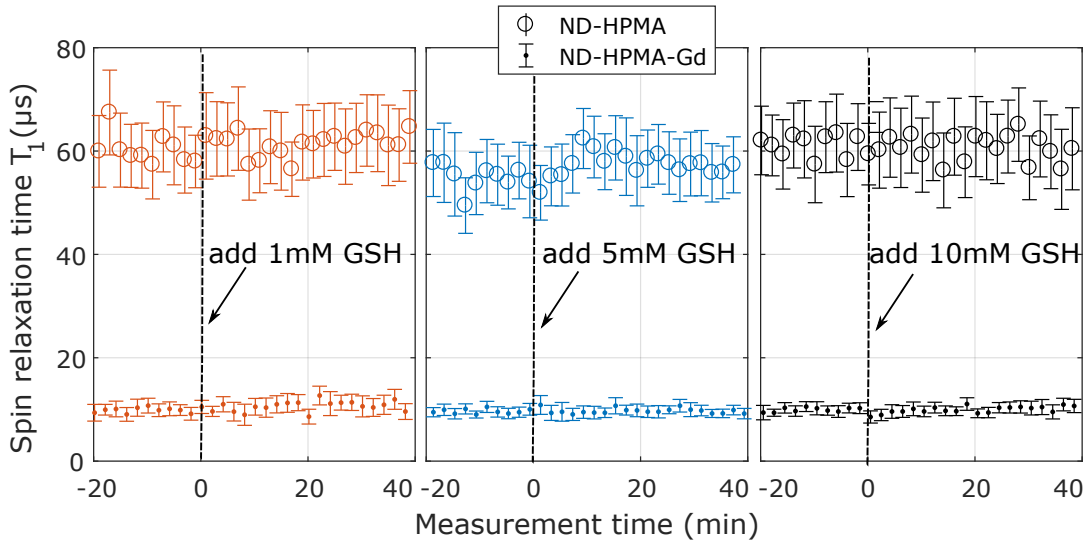

Figure 7.16. Response of control sample ND-HPMA and ND-HPMA-Gd on GSH: Zero indicates the time when GSH has been added: 1 mM (red), 5 mM(blue), 10 mM (black)

Response of control samples to changes in the ionic strength

To examine, if a variation of ionic strength affects T_1, the conductivity of the solution (which corresponds directly to the ionic strength) was varied by the addition of different amounts of sodium chloride to the buffers with pH 7.4 and pH

2 (buffer system 1, appendix C.1). As seen in figure 7.17, no significant change in T_1 is observed. The accumulation time for one data point was around 10 min.

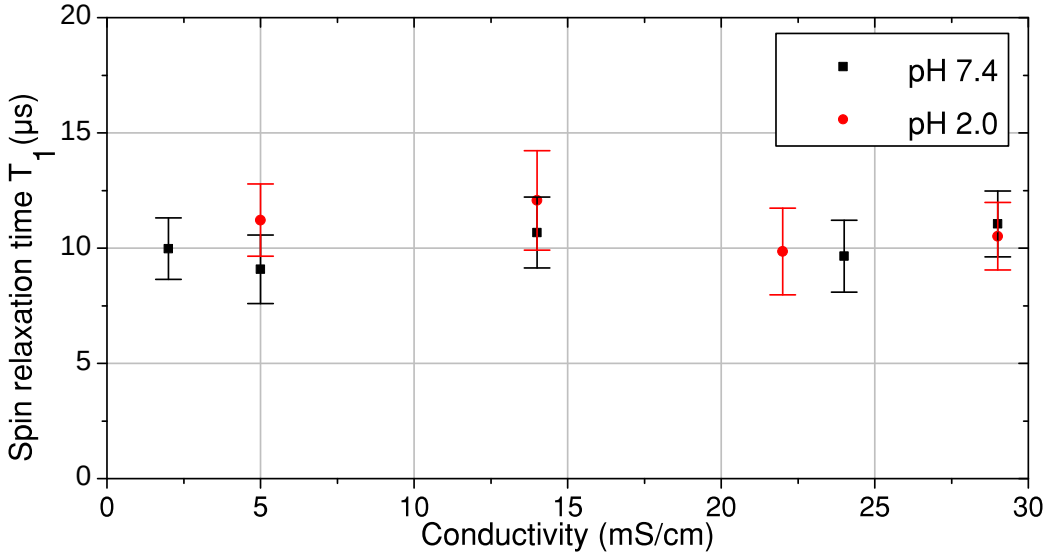

Figure 7.17. Response of control sample ND-HPMA-Gd to changes in ionic strength of the buffer system for two different buffers at pH 7.4 and pH 2.0. The ionic strength is expressed as conductivity.

Response of control samples to laser irradiation

To investigate, if modulations in the laser excitation changes the readout T_1 time, the latter was monitored, while changing the laser excitation from 500 µW to 16 mW (see figure 7.18) using the control sample ND-HPMA-Gd. No significant change for T_1 within the calculated uncertainty (95 % confidence interval) was visible. In experiments utilizing an droplet of any sample, typically 4 mW to 8 mW are used. The error weighted average of T_1 is ~ 11 µs. The original sample has been diluted by adding 19 parts of a buffer pH 7.4 (buffer Sysem 1) to one part of sample.

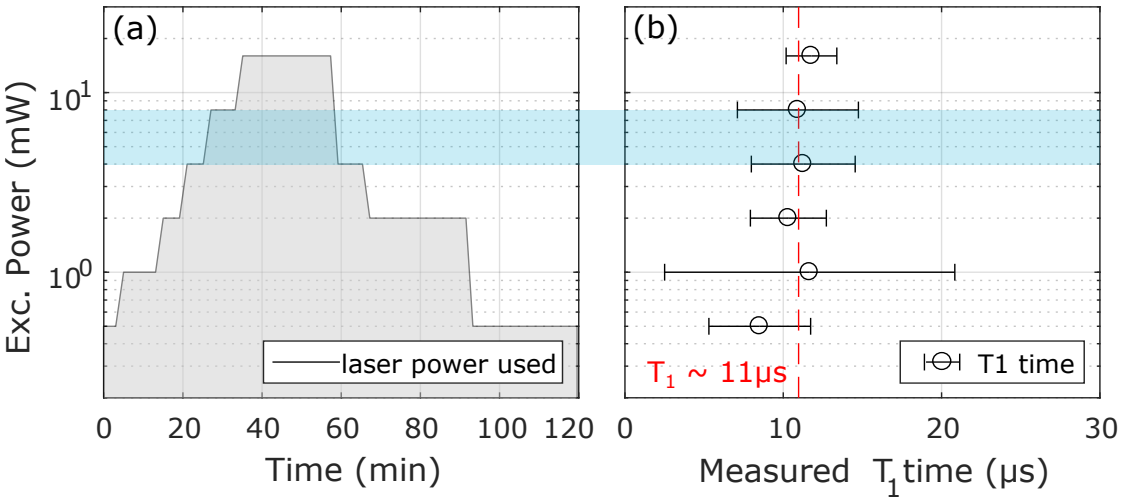

Figure 7.18. Response of control sample ND-HPMA-Gd to changes in excitation power. (a): Excitation laser power has been varied over time. **(b):** Measured T_1 time averaging over the intervals with same laser power. The red line indicates the weighted average of all intervals at $\sim 11\,\mu s$. (Blue area): Region of used laser power during a typical experiment.

7.1.4. pH sensor

First the pH sensitive hybrid sensor was tested for its response to buffer solutions with different pH between 2 and 7.4. Figure 7.19 shows the cleavage of the pH sensitive linker group (hydrazone), which is grafted to the diamond surface. Depending on the amount of H_3O^+-ions in solution the cleavage rate of the linker group increases [159].

Similar to the controls, the sample was mixed as 1 part sample and 9 parts buffer solution with the corresponding pH. Again, an overall volume of at least 30 µl has been prepared. The sample was mixed before acquiring T_1, and put into a PDMS chamber. Afterwards, the latter was sealed by a cover slide. The environmental temperature for all pH experiments was around $(25 \pm 2)\,°C$. The delay between sample preparation (mixing) and the start of the measurement was kept below 5 s. Changes in T_1 seem to follow a linear increase, especially in the first minutes after mixing. As a first estimate one can fit the slope to a linear increase and use the change to estimate the pH value inside solution. Therefore a second buffer system was prepared (buffer system 2, see appendix C.1), a so called B&R buffer [29], and

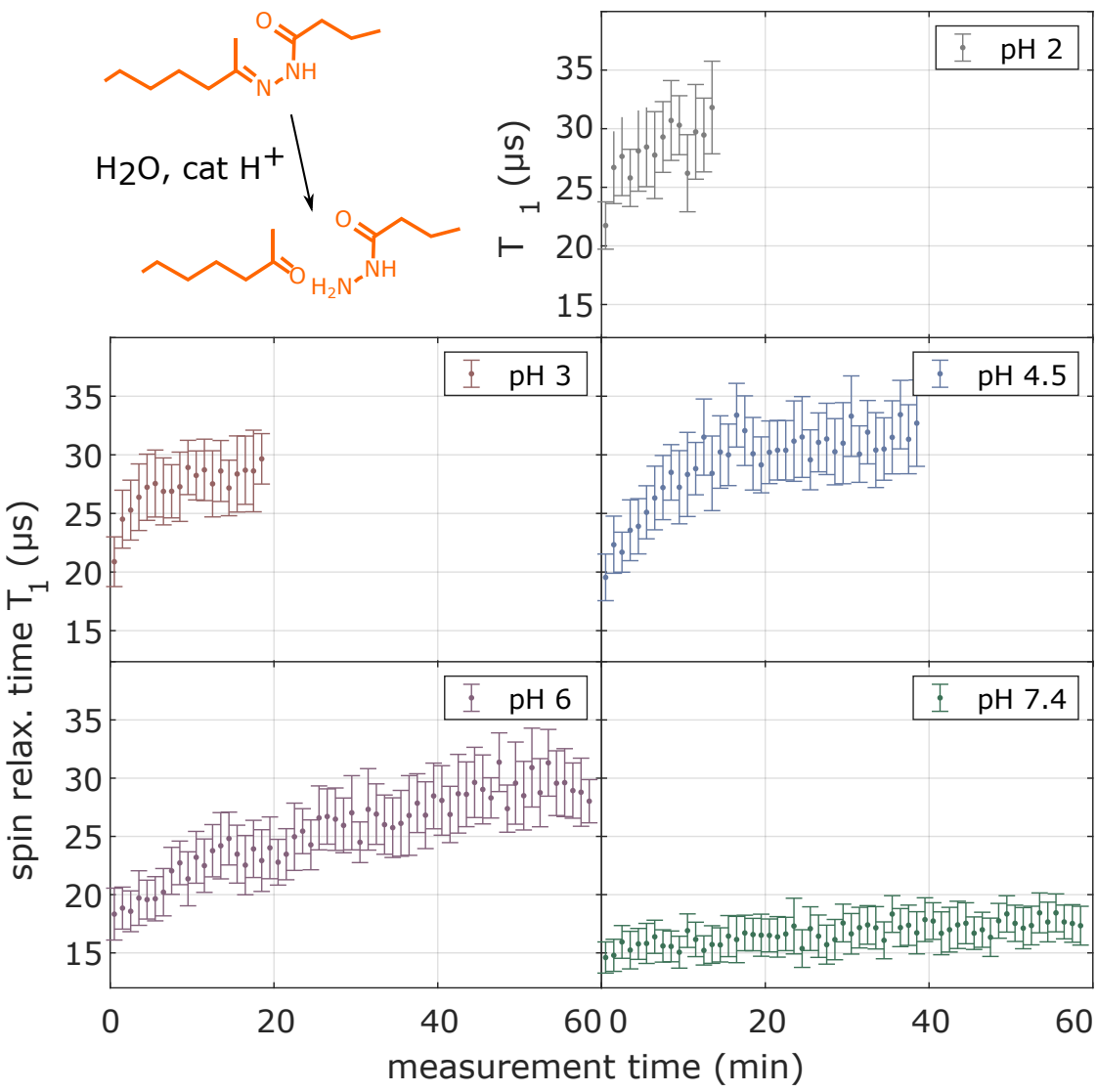

Figure 7.19. pH response of pH-sensor. From top to bottom from pH 2 to pH 7.4. Buffer compositions see text. Top left shows the chemical reaction, which leads to the release of the Gd(III)-complex from the polymer.

T_1 was extracted for the first minutes after mixing. The second buffer system has the advantage, that the pH value can be adjusted much better, and simultaneously the ionic strength of the solution can be kept constant over a wide rage of pH values [29].

By repeating different pH at least three times, one finds the change in T_1 shown in figure 7.20. The graph also includes a linear regressions as guide for the eye. Based on figure 7.20 one can conclude that for the give experimental setting, one can distinguish between two different pH values with at least a difference of 0.8 in solution. Thereby one just has to monitor the change in T_1. The fitted release slope (increase of T_1 per minute and pH) is $(0.17 \pm 0.05)\,\mu s\,min^{-1}\,pH^{-1}$.

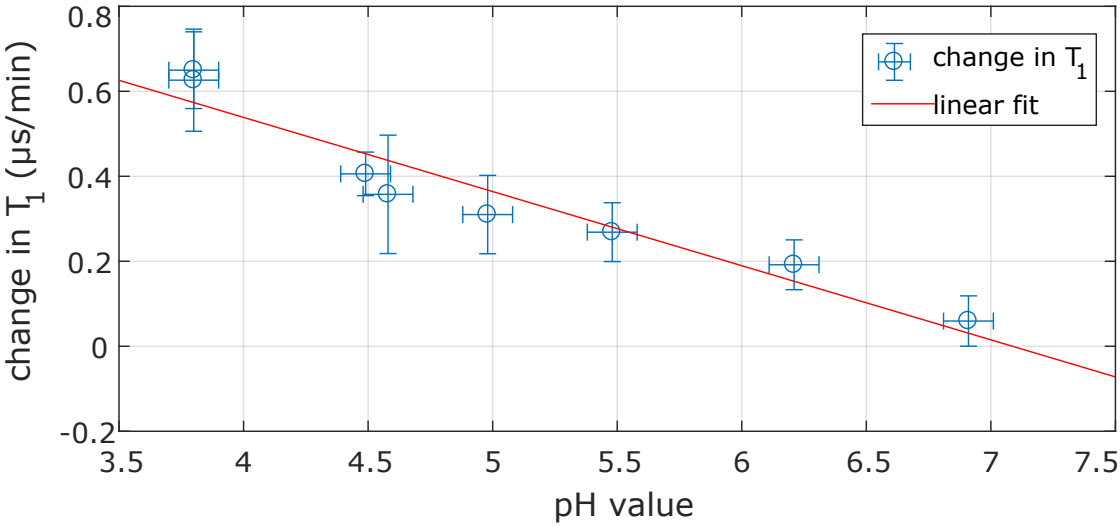

Figure 7.20. T_1 **change versus pH in solution, buffer system 2:** The change in T_1 of NV^- has been extracted by fitting the first minutes of the data collected with the buffer system 2 with linear regression.

T_1 **imaging** As the used chirp pulse scheme allows robust readout of the NV spin state, one can measure T_1 of different oriented NVs with almost the same efficiency. As chemical sensing is managed by measuring T_1, it should be possible to measure a contrast image similar to MRI, and to differentiation between sensors in different states *via* 2D-T_1 imaging. To test this assumption, a PDMS chamber system was loaded with the pH-Sensor diluted in buffer with pH 7.4 (buffer system 1). The buffer was removed and the particles adsorbed were incubated with a buffer pH 2.0

(buffer system 1) for more than half an hour. The medium inside the chamber was again replaced by pH 7.4 buffer and a confocal scan was acquired (figure 7.21(a)). Then a freshly prepared sample, again with pH 7.4, was added to the chamber. After a sufficient number of particles was adsorbed in the field of view under study, the chamber was rinsed again with pH 7.4 to remove still freely diffusing particles within the chamber. In a final, step a T_1 imaging was acquired (figure 7.21(b)).

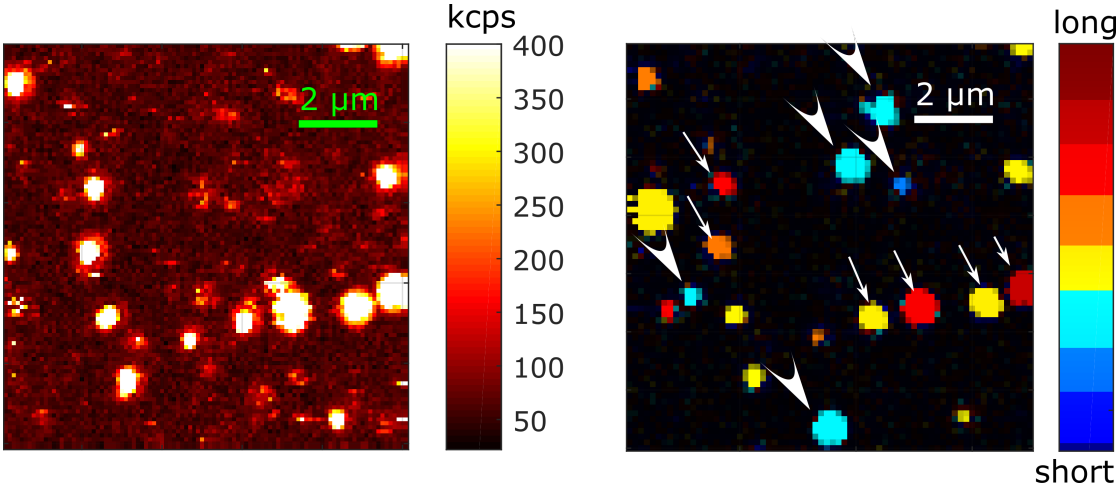

Figure 7.21. T_1 **contrast image of pH sensor: (a):** confocal scan of pH-sensor after washing with pH 2 and pH 7.4 solution. **(b):** T_1 weighted image (see text) after acquiring (a) and adding new sample. Thin arrows indicate some fluorescent spots already present in (a). Flat arrows mark some spots that appear in (b) only.

Fluorescence was probed on every voxel of the scan for a fixed waiting time, with and without applying a chirp pulse, and for two different waiting times (overall probe time 2.5 µs and 22.5 µs). Thereby the spin contrast in the first data set for the same shorter waiting time has been used as a normalization for the longer one. If T_1 is below 22.5 µs, the relative fraction will be smaller in difference to T_1 being well above 22.5 µs. Translating the relative fraction into a color code one obtains figure 7.21(b). In the extracted T_1 contrast image the red colored areas represent a large T_1, blue colored areas represent low T_1. In addition, two types of fluorescent spots have been marked. The thin arrows indicate fluorescent spots, that were already present in the confocal spot before injecting the new sample. Flat arrows mark spots that appeared after injection and flushing. Whereas first one mentioned are primary pointing towards more reddish spots, the second ones do the same for

more blueish spots. This clearly demonstrates that the pH sensor responded to the change in pH.

7.1.5. Redox potential sensor

Similar to the previous section, the redox sensor was analyzed in an open droplet. To recall the mechanism behind the release: GSH can reduce the di-sulfide bridge of the linker and recombines with a second oxidized GSH to GSSG. In the beginning the sample was placed in a PDMS chamber and after waiting 20 min a GSH containing solution was injected. (see also section 7.1.3 for more details). For pH 7.4 a 50 mM Hepes buffer, and for pH 8.5 a 50 mM TRIS buffer was used (see also appendix C.2, page 233). All data sets shown have been acquired within an incubator system set to 37 °C and are an average of at least two data sets. Interestingly, the capability of GSH to reduce the di-sulfide linker seemed to be depended on pH. This is consisted with literature [174] as the reduction potential of redox couples can be pH dependent. Similar to the pH sensor the slope of the T_1 time, as a function of concentration, has a linear behavior. In the simulation section one will see that this behavior corresponds well to a mono exponential release of Gd(III)-complexes (see page 218).

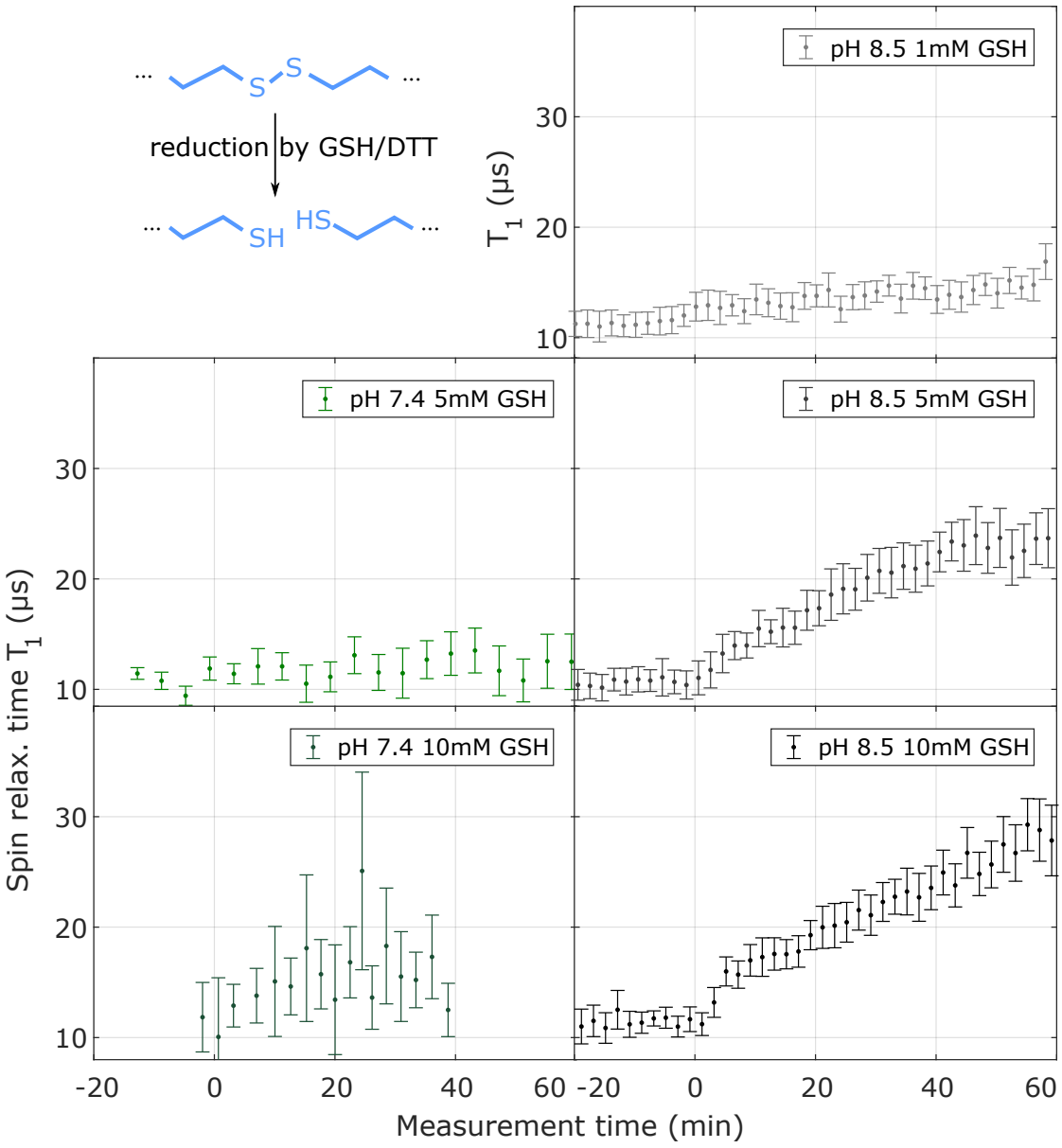

Figure 7.22. Response of redox potential sensor to reduction agent GSH: The response to GSH has been tested for two pH, pH 7.4 and pH 8.5 and different GSH concentrations: $1\,\mathrm{mM}$, $5\,\mathrm{mM}$ and $10\,\mathrm{mM}$. The upper graph shows the release mechanism. See text for more information.

7.1.6. Deep analysis of spin lattice relaxation time

Up to now T_1 decay analysis has been performed by using a simple mono exponential decay. As the obtained experimental data originates from an ensemble of NV with various ND sizes, the decay itself also encodes information about the homogeneity of the given sample. Conversely, if the (in)homogeneity of the sample under study is well characterized, one can use this information for modeling the relaxivity of the Gd(III)-complex in the polymer shell. To this end the data of the former section is re-analyzed with a "streched exponential", defined in equation (3.108). The latter converges with a simple exponential decay for the stretching parameter $\beta = 1$. Figure 7.23 shows the result of this analysis. For the control samples ND-HPMA and ND-HPMA-Gd the average values had been summarized in table 7.1.

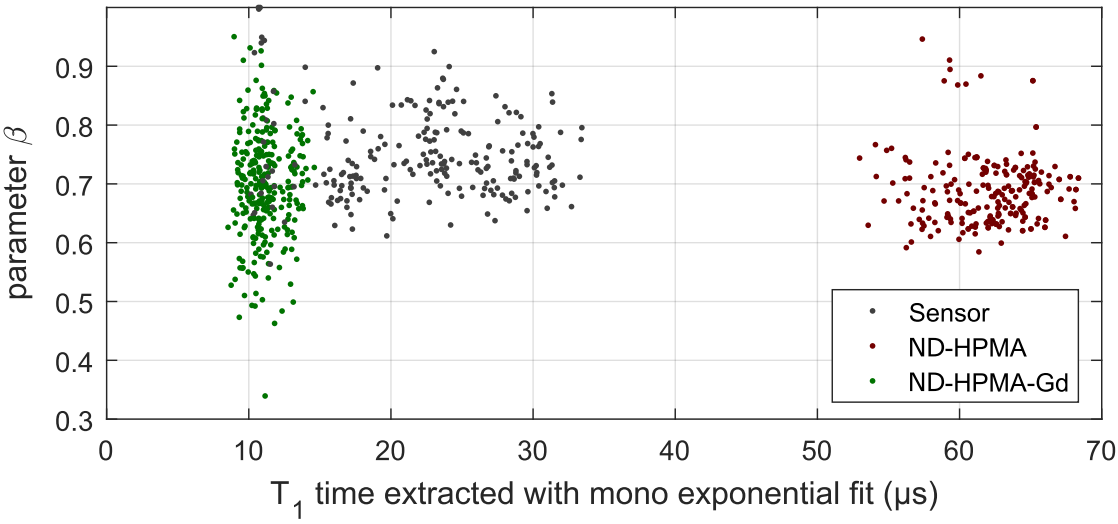

Figure 7.23. Deep analysis of spin lattice relaxation time: Extracted β parameter used to describe the shape of a stretched exponential over the extracted (T_1) setting $\beta = 1$ (see equation (3.108) with $\Gamma_{avg} = 1/T_1$)

sample	β	$T_1^{(\beta)}$ in (μs)	$T_1^{(\beta=1)}$ in (μs)
ND-HPMA	0.69 ± 0.01	55.9 ± 0.2	62.1 ± 0.2
ND-HPMA-Gd	0.69 ± 0.01	8.1 ± 0.1	11.2 ± 0.1

Table 7.1. Deep analysis of spin lattice relaxation time: Average values obtained from plotted data in figure 7.23.

7.2. Simulations

In the following the behavior of Gd(III)-complexes onto the spin lifetime of NV^- has been modeled, using the formalism developed in the basics section. Afterwards the experimental data are compared to the performed simulations. Finally, the measured T_1 times are converted into Gd-concentrations.

7.2.1. Modeling NV relaxometry influenced by Gd(III)-complexes

As stated in equation (3.94), the decay rates of individual decay channels just sum up, or in case of an ensemble, convolves with other independent rates. The sample ND-HPMA (without Gd(III)-complex) was used to describe the intrinsic relaxation channel and another decay channel was induced by a spin bath, provided by Gd(III)-complexes. The calculation of the decay rate introduced by latter demands a proper description of the magnetic fields variance $B_\perp^2$. For a spherical particle equation (3.98) is used:

$$B_\perp^2 = \mathrm{Tr}[\rho B_{x,j}^2] + \mathrm{Tr}[\rho B_{y,j}^2] = \left(\frac{\mu_0}{4\pi}\gamma_j\hbar\right)^2 \cdot C_s \cdot \frac{2+3\sin^2(\alpha_j)}{r_j^6}. \tag{7.3}$$

With

$$C_s = \frac{1}{2S+1}\sum_{m=-S}^{S} m^2 = \frac{S(S+1)}{3}. \tag{7.4}$$

For the description of all other parameters see page 71 in section 3.4.5.

Modeling spins in a thick layer on a sphere. To derive an expression for $B_\perp^2$, one considers several spins homogeneously distributed in the vicinity of the nanodiamond surface. The layer shall have a thickness of δd. The spins have the gyromagnetic ratio γ_L and a density σ_L. The nanodiamond is considered to be a sphere with diameter d_0. The square of the magnetic field experienced by the NV for all spins

in the layer can then be summarized in spherical coordinates:

$$B_\perp^2 = \sum_j B_{\perp,j}^2 = \left(\frac{\mu_0}{4\pi}\gamma_L\hbar\right)^2 \cdot C_s \cdot \sigma_L \cdot \int_{d_0/2}^{d_0/2+\delta d} dr' \int_0^{2\pi} d\varphi \int_0^{\pi} d\theta\beta \cdot r^2 \sin(\theta)\ \frac{2+3\sin^2(\alpha)}{r^6}. \quad (7.5)$$

With

$$\sin^2(\alpha) = \sin^2(\theta), \quad (7.6)$$

and

$$r = \sqrt{r'^2 - \delta r^2 \sin^2(\theta)} + \delta r \cos(\theta), \quad (7.7)$$

when moving δr from the center of a spherical shaped nanodiamond along the NV spin quantization axis (parallel to the NV axis). Whereas β is the Jacobi determinant of the substitution $dr \to dr'$:

$$\beta = \frac{1}{\sqrt{1 - \frac{\delta r^2}{r'^2}\sin^2(\theta)}}. \quad (7.8)$$

If the NV is moved on a path perpendicular to its quantization axis, then $\sin^2(\alpha)$ is replaced by [200]

$$\sin^2(\alpha) = \cos^2(\theta) + \sin^2(\theta)\sin^2(\varphi). \quad (7.9)$$

The total fluctuation rate of the Gd(III)-complex is $\Gamma^{Gd} = 1/\tau_c = \Gamma^{Gd}_{\text{dip}} + \Gamma^{Gd}_{\text{int}}$, whereas Γ^{Gd}_{dip} is due to the intra-bath dipolar coupling, while Γ^{Gd}_{int} is caused by intrinsic spin relaxation of the Gd(III)-complex or the rotation of the complex itself [31]. In the current study, a typical value of $\Gamma^{Gd}_{\text{int}} \approx 14\,\text{GHz}$ for the Gd(III)-complex is adapted [31, 170]. In the following, Γ^{Gd}_{dip} shall be calculated using equation (3.101) and (3.102). The temporal average of $< H_{kl}^2 >= \text{Tr}[\rho H_{kl}^2]$ has in spherical coordinates the form

$$< H_{kl}^2 >= \frac{3}{4r^6(1+\cos(2\theta))^5} \cdot \left(\frac{\mu_0}{4\pi} g_k \mu_k \cdot g_l \mu_l\right)^2 \cdot C_s^2$$
$$\cdot(24\sin^4(\theta)\cos(4\varphi) - 16\sin^2(\theta)(\cos(2\theta)+3)\cos(2\varphi) + 3(4\cos(2\theta) + 7(\cos(4\theta)+3))). \tag{7.10}$$

With θ being the polar, and φ the azimuthal angle. In a next step the sum in (3.102) is replaced by an integral in spherical coordinates, assuming a homogenous spin density σ_L:

$$\sum_{k \neq l} \approx \sigma_L \int_0^{2\pi} \mathrm{d}\varphi \int_0^{\pi} \mathrm{d}\theta \int_{r_{\min}}^{r_{\max}} \mathrm{d}r \; r^2 \sin(\theta). \tag{7.11}$$

Where $r_{\min}$ accounts for the minimal distance between to neighbour spins, since they cannot be infinitesimally dense packed. As the dipolar interaction between to spins rapidly drops with $1/r^3$, $r_{\max}$ is driven to ∞. Calculating $\sum_{k \neq l} \langle H_{kl}^2 \rangle$ reveals with (7.10) and (7.11)

$$\sum_{k \neq l} \left\langle H_{kl}^2 \right\rangle \approx \left(\frac{\mu_0}{4\pi} g_k \mu_k \cdot g_l \mu_l\right)^2 \cdot C_s^2 \cdot \frac{3\pi(8+3\pi)}{16} \cdot \frac{\sigma_L}{r_{\min}^3}. \tag{7.12}$$

Then Γ_{dip} becomes for spins of equal nature:

$$\Gamma_{\mathrm{dip}} \approx 0.2549 \cdot \mu_0 C_s \frac{g_k^2 \mu_k^2}{h} \cdot \sqrt{\frac{\sigma_L}{r_{\min}^3}}. \tag{7.13}$$

Including pulse length correction. As the pulse scheme needs a certain time, very fast decay rates will contribute less, as the spin state already decays during a flip of the spin state. To account for this effect, the Bloch equations are simulated for different T_1 with and without a chirp pulse. Again, the ordinary differential equation solver "ode45" in "Matlab" has been used to solve the Bloch equations in the rotating frame:

$$\frac{\mathrm{d}\vec{M}(t)}{\mathrm{d}t} = \gamma \vec{M}(t) \times \vec{B}_{\mathrm{eff}}(t) + \begin{pmatrix} -M_x/T_2 \\ -M_y/T_2 \\ -M_z/T_1 \end{pmatrix}. \tag{7.14}$$

Whereas $\vec{B}_{\text{eff}}$ is the magnetic field vector in the rotating frame. For the simulation the parameters $T_2 = 1\,\mu s$ and the typical pulse length of $2.5\,\mu s$ has been used. The weighting factor $w(\Gamma)$ is then directly the contrast between inverted and non-inverted population (see figure 7.24).

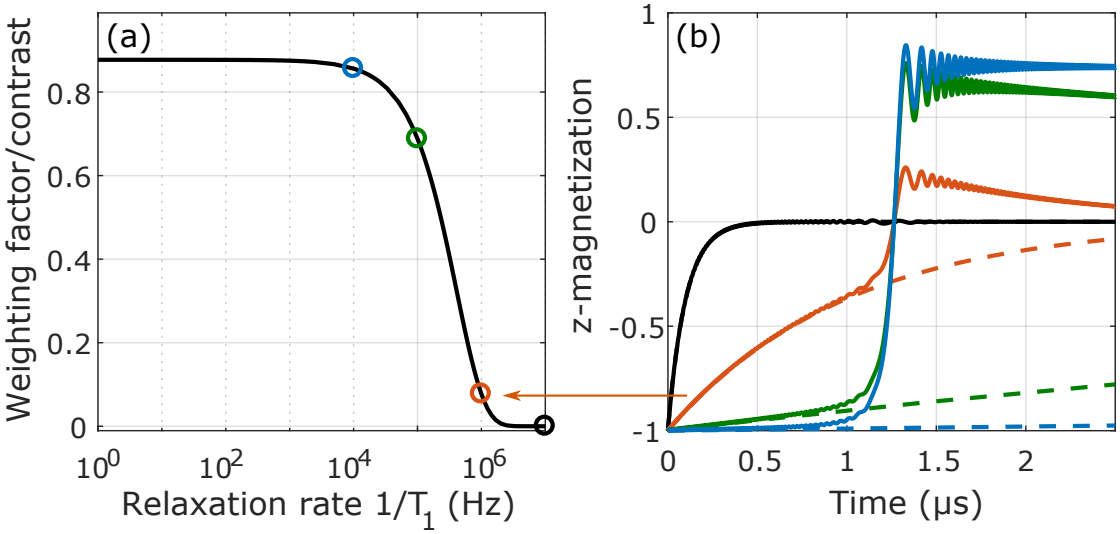

Figure 7.24. Simulating the T_1 contrast for a certain T_1 time. To calculate the weighting factor the Bloch equations in (7.14) has been solved numerically. **(a):** weighting factor / contrast w plotted over the inverse of T_1 with T_2 fixed to $1\,\mu s$. **(b)**: examples for the evolution of the z-magnetization for $T_1 = 100\,ns$ (black), $T_1 = 1\,\mu s$ (red), $T_1 = 10\,\mu s$ (green), $T_1 = 100\,\mu s$ (blue). Dashed lines indicate free evolution, solid lines the evolution utilizing a chirp pulse. The data plot in (b) are indicated in (a) as cycles with same color.

The tailored Γ distribution $R_\beta^{\text{obs}}(\Gamma)$ reads then

$$R_\beta^{\text{obs}}(\Gamma) = w(\Gamma) \cdot R_\beta(\Gamma). \tag{7.15}$$

To calculate $R_{\text{env}}(\Gamma)$ the diamond is modeled as a sphere with diameter d_0 (see figure 7.25(a)). In the following paragraph the index "env" will be neglected for better readability.

Considering the ND to be homogeneously decorated with NVs, the probability $p_{\text{NV}^-}(r)$ to find an NV at distance r to the center, will scale with the volumetric fraction $\propto r^3$. The corresponding decay constant is $\Gamma_{d_0}(\delta r)$. In later simulations the shifting parameter δr of equation (7.8) will be sliced in l steps from 0 to $d_0/2 - d_{\text{dep}}$,

whereas d_{dep} is the cutoff close to the surface, where no NV^- fluorescence is expectable. After histogramming $\Gamma_{d_0}(\delta r)$ using the weights $p_{\mathrm{NV}^-}(r)$, one gets $R^0_{\beta,d_0}(\Gamma)$ for a certain nanodiamond size. As a final step one has to average over

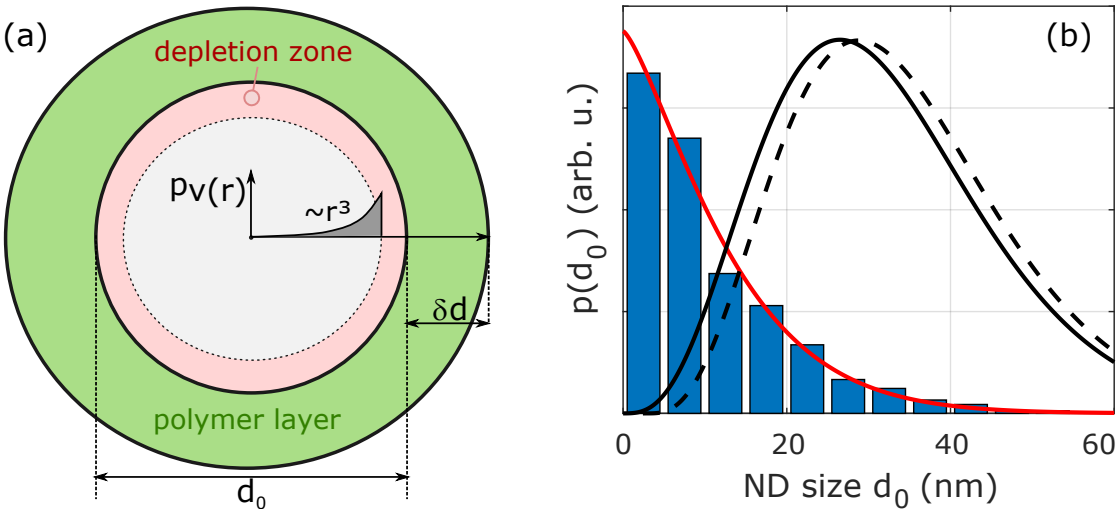

Figure 7.25. Description of simulation model. (a): The ND is modeled as a sphere with diameter d_0 and the polymer on top (green). The depletion zone is also indicated in red, where no NV^- or even NV fluorescence is expected. **(b):** The typical ND distribution of the used sample extracted from [157] as blue bars. (red): Stretched exponential fit to describe the distribution. (black,solid): volume weighted NV distribution.(black,dashed): volume weighted NV^- distribution by taking into account a depletion zone of $1.5\,\mathrm{nm}$.

the ensemble of possible diameters. To do so, the size distribution of [157] has been used, as the diamonds have been fabricated by the very same protocol (see also figure 7.25(b), blue bars). As larger nanodiamonds contain more NVs one has to weight again the bare distribution with $p_{\mathrm{NV}^-}(d_0)$ by taking into account that NV^- will not be present in the vicinity of the surface. The difference between considering a depletion zone or not are pictured in 7.25(b) (solid and dashed line black line). Finally $R_{\mathrm{env}}(\Gamma)$ is

$$R_{\mathrm{env}}(\Gamma) = \int_{d_{\mathrm{min}}}^{d_{\mathrm{max}}} \mathrm{d}d_0 \; p_{NV^-}(d_0) \cdot R_{\beta,d_0}(\Gamma). \tag{7.16}$$

With

$$p_{\mathrm{NV}^-}(d_0) = \; p^0_{\mathrm{NV}^-} \cdot (d_0 - 2 \cdot d_{\mathrm{dep}})^3 \tag{7.17}$$

and

$$R_{\beta,d_0}(\Gamma) = \text{histogram}\left[p_{d_0}(\delta r)\cdot\Gamma(\delta r)\right] \tag{7.18}$$

and

$$p_{d_0}(\delta r) = p^0_{d_0}\cdot\left[(\delta r+\epsilon)^3-(\delta r-\epsilon)^3\right]. \tag{7.19}$$

An example for $R_{\text{env}}(\Gamma)$ for a low Gd(III)-concentration (around 20 mM) is plotted in figure 3.15.

Estimate Gd(III)-concentration inside the polymer shell

The relative amount of Gd ions N_{Gd} versus Carbon ions N_{C} originated from diamond has been measured to be 2.3×10^{-3}. As the number of ions in the polymer layer surrounding the ND depends in a non-linear manner on the size of the ND, for every ND size an individual amount of Gd(III)-complexes has to be calculated. Assuming that the polymer surrounding the ND is decorated with a similar amount of Gd(III)-complexes, one can state that the Gd(III)-concentration ρ_{Gd} is similar inside the shell for all ND sizes. The overall amount of Gd(III)-ions N_{Gd} measured by collaboration partners *via* induced coupled plasma optical emission spectrometry (ICP-OES) is then

$$N_{\text{Gd}} = \int_{r^{\text{ND}}_{\text{min}}}^{r^{\text{ND}}_{\text{max}}} \rho_{\text{Gd}}\cdot V_L(r,\delta d)\cdot p(r)\mathrm{d}r. \tag{7.20}$$

Where $V_L(r,\delta d)$ is the shell volume with a given height δd and the unnormalized distribution function $p(r)$ for a given size in the interval from $r^{\text{ND}}_{\text{min}}$ to $r^{\text{ND}}_{\text{max}}$.

The number of carbon atoms is

$$N_{\text{c}} = \int_{r^{\text{ND}}_{\text{min}}}^{r^{\text{ND}}_{\text{max}}} N(r)p(r)\mathrm{d}r \tag{7.21}$$

Where $N(r)$ is the number of carbon atoms needed to form a single ND:

$$N(r) = \frac{4}{3}\cdot\frac{\rho_D}{m_C}\pi r^3 \tag{7.22}$$

With the mass m_C of of a single carbon atom and ρ_D the density of diamond.

The relative amount of N_{Gd} per N_{C} ions is then

$$\frac{N_{\mathrm{Gd}}}{N_{\mathrm{C}}} = \rho_{\mathrm{Gd}} \cdot \frac{\int_{r_{\mathrm{min}}^{\mathrm{ND}}}^{r_{\mathrm{max}}^{\mathrm{ND}}} V_L(r, \delta d) \cdot p(r)\ \mathrm{d}r}{\int_{r_{\mathrm{min}}^{\mathrm{ND}}}^{r_{\mathrm{max}}^{\mathrm{ND}}} N(r) \cdot p(r)\ \mathrm{d}r}. \tag{7.23}$$

The fraction $\frac{N_{\mathrm{Gd}}}{N_{\mathrm{C}}}$ is then equal to the value given above. Using the here developed theory, one can calculate the individual amount of Gd(III)-complexes per ND size and layer thickness using

$$N_{\mathrm{Gd}}/_{ND} = \rho_{\mathrm{Gd}} \cdot V_L(r, \delta d). \tag{7.24}$$

The individual amount of Gd-ions N_{Gd} is plotted in figure 7.26.

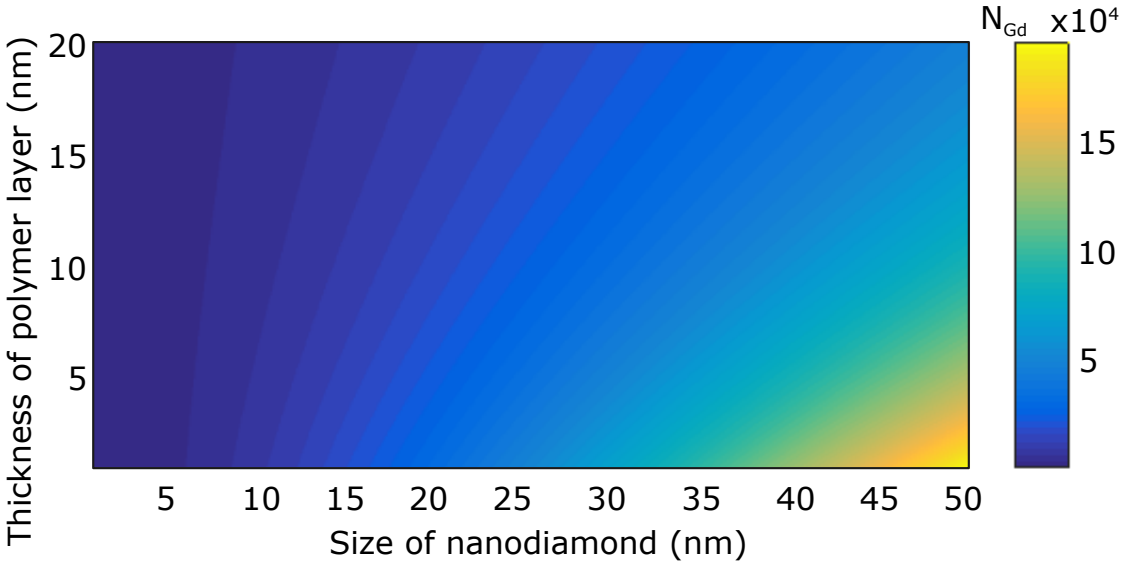

Figure 7.26. Individual Gd concentration per ND: The individual concentration of Gd-ions per ND is shown as function of layer thickness and nanodiamond size based on equation (7.24).

7.2.2. Simulation results: Spherical nanodiamonds

In the following the procedure for simulating the spin lattice relaxation time of NV is stepwise summarized based on the developed theory in the former paragraph and the basics section:

Estimating the thickness of polymer layer on ND

1. The Gd(III)-concentration is calculated for a fixed polymer layer thickness δd using equation (7.23) with the ND-distribution plotted in figure 7.25(b) using $N_{\mathrm{Gd}}/N_{\mathrm{C}} = 2.4 \times 10^{-3}$. d_{dep} has been set to 2 nm.

2. The correlation time for the Gd(III)-complex is calculated by summing over the intrinsic relaxation rate and the calculated dipol-dipol interaction (see euqation (7.13)). For the intrinsic relaxation rate, a value of 14.3 GHz has been used, mainly dominated by the rotational correlation time of the complex [170] (The lifetime of the complex is some orders of magnitude higher than τ_R)

3. Calculate $\langle B^2 \rangle$ of Gd for various position of NV and ND sizes for both perpendicular and parallel arrangement with equations (3.99) to (7.9).

4. Calculate $R_{\mathrm{env}}(\Gamma)$ using equation (7.15) to (7.17). Perpendicular and parallel arrangements are incorporated.

5. Calculating $R_{\mathrm{int}}(\Gamma)$ using equation (31) in [18] with $\beta = 0.69$ and $T_1 = 55.8\,\mu\mathrm{s}$ as extracted in paragraph 7.1.6.

6. Calculate the overall rate $R_{\beta}(\Gamma)$.

The result is shown in figure 7.27. As the polymer shell increases in size, the spin lattice relaxation time T_1 increases almost linearly. One can conclude from this

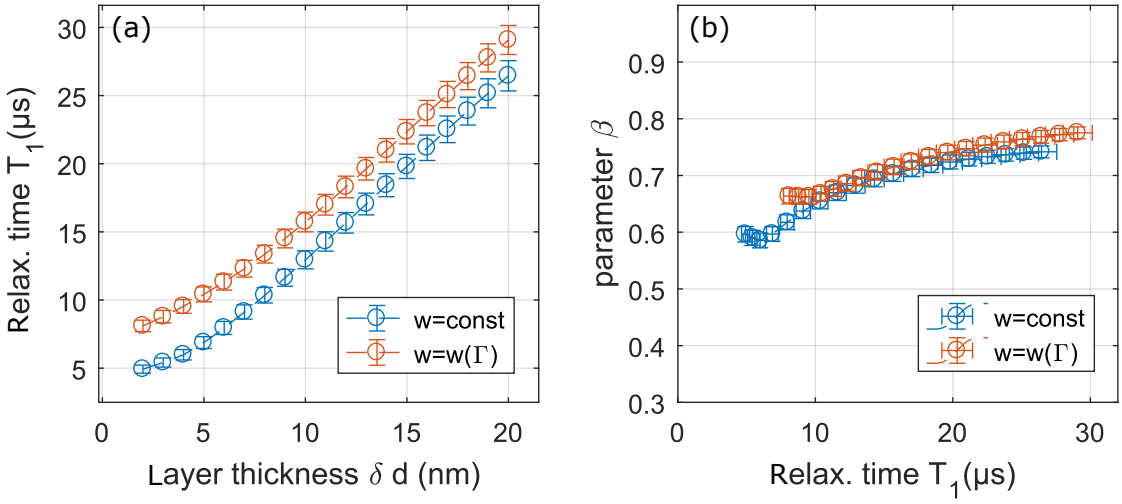

Figure 7.27. T1 **dependence on polymer layer thickness. (a):** Calculated T_1 for different layer thicknesses with (red) and without tailoring (blue) $R_\beta(\Gamma)$. **(b):** Extracted β parameter used to describe the shape of a stretched exponential over the extracted T_1 setting $\beta = 1$.

behavior, if the polymer swells or shrinks significantly in the performed experiment, one would be able to see this in changes of T_1. Comparing the measured T_1 to the simulated data in figure 7.27 yields to a polymer shell thickness of around 6 nm in solution.

Estimating T_1 dependence of Gd(III)-concentration in polymer layer In a next step the polymer shell thickness is fixed to this value (6 nm) and the release of Gd(III)-ions is simulated (see figure 7.28) by changing the concentration of Gd(III)-ions in the polymer shell. It turns out, that the hybrid-sensor has quite a remarkable dynamic range over more then two orders of magnitude in the Gd(III)-concentration of the polymer shell (0.2 M to 1 mM). In terms of total Gd complexes per nanodiamond this translates for a 32 nm sized nanodiamond being sensitive from several thousend to several tens of Gd(III)-ions.

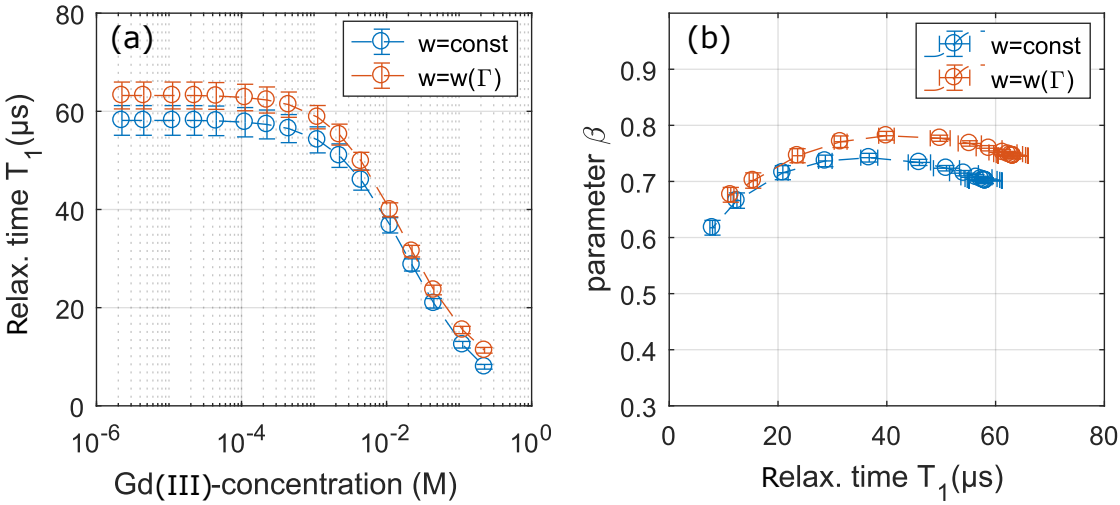

Figure 7.28. T_1 dependence on Gd(III)-concentration for a fixed polymer layer thickness: (a): Calculated T_1 for different Gd(III)-concentrations with (red) and without tailoring (blue) $R_\beta\Gamma$. **(b):** extracted β parameter used to describe the shape of a stretched exponential over the extracted T_1 setting $\beta = 1$.

Comparing simulation to experimental results. In figure 7.29 simulation results have been plotted together with rebinned experimental data, shown in figure 7.23. As one can see, both match very well. This match justifies the here developed theory for the determination of the Gd(III)-concentration by measuring T_1.

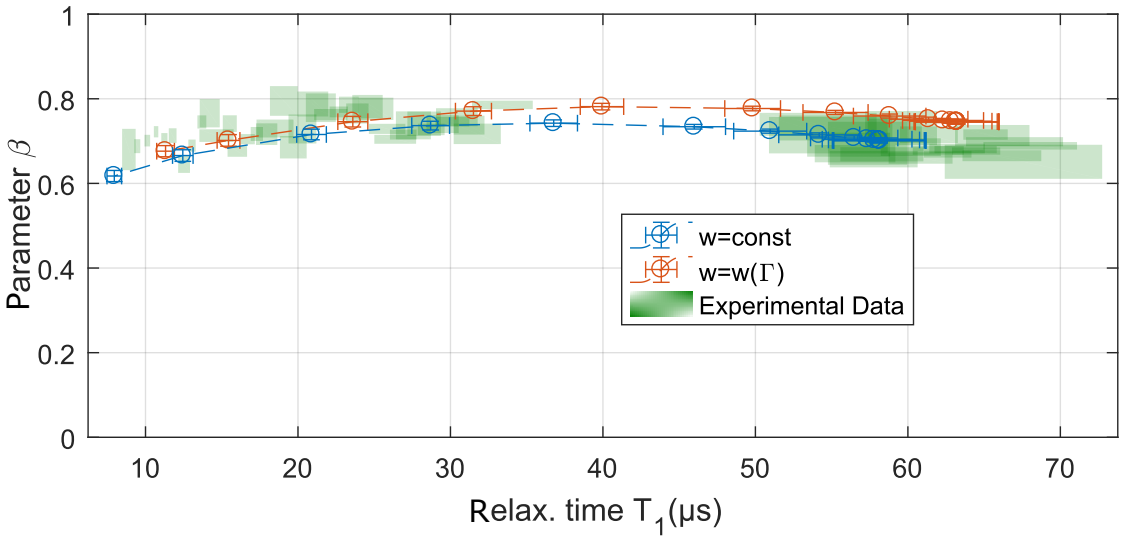

Figure 7.29. Comparing simulation to experimental results. Parameter β versus extracted T_1 time ($\beta = 1$).

Calculating Gd(III)-complex release rates *via* T_1. With the simulation results obtained, one gains an inverse transformation to calculate the Gd(III)-release with a given T_1 time. This has been done for the pH sensor in buffer system 1 as plotted in figure 7.30. In (a) an example is shown for the pH sensor in pH 4.5 solution. The slope of all data sets (some are shown in figure 7.19) was fitted to a mono exponential function, and the release rate was extracted. Comparing the extracted result to ICP-MS data acquired by Jitka Neburkova [159], one sees a good agreement. The corresponding set at pH 2 does not match. The possible reason for this disagreement can be that the minimum resolution set in T_1 to 30 s being longer than the release time around 20 s at pH 2. Figure 7.31 shows the same analysis done for the redox sensor. The most obvious observation of figure 7.31(b) is that the redox potential of GSH is depending on pH, that is also confirmed again by ICP-MS data from Jitka Neburkova. The qualitative behavior is again in good

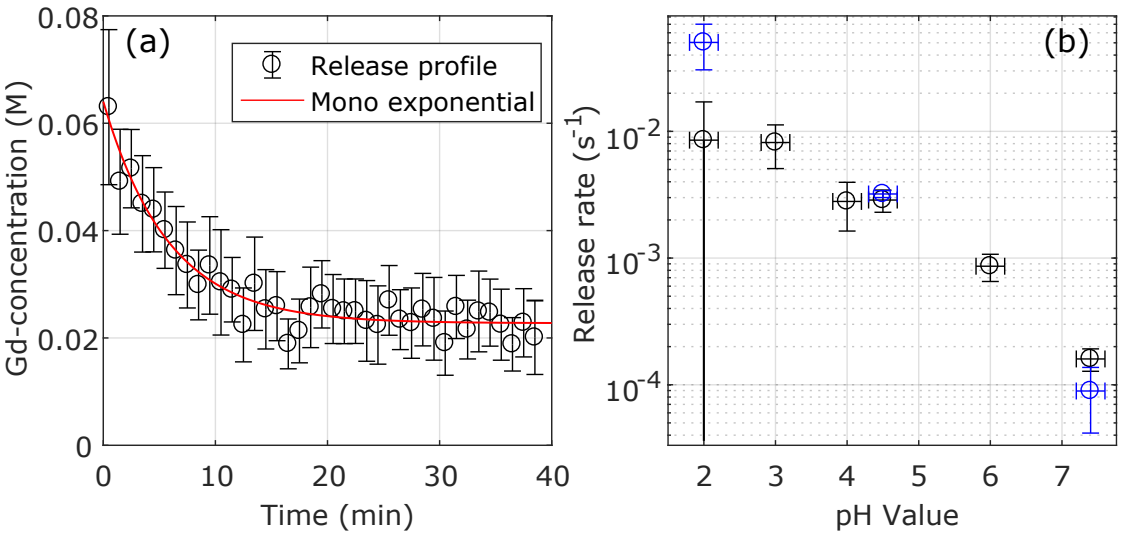

Figure 7.30. Calculated Gd(III) release for the pH sensor. (a): Example for calculated Gd(III)-release over time for a pH of 4.5. A mono Exponential had been fit to the data set. The extracted release rates are plotted in **(b):**.(Black): Data analyzed correspond to the measurements shown in figure 7.19.(blue): Data from Jitka Neburkova, measured *via* ICP-MS.

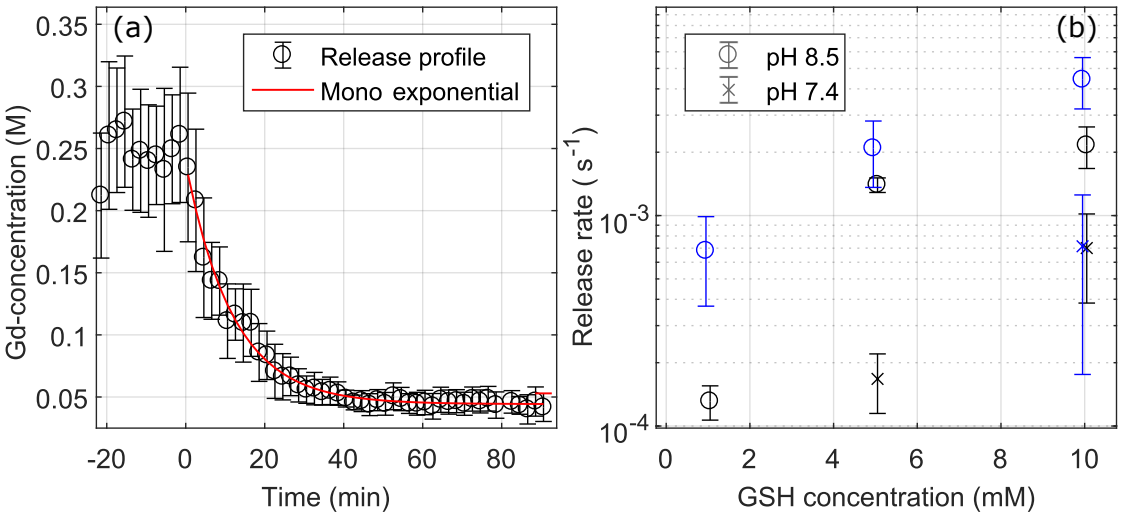

Figure 7.31. Calculated Gd(III) release for the redox sensor. (a): Example for calculated Gd(III)-release over time for pH of 8.5 and $5\,\mathrm{mM}$ GSH. A mono Exponential has been fitted to the data set. The extracted release rates are plotted in **(b)**. (black): Data analyzed correspond to the measurements shown in figure 7.22. (blue): Data from Jitka Neburkova, measured *via* ICP-MS.

agreement with observations in literature [174].

7.3. Summary, Conclusion and Outlook

A new modular hybrid sensor platform has been developed, utilizing NV^- to probe chemical quantities in the vicinity of ND. T_1 relaxometry is applied to sense Gd(III)-complexes close to the NV. The cleavage of Gd(III)-complexes is activated by changes in pH or the presencee of a reducing agent. The resulting change in T_1 is used as a measure for this quantities. To enable crosstalk free determination of the NV spin lattice relaxation time, a robust pulse scheme, namely a linear chirp pulse, has been adapted to NV relaxometry. Experiments and simulations suggest that one can gain a factor of two in sensitivity by using linear chirp pulses instead of square pulses. In addition, less knowledge for initial microwave pulse parameters is needed, as the chirp pulse shows a wide acceptance range. Therefore the adiabatic condition has to be fulfilled. Expressed in terms of the adiabaticity factor, Q must be at least two to reach half of the maximum contrast possible. Experimentally values between 1.5 and 10 were observed. The latter were estimated based on the spin contrast of individual data set.
Due to the robustness of the used pulse scheme, 2D imaging of individual sensor units could be accomplished. Thereby these have been fixed on a cover slide and were activated. One can clearly distinguish between the activated and new sensor units, which have been introduced after activation.
The performed simulations allowed to correlate the measured T_1 time to a corresponding Gd(III)-concentration. Furthermore one can calculate the release rates of Gd(III)-complexes. Comparing the own data to ICP-MS measurements done by collaboration partners, yield a good agreement for the extracted release rates. Plotting the release rate versus pH reveals a linear behavior on a logarithmic scale. In case of the fluorescent measurements, a saturating to lower pH values was observed. The same analysis was performed for the chemical redox sensor for different GSH concentrations and two different pH. Thereby the release rate for pH 7.4 is almost one order of magnitude lower then at pH 8.5. This is qualitatively consistent with literature [174], as the reductive behavior of GSH is pH dependent. Reference samples with a non-cleavable linker showed slight change in T_1 for changes in the ionic strength or pH of different buffer solution. Simulation results suggest that no significant swelling or collapse of the polymer shell occur. Experimental results

have been published in [159].
The modular hybrid sensor system has been designed in a irreversible fashion. Sensing of a chemical compound is achieved by activating the release of Gd(III)-complexes. In principle every linker that is cleavable by the presents of a certain quantity can be considered, making the present approach an universal ansatz.
But also a different design could be considered with some modifications. Therefore the linker shall be non-responsive, similar to the control sample, and the sensing capacity is mapped onto the polymer. As shown in [102], some polymers show a strong swelling/collapse behavior by changing for example pH or temperature. As figure 7.27 suggests, swelling or the collapse of polymer will change T_1. Taking for example the swelling/collapse ratio of a pH sensitive nanogel in [196], the nanogel particles change their hydrodynamic radius from 40 nm to 60 nm depending on the pH. The volumetric change, the nanogel undergoes, is a factor of around 3. In case of a 32 nm sized nanodiamond with a Gd(III) decorated polymer shell, having a thickness of 10 nm in the collapsed state, one will see an extension of the shell to around 22 nm. The corresponding change in T_1 will be around 15 µs to 30 µs. For optimal parameters the sensitivity can reach $\sim 2.8\,\mu s/\sqrt{Hz}$ (see section C.3 for calculation). As the swelling and collapse of polymers is connected to the (de)protonation of specific groups within the polymer, a rapid change of the polymer volume occurs around its pK_s value. Using the latter as a working point, one could design very sensitive pH sensors. For example, if the swelling to collapse occurs in a range of one pH values, the sensitivity with the given method would be around $\sim 0.2\ pH/\sqrt{Hz}$ in the vicinity of the given pK_s value.

A. CW nano thermometry

A.1. Testing absorption of microwave structure

A.1.1. Setup: Temperature change of NV versus Thermistor

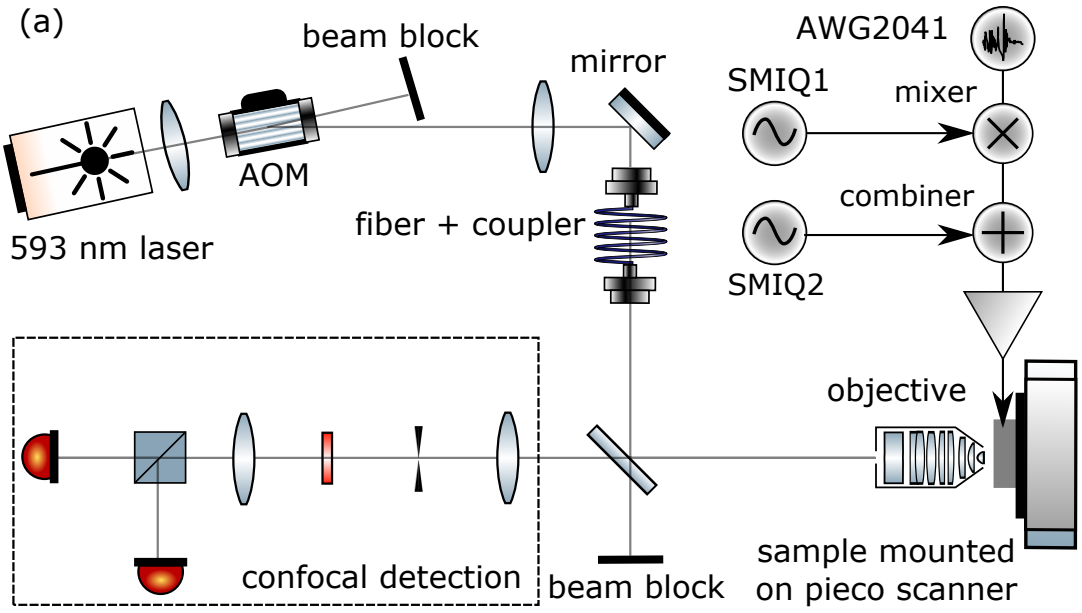

Figure A.1. Testing influence of microwave heating. Setup used for testing microwave heating. see section 5.3.1

A.1.2. Setup: Measuring the absorption of used sample chamber design

To calculate the relative power absorbed by the used sample chamber design, equation (A.1) has been used:

$$\frac{\Delta P}{P_0} = 1 - \frac{T + (R - R_{res})}{P_0} \tag{A.1}$$

For details of the individual components see figure A.1

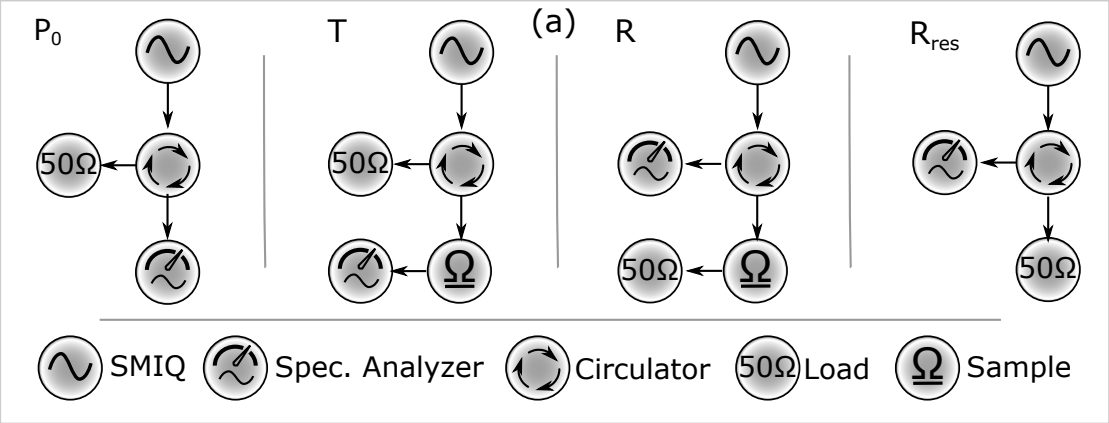

Figure A.2. Testing microwave absorption of used sample chamber.

A.1.3. Ionic strength of surrounding and microwave heating

Solutions used to acquire Figure 5.11(b):

0 mM : Purified water
150 mM : Cell medium (see A.3)
500 mM : phosphate-buffered saline (PBS) buffer 500 mM pH 7.4
1000 mM : PBS buffer 1000 mM pH 7.4
2000 mM : 2000 mM NaCl in H_2O

Solutions used to acquire Figure 5.11(c):

100 mM : HEPES buffer 50 mM pH 7.4 with 100 mM NaCl
200 mM : HEPES buffer 50 mM pH 7.4 with 200 mM NaCl

300 mM : HEPES buffer 50 mM pH 7.4 with 300 mM NaCl
400 mM : HEPES buffer 50 mM pH 7.4 with 400 mM NaCl
500 mM : HEPES buffer 50 mM pH 7.4 with 500 mM NaCl
1000 mM :HEPES buffer 50 mM pH 7.4 with 1000 mM NaCl

A.2. Individual results for CCCP stimulation of single HepG2 cells.

To get further inside into individual result for CCCP stimulation of single cells, every performed measurement has been plotted in Figure A.3

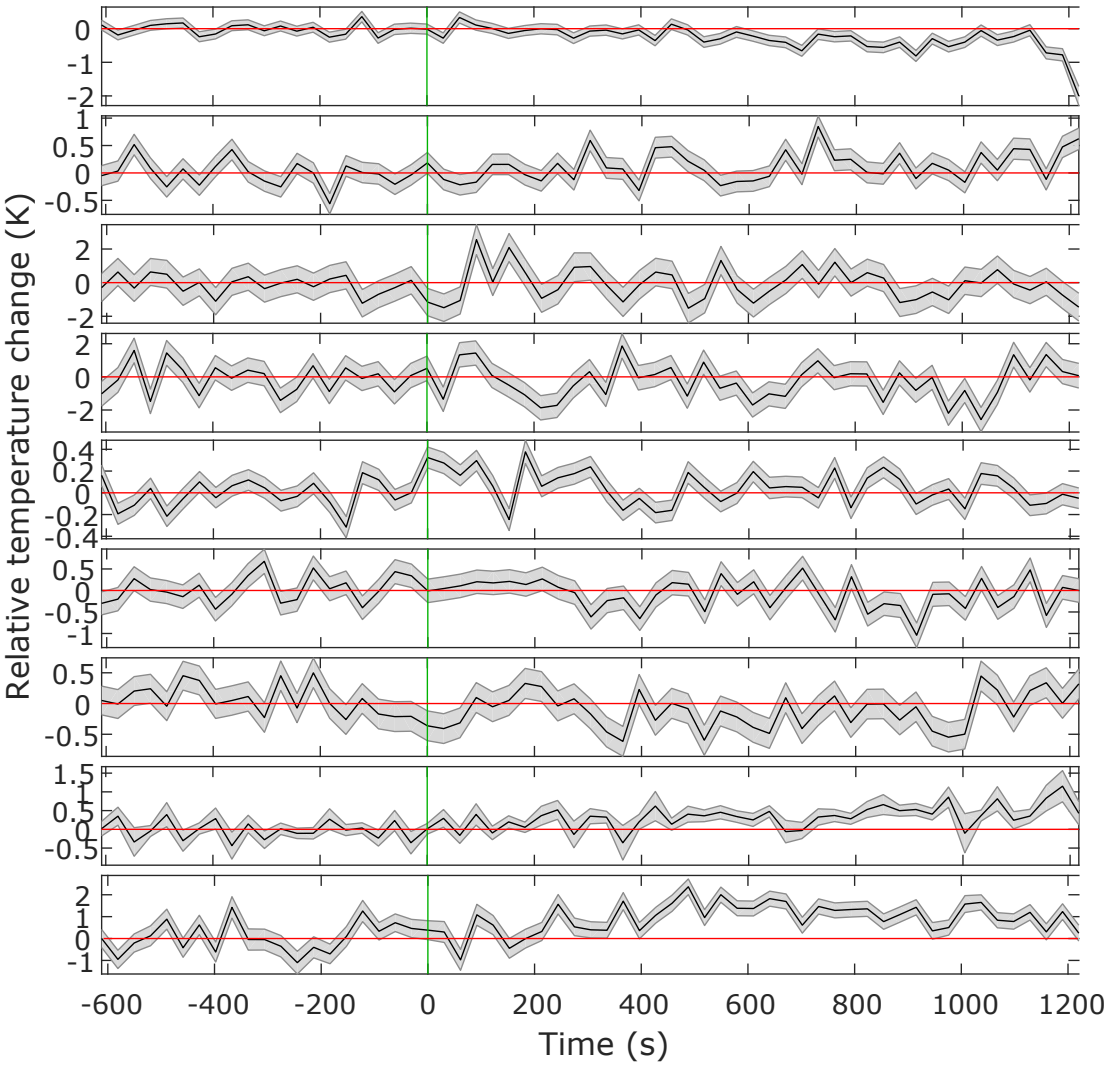

Figure A.3. Individual results for CCCP stimulation of single HepG2 cells. The green line indicates the injection point of CCCP solution

A.3. Endocytosis: Introducing NDs into living cells

Human liver carcinoma cells (HepG2) were obtained from the company ATCC and grown in Dulbecco's modified Eagle's medium (DMEM High Glucose w/ L-Glutamine w/ Sodium Pyruvate, Biowest), supplemented with 10 % heat inactivated fetal calf serum (Biowest), 100 mM HEPES pH 7.4 (Carl Roth) , 100 IU mL^{-1} Penicillin G Sodium salt and 100 µg mL^{-1} Streptomycin (Carl Roth). Cells were maintained in a standard cell culture incubator at 37 °C in a humidified atmosphere with 5 % CO_2. Home-built confocal dishes were sterilized in 70 % Ethanol and coated with 0.01 % poly-L-Lysine solution (MW 150000-300000, Sigma) before cell seeding. For intracellular location studies of NDs, cells were seeded in confocal dish 1×10^5 cells in 2 mL complete DMEM medium). After 24 h the cells were incubated with 10 µg mL^{-1} NDs for additional 24 h in 2 mL DMEM medium without calf serum). Cell preparations has been carried out by Andrea Zappe.

A.4. TPP-modification of nanodiamonds

ND particles were obtained by high pressure high temperature HPHT synthesis [33]. The ND-TPP particles were prepared, using the protocol in Marrache et al. [120] with minor modification. Specifically, an 1 mL aqueous solution of ND (1 mg mL^{-1}) particles were mixed with 10 mL (3-aminopropyl)triethoxysilane (Sigma A3648) while stirring for 2 h at room temperature. Then ND particles were separated *via* centrifugation. Afterwards, 1 mL ND-(3-aminopropyl)triethoxysilane (APTES) particles, dispersed in Dimethyl sulfoxide, were mixed with 60 mg (4-Carboxybutyl)triphenylphosphonium bromide (Sigma 157945), 20 mg N-(3-Dimethylaminopropyl)-N-ethylcarbodiimide hydrochloride (Sigma 03445) and 10 mg N-Hydroxysuccinimide (Sigma 130672). The mixture was stirred over night at room temperature. To isolated ND-TPP particles, again a centrifuge was used. Protocol and preparation of ND-TPP particles has been developed and carried out by Zhiqin Chu.

A.5. Stimulation of HepG2 cells with CCCP

Before stimulation cells were stained with "Mitotracker green FM" (Thermo Fisher Scientific M7514) according the manufacturers instructions. After staining, the cells were transferred to the confocal setup and incubated until the cell culture is in thermal equilibrium with the cell incubator. A 10 mM stock solution of CCCP (Sigma C2759) in dimethylsulfoxide was prepared and 4 µl of this solution were added to 100 µl dulbecco modified eagle medium (DMEM) without fetal bovine serum. The solution was filled into a syringe with a tube attached and was injected into the cell culture for stimulation. Thereby the tube is inside the incubator and selves as a reservoir for the CCCP solution before injection.

A.6. MTT Assay for cell viability test after CCCP stimulation

HepG2 cells were seeded in a 96 well cell culture plate in dulbecco modified eagle medium (DMEM) media with the addition of 10 % fetal calf serum (5000 cells per well in 100 µl media). On the next day DMEM media (without fetal bovine serum) with the addition of 0, 5, 10, 50, 100 and 200 µM CCCP was prepared. The cell culture media wash changed against 100 µM of this media. And the cells were incubated for 2 h at 37 °C with the different CCCP concentrations.
A MTT solution in PBS (5 mg ml^{-1}) was prepared. 10 µl of this solution were added to 90 µl DMEM media (without fetal bovine serum). The media with CCCP was removed and the cells were incubated for 3.5 h with the MTT containing media. The media was removed once again and the cells were washed with PBS. Then 200 µl of dimethyl sulfoxide were added to every well, to so solubilize the formed Formazan. The plate was covered with aluminium foil and was incubated for 15 min on an orbital shaker. The absorbance at 590 nm (reference 620 nm) was measured with a Tecan Reader. The measurement was done by Andrea Zappe.

B. Robust-pulsed nano thermometry

$P_{xy}^{(1')}$ and $P_{xy}^{(2')}$ project in the subspace of $|0\rangle$,$|-1\rangle$ and $|0\rangle$,$|+1\rangle$ onto a superpositions state, but do not lead to an unphysical reduction of the population in the quantum system, as it is the case for $P_{xy}^{(1)}$ and $P_{xy}^{(2)}$.

$$P_{xy}^{(1')} = \begin{pmatrix} 1 & 0 & 0 & 0 & 0 & 0 & 0 & 0 & 0 \\ 0 & 0 & 0 & 0 & 0 & 0 & 0 & 0 & 0 \\ 0 & 0 & 0 & 0 & 0 & 0 & 0 & 0 & 0 \\ 0 & 0 & 0 & 0 & 0 & 0 & 0 & 0 & 0 \\ 0 & 0 & 0 & 0 & 0.5 & 0 & 0 & 0 & 0.5 \\ 0 & 0 & 0 & 0 & 0 & 1 & 0 & 0 & 0 \\ 0 & 0 & 0 & 0 & 0 & 0 & 0 & 0 & 0 \\ 0 & 0 & 0 & 0 & 0 & 0 & 0 & 1 & 0 \\ 0 & 0 & 0 & 0 & 0.5 & 0 & 0 & 0 & 0.5 \end{pmatrix}, P_{xy}^{(2')} = \begin{pmatrix} 0.5 & 0 & 0 & 0 & 0.5 & 0 & 0 & 0 & 0 \\ 0 & 1 & 0 & 0 & 0 & 0 & 0 & 0 & 0 \\ 0 & 0 & 0 & 0 & 0 & 0 & 0 & 0 & 0 \\ 0 & 0 & 0 & 1 & 0 & 0 & 0 & 0 & 0 \\ 0.5 & 0 & 0 & 0 & 0.5 & 0 & 0 & 0 & 0 \\ 0 & 0 & 0 & 0 & 0 & 0 & 0 & 0 & 0 \\ 0 & 0 & 0 & 0 & 0 & 0 & 0 & 0 & 0 \\ 0 & 0 & 0 & 0 & 0 & 0 & 0 & 0 & 0 \\ 0 & 0 & 0 & 0 & 0 & 0 & 0 & 0 & 1 \end{pmatrix}. \tag{B.1}$$

$P_{xy}^{(1'b)}$ and $P_{xy}^{(2'b)}$ project in the subspace of $|0\rangle$,$|-1\rangle$ and $|0\rangle$,$|+1\rangle$ onto a superpositions state, but do not lead to an unphysical reduction of the population in the quantum system as it is the case for $P_{xy}^{(1b)}$ and $P_{xy}^{(2b)}$. In addition, same to $P_{xy}^{(1b)}$

and $P_{xy}^{(2b)}$, a phase of $\pi/2$ and $-\pi/2$ is added, respectively.

$$P_{xy}^{(1'b)} = \begin{pmatrix} 1 & 0 & 0 & 0 & 0 & 0 & 0 & 0 & 0 \\ 0 & 0 & 0 & 0 & 0 & 0 & 0 & 0 & 0 \\ 0 & 0 & 0 & 0 & 0 & 0 & 0 & 0 & 0 \\ 0 & 0 & 0 & 0 & 0 & 0 & 0 & 0 & 0 \\ 0 & 0 & 0 & 0 & 0.5 & 0 & 0 & 0 & 0.5 \\ 0 & 0 & 0 & 0 & 0 & \mathrm{i} & 0 & 0 & 0 \\ 0 & 0 & 0 & 0 & 0 & 0 & 0 & 0 & 0 \\ 0 & 0 & 0 & 0 & 0 & 0 & 0 & -\mathrm{i} & 0 \\ 0 & 0 & 0 & 0 & 0.5 & 0 & 0 & 0 & 0.5 \end{pmatrix}, P_{xy}^{(2'b)} = \begin{pmatrix} 0.5 & 0 & 0 & 0 & 0.5 & 0 & 0 & 0 & 0 \\ 0 & \mathrm{i} & 0 & 0 & 0 & 0 & 0 & 0 & 0 \\ 0 & 0 & 0 & 0 & 0 & 0 & 0 & 0 & 0 \\ 0 & 0 & 0 & -\mathrm{i} & 0 & 0 & 0 & 0 & 0 \\ 0.5 & 0 & 0 & 0 & 0.5 & 0 & 0 & 0 & 0 \\ 0 & 0 & 0 & 0 & 0 & 0 & 0 & 0 & 0 \\ 0 & 0 & 0 & 0 & 0 & 0 & 0 & 0 & 0 \\ 0 & 0 & 0 & 0 & 0 & 0 & 0 & 0 & 0 \\ 0 & 0 & 0 & 0 & 0 & 0 & 0 & 0 & 1 \end{pmatrix}. \tag{B.2}$$

$P^{(1'')}$ and $P^{(2'')}$ remove coherence, if the quantum system is not in a superposition state in the subspace of $|0\rangle$,$|-1\rangle$ and $|0\rangle$,$|+1\rangle$.

$$P^{(1'')} = \begin{pmatrix} 1 & 0 & 0 & 0 & 0 & 0 & 0 & 0 & 0 \\ 0 & 0 & 0 & 0 & 0 & 0 & 0 & 0 & 0 \\ 0 & 0 & 0 & 0 & 0 & 0 & 0 & 0 & 0 \\ 0 & 0 & 0 & 0 & 0 & 0 & 0 & 0 & 0 \\ 0 & 0 & 0 & 0 & 1 & 0 & 0 & 0 & 0 \\ 0 & 0 & 0 & 0 & 0 & 1 & 0 & 0 & 0 \\ 0 & 0 & 0 & 0 & 0 & 0 & 0 & 0 & 0 \\ 0 & 0 & 0 & 0 & 0 & 0 & 0 & 1 & 0 \\ 0 & 0 & 0 & 0 & 0 & 0 & 0 & 0 & 1 \end{pmatrix}, P^{(2'')} = \begin{pmatrix} 1 & 0 & 0 & 0 & 0 & 0 & 0 & 0 & 0 \\ 0 & 1 & 0 & 0 & 0 & 0 & 0 & 0 & 0 \\ 0 & 0 & 0 & 0 & 0 & 0 & 0 & 0 & 0 \\ 0 & 0 & 0 & 1 & 0 & 0 & 0 & 0 & 0 \\ 0 & 0 & 0 & 0 & 1 & 0 & 0 & 0 & 0 \\ 0 & 0 & 0 & 0 & 0 & 0 & 0 & 0 & 0 \\ 0 & 0 & 0 & 0 & 0 & 0 & 0 & 0 & 0 \\ 0 & 0 & 0 & 0 & 0 & 0 & 0 & 0 & 0 \\ 0 & 0 & 0 & 0 & 0 & 0 & 0 & 0 & 1 \end{pmatrix}. \tag{B.3}$$

$P^{(1''b)}$ and $P^{(2''b)}$ remove coherence, if the quantum system is not in a superposition state in the subspace of $|0\rangle$,$|-1\rangle$ and $|0\rangle$,$|+1\rangle$, and add similar to $P_{xy}^{(1b)}$ and

$P_{xy}^{(2b)}$, a phase of $\pi/2$ and $-\pi/2$, respectively.

$$P^{(1''b)} = \begin{pmatrix} 1 & 0 & 0 & 0 & 0 & 0 & 0 & 0 & 0 \\ 0 & 0 & 0 & 0 & 0 & 0 & 0 & 0 & 0 \\ 0 & 0 & 0 & 0 & 0 & 0 & 0 & 0 & 0 \\ 0 & 0 & 0 & 0 & 0 & 0 & 0 & 0 & 0 \\ 0 & 0 & 0 & 0 & 1 & 0 & 0 & 0 & 0 \\ 0 & 0 & 0 & 0 & 0 & \mathrm{i} & 0 & 0 & 0 \\ 0 & 0 & 0 & 0 & 0 & 0 & 0 & 0 & 0 \\ 0 & 0 & 0 & 0 & 0 & 0 & 0 & -\mathrm{i} & 0 \\ 0 & 0 & 0 & 0 & 0 & 0 & 0 & 0 & 1 \end{pmatrix}, P^{(2''b)} = \begin{pmatrix} 1 & 0 & 0 & 0 & 0 & 0 & 0 & 0 & 0 \\ 0 & \mathrm{i} & 0 & 0 & 0 & 0 & 0 & 0 & 0 \\ 0 & 0 & 0 & 0 & 0 & 0 & 0 & 0 & 0 \\ 0 & 0 & 0 & -\mathrm{i} & 0 & 0 & 0 & 0 & 0 \\ 0 & 0 & 0 & 0 & 1 & 0 & 0 & 0 & 0 \\ 0 & 0 & 0 & 0 & 0 & 0 & 0 & 0 & 0 \\ 0 & 0 & 0 & 0 & 0 & 0 & 0 & 0 & 0 \\ 0 & 0 & 0 & 0 & 0 & 0 & 0 & 0 & 0 \\ 0 & 0 & 0 & 0 & 0 & 0 & 0 & 0 & 1 \end{pmatrix}. \tag{B.4}$$

C. Chemical sensing

C.1. Buffer Systems: pH Sensor

In the following the buffer systems for different chemical sensors are described.

Buffer System 1 pH 7.4: 50 mM HEPES adjusted with 1 M NaOH
pH 6.0: 50 mM Sodium acetate adjusted with 50 mM Acetic acid
pH 4.5: 50 mM Sodium acetate adjusted with 1 M HCl
pH 2: 50 mM Citric acid adjusted with 1 M HCl

Buffer System 2 The Buffer System 2 is a so called B&R buffer. See also reference [29]. A 0.5 M stock solution pH 3.29 was prepared by mixing 0.0667 g Sodium hydroxide , 0.0664 mL Acetic acid, 0.114 mL Phosphoric acid, 0.103 g Boric acid and 1.729 g Potassium chloride.
The stock solution was diluted to 50 mM concentration and adjusted to pH 3.8, 4.5, 5.5, 6.2 and 6.9 by the addition of NaOH. The conductivity of all solutions was adjusted to the same value (6.40 mS) by the addition of Potassium chloride.

C.2. Buffer Systems: Redox Sensor

pH 7.4: 50 mM HEPES pH 7.4 adjusted with 1 M NaOH
pH 8.5: 50 mM TRIS pH 8.5 adjusted with 1 M HCl

C.3. Sensitivity calculation for T_1 relaxometry.

The overall number of photons $I_0(\tau)$ and $I_{\pm1}(\tau)$ one collects during a measurement for the spin sublevel $m_s = 0$ and $m_s = \pm$, can be written as

$$\begin{aligned} I_0(\tau) &= \frac{R \cdot T_{\text{read}} \Delta t}{\tau} \cdot \left[1 + |c_0| \cdot \exp\left(-(\tau/T_1)^{\beta}\right)\right] \\ I_{\pm1}(\tau) &= \frac{R \cdot T_{\text{read}} \Delta t}{\tau} \cdot \left[1 - |c_1| \cdot \exp\left(-(\tau/T_1)^{\beta}\right)\right]. \end{aligned} \tag{C.1}$$

Thereby τ is the waiting time after reading out a certain spin state, R the detected photon flux, Δt the measurement time, T_{read} the length of the read out interval and c_0/c_1 the spin contrast of the corresponding state. To calculate the sensitivity of a measurement, the power noise equivalent δT_1 is calculated:

$$\delta T_1 = \frac{\sigma_I}{\partial S(T_1)/\partial T_1}. \tag{C.2}$$

σ_I is the standard deviation of the measured signal that is assumed to be shot noise limited:

$$\sigma_I = \sqrt{I_0 + I_{\pm1}}. \tag{C.3}$$

$S(T_1)$, the signal function, is defined as the difference between I_0 and $I_{\pm1}$. Calculating δT_1 reveals

$$\delta T_1 = \frac{2 \cdot T_1^{1+\beta} \cdot \tau^{1/2-\beta}}{c \cdot \beta \sqrt{R \cdot T_{\text{read}}}} \frac{1}{\sqrt{T}} \exp\left((\tau/T_1)^{\beta}\right). \tag{C.4}$$

Therefore one assumes the relation $||c_0| - |c_1|| \ll 1$ and $|c_0| + |c_1| = c$. As one probes $m_s = 0$ and $m_s = \pm1$ during a full sequence, Δt has been replaced by half of the overall measurement time T. The optimum set point for $\beta = 1$ is $\tau = T_1/2$, and the minimum sensitivity becomes

$$\delta T_1 \approx \frac{4.66 \cdot T_1^{3/2}}{c\sqrt{R \cdot T_{\text{read}}}} \frac{1}{\sqrt{T}}. \tag{C.5}$$

In the performed experiments a maximum spin contrast of around 11 % was reached. Analyzing the PL spectra (see section 7.1.3, page 196) of the used nanodiamonds,

reveals that already 1/3 of the contrast is lost by also exciting NV^0. If orange laser light is used for readout, one will only excite NV^-. As a consequence the spin contrast will increase. For a spin contrast of 17 %, a typical photon flux R of 1.5 Mcps (5 NVs), a typical readout interval of 500 ns and a T_1 time of 20 µs, δT_1 is around $2.8\,\mu s/\sqrt{Hz}$.

Acknowledgements

I want to thank Prof. Dr. Wrachtrup for giving me the opportunity to do my doctoral degree at the 3th Institute of Physics in Stuttgart. For his positively inspiring attitude and inputs and that he always gave me the feeling to be welcome during the past years.
I would also like to thank Prof. Dr. Peter Michler and Prof. Dr. Hans Peter Büchler for taking their time to evaluate this dissertations.

In addition, I want to thank Dr. Andrea Zappe, Dr. Philipp Neumann, Dr. Rolf Reuter, Philipp Konzelmann, Matthias Niethammer, Matthias Widmann, Stefan Lasse and Britta Lenz for cross reading my thesis and giving me valuable inputs. Sometimes projects stand and fall with the details: Especially Dr. Andrea Zappe, Rolf Reuter and Philipp Neumann helped me a lot during the last years with their knowledge and I'm grateful that you shared your expertise with me. In that sense I also want to thank Prof. Dr. Fedor Jelesko, Dr. Boris Naydenov, Dr. Roman Kolesov, Dr. Rainer Stöhr and Dr. Sang-Yun Lee.
I also want to say many thanks to our former secretary Mrs. Schettler and her replacement Mrs. Unger and to our former cleaning personal Mrs. Faletar and her replacement Mrs. Spajic for their commitment beyond the standard business.

Last years would have been that fun without the right people in my enviroment. Therefore I want to thank again Matthias Widmann, Stefan Lasse, Matthias Niethammer, Denis Uhland, Thomas Kornhe, Rolf Reuter, Andrea Zappe, Philipp Neumann, Sang-Yun Lee, Seoyoung Paik, Philipp Konzelmann, Thomas Häberele, Steffen Steinert, Denis Antonov, Florian Dolde, Fedor Jelezko, Michael Börsch, Karin Seyfert, Eva, Nawid Zarrabi, Stefan Ernst, Merle Becker, Tobias Staudacher, Ingmar Jakobi, Roman Kolesov, Julia Michl, Matthias Pfender, Sina Burk, Rainer Stöhr, Sebastian Zaiser, Florestan Ziem, Fedor Jelesko, Boris Naydenov, Nathan Chejanovsky Daniel Arnold, Nabeel Aslam, Andreas Brunner, Durga Dasari, Andrej Denisenko, Ilja Gerhardt, Johannes Greiner, Stephan Hirschmann, Kai Kirn, Seyed Ali Momenzadeh, Roland Nagy, Thomas Oeckinghaus, Mohammad Rezai, Dominik Schmid-Lorch, Farida Shagieva, Andreas Volkmer, Claudia Unger,

Ivanka Spajic and all the other (former) members of the 3th Institute of Physics for the great time we had together.

I want to thank Florian Dolde and the company Diamond Nanotechnologies Inc. for providing the nanodiamonds sample used in the chapter robust pulsed nano thermometry.
I thank Zhiqin Chu for modifications on ND with TPP and to establish contract to Petr Cigler. Furthermore I want to thank Peter Cigler, Jitka Neburkova an Jan Vavra for the smooth and inspiring collaborations.

Nicht zuletzt möchte ich meiner ganzen Familie für den kompromisslosen Rückhalt über viele Jahre danken: Meiner Mutter Annemarie und meinem Vater Günther Rendler, die mich jahrelang mental unterstützt haben und eingesprungen sind, wenn mal wieder Not am Mann/der Frau war. Auch möchte ich meinem Bruder Norman, meiner Schwester Susanne und ganz besonders meinem kleineren Bruder "Babysitter" Marvin danken.
Zuletzt möchte ich ganz herzlich meinen Kindern Cornelius und Gabriel, sowie meiner geliebten Frau Thuy für ihre ewige Geduld und Verständnis gerade im letzten Jahr danken. Ohne euch wäre das alles so nicht möglich gewesen.

Ehrenwörtliche Erklärung

Ich erkläre hiermit, dass ich die vorliegende Arbeits sebstständig verfasst habe, und nur die angegebenen Hilfsmittel und Quellen benutzt habe.
Stuttgart, 19th March 2018

Torsten Rendler

List of Publications

1. Torsten Rendler, Jitka Neburkova, Ondrej Zemek, Jan Kotek, Andrea Zappe, Zhiqin Chu, Petr Cigler, Jörg Wrachtrup, *"Optical imaging of localized chemical events using programmable diamond quantum nanosensors"*, Nature Communications 8 (2017), Pages 14701

2. Marina Radulaski, Matthias Widmann, Matthias Niethammer, Jingyuan Linda Zhang, Sang-Yun Lee, Torsten Rendler, Konstantinos G Lagoudakis, Nguyen Tien Son, Erik Janzen, Takeshi Ohshima, Jörg Wrachtrup, Jelena Vuckovic, "Scalable Quantum Photonics with Single Color Centers in Silicon Carbide", Nano Letters 17 (2017), Issue 3, Pages 1782-1786

3. Sebastian Zaiser, Torsten Rendler, Ingmar Jakobi, Thomas Wolf, Sang-Yun Lee, Samuel Wagner, Ville Bergholm, Thomas Schulte-Herbrüggen, Philipp Neumann, Jörg Wrachtrup, "Enhancing quantum sensing sensitivity by a quantum memory", Nature communications 7 (2016), Pages 12279

4. Denis Uhland, Torsten Rendler, Matthias Widmann, Sang-Yun Lee, Jörg Wrachtrup, Ilja Gerhardt, *"Single molecule DNA detection with an atomic vapor notch filter"*, EPJ Quantum Technology 2 (2015), Issue 1,Pages 20

5. Matthias Widmann, Sang-Yun Lee, Torsten Rendler, Nguyen Tien Son, Helmut Fedder, Seoyoung Paik, Nan Zhao, Sen Yang, Ian Booker, Andrej Denisenko, Mohammad Jamali, SA Momenzadeh, T Ohshima, Adam Gali, Erik Janzén, Jörg Wrachtrup, *"Coherent control of single spins in silicon carbide at ambient condition"*, Nature material 14 (2014), Pages 164-168

6. Igor I Vlasov, Andrey A Shiryaev, Torsten Rendler, Steffen Steinert, Sang-Yun Lee, Denis Antonov, Márton Vörös, Fedor Jelezko, Anatolii V Fisenko, Lubov F Semjonova, Johannes Biskupek, Ute Kaiser, Oleg I Lebedev, Ilmo Sildos, Philip R Hemmer, Vitaly I Konov, Adam Gali, Jörg Wrachtrup, *"Molecular-sized fluorescent nanodiamonds"*, Nature nanotechnology 9 (2014), Issue 1, Pages 54-58

7. E Petkov, T Rendler, C Petkov, F Schnabel, JP Reithmaier, J Wrachtrup, C Popov, W Kulisch, *"Investigation of NV centers in nano-and ultrananocrystalline diamond pillars"*, physica status solidi (a) 210 (2013), Issue 10, Pages 2066-2073

8. Sang-Yun Lee, Matthias Widmann, Torsten Rendler, Marcus W Doherty, Thomas M Babinec, Sen Yang, Moritz Eyer, Petr Siyushev, Birgit JM Hausmann, Marko Loncar, Zoltán Bodrog, Adam Gali, Neil B Manson, Helmut Fedder, Jörg Wrachtrup, *"Readout and control of a single nuclear spin with a metastable electron spin ancilla"*, Nature nanotechnology 8 (2013), Issue 7, Pages 487-492

9. Emil Petkov, Cyril Popov, Torsten Rendler, Christo Petkov, Florian Schnabel, Helmut Fedder, Sang-Yun Lee, Wilhelm Kulisch, Johann Peter Reithmaier, Jörg Wrachtrup,*"Investigation of NV centers in diamond nanocrystallites and nanopillars"*, physica status solidi (b) 250 (2013), Issue 1, Pages 48-50

10. Jan Havlik, Vladimira Petrakova, Ivan Rehor, Vaclav Petrak, Michal Gulka, Jan Stursa, Jan Kucka, Jan Ralis, Torsten Rendler, San-Yung Lee, Rolf Reuter, Joerg Wrachtrup, Miroslav Ledvina, Milos Nesladek, Petr Cigler *"Boosting nanodiamond fluorescence: towards development of brighter probes"*, Nanoscale 5 (2013), Issue 8, Pages 3208-3211

Bibliography

[1] Reza Abbaschian, Henry Zhu, and Carter Clarke, *High pressure–high temperature growth of diamond crystals using split sphere apparatus*, Diamond and Related Materials **14** (2005), no. 11, 1916–1919. | Cited on page 26.

[2] Abcam, *Protocol Booklet. JC1 -Mitochondrial Membrane Potential Assay Kit (ab113850), Version 3, Last Updated 05/06/2017*, 2017. | Cited on page 116.

[3] Shawn M Abernathy and Robert R Sharp, *Spin dynamics calculations of electron and nuclear spin relaxation times in paramagnetic solutions*, The Journal of Chemical Physics **106** (1997), no. 22, 9032. | Cited on page 76.

[4] V. M. Acosta, E. Bauch, M. P. Ledbetter, A. Waxman, L. S. Bouchard, and D. Budker, *Temperature dependence of the nitrogen-vacancy magnetic resonance in diamond*, Physical Review Letters **104** (2010), no. 7, 1–4. | Cited on pages 36, 41, 128, and 175.

[5] Thiago P. Mayer Alegre, Charles Santori, Gilberto Medeiros-Ribeiro, and Raymond G. Beausoleil, *Polarization-selective excitation of nitrogen vacancy centers in diamond*, Physical Review B **76** (2007), no. 16, 1–5. | Cited on page 150.

[6] a. G. Alekseev, V. N. Amosov, a. V. Krasil'nikov, S. N. Tugarinov, V. V. Frunze, and a. Yu. Tsutskikh, *Transformation of GR1 defects in annealed natural type IIa diamonds*, Technical Physics Letters **26** (2000), no. 6, 496–498. | Cited on page 47.

[7] Robert Alicki and K. Lendi, *Quantum Dynamical Semigroups and Applications*, Springer-Verlag, 2007. | Cited on page 55.

[8] Anke Krueger, Jochen Stegk, Yuejiang Liang, Lu Li, and Jarre Gerald, *Biotinylated Nanodiamond: Simple and Efficient Functionalization of Detonation Diamond*, Langmuir **24** (2008), no. 8, 4200–4204. | Cited on page 30.

[9] Riikka Arppe, Tuomas Näreoja, Sami Nylund, Leena Mattsson, Sami Koho, Jessica M Rosenholm, Tero Soukka, and Michael Schäferling, *Photon upconversion sensitized nanoprobes for sensing and imaging of pH.*, Nanoscale **6** (2014), 6837–6843. | Cited on page 179.

[10] Nabeel Aslam, Matthias Pfender, Philipp Neumann, Rolf Reuter, Andrea Zappe, Felipe Fávaro de Oliveira, Andrej Denisenko, Hitoshi Sumiya, Shinobu Onoda, Junichi Isoya, and Jörg Wrachtrup, *Nanoscale nuclear magnetic resonance with chemical resolution*, Science **357** (2017), 67–71. | Cited on page 31.

[11] Nabeel Aslam, Gerhald Waldherr, Philipp Neumann, Fedor Jelezko, and Joerg Wrachtrup, *Photo-induced ionization dynamics of the nitrogen vacancy defect in diamond investigated by single-shot charge state detection*, New Journal of Physics **15** (2013), no. 1, 013064. | Cited on pages 33, 34, and 35.

[12] Guillaume Baffou, Hervé Rigneault, Didier Marguet, and Ludovic Jullien, *A critique of methods for temperature imaging in single cells.*, Nature methods **11** (2014), no. 9, 899–901. | Cited on pages 105, 123, and 143.

[13] Gopalakrishnan Balasubramanian, Philipp Neumann, Daniel Twitchen, Matthew Markham, Roman Kolesov, Norikazu Mizuochi, Junichi Isoya, Jocelyn Achard, Johannes Beck, Julia Tissler, Vincent Jacques, Philip R Hemmer, Fedor Jelezko, and Jörg Wrachtrup, *Ultralong spin coherence time in isotopically engineered diamond.*, Nature materials **8** (2009), no. 5, 383–7. | Cited on pages 39 and 121.

[14] A S Barnard, S P Russo, and I K Snook, *Size dependent phase stability of carbon nanoparticles: Nanodiamond versus fullerenes*, The Journal of Chemical Physics **118** (2003), no. 11, 5094. | Cited on page 48.

[15] A. S. Barnard and M. Sternberg, *Substitutional nitrogen in nanodiamond and bucky-diamond particles*, Journal of Physical Chemistry B **109** (2005), no. 36, 17107–17112. | Cited on pages 28, 48, and 87.

[16] A. S. Barnard, I. I. Vlasov, and V. G. Ralchenko, *Predicting the distribution and stability of photoactive defect centers in nanodiamond biomarkers*, Journal of Materials Chemistry **19** (2009), no. 3, 360. | Cited on pages 43 and 48.

[17] Elie Belorizky and Pascal H Fries, *Simple analytical approximation of the longitudinal electronic relaxation rate of Gd(III) complexes in solutions*, Phys. Chem. Chem. Phys. **6** (2004), 2341–2351. | Cited on pages 76 and 77.

[18] M N Berberan-Santos, E N Bodunov, and B Valeur, *Mathematical functions for the analysis of luminescence decays with underlying distributions 1. Kohlrausch decay function (stretched exponential)*, Chemical Physics **315** (2005), no. 1-2, 171–182. | Cited on pages 78 and 215.

[19] Jeremy M. Berg, John L. Tymoczko, and Lubert Stryer, *Stryer Biochemie*, Spektrum, 2012. | Cited on pages 80, 81, and 83.

[20] Alexios Beveratos, Rosa Brouri, Thierry Gacoin, Jean-philippe Poizat, and Philippe Grangier, *Nonclassical radiation from diamond nanocrystals*, Physical Review A **64** (2001), no. 6, 061802. | Cited on page 92.

[21] Vasudevanpillai Biju, Tamitake Itoh, Abdulaziz Anas, Athiyanathil Sujith, and Mitsuru Ishikawa, *Semiconductor quantum dots and metal nanoparticles: syntheses, optical properties, and biological applications*, Analytical and Bioanalytical Chemistry **391** (2008), no. 7, 2469–2495. | Cited on page 87.

[22] Asaf Bolker, Cecile Saguy, Moshe Tordjman, and Rafi Kalish, *Quantum confinement and Coulomb blockade in isolated nanodiamond crystallites*, Physical Review B **88** (2013), no. 3, 035442. | Cited on pages 31 and 48.

[23] Yu Borzdov, Yu Pal'yanov, I Kupriyanov, V Gusev, A Khokhryakov, A Sokol, and A Efremov, *HPHT synthesis of diamond with high nitrogen content from an Fe3N-C system*, Diamond and Related Materials **11** (2002), no. 11, 1863–1870. | Cited on page 26.

[24] C Bradac, T Gaebel, N Naidoo, M J Sellars, J Twamley, L J Brown, A S Barnard, T Plakhotnik, A V Zvyagin, and J R Rabeau, *Observation and control of blinking nitrogen-vacancy centres in discrete nanodiamonds*, Nature Nanotechnology **5** (2010), no. 5, 345–349. | Cited on pages 28, 35, 36, 48, 103, and 187.

[25] Carlo Bradac, Torsten Gaebel, Nishen Naidoo, James R. Rabeau, and Amanda. S. Barnard, *Prediction and Measurement of the Size-Dependent Stability of Fluorescence in Diamond over the Entire Nanoscale*, Nano Letters **9** (2009), no. 10, 3555–3564. | Cited on pages 28 and 48.

[26] Michael Braun and Steffen J. Glaser, *Concurrently optimized cooperative pulses in robust quantum control: Application to broadband Ramsey-type pulse sequence elements*, New Journal of Physics **16** (2014), 115002. | Cited on pages 62 and 144.

[27] Heinz-Peter Breuer and Francesco Petruccione, *The Theory of Open Quantum Systems*, Oxford University Press, 2007. | Cited on pages 52 and 54.

[28] C. D S Brites, P. P. Lima, N. J O Silva, A. Millán, V. S. Amaral, F. Palacio, and L. D. Carlos, *Thermometry at the nanoscale*, Nanoscale **4** (2013), 4799–4829. | Cited on page 105.

[29] Hubert Thomas Stanley Britton and Robert Anthony Robinson, *Universal buffer solutions and the dissociation constant of veronal*, J. Chem. Soc. (1931), 1456–1462. | Cited on pages 201, 203, and 233.

[30] R. Buchner, J. Barthel, and J. Stauber, *The dielectric relaxation of water between 0°C and 35°C*, Chemical Physics Letters **306** (1999), no. 1, 57–63. | Cited on page 123.

[31] P Caravan, J J Ellison, T J McMurry, and R B Lauffer, *Gadolinium(III) Chelates as MRI Contrast Agents: Structure, Dynamics, and Applications.*, Chemical Reviews **99** (1999), no. 9, 2293–2352. | Cited on pages 75, 77, and 209.

[32] Peter Caravan, Christian T. Farrar, Luca Frullano, and Ritika Uppal, *Influence of molecular parameters and increasing magnetic field strength on relaxivity of gadolinium- and manganese-based T1 contrast agents*, Contrast Media and Molecular Imaging **4** (2009), no. 2, 89–100. | Cited on page 75.

[33] Yi-Ren Chang, Hsu-Yang Lee, Kowa Chen, Chun-Chieh Chang, Dung-Sheng Tsai, Chi-Cheng Fu, Tsong-Shin Lim, Yan-Kai Tzeng, Chia-Yi Fang, Chau-Chung Han, Huan-Cheng Chang, and Wunshain Fann, *Mass production and dynamic imaging of fluorescent nanodiamonds*, Nature Nanotechnology **3** (2008), 284–288. | Cited on page 227.

[34] X. D. Chen, C. H. Dong, F. W. Sun, C. L. Zou, J. M. Cui, Z. F. Han, and G. C. Guo, *Temperature dependent energy level shifts of nitrogen-vacancy centers in diamond*, Applied Physics Letters **99** (2011), no. 16, 2009–2012. | Cited on pages 41, 108, and 128.

[35] K.L. Choy, *Chemical vapour deposition of coatings*, Progress in Materials Science **48** (2003), no. 2, 57–170. | Cited on page 27.

[36] Zhiqin Chu, Silu Zhang, Bokai Zhang, Chunyuan Zhang, Chia-Yi Fang, Ivan Rehor, Petr Cigler, Huan-Cheng Chang, Ge Lin, Renbao Liu, and Quan Li, *Unambiguous observation of shape effects on cellular fate of nanoparticles*, Scientific reports **4** (2014), 4495. | Cited on pages 81 and 106.

[37] Michael I. Current, Norman L. Turner, T.C. Smith, and Dave Crane, *Planar channeling effects in Si(100)*, Nuclear Instruments and Methods in Physics Research Section B: Beam Interactions with Materials and Atoms **6** (1985), 336–348. | Cited on page 47.

[38] T.L. Daulton, D.D. Eisenhour, T.J. Bernatowicz, R.S. Lewis, and P.R. Buseck, *Genesis of presolar diamonds: Comparative high-resolution transmission electron microscopy study of meteoritic and terrestrial nano-diamonds*, Geochimica et Cosmochimica Acta **60** (1996), no. 23, 4853–4872. | Cited on page 28.

[39] P De Fouquieres, S G Schirmer, S J Glaser, and Ilya Kuprov, *Second order gradient ascent pulse engineering*, Journal of Magnetic Resonance **212** (2011), 412–417. | Cited on page 61.

[40] Paul S. DeCarli and John C. Jamieson, *Formation of Diamond by Explosive Shock*, Science **133** (1961), no. 3467, 1821–1822. | Cited on page 27.

[41] Davide Degli Esposti, Jocelyne Hamelin, Nelly Bosselut, Raphaël Saffroy, Mylène Sebagh, Alban Pommier, Cécile Martel, and Antoinette Lemoine, *Mitochondrial roles and cytoprotection in chronic liver injury*, Biochemistry Research International **2012** (2012), no. 387626, 16 pages. | Cited on page 82.

[42] U. F. S. D'Haenens-Johansson, A. M Edmonds, B. L Green, and M. E. Newton, *Optical properties of the neutral silicon split-vacancy center in diamond*, Physical Review B **84** (2011), no. 24, 245208. | Cited on page 44.

[43] Siddharth Dhomkar, Jacob Henshaw, Harishankar Jayakumar, and Carlos A. Meriles, *Long-term data storage in diamond*, Science Advances **2** (2016), no. 10, e1600911. | Cited on page 35.

[44] M. W. Doherty, V. M. Acosta, A. Jarmola, M. S. J. Barson, N. B. Manson, D. Budker, and L. C. L. Hollenberg, *Temperature shifts of the resonances of the NV^- center in diamond*, Physical Review B **90** (2014), no. 4, 041201(R). | Cited on page 41.

[45] M. W. Doherty, F. Dolde, H. Fedder, F. Jelezko, J. Wrachtrup, N. B. Manson, and L. C L Hollenberg, *Theory of the ground-state spin of the NV^- center in diamond*, Physical Review B **85** (2012), no. 20, 1–21. | Cited on page 37.

[46] M. W. Doherty, N. B. Manson, P. Delaney, and L. C. L. Hollenberg, *The negatively charged nitrogen-vacancy centre in diamond: the electronic solution*, New Journal of Physics **13** (2011), no. 2, 025019. | Cited on pages 32 and 33.

[47] Marcus W. Doherty, Neil B. Manson, Paul Delaney, Fedor Jelezko, Jörg Wrachtrup, and Lloyd C.L. Hollenberg, *The nitrogen-vacancy colour centre in diamond*, Physics Reports **528** (2013), no. 1, 1 – 45, The nitrogen-vacancy colour centre in diamond. | Cited on page 87.

[48] F. Dolde, I. Jakobi, B. Naydenov, N. Zhao, S. Pezzagna, C. Trautmann, J. Meijer, P. Neumann, F. Jelezko, and J. Wrachtrup, *Room-temperature*

entanglement between single defect spins in diamond, Nature Phyiscs **9** (2013), 139–143. | Cited on page 46.

[49] Florian Dolde, Helmut Fedder, Marcus W. Doherty, Tobias Nöbauer, Florian Rempp, Gopalakrishnan Balasubramanian, Thomas Wolf, Friedemann Reinhard, Lloyd C. L. Hollenberg, Fedor Jelezko, and Jörg Wrachtrup, *Sensing electric fields using single diamond spins*, Nature Physics **7** (2011), 459–463. | Cited on pages 31 and 36.

[50] Valerii Yu Dolmatov, *Detonation synthesis ultradispersed diamonds: properties and applications*, Russian Chemical Reviews **70** (2001), no. 7, 607–626. | Cited on page 27.

[51] J S Donner, S A Thompson, M P Kreuzer, G Baffou, and R Quidant, *Mapping intracellular temperature using green fluorescent protein*, Nano Letters **12** (2012), no. 4, 2107–2111. | Cited on page 105.

[52] A. Dréau, M. Lesik, L. Rondin, P. Spinicelli, O. Arcizet, J. F. Roch, and V. Jacques, *Avoiding power broadening in optically detected magnetic resonance of single NV defects for enhanced dc magnetic field sensitivity*, Physical Review B **84** (2011), no. 19, 1–9. | Cited on page 131.

[53] Jörg Enderlein, Thomas Ruckstuhl, and Stefan Seeger, *Highly efficient optical detection of surface-generated fluorescence*, Applied Optics **38** (1999), no. 4, 724. | Cited on page 101.

[54] Felipe Fávaro De Oliveira, Denis Antonov, Ya Wang, Philipp Neumann, Seyed Ali Momenzadeh, Timo Häuermann, Alberto Pasquarelli, Andrej Denisenko, and Jörg Wrachtrup, *Tailoring spin defects in diamond by lattice charging*, Nature Communications **8** (2017), 15409. | Cited on page 47.

[55] Felipe Fávaro de Oliveira, Seyed Ali Momenzadeh, Denis Antonov, Helmut Fedder, Andrej Denisenko, and Jörg Wrachtrup, *On the efficiency of combined ion implantation for the creation of near-surface nitrogen-vacancy centers in diamond*, Physica Status Solidi (A) Applications and Materials Science **213** (2016), no. 8, 2044–2050. | Cited on page 47.

[56] S. Felton, A. M. Edmonds, M. E. Newton, P. M. Martineau, D. Fisher, D. J. Twitchen, and J. M. Baker, *Hyperfine interaction in the ground state of the negatively charged nitrogen vacancy center in diamond*, Physical Review B **79** (2009), 075203. | Cited on pages 36 and 37.

[57] M. Fischer, S. Gsell, M. Schreck, R. Brescia, and B. Stritzker, *Preparation of 4-inch Ir/YSZ/Si(001) substrates for the large-area deposition of single-crystal diamond*, Diamond and Related Materials **17** (2008), no. 7, 1035–1038. | Cited on page 27.

[58] P. H. Fries, G. Ferrante, E. Belorizky, and S. Rast, *The rotational motion and electronic relaxation of the gd(iii) aqua complex in water revisited through a full proton relaxivity study of a probe solute*, Journal of Chemical Physics **119** (2003), no. 16, 8636. | Cited on page 77.

[59] Chi-Cheng Fu, Hsu-Yang Lee, Kowa Chen, Tsong-Shin Lim, Hsiao-Yun Wu, Po-Keng Lin, Pei-Kuen Wei, Pei-Hsi Tsao, Huan-Cheng Chang, and Wunshain Fann, *Characterization and application of single fluorescent nanodiamonds as cellular biomarkers.*, Proceedings of the National Academy of Sciences of the United States of America **104** (2007), no. 3, 727–732. | Cited on page 30.

[60] K.-M. C. Fu, C. Santori, P. E. Barclay, and R. G. Beausoleil, *Conversion of neutral nitrogen-vacancy centers to negatively charged nitrogen-vacancy centers through selective oxidation*, Applied Physics Letters **96** (2010), no. 12, 121907. | Cited on page 35.

[61] T. Gaebel, M. Domhan, C. Wittmann, I. Popa, F. Jelezko, J. Rabeau, A. Greentree, S. Prawer, E. Trajkov, P.R. R. Hemmer, and J. Wrachtrup, *Photochromism in single nitrogen-vacancy defect in diamond*, Applied Physics B: Lasers and Optics **82** (2006), no. 2, 243–246. | Cited on page 35.

[62] T. Gaebel, I. Popa, A. Gruber, M. Domhan, F. Jelezko, and J. Wrachtrup, *Stable single-photon source in the near infrared*, New Journal of Physics **6** (2004), no. 1, 98–98. | Cited on page 20.

[63] Adam Gali, *Theory of the neutral nitrogen-vacancy center in diamond and its application to the realization of a qubit*, Physical Review B **79** (2009), no. 23, 235210. | Cited on page 33.

[64] Adam Gali and Jeronimo R. Maze, *Ab initio study of the split silicon-vacancy defect in diamond: Electronic structure and related properties*, Physical Review B **88** (2013), no. 23, 235205. | Cited on pages 43, 44, and 45.

[65] M. Garwood and L. DelaBarre, *The return of the frequency sweep: designing adiabatic pulses for contemporary NMR*, Journal of Magnetic Resonance **153** (2001), no. 2, 155–177. | Cited on pages 56, 57, 58, and 184.

[66] William A. Goddard III, Donald W. Brenner, Sergey Edward Lyshevski, and Gerald J. Iafrate, *Handbook of nanoscience, engineering, and technology*, CRC Press, 2012. | Cited on page 27.

[67] S. K. Gordeev and S. B. Korchagina, *On the stability of small-sized nanodiamonds*, Journal of Superhard Materials **29** (2007), no. 2, 124–125. | Cited on page 29.

[68] JP Goss, R. Jones, SJ Breuer, PR Briddon, and S. Öberg, *The Twelve-Line 1.682 eV Luminescence Center in Diamond and the Vacancy-Silicon Complex.*, Physical Review Letters **77** (1996), no. 14, 3041–3044. | Cited on pages 43, 44, and 91.

[69] Chie Gota, Kohki Okabe, Takashi Funatsu, Yoshie Harada, and Seiichi Uchiyama, *Hydrophilic fluorescent nanogel thermometer for intracellular thermometry*, Journal of the American Chemical Society **131** (2009), no. 8, 2766–2767. | Cited on page 105.

[70] Bernhard Grotz, Moritz V. Hauf, Markus Dankerl, Boris Naydenov, Sébastien Pezzagna, Jan Meijer, Fedor Jelezko, Jörg Wrachtrup, Martin Stutzmann, Friedemann Reinhard, and Jose A. Garrido, *Charge state manipulation of qubits in diamond*, Nature communications **3** (2012), 729. | Cited on pages 33, 35, and 36.

[71] Marcus Gutscher, Anne-Laure Pauleau, Laurent Marty, Thorsten Brach, Guido H Wabnitz, Yvonne Samstag, Andreas J. Meyer, and Tobias P. Dick, *Real-time imaging of the intracellular glutathione redox potential*, Nature Methods **5** (2008), no. 6, 553–559. | Cited on page 179.

[72] T. Häberle, D. Schmid-Lorch, F. Reinhard, and J. Wrachtrup, *Nanoscale nuclear magnetic imaging with chemical contrast.*, Nature Nanotechnology **10** (2015), 125–128. | Cited on page 183.

[73] E. L. Hahn, *Spin Echoes*, Physical Review **80** (1950), no. 4, 580–594. | Cited on page 65.

[74] Hermann Haken and Christoph Wolf, *Molekülphysik und Quantenchemie*, Springer-Verlag, 2006. | Cited on page 36.

[75] Bingyan Han, Jipei Yuan, and Erkang Wang, *Sensitive and Selective Sensor for Biothiols in the Cell Based on the Recovered Fluorescence of the CdTe Quantum Dots-Hg(II) System*, Analytical Chemistry **81** (2009), no. 13, 5569–5573. | Cited on page 179.

[76] R. Hanbury Brown and R. Q. Twiss, *Correlation between Photons in two Coherent Beams of Light*, Nature **177** (1956), no. 4497, 27–29. | Cited on page 23.

[77] J. Harrison, M. J. Sellars, and N. B. Manson, *Optical spin polarisation of the N-V centre in diamond*, Journal of Luminescence **107** (2004), no. 1, 245–248. | Cited on page 33.

[78] M. V. Hauf, B. Grotz, B. Naydenov, M. Dankerl, S. Pezzagna, J. Meijer, F. Jelezko, J. Wrachtrup, M. Stutzmann, F. Reinhard, and J. A. Garrido, *Chemical control of the charge state of nitrogen-vacancy centers in diamond*, Physical Review B **83** (2011), no. 8, 081304(R). | Cited on pages 33 and 36.

[79] Birgit J.M. M. Hausmann, Mughees Khan, Yinan Zhang, Tom M. Babinec, Katie Martinick, Murray Mccutcheon, Phil R. Hemmer, and Marko Lončar,

Fabrication of diamond nanowires for quantum information processing applications, Diamond and Related Materials **19** (2010), no. 5-6, 621–629. | Cited on page 101.

[80] Timothy F. Havel, *Robust procedures for converting among Lindblad, Kraus and matrix representations of quantum dynamical semigroups*, Journal of Mathematical Physics **44** (2003), no. 2, 534. | Cited on page 54.

[81] Jan Havlik, Vladimira Petrakova, Ivan Rehor, Vaclav Petrak, Michal Gulka, Jan Stursa, Jan Kucka, Jan Ralis, Torsten Rendler, San-Yung Lee, Rolf Reuter, Joerg Wrachtrup, Miroslav Ledvina, Milos Nesladek, and Petr Cigler, *Boosting nanodiamond fluorescence: towards development of brighter probes*, Nanoscale **5** (2013), no. 8, 3208. | Cited on pages 47 and 197.

[82] S. W. Hell, *Far-field optical nanoscopy*, Science **316** (2007), no. 5828, 1153–1158. | Cited on page 19.

[83] Christian Hepp, Tina Müller, Victor Waselowski, Jonas N Becker, Benjamin Pingault, Hadwig Sternschulte, Doris Steinmüller-Nethl, Adam Gali, Jeronimo R Maze, Mete Atatüre, and Christoph Becher, *Electronic Structure of the Silicon Vacancy Color Center in Diamond*, Physical Review Letters **112** (2014), no. 3, 036405. | Cited on page 43.

[84] J. S. Hodges, N. Y. Yao, D. Maclaurin, C. Rastogi, M. D. Lukin, and D. Englund, *Timekeeping with electron spin states in diamond*, Physical Review A **87** (2013), no. 3, 032118. | Cited on page 67.

[85] L.-C. Lora Huang and Huan-Cheng Chang, *Adsorption and immobilization of cytochrome c on nanodiamonds*, Langmuir **20** (2004), no. 14, 5879–5884. | Cited on page 29.

[86] Shintaro Ida, Toshiki Tsubota, Osamu Hirabayashi, Masanori Nagata, Yasumichi Matsumoto, and Akira Fujishima, *Chemical reaction of hydrogenated diamond surface with peroxide radical initiators*, Diamond and Related Materials **12** (2003), no. 3-7, 601–605. | Cited on page 29.

[87] Naoki Inomata, Masaya Toda, Masaaki Sato, Akihiko Ishijima, and Takahito Ono, *Pico calorimeter for detection of heat produced in an individual brown fat cell*, Applied Physics Letters **100** (2012), no. 15, 154104. | Cited on pages 105 and 143.

[88] Viktor Ivády, Tamás Simon, Jeronimo R Maze, I A Abrikosov, and Adam Gali, *Pressure and temperature dependence of the zero-field splitting in the ground state of NV centers in diamond: A first-principles study*, Physical Review B **90** (2014), no. 23, 235205. | Cited on page 41.

[89] K. D. Jahnke, B. Naydenov, T. Teraji, S. Koizumi, T. Umeda, J. Isoya, and F. Jelezko, *Long coherence time of spin qubits in ^{12}C enriched polycrystalline chemical vapor deposition diamond*, Applied Physics Letters **101** (2012), no. 1, 012405. | Cited on page 27.

[90] Kay D. Jahnke, Alp Sipahigil, Jan M. Binder, Marcus W. Doherty, Mathias Metsch, Lachlan J. Rogers, Neil B. Manson, Mikhail D. Lukin, and Fedor Jelezko, *Electron-phonon processes of the silicon-vacancy centre in diamond*, New Journal of Physics **17** (2015), no. 4, 043011. | Cited on pages 43, 44, and 92.

[91] Uwe Jantzen, Andrea B. Kurz, Daniel S. Rudnicki, Clemens Schäfermeier, Kay D. Jahnke, Ulrik L. Andersen, Valery A. Davydov, Viatcheslav N. Agafonov, Alexander Kubanek, Lachlan J. Rogers, and Fedor Jelezko, *Nanodiamonds carrying silicon-vacancy quantum emitters with almost lifetime-limited linewidths*, New Journal of Physics **18** (2016), no. 7, 073036. | Cited on pages 43 and 45.

[92] Kasper Jensen, Pauli Kehayias, and Dmitry Budker, *Magnetometry with nitrogen-vacancy centers in diamond*, pp. 553–576, Springer International Publishing, Cham, 2017. | Cited on page 31.

[93] D. C. Johnston, *Stretched exponential relaxation arising from a continuous sum of exponential decays*, Physical Review B **74** (2006), no. 18, 184430. | Cited on page 78.

[94] Yasuhiro Kamei, Motoshi Suzuki, Kenjiro Watanabe, Kazuhiro Fujimori, Takashi Kawasaki, Tomonori Deguchi, Yoshihiro Yoneda, Takeshi Todo, Shin Takagi, Takashi Funatsu, and Shunsuke Yuba, *Infrared laser–mediated gene induction in targeted single cells in vivo*, Nature Methods **6** (2009), no. 1, 79–81. | Cited on page 105.

[95] Stefan Kaufmann, David A. Simpson, Liam T. Hall, Viktor Perunicic, Philipp Senn, Steffen Steinert, Liam P. McGuinness, Brett C. Johnson, Takeshi Ohshima, Frank Caruso, Jörg Wrachtrup, Robert E. Scholten, Paul Mulvaney, and Lloyd Hollenberg, *Detection of atomic spin labels in a lipid bilayer using a single-spin nanodiamond probe*, Proceedings of the National Academy of Sciences of the United States of America **110** (2013), no. 27, 10894–10898. | Cited on page 179.

[96] Moloud Kaviani, Peter Deák, Bálint Aradi, Thomas Frauenheim, Jyh Pin Chou, and Adam Gali, *Proper surface termination for luminescent near-surface NV centers in diamond*, Nano Letters **14** (2014), no. 8, 4772–4777. | Cited on page 35.

[97] Navin Khaneja, Timo Reiss, Cindie Kehlet, Thomas Schulte-Herbrüggen, and Steffen J. Glaser, *Optimal control of coupled spin dynamics: design of NMR pulse sequences by gradient ascent algorithms*, Journal of Magnetic Resonance **172** (2005), no. 2, 296–305. | Cited on pages 54, 59, and 60.

[98] Filip Kielar, Lorenzo Tei, Enzo Terreno, and Mauro Botta, *Large Relaxivity Enhancement of Paramagnetic Lipid Nanoparticles by Restricting the Local Motions of the Gd(III) Chelates*, Journal of American Chemical Society **132** (2010), no. 23, 7836–7837. | Cited on page 75.

[99] S. C. Kitson, P. Jonsson, J. G. Rarity, and P. R. Tapster, *Intensity fluctuation spectroscopy of small numbers of dye molecules in a microcavity*, Physical Review A **58** (1998), no. 1, 620–627. | Cited on page 21.

[100] Shigeki Kiyonaka, Taketoshi Kajimoto, Reiko Sakaguchi, Daisuke Shinmi, Mariko Omatsu-Kanbe, Hiroshi Matsuura, Hiromi Imamura, Takenao

Yoshizaki, Itaru Hamachi, Takashi Morii, and Yasuo Mori, *Genetically encoded fluorescent thermosensors visualize subcellular thermoregulation in living cells*, Nature Methods **10** (2013), no. 12, 1232–1238. | Cited on page 105.

[101] Seymour H. Koenig and Rodney D. Brown, *Field-cycling relaxometry of protein solutions and tissue: Implications for MRI*, Progress in Nuclear Magnetic Resonance Spectroscopy **22** (1990), no. 6, 487–567. | Cited on page 77.

[102] Michael C. Koetting, Jonathan T. Peters, Stephanie D. Steichen, and Nicholas A. Peppas, *Stimulus-responsive hydrogels: Theory, modern advances, and applications*, Materials Science and Engineering R: Reports **93** (2015), 1–49. | Cited on page 222.

[103] Oleg Krichevsky and Grégoire Bonnet, *Fluorescence correlation spectroscopy: the technique and its applications*, Reports on Progress in Physics **65** (2002), no. 2, 251–297. | Cited on page 22.

[104] Anke Krueger and Daniel Lang, *Functionality is Key: Recent Progress in the Surface Modification of Nanodiamond*, Advanced Functional Materials **22** (2012), no. 5, 890–906. | Cited on pages 28, 29, and 30.

[105] G. Kucsko, P. C. Maurer, N. Y. Yao, M. Kubo, H. J. Noh, P. K. Lo, H. Park, and M. D. Lukin, *Nanometre-scale thermometry in a living cell*, Nature **500** (2013), no. 7460, 54–58. | Cited on pages 41, 106, and 128.

[106] Christian Kurtsiefer, Patrick Zarda, Sonja Mayer, and Harald Weinfurter, *The breakdown flash of silicon avalanche photodiodes-back door for eavesdropper attacks?*, Journal of Modern Optics **48** (2001), no. 13, 2039–2047. | Cited on pages 23 and 24.

[107] Abdelghani Laraoui, Florian Dolde, Christian Burk, Friedemann Reinhard, Jörg Wrachtrup, and Carlos A. Meriles, *High-resolution correlation spectroscopy of 13C spins near a nitrogen-vacancy centre in diamond*, Nature Communications **4** (2013), 1651. | Cited on pages 31 and 143.

[108] Abdelghani Laraoui, Jonathan S. Hodges, and Carlos A. Meriles, *Nitrogen-Vacancy-Assisted Magnetometry of Paramagnetic Centers in an Individual Diamond Nanocrystal*, Nano Letters **12** (2012), no. 7, 3477–3482. | Cited on page 186.

[109] Roy S. Lewis, Edward Anders, and Bruce T. Draine, *Properties, detectability and origin of interstellar diamonds in meteorites*, Nature **339** (1989), no. 6220, 117–121. | Cited on page 28.

[110] Jet Phey Lim and Paul A. Gleeson, *Macropinocytosis: an endocytic pathway for internalising large gulps*, Immunology and Cell Biology **89** (2011), no. 8, 836–843. | Cited on page 81.

[111] Yu Liu, Zhenning Gu, John L. Margrave, and Valery N. Khabashesku, *Functionalization of nanoscale diamond powder: Fluoro-, alkyl-, amino-, and amino acid-nanodiamond derivatives*, Chemistry of Materials **16** (2004), no. 20, 3924–3930. | Cited on page 29.

[112] Harvey F. Lodish, *Molecular cell biology*, W.H. Freeman, 2008. | Cited on page 81.

[113] B. B. Lowell and B. M. Spiegelman, *Towards a molecular understanding of adaptive thermogenesis*, Nature **404** (2000), 652–660. | Cited on page 105.

[114] Volodymyr I. Lushchak, *Glutathione Homeostasis and Functions: Potential Targets for Medical Interventions*, Journal of Amino Acids **2012** (2012), no. 736837, 1–26. | Cited on page 84.

[115] Qiang Ma and Xingguang Su, *Advances in the application of QD-based intracellular sensing systems*, Applied Spectroscopy Reviews **51** (2015), no. 2, 162–181. | Cited on page 179.

[116] S. Machnes, U. Sander, S. J. Glaser, P. Defouquì Eres, A. Gruslys, S. Schirmer, and T. Schulte-Herbrüggen, *Comparing, optimizing, and benchmarking quantum-control algorithms in a unifying programming framework*, PHYSICAL REVIEW A **84** (2011), 022305. | Cited on page 61.

[117] Pamela Maher, *The effects of stress and aging on glutathione metabolism*, Ageing Research Reviews **4** (2005), no. 2, 288–314. | Cited on page 84.

[118] F. Maier, M. Riedel, B. Mantel, J. Ristein, and L. Ley, *Origin of surface conductivity in diamond*, Physical Review Letters **85** (2000), no. 16, 3472–3475. | Cited on page 29.

[119] N.B. Manson and J.P. Harrison, *Photo-ionization of the nitrogen-vacancy center in diamond*, Diamond and Related Materials **14** (2005), no. 10, 1705–1710. | Cited on page 35.

[120] Sean Marrache, Shanta Dhar, and By Robert Langer, *Engineering of blended nanoparticle platform for delivery of mitochondria-acting therapeutics*, Proceedings of the National Academy of Sciences of the United States of America **109** (2012), no. 40, 16288–16293. | Cited on pages 113 and 227.

[121] J. R. Maze, A. Gali, E. Togan, Y. Chu, A. Trifonov, E. Kaxiras, and M. D. Lukin, *Properties of nitrogen-vacancy centers in diamond: the group theoretic approach*, New Journal of Physics **13** (2011), no. 2, 025025. | Cited on page 32.

[122] L. P. McGuinness, Y. Yan, A. Stacey, D. A. Simpson, L. T. Hall, D. Maclaurin, S. Prawer, P. Mulvaney, J. Wrachtrup, F. Caruso, R. E. Scholten, and L. C. L. Hollenberg, *Quantum measurement and orientation tracking of fluorescent nanodiamonds inside living cells*, Nature Nanotechnology **6** (2011), 358–363. | Cited on pages 36, 121, 185, and 187.

[123] T C Mcilvaine, *A Buffer Solution for colorimetric comparison*, Journal of Biological Chemistry **49** (1921), 183–186. | Cited on page 128.

[124] Ralf Metzler and Joseph Klafter, *The restaurant at the end of the random walk: recent developments in the description of anomalous transport by fractional dynamics*, Journal of Physics A: Mathematical and General **37** (2004), no. 31, 161–208. | Cited on page 84.

[125] Julia Michl, Tokuyuki Teraji, Sebastian Zaiser, Ingmar Jakobi, Gerald Waldherr, Florian Dolde, Philipp Neumann, Marcus W. Doherty, Neil B. Manson,

Junichi Isoya, and Jörg Wrachtrup, *Perfect alignment and preferential orientation of nitrogen-vacancy centers during chemical vapor deposition diamond growth on (111) surfaces*, Applied Physikal Letters **104** (2014), no. 10, 102407. | Cited on pages 27 and 47.

[126] Dimitar P. Mitev, Ashley T. Townsend, Brett Paull, and Pavel N. Nesterenko, *Microwave-assisted purification of detonation nanodiamond*, Diamond and Related Materials **48** (2014), 37–46. | Cited on page 28.

[127] Kim I. Mortensen, L. Stirling Churchman, James A. Spudich, and Henrik Flyvbjerg, *Optimized localization analysis for single-molecule tracking and super-resolution microscopy*, Nature methods **7** (2010), no. 5, 377–381. | Cited on page 95.

[128] Nawid Zarrabi, *Hidden Markov Modelle für Einzelmolekül̈daten*, Ph.D. thesis, Universität Stuttgart, 2010. | Cited on page 99.

[129] B. Naydenov, S. Pezzagna, F. Dolde, F. Jelezko, J. Wrachtrup, C. Trautmann, and J. Meijer, *Nano-pore channels in a mica sheet with high aspect ratio as a mask*, GSI SCIENTIFIC REPORT (2010), 2010. | Cited on page 46.

[130] Boris Naydenov, Friedemann Reinhard, Anke Laemmle, V. Richter, Rafi Kalish, Ulrika F. S. D'Haenens-Johansson, Mark Newton, Fedor Jelezko, and Joerg Wrachtrup, *Increasing the coherence time of single electron spins in diamond by high temperature annealing*, Applied Physics Letters **97** (2010), no. 24, 242511. | Cited on page 47.

[131] Boris Naydenov, V. Richter, Johannes Beck, Matthias Steiner, Philipp Neumann, Gopalakrishnan Balasubramanian, Jocelyn Achard, Fedor Jelezko, Joerg Wrachtrup, and Rafi Kalish, *Enhanced generation of single optically active spins in diamond by ion implantation*, Applied Physics Letters **96** (2010), no. 16, 163108. | Cited on page 47.

[132] Jitka Neburkova, Jan Vavra, and Petr Cigler, *Coating nanodiamonds with biocompatible shells for applications in biology and medicine*, Current Opinion in Solid State and Materials Science **21** (2017), no. 1, 43–53. | Cited on page 179.

[133] E. Neu, C. Arend, E. Gross, F. Guldner, C. Hepp, D. Steinmetz, E. Zscherpel, S. Ghodbane, H. Sternschulte, D. Steinmueller-Nethl, Y. Liang, a. Krueger, and C. Becher, *Narrowband fluorescent nanodiamonds produced from chemical vapor deposition films*, Applied Physics Letters **98** (2011), no. 24, 243107. | Cited on page 91.

[134] Elke Neu, Roland Albrecht, Martin Fischer, Stefan Gsell, Matthias Schreck, and Christoph Becher, *Electronic transitions of single silicon vacancy centers in the near-infrared spectral region*, Physical Review B **85** (2012), 245207. | Cited on page 44.

[135] Elke Neu, David Steinmetz, Janine Riedrich-Möller, Stefan Gsell, Martin Fischer, Matthias Schreck, and Christoph Becher, *Single photon emission from silicon-vacancy colour centres in chemical vapour deposition nano-diamonds on iridium*, New Journal of Physics **13** (2011), no. 2, 025012. | Cited on pages 21, 44, and 91.

[136] Felix Neugart, Andrea Zappe, Fedor Jelezko, C. Tietz, Jean Paul Boudou, Anke Krueger, and Joerg Wrachtrup, *Dynamics of Diamond Nanoparticles in Solution and Cells*, Nano Letters **7** (2007), no. 12, 3588–3591. | Cited on page 30.

[137] P. Neumann, I. Jakobi, F. Dolde, C. Burk, R. Reuter, G. Waldherr, J. Honert, T. Wolf, A. Brunner, J. H. Shim, D. Suter, H. Sumiya, J. Isoya, and J. Wrachtrup, *High-Precision Nanoscale Temperature Sensing Using Single Defects in Diamond*, Nano Letters **13** (2013), no. 6, 2738–2742. | Cited on pages 31, 41, 66, 106, 128, 144, 145, 152, and 175.

[138] I. I. Obraztsova and N. K. Eremenko, *Physicochemical modification of nanodiamonds*, Russian Journal of Applied Chemistry **81** (2008), no. 4, 603–608. | Cited on page 29.

[139] Kenichi Ohno, F. Joseph Heremans, Lee C. Bassett, Bryan A. Myers, David M. Toyli, Ania C. Bleszynski Jayich, Christopher J. Palmstrøm, and David D. Awschalom, *Engineering shallow spins in diamond with nitrogen delta-doping*,

Applied Physics Letters **101** (2012), no. 8, 082413. | Cited on pages 27 and 47.

[140] Kohki Okabe, Noriko Inada, Chie Gota, Yoshie Harada, Takashi Funatsu, and Seiichi Uchiyama, *Intracellular temperature mapping with a fluorescent polymeric thermometer and fluorescence lifetime imaging microscopy*, Nature Communications **3** (2012), no. 705, 1–9. | Cited on page 105.

[141] E. van Oort, N. B. Manson, and M. Glasbeek, *Optically detected spin coherence of the diamond n-v centre in its triplet ground state*, Journal of Physics C: Solid State Physics **21** (1988), no. 23, 4385. | Cited on page 31.

[142] S. Osswald, M. Havel, V. Mochalin, G. Yushin, and Y. Gogotsi, *Increase of nanodiamond crystal size by selective oxidation*, Diamond and Related Materials **17** (2008), no. 7-10, 1122–1126. | Cited on page 29.

[143] A. M. Panich, N. A. Sergeev, A. I. Shames, V. Yu Osipov, JP. Boudou, and S. D. Goren, *Size dependence of 13C nuclear spin-lattice relaxation in micro- and nanodiamonds.*, Journal of physics. Condensed matter : an Institute of Physics journal **27** (2015), no. 7, 072203. | Cited on page 74.

[144] E. Petkov, T. Rendler, C. Petkov, F. Schnabel, J.P. P. Reithmaier, J. Wrachtrup, C. Popov, and W. Kulisch, *Investigation of NV centers in nano- and ultrananocrystalline diamond pillars*, Physica Status Solidi (A) Applications and Materials Science **210** (2013), no. 10, 2066–2073. | Cited on page 27.

[145] V. Petrakova, I. Rehor, J. Stursa, M. Ledvina, M. Nesladek, and P. Cigler, *Charge-sensitive fluorescent nanosensors created from nanodiamonds*, Nanoscale **7** (2015), no. 29, 12307–12311. | Cited on pages 36 and 179.

[146] Vladimira Petrakova, *Interactions of nitrogen-vacancy centers with charged surfaces of functionalized nanodiamond particles for the detection of cellular processes*, Ph.D. thesis, Czech Technical University in Prague, 2012. | Cited on page 36.

[147] Vladimíra Petráková, Andrew Taylor, Irena Kratochvílová, František Fendrych, Jiří Vacík, Jan Kučka, Jan Štursa, Petr Cígler, Miroslav Ledvina, Anna Fišerová, Peter Kneppo, and Miloš Nesládek, *Luminescence of Nanodiamond Driven by Atomic Functionalization: Towards Novel Detection Principles*, Advanced Functional Materials **22** (2012), no. 4, 812–819. | Cited on page 36.

[148] Sébastien Pezzagna, Dominik Wildanger, Paul Mazarov, Andreas D. Wieck, Yanko Sarov, Ivo Rangelow, Boris Naydenov, Fedor Jelezko, Stefan W. Hell, and Jan Meijer, *Nanoscale Engineering and Optical Addressing of Single Spins in Diamond*, Small **6** (2010), no. 19, 2117–2121. | Cited on pages 46 and 47.

[149] Matthias Pfender, Nabeel Aslam, Patrick Simon, Denis Antonov, Gergő Thiering, Sina Burk, Felipe Fávaro de Oliveira, Andrej Denisenko, Helmut Fedder, Jan Meijer, Jose A. Garrido, Adam Gali, Tokuyuki Teraji, Junichi Isoya, Marcus William Doherty, Audrius Alkauskas, Alejandro Gallo, Andreas Grüneis, Philipp Neumann, and Jörg Wrachtrup, *Protecting a Diamond Quantum Memory by Charge State Control*, Nano Letters **17** (2017), no. 10, 5931–5937. | Cited on pages 33 and 36.

[150] Christoph M. Pieper and Jörg Enderlein, *Fluorescence correlation spectroscopy as a tool for measuring the rotational diffusion of macromolecules*, Chemical Physics Letters **516** (2011), no. 1-3, 1–11. | Cited on page 22.

[151] Hugh O Pierson, *HANDBOOK OF CARBON , GRAPHITE , DIAMOND AND FULLERENES*, Elsevier Fachverlag, 1993. | Cited on page 25.

[152] Benjamin Pingault, Jonas N. Becker, Carsten H H Schulte, Carsten Arend, Christian Hepp, Tillmann Godde, Alexander I. Tartakovskii, Matthew Markham, Christoph Becher, and Mete Atatüre, *All-optical formation of coherent dark states of silicon-vacancy spins in diamond*, Physical Review Letters **113** (2014), no. 26, 263601. | Cited on page 43.

[153] Norman F. Ramsey, *A Molecular Beam Resonance Method with Separated Oscillating Fields*, Physical Review **78** (1950), no. 6, 695–699. | Cited on page 65.

[154] Jean-Yves Raty, Giulia Galli, C. Bostedt, Tony W. Van Buuren, and Louis J. Terminello, *Quantum Confinement and Fullerenelike Surface Reconstructions in Nanodiamonds*, Physical Review Letters **90** (2003), no. 3, 037401. | Cited on page 48.

[155] M.A. Ray, T. Tyler, B. Hook, A. Martin, G. Cunningham, O. Shenderova, J.L. Davidson, M. Howell, W.P. Kang, and G. McGuire, *Cool plasma functionalization of nano-crystalline diamond films*, Diamond and Related Materials **16** (2007), no. 12, 2087–2089. | Cited on page 29.

[156] Web Reference, *Diamond - molecule of the month | http://www.bris.ac.uk/depts/chemistry/motm/diamond/diamond.htm | 2017-09-27.* | Cited on page 26.

[157] Ivan Rehor and Petr Cigler, *Precise estimation of HPHT nanodiamond size distribution based on transmission electron microscopy image analysis*, Diamond and Related Materials **46** (2014), 21–24. | Cited on pages 179 and 212.

[158] Ivan Rehor, Hana Mackova, Sergey K. Filippov, Jan Kucka, Vladimir Proks, Jitka Slegerova, Stuart Turner, Gustaaf Van Tendeloo, Miroslav Ledvina, Martin Hruby, and Petr Cigler, *Fluorescent Nanodiamonds with Bioorthogonally Reactive Protein-Resistant Polymeric Coatings*, ChemPlusChem **79** (2014), no. 1, 21–24. | Cited on pages 30 and 179.

[159] Torsten Rendler, Jitka Neburkova, Ondrej Zemek, Jan Kotek, Andrea Zappe, Zhiqin Chu, Petr Cigler, and Jörg Wrachtrup, *Realtime optical imaging of localized chemical events using programmable diamond quantum nanosensors*, Nature Communications **8** (2017), no. 14701, 1–9. | Cited on pages 7, 16, 30, 179, 180, 201, 218, and 222.

[160] Michael Retsky, Gianni Bonadonna, Romano Demicheli, Judah Folkman, William Hrushesky, and Pinuccia Valagussa, *Hypothesis: Induced angiogenesis*

after surgery in premenopausal node-positive breast cancer patients is a major underlying reason why adjuvant chemotherapy works particularly well for those patients, Breast Cancer Research **6** (2004), no. 4, R372–R374. | Cited on page 75.

[161] Lucio Robledo, Hannes Bernien, Ilse Van Weperen, and Ronald Hanson, *Control and Coherence of the Optical Transition of Single Nitrogen Vacancy Centers in Diamond*, Physical Review Letters **105** (2010), no. 17, 177403. | Cited on page 35.

[162] L. J. Rogers, S. Armstrong, M. J. Sellars, and Manson, *Infrared emission of the NV centre in diamond: Zeeman and uniaxial stress studies*, New Journal of Physics **10** (2008), no. 10, 103024. | Cited on page 33.

[163] Lachlan J. Rogers, Kay D. Jahnke, Marcus W. Doherty, Andreas Dietrich, Liam P. Mcguinness, Christoph Müller, Tokuyuki Teraji, Hitoshi Sumiya, Junichi Isoya, Neil B. Manson, and Fedor Jelezko, *Electronic structure of the negatively charged silicon-vacancy center in diamond*, Physical Review B **89** (2014), no. 23, 235101. | Cited on pages 44, 45, and 97.

[164] Lachlan J. Rogers, Kay D. Jahnke, Mathias H. Metsch, Alp Sipahigil, Jan M. Binder, Tokuyuki Teraji, Hitoshi Sumiya, Junichi Isoya, Mikhail D. Lukin, Philip Hemmer, and Fedor Jelezko, *All-Optical Initialization, Readout, and Coherent Preparation of Single Silicon-Vacancy Spins in Diamond*, Physical Review Letters **113** (2014), no. 26, 263602. | Cited on pages 43 and 44.

[165] Y. Romach, C. Müller, T. Unden, L. J. Rogers, T. Isoda, K. M. Itoh, M. Markham, A. Stacey, J. Meijer, S. Pezzagna, B. Naydenov, L. P. McGuinness, N. Bar-Gill, and F. Jelezko, *Spectroscopy of surface-induced noise using shallow spins in diamond*, Physical Review Letters **114** (2015), no. 1, 017601. | Cited on page 74.

[166] L. Rondin, G. Dantelle, a. Slablab, F. Grosshans, F. Treussart, P. Bergonzo, S. Perruchas, T. Gacoin, M. Chaigneau, H.-C. Chang, V. Jacques, and J.-F. Roch, *Surface-induced charge state conversion of nitrogen-vacancy defects*

in nanodiamonds, Physical Review B **82** (2010), no. 11, 115449. | Cited on pages 30 and 35.

[167] Xing Rong, Jianpei Geng, Fazhan Shi, Ying Liu, Kebiao Xu, Wenchao Ma, Fei Kong, Zhen Jiang, Yang Wu, and Jiangfeng Du, *Experimental fault-tolerant universal quantum gates with solid-state spins under ambient conditions*, Nature Communications **6** (2015), 8748. | Cited on page 31.

[168] Sandra J. Rosenthal, Jerry C. Chang, Oleg Kovtun, James R. McBride, and Ian D. Tomlinson, *Biocompatible quantum dots for biological applications.*, Chemistry & biology **18** (2011), no. 1, 10–24. | Cited on page 87.

[169] T. Rosskopf, A. Dussaux, K. Ohashi, M. Loretz, R. Schirhagl, H. Watanabe, S. Shikata, K. M. Itoh, and C. L. Degen, *Investigation of Surface Magnetic Noise by Shallow Spins in Diamond*, Physical Review Letters **112** (2014), no. 14, 147602. | Cited on pages 73 and 74.

[170] Jakub Rudovský, Petr Cígler, Jan Kotek, Petr Hermann, Pavel Vojtíšek, Ivan Lukeš, Joop A. Peters, Luce Vander Elst, and Robert N. Muller, *Lanthanide(III) Complexes of a Mono(methylphosphonate) Analogue of H_4dota: The Influence of Protonation of the Phosphonate Moiety on the TSAP/SAP Isomer Ratio and the Water Exchange Rate*, Chemistry - A European Journal **11** (2005), no. 8, 2373–2384. | Cited on pages 209 and 215.

[171] Maria J. Ruedas-Rama, Jamie D. Walters, Angel Orte, and Elizabeth A. H. Hall, *Fluorescent nanoparticles for intracellular sensing: A review*, Analytica Chimica Acta **751** (2012), 1–23. | Cited on page 179.

[172] Kamatchi Jothiramalingam Sankaran, Yen-Fu Lin, Wen-Bin Jian, Huang-Chin Chen, Kalpataru Panda, Balakrishnan Sundaravel, Chung-Li Dong, Nyan-Hwa Tai, and I-Nan Lin, *Structural and electrical properties of conducting diamond nanowires*, ACS Applied Materials & Interfaces **5** (2013), no. 4, 1294–1301, PMID: 23327783. | Cited on page 25.

[173] Michael J. Saxton and Ken Jacobson, *SINGLE-PARTICLE TRACKING:Applications to Membrane Dynamics*, Annual Review of Biophysics and Biomolecular Structure **26** (1997), no. 1, 373–399. | Cited on page 84.

[174] Freya Q. Schafer and Garry R. Buettner, *Redox environment of the cell as viewed through the redox state of the glutathione disulfide/glutathione couple*, Free Radical Biology & Medicine **30** (2001), no. 11, 1191–1212. | Cited on pages 205, 220, and 221.

[175] Wolfgang Schnitzler, Georg Jacob, Robert Fickler, Ferdinand Schmidt-Kaler, and Kilian Singer, *Focusing a deterministic single-ion beam*, New Journal of Physics **12** (2010), no. 6, 065023. | Cited on page 46.

[176] Amanda M. Schrand, Houjin Huang, Cataleya Carlson, John J. Schlager, Eiji O. H. Sawa, Saber M. Hussain, and Liming Dai, *Are Diamond Nanoparticles Cytotoxic?*, The Journal of Physical Chemistry B **111** (2007), 2–7. | Cited on pages 87 and 106.

[177] Olga A. Shenderova, Igor I. Vlasov, Stuart Turner, Gustaaf Van Tendeloo, Sergey B. Orlinskii, Andrey A. Shiryaev, Andrey A. Khomich, Sergey N. Sulyanov, Fedor Jelezko, and Joerg Wrachtrup, *Nitrogen Control in Nanodiamond Produced by Detonation Shock-Wave-Assisted Synthesis*, The Journal of Physical Chemistry C **115** (2011), no. 29, 14014–14024. | Cited on page 28.

[178] A.A. Shiryaev, A.V. Fisenko, I.I. Vlasov, L.F. Semjonova, P. Nagel, and S. Schuppler, *Spectroscopic study of impurities and associated defects in nanodiamonds from Efremovka (CV3) and Orgueil (CI) meteorites*, Geochimica et Cosmochimica Acta **75** (2011), no. 11, 3155–3165. | Cited on page 28.

[179] A. Sipahigil, K. D. Jahnke, L. J. Rogers, T. Teraji, J. Isoya, A. S. Zibrov, F. Jelezko, and M. D. Lukin, *Indistinguishable photons from separated silicon-vacancy centers in diamond*, Physical Review Letters **113** (2014), no. 11, 113602. | Cited on page 43.

[180] P. Siyushev, H. Pinto, M. Vörös, A. Gali, F. Jelezko, and J. Wrachtrup, *Optically Controlled Switching of the Charge State of a Single Nitrogen-Vacancy Center in Diamond at Cryogenic Temperatures*, Physical Review Letters **110** (2013), no. 16, 167402. | Cited on pages 33, 34, and 35.

[181] Jitka Slegerova, Miroslav Hajek, Ivan Rehor, Frantisek Sedlak, Jan Stursa, Martin Hruby, and Petr Cigler, *Designing the nanobiointerface of fluorescent*

nanodiamonds: highly selective targeting of glioma cancer cells, Nanoscale **7** (2015), no. 2, 415–420. | Cited on page 30.

[182] Charles P. Slichter, *Prinziple of magnetic resonance*, Springer-Verlag, 1990. | Cited on pages 50, 68, and 72.

[183] Bradley R. Smith, David W. Inglis, Bjornar Sandnes, James R. Rabeau, Andrei V. Zvyagin, Daniel Gruber, Christopher J. Noble, Robert Vogel, Eiji Osawa, and Taras Plakhotnik, *Five-Nanometer Diamond with Luminescent Nitrogen-Vacancy Defect Centers*, Small **5** (2009), no. 14, 1649–1653. | Cited on page 28.

[184] W. V. Smith, P. P. Sorokin, I. L. Gelles, and G. J. Lasher, *Electron-Spin Resonance of Nitrogen Donors in Diamond*, Physical Review **115** (1959), no. 6, 1546–1552. | Cited on page 74.

[185] Xuerui Song, Guanzhong Wang, Xiaodi Liu, Fupan Feng, Junfeng Wang, Liren Lou, and Wei Zhu, *Generation of nitrogen-vacancy color center in nanodiamonds by high temperature annealing*, Applied Physics Letters **102** (2013), no. 13, 133109. | Cited on page 47.

[186] Nick Sperelakis, *Cell physiology sourcebook : essentials of membrane biophysics*, Elsevier, 2012. | Cited on page 83.

[187] P. Spinicelli, A. Dréau, L. Rondin, F. Silva, J. Achard, S. Xavier, S. Bansropun, T. Debuisschert, S. Pezzagna, J. Meijer, V. Jacques, and J-F Roch, *Engineered arrays of nitrogen-vacancy color centers in diamond based on implantation of CN^- molecules through nanoapertures*, New Journal of Physics **13** (2011), no. 2, 025014. | Cited on page 46.

[188] B. V. Spitsyn, S. A. Denisov, N. A. Skorik, A. G. Chopurova, S. A. Parkaeva, L. D. Belyakova, and O. G. Larionov, *The physical-chemical study of detonation nanodiamond application in adsorption and chromatography*, Diamond and Related Materials **19** (2010), no. 2-3, 123–127. | Cited on page 29.

[189] T. Staudacher, F. Shi, S. Pezzagna, J. Meijer, J. Du, C. A. Meriles, F. Reinhard, and J. Wrachtrup, *Nuclear Magnetic Resonance Spectroscopy on a*

(5-Nanometer)^3 *Sample Volume*, Science **339** (2013), no. 6119, 561–563. | Cited on page 31.

[190] Stepan Stehlik, Marian Varga, Martin Ledinsky, Vit Jirasek, Anna Artemenko, Halyna Kozak, Lukas Ondic, Viera Skakalova, Giacomo Argentero, Timothy Pennycook, Jannik C Meyer, Antonin Fejfar, Alexander Kromka, and Bohuslav Rezek, *Size and Purity Control of HPHT Nanodiamonds down to 1 nm*, Journal of Physical Chemistry C **119** (2015), no. 49, 27708–27720. | Cited on page 26.

[191] Stepan Stehlik, Marian Varga, Martin Ledinsky, Daria Miliaieva, Halyna Kozak, Viera Skakalova, Clemens Mangler, Timothy J. Pennycook, Jannik C. Meyer, Alexander Kromka, and Bohuslav Rezek, *High-yield fabrication and properties of 1.4 nm nanodiamonds with narrow size distribution*, Scientific Reports **6** (2016), 38419. | Cited on pages 28 and 103.

[192] H. Sternschulte, K. Thonke, R. Sauer, P. C. Münzinger, and P. Michler, *1.681-eV luminescence center in chemical-vapor-deposited homoepitaxial diamond films*, Physical Review B **50** (1994), no. 19, 554–560. | Cited on page 92.

[193] Erik Strandberg and Per-Olof Westlund, *^{1}H NMRD Profile and ESR Lineshape Calculation for an Isotropic Electron Spin System with S = 7/2. A Generalized Modified Solomon-Bloembergen-Morgan Theory for Nonextreme-Narrowing Conditions*, Journal of Magnetic Resonance, Series A **122** (1996), no. 2, 179–191. | Cited on page 76.

[194] Kazunori Sugiura, Takeharu Nagai, Masahiro Nakano, Hiroshi Ichinose, Takakazu Nakabayashi, Nobuhiro Ohta, and Toru Hisabori, *Redox sensor proteins for highly sensitive direct imaging of intracellular redox state*, Biochemical and Biophysical Research Communications **457** (2015), no. 3, 242–248. | Cited on page 179.

[195] Kenichi Suzuki, Ken Ritchie, Eriko Kajikawa, Takahiro Fujiwara, and Akihiro Kusumi, *Rapid Hop Diffusion of a G-Protein-Coupled Receptor in the Plasma Membrane as Revealed by Single-Molecule Techniques*, Biophysical Journal **88** (2005), no. 5, 3659–3680. | Cited on page 113.

[196] Goshu Tamura, Yuya Shinohara, Atsushi Tamura, Yusuke Sanada, Motoi Oishi, Isamu Akiba, Yukio Nagasaki, Kazuo Sakurai, and Yoshiyuki Amemiya, *Dependence of the swelling behavior of a pH-responsive PEG-modified nanogel on the cross-link density*, Polymer Journal **44** (2011), 240–244. | Cited on page 222.

[197] V. F. Tatsii, A. V. Bochko, and G. S. Oleinik, *Structure and Properties of Dalan Detonation Diamonds*, Combustion, Explosion, and Shock Wave **45** (2009), no. 1, 95–103. | Cited on page 27.

[198] Arthur Taylor, Katie M. Wilson, Patricia Murray, David G. Fernig, and Raphaeï Lévy, *Long-term tracking of cells using inorganic nanoparticles as contrast agents: are we there yet?*, Chem. Soc. Rev. **41** (2012), no. 41, 2707–2717. | Cited on page 87.

[199] Tokuyuki Teraji, Takashi Taniguchi, Satoshi Koizumi, Kenji Watanabe, Meiyong Liao, Yasuo Koide, and Junichi Isoya, *Chemical Vapor Deposition of* $^{1}2C$ *Isotopically Enriched Polycrystalline Diamond*, Japanese Journal of Applied Physics **51** (2012), 090104. | Cited on page 27.

[200] J.-P P. Tetienne, T. Hingant, L. Rondin, A. Cavaillès, L. Mayer, G. Dantelle, T. Gacoin, J. Wrachtrup, J.-F F. Roch, V. Jacques, A Cavailì Es, L. Mayer, G. Dantelle, T. Gacoin, J. Wrachtrup, J.-F F. Roch, and V. Jacques, *Spin relaxometry of single nitrogen-vacancy defects in diamond nanocrystals for magnetic noise sensing*, Physical Review B **87** (2013), no. 23, 235436. | Cited on pages 74, 179, and 209.

[201] Julia Tisler, Gopalakrishnan Balasubramanian, Boris Naydenov, Roman Kolesov, Bernhard Grotz, Rolf Reuter, Jean-Paul Boudou, Patrick A. Curmi, Mohamed Sennour, Alain Thorel, Michael Börsch, Kurt Aulenbacher, Rainer Erdmann, Philip R. Hemmer, Fedor Jelezko, and Jö Rg Wrachtrup, *Fluorescence and Spin Properties of Defects in Single Digit Nanodiamonds*, ACS Nano **3** (2009), no. 7, 1959–1965. | Cited on pages 92 and 186.

[202] Norio Tokuda, *Homoepitaxial diamond growth by plasma-enhanced chemical vapor deposition*, pp. 1–29, Springer International Publishing, Cham, 2015. | Cited on page 29.

[203] David M. Toyli, Charles F. de las Casas, David J. Christle, Viatcheslav V. Dobrovitski, and David D. Awschalom, *Fluorescence thermometry enhanced by the quantum coherence of single spins in diamond*, Proceedings of the National Academy of Sciences of the United States of America **110** (2013), no. 21, 8417–8421. | Cited on pages 31 and 67.

[204] David M. Toyli, Christoph D. Weis, Gregory D. Fuchs, Thomas Schenkel, and David D. Awschalom, *Chip-scale nanofabrication of single spins and spin arrays in diamond*, Nano letters **10** (2010), no. 8, 3168–3172. | Cited on page 46.

[205] Matthew E. Trusheim, Luozhou Li, Abdelghani Laraoui, Edward H. Chen, Hassaram Bakhru, Tim Schröder, Ophir Gaathon, Carlos A. Meriles, and Dirk Englund, *Scalable fabrication of high purity diamond nanocrystals with long-spin-coherence nitrogen vacancy centers*, Nano Letters **14** (2014), no. 1, 32–36. | Cited on page 186.

[206] Kim M Tsoi, Qin Dai, Benjamin A Alman, and Warren C W Chan, *Are Quantum Dots Toxic? Exploring the Discrepancy Between Cell Culture and Animal Studies*, ACCOUNTS OF CHEMICAL RESEARCH **46** (2013), no. 3, 662–671. | Cited on page 87.

[207] Denis Uhland, Torsten Rendler, Matthias Widmann, Sang-Yun Lee, Jörg Wrachtrup, and Ilja Gerhardt, *Single Molecule DNA Detection with an Atomic Vapor Notch Filter*, EPJ Quantum Technology **2** (2015), no. 20, 1–12. | Cited on page 18.

[208] C. Uzan-Saguy, C. Cytermann, R. Brener, V. Richter, M. Shaanan, and R. Kalish, *Damage threshold for ion-beam induced graphitization of diamond*, Applied Physical Letters **67** (1995), no. 9, 1194–1196. | Cited on page 47.

[209] Vairakkannu Vaijayanthimala, Yan-Kai Tzeng, Huan-Cheng Chang, and Chung-Leung Li, *The biocompatibility of fluorescent nanodiamonds and their*

mechanism of cellular uptake, Nanotechnology **20** (2009), no. 42, 425103. | Cited on pages 87 and 106.

[210] Mads S. Vinding, Ivan I. Maximov, Zdenek Tosner, and Niels Chr. Nielsen, *Fast numerical design of spatial-selective rf pulses in MRI using Krotov and quasi- Newton based optimal control methods Fast numerical design of spatial-selective rf pulses in MRI using Krotov and quasi-Newton based optimal control methods*, The Journal of Chemical Physics **137** (2012), no. 5, 054203. | Cited on page 61.

[211] L. Viola, E. M. Fortunato, S. Lloyd, C. Tseng, and D. G. Cory, *Stochastic Resonance and Nonlinear Response using NMR Spectroscopy*, Physical Review Letters **84** (2000), no. 24, 5466–5469. | Cited on page 55.

[212] Igor I. Vlasov, Amanda S. Barnard, Victor G. Ralchenko, Oleg I. Lebedev, Mikhail V. Kanzyuba, Alexey V. Saveliev, Vitaly I. Konov, and Etienne Goovaerts, *Nanodiamond Photoemitters Based on Strong Narrow-Band Luminescence from Silicon-Vacancy Defects*, Advanced Materials **21** (2009), no. 7, 808–812. | Cited on pages 43 and 48.

[213] Igor I. Vlasov, Olga Shenderova, Stuart Turner, Oleg I. Lebedev, Artem A. Basov, Ilmo Sildos, Mickel Rähn, Andrey A. Shiryaev, and Gustaaf Van Tendeloo, *Nitrogen and Luminescent Nitrogen-Vacancy Defects in Detonation Nanodiamond*, Small **6** (2010), no. 5, 687–694. | Cited on page 28.

[214] Igor I. Vlasov, Andrey a Shiryaev, Torsten Rendler, Steffen Steinert, Sang-Yun Lee, Denis Antonov, Márton Vörös, Fedor Jelezko, Anatolii V. Fisenko, Lubov F. Semjonova, Johannes Biskupek, Ute Kaiser, Oleg I. Lebedev, Ilmo Sildos, Philip R. Hemmer, Vitaly I. Konov, Adam Gali, and Jörg Wrachtrup, *Molecular-sized fluorescent nanodiamonds*, Nature Nanotechnology **9** (2013), 54–58. | Cited on pages 3, 12, 28, 43, 48, 87, 88, 89, 90, 101, and 102.

[215] Changling Wang, Ruizhi Xu, Wenjuan Tian, Xiaoli Jiang, Zhengyu Cui, Meng Wang, Huaming Sun, Kun Fang, and Ning Gu, *Determining intracellular temperature at single-cell level by a novel thermocouple method*, Cell Research **21** (2011), no. 10, 1517–1519. | Cited on page 105.

[216] Chenguang Wang, Masayasu Taki, Yoshikatsu Sato, Aiko Fukazawa, Tetsuya Higashiyama, and Shigehiro Yamaguchi, *Super-Photostable Phosphole-Based Dye for Multiple-Acquisition Stimulated Emission Depletion Imaging*, Journal of the American Chemical Society **139** (2017), no. 30, 10374–10381. | Cited on page 87.

[217] Chunlang Wang, Christian Kurtsiefer, Harald Weinfurter, and Bernd Burchard, *Single photon emission from SiV centres in diamond produced by ion implantation*, Journal of Physics B: Atomic, Molecular and Optical Physics **39** (2006), 37–41. | Cited on pages 44 and 100.

[218] Robert H Webb, *Confocal optical microscopy*, Rep. Prog. Phys **59** (1996), no. 3, 427. | Cited on page 19.

[219] M. Widmann, S.-Y. Lee, T. Rendler, N.T. Son, H. Fedder, S. Paik, L.-P. Yang, N. Zhao, S. Yang, I. Booker, A. Denisenko, M. Jamali, S. Ali Momenzadeh, I. Gerhardt, T. Ohshima, A. Gali, E. Janz?n, and J. Wrachtrup, *Coherent control of single spins in silicon carbide at room temperature*, Nature Materials **14** (2015), 164–168. | Cited on page 23.

[220] Oliver A. Williams, Jakob Hees, Christel Dieker, Wolfgang Jäger, Lutz Kirste, and Christoph E. Nebel, *Size-Dependent Reactivity of Diamond Nanoparticles*, ACS Nano **4** (2010), no. 8, 4824–4830. | Cited on page 29.

[221] Yuzhou Wu, Fedor Jelezko, Martin B. Plenio, and Tanja Weil, *Diamond Quantum Devices in Biology*, Angewandte Chemie - International Edition **55** (2016), no. 23, 6586–6598. | Cited on page 28.

[222] B. V. Yavkin, G. V. Mamin, M. R. Gafurov, and S. B. Orlinskii, *Size-dependent concentration of N0 paramagnetic centres in HPHT nanodiamonds*, Magnetic Resonance in Solids **17** (2015), no. 1, 1–7. | Cited on page 74.

[223] M. Yeganeh, P. R. Coxon, A. C. Brieva, V. R. Dhanak, L. Šiller, and Yu V. Butenko, *Atomic hydrogen treatment of nanodiamond powder studied with photoemission spectroscopy*, Physical Review B **75** (2007), no. 15, 155404. | Cited on page 29.

[224] Sebastian Zaiser, Torsten Rendler, Ingmar Jakobi, Thomas Wolf, Sang-Yun S.-Y. Lee, Samuel Wagner, Ville Bergholm, T. Schulte-Herbrüggen, Philipp Neumann, and Jörg Wrachtrup, *Enhancing quantum sensing sensitivity by a quantum memory*, Nature Communications **7** (2016), 12279. | Cited on page 143.

[225] Alexandr M. Zaitsev, *Optical Properties of Diamond : a Data Handbook*, Springer-Verlag, 2001. | Cited on pages 31 and 46.

[226] Yafei Zhang, Chuanyi Zang, Hongan Ma, Zhongzhu Liang, Lin Zhou, Shangsheng Li, and Xiaopeng Jia, *HPHT synthesis of large single crystal diamond doped with high nitrogen concentration*, Diamond and Related Materials **17** (2008), no. 2, 209–211. | Cited on page 26.